Microwave Transmissivity of Sub-Wavelength Metallic Structures

Submitted by **James David Edmunds**
to the University of Exeter
as a thesis for the degree of
Doctor of Philosophy in Physics
May 2011

I certify that all material in this thesis which is not my own work has been identified and that no material has previously been submitted and approved for the award of a degree by this or any other University.

Signature: ……

Abstract

The use of patterned metallic surfaces for the control of the transmission of microwave radiation has been reinvigorated in recent years due to the success and interest in metamaterial research. These metallic periodic structures, commonly referred to as frequency selective screens (FSSs), allow responses to be tailored according to the geometry of the metallic structure as opposed to the material composition. A consequence of the presence of a metallic corrugation is the possible excitation of surfaces waves (commonly referred to as surface plasmon polaritons at visible frequencies). Surface waves can be utilised to achieve further control of the transmission properties of a structure. In this thesis several highly original metallic structures are investigated which use FSS and surface wave concepts. These structures exhibit interesting and previously unexplained transmission behaviour.

The experimental chapters within this thesis are divided into two areas. The first three experimental chapters (4-6) present original investigations into the excitation of diffractively coupled surface waves on metallic hole/patch arrays and their role in the enhanced transmission/reflection of microwave radiation. The importance of metallic connectivity within arrays is highlighted through measurements of the metallic filling fraction dependence on the transmission properties of regular periodic and random arrays.

The last two experimental chapters (7-8) contain investigations into the transmission properties of two novel resonant cavities. The structure studied in chapter 7 provides a mechanism for remarkably enhanced microwave transmission on resonance through an otherwise opaque continuous thin metal film. The second resonant cavity structure in chapter 8 uses a resonant array of metallic crosses to form a ‘resonant mirror’ Fabry-Perot cavity. These resonant FSSs exhibit a frequency dependent transmission/reflection and phase response thus producing an interesting series of modes which have very different properties to those supported by a non-resonant mirror etalon.

Table of Contents

List of Figures

Acknowledgements

There are a number of people that I would like to thank for their help throughout my time working within the photonics group here at Exeter. First of all I would like to thank Roy and Alastair for giving me the opportunity to work with them within their microwave photonics group. The microwave group has grown by an enormous amount over the last few years and Alastair should be very proud of what he has achieved. I would also like to thank Ian Youngs and Dstl for the support and funding they have provided throughout the duration of my studies. I also need to thank Euan Hendry for his help with modal-matching modelling and general theory of hole arrays, he has such a broad knowledge of physics and is one of the most enthusiastic people in the group. My thanks also go to Julian Moger for being my mentor over the last few years.

The experiments I have performed could of course not have been realised without the support of the stores and mechanical workshop, especially the help from Pete Cann, Nick Cole, Matt Wears, Kevyn White and John Meakin. A job was never too big for them and they were always full of ideas to solve the numerous problems I brought to them.

I would also like to thank the other members of the photonics group, Ian Hooper who always had helpful suggestions. Matt Lockyear, for helping with experiments and for attempting to teach me how to snowboard in Austria. James Parsons, who helped me get started with HFSS, was always helpful whenever I had a problem, and kept everyone entertained with his antics. Martyn Gadsdon, who we have had the pleasure of returning to Exeter, for his help with Fourier modal method modelling, he also always knows how to liven up the mood with one of his anecdotes about his numerous past ‘experiences’. Members of the microwave group, Helen Rance and Rob Kelly for helping me out with sample fabrication and experiments when I first started, as well as Celia Butler, ‘Sergeant’ Mel Taylor, Matt ‘Biggy’ Biginton, Lizzy Brock and Simon Berry for being good work colleagues and offering helpful suggestions whenever I had a problem. I would also like to thank Joe Noyes and Ed Stone for working with me in the second year lab whilst we tried to encourage the undergraduates to do some work. Also the other ‘Basement’ members of the group need a mention, Steve Luke, Chris Holmes, Tom Constant, Caroline Pouya, Alfie Lethbridge and the new members of the group, Tim Starkey, Matt Nixon and Alasdair Murray. I would like to thank Chris

Burrows for being a good flat and office sharer as well as the other guys who later joined the office, Evgeny and Chinna for being good company. I would also like to thank all of the people who offered helpful suggestions in group meetings as well as all of the people I have forgotten to mention as I am sure there are many.

Finally I would like to thank my friends and family for supporting me over the last few years.

1 Introduction

The work in this thesis focuses on the control of microwave transmission through the use of metallic structure. This area of physics has been popular for a number of years particularly in the design of frequency selective surfaces (FSSs) (Munk et al.[1] and references therein), which utilise metallic structure to give the frequency dependent response desired. Use of metallic structure to generate tailor made responses has been reinvigorated in recent years due to the popularity of attempts to create designer 'metamaterial' structures[2-4]. These metamaterial structures make use of metallic structuring in order to generate electromagnetic properties that cannot be found in nature. Another area of research involving structured metallic surfaces which has been known for at least a century but has become increasingly studied over the last two decades is the excitation and manipulation of surface waves[5-11]. Interest in surface waves (or surface plasmons, as they are commonly known at optical frequencies) was reignited in 1998 through Ebbesen and co-workers[12] observation of enhanced optical transmission (EOT) where they confirmed that transmission through an array of below-waveguide cut-off holes could far exceed that predicted by Bethe[13] for an isolated hole. This transmission enhancement was later attributed to the excitation of diffractively coupled surface waves[14]. In this thesis a number of original structures which utilise surface wave excitation, frequency selective screen concepts and other resonances such as waveguide modes have been experimentally investigated and explained with the use of the finite-element method and other modelling techniques.

In chapters 2 and 3 the background theory related to the experimental chapters in this thesis is introduced. Chapters 4 through 8 present original experimental investigations into metallic structured surfaces studied at microwave frequencies. These experimental chapters are divided into two areas, chapters 4 through 6, are primarily concerned with the excitation of diffractively coupled surface waves, while chapters 7 and 8 present investigations into resonant cavities that mediate new and interesting transmission properties.

In chapter 2 a general background on the microwave transmission properties of structured metallic surfaces and methods through which transmission can be manipulated is presented. The concept of a frequency selective surface (FSS) and the

fundamental physics behind how different structures transmit/reflect selective frequencies is introduced. The importance of Babinet's principle[15,16] is also derived and discussed, this principle allows the response of complementary PEC structures to be easily predicted. The dispersion of the electromagnetic surface wave supported on the interface of two dissimilar materials is derived and its properties at microwave frequencies discussed. Manipulation of the surface wave dispersion and confinement through use of surface structuring is also covered.

In chapter 3 the experimental and modelling methods through which data were acquired for the experimental chapters of the thesis is explained. All of the experiments in this thesis were performed at microwave frequencies with a free-space collimated beam setup that utilises parabolic mirrors with source and detector horns. Modelling is presented in the experimental chapters alongside data to compare experimental results with theoretical predictions. Field plots generated from these models allow a further understanding of the underlying physics to be gained. The main modelling method used was the finite element method implemented by the commercial software package Ansoft's HFSS[17]. In chapter 3, discussion on the finite element method can be found as well as detailed descriptions of the individual models used. When the finite element method was not suitable for a particular modelling task, another modelling technique was chosen. Descriptions of these other techniques, the modal-matching technique and the Fourier modal method are also given within this chapter.

Chapter 4 is the first experimental chapter in this thesis, in which the effect of metallic connectivity on the transmission properties of metal-dielectric composite arrays is explored. One may initially expect the microwave transmission through a metallic array to be determined by the percentage occupancy of the metal due to its perfectly conducting characteristic however this is not always the case. The structure of the array has a strong effect on the response. In this chapter a unique experimental study into both regular and random metallic arrays is presented showing vastly different responses. Samples were fabricated for a range of metallic occupancies spanning across the connectivity (or percolation for the random case) threshold. The results from the two types of arrays (regular and random) differ due to the incident radiation being able to diffractively couple strongly to surface waves on the regular arrays since they have a well defined periodicity, producing a strong feature in the transmission response. This resonant feature leads to a strong dependence of the transmission level on connectivity

across the 50% threshold. Random arrays lack the well defined periodicity and as such no strong resonant modes are excited leading to a much more gradual transition across the percolation threshold.

Chapter 5 further investigates the excitation of diffractively coupled surface waves on regular metallic arrays, in particular focusing on the dispersion of these modes. An experimental incident angle dependent investigation into a complementary pair of structures, a patch array and a hole array is performed showing that coupling to the surface wave on the patch array is achieved by scattering from the orthogonal grating vector to that on the hole array for the same incident polarisation and plane of incidence. These new and interesting results are compared to that expected from Babinet's principle and explained through the use of electric and magnetic field predictions generated through FEM modelling. It is found that the different results obtained for the patch and hole array structures are a result of the connectivity of the structure. The connected structures can support currents which induce magnetic fields. The periodicity in these magnetic fields determines which grating vector induces the strongest scattering and hence the form of the dispersion of the surface modes.

In chapter 6 a new experimental study into coupled surface waves on deep hole arrays is presented. Measurements are focused on two regimes, one where the array is composed of small holes such that their waveguide cut-off frequency lies above the onset of diffraction and a second case of large holes where the cut-off frequency lies below the onset of diffraction. Samples were milled from aluminium plates of different thicknesses to allow a thickness dependence study to be performed. Below the diffraction edge results for the two regimes are vastly different; arrays of small holes only support two modes with evanescent field solutions due to being below the waveguide cut-off. Large holes however are able to support propagating fields and therefore can support many modes, with electric field quantisation inside the hole, the number of modes supported being dependent on the thickness of the array.

In chapter 7 an experimental study of a novel resonant cavity that provides enhanced transmission through an otherwise opaque thin metal film is presented. A thin metal film of thickness as little as 60 nm is sufficient to reduce microwave transmission to < 0.1 %. This is due to the large complex refractive index of the film and therefore large impedance mismatch at the air/metal interface. The resonant cavity presented is an

extension to one that was first presented by Hibbins et al.[18], their structure supported a series of standing wave resonances and is an efficient thin microwave absorber. The structure of interest here is comprised of a pair of metallic lamellar gratings separated by a dielectric region with a thin metal film in the centre. The metal film acts as a tunnel barrier such that on resonance of the cavity, high fields either side of the film allow tunnelling to occur and therefore transmission of ~ 30 % on resonance of the fundamental mode. Angle dependent studies of the first three modes have been performed and the coupling conditions described. Due to the symmetry of the fields only the odd modes can be coupled to at normal incidence as the even modes require a phase shift in the incident electric field across the cavity openings for coupling to occur.

In chapter 8 the experimental study of arrays of metallic crosses is performed. Arrays of crosses have been previously investigated by Ulrich[19] and shown to exhibit a stop-band on resonance at a resonant wavelength of $\sim 2l$, where l is the length of the cross bars. On resonance the radiation reradiated from the crosses destructively interferes with the incident radiation leading to a transmission minimum and a reflection maximum. In this chapter, two arrays of crosses are used to form a resonant cavity much like a Fabry-Perot etalon which can support standing waves in the region between the two arrays. Since the arrays have a frequency dependent reflectivity and phase due to their resonant behaviour the modes observed are not simple standing waves, as the boundary condition at the reflecting surfaces is frequency dependent. This means that the frequency of the modes is highly dependent on the proximity of the standing wave condition to the resonant frequency of the array.

Chapter 9 contains a summary of the original and interesting work presented in this thesis and possible ideas for future experiments are discussed. A list of publications and conferences attended is provided along with planned future journal submissions.

2 Microwave Transmission through Structured Metallic Surfaces

2.1 Introduction

For many years metallic structure has been utilised to control the transmission of electromagnetic (EM) radiation in many regions of the spectrum[1,20-23]. The area focused on in this thesis is the microwave regime. Microwaves have many applications, one of the major uses being in communications; microwaves are used in satellite and radar communications as well as other wireless devices such as mobile broadband. Other uses include radio astronomy, spectroscopy and power transfer devices such as the microwave oven and crowd control devices. All of these applications rely on devices and components which are able to control and manipulate microwaves to produce a desired response. Some of the initially studied structures used to control microwave transmission were simple frequency selective screens (FSSs) which incorporate periodic metallic elements to produce a desired frequency dependent response. These screens use elements of differing sizes and geometries to manipulate the response of electrons to an incident electromagnetic field in order to produce a frequency dependent response. They are often used to shield buildings and devices from unwanted radiation. These devices have continued to become more sophisticated as greater demands are required of them such as increased bandwidth and operation over a larger range of incident angle.

One of the consequences of using periodic metallic structure in a microwave system is the excitation of surface modes close to the onset of diffraction. Surface modes are confined at the interface between a metal and dielectric and propagate along the surface with fields that decay exponentially into the media either side. These surface waves lie outside of the light cone and are non-radiative. They however can be coupled to diffractively with incident radiation if the surface is not flat or more often has a periodic corrugation. Surface waves can sometimes be an unwanted consequence of using a metallic periodic structure to give a filter response however surface waves can also be used to help facilitate selective transmission[12,24] as well as absorption[25,26].

Research into the field of periodic metallic structures has been reinvigorated in recent years due to the emergence of metamaterial[27] research. Metamaterials are artificial materials composed of periodic sub-wavelength inclusions that produce a response that is governed by their structure as well as their material composition. Such structures can produce responses that are unattainable with materials found in nature. Since these structures are composed of elements that are sub-wavelength they can be described as having effective macroscopic properties, i.e. an effective permittivity, permeability and refractive index. Metamaterials can be used to create effective media which are classed as single negative (SNG), for which either the permittivity[28] or permeability[29] is effectively negative; double negative (DNG) or negative index media can also be created with the use of metamaterials for which both the effective permittivity and the effective permeability are simultaneously negative yielding a negative refractive index[4,30] leading to the possibility of negative refraction. These DNG media have potential for application in cloaking[31-34] and lensing[35,36]. Other uses of metamaterials include designer plasmonic[2,3] and high impedance surfaces[11] as well as electromagnetic band gap[37] and chiral metamaterials[38,39].

In this chapter the principles governing the transmissive behaviour of metallic structures is briefly reviewed. The basic principles of FSS design will be introduced along with Babinet's principle, which is used to predict the response of complementary PEC screens. Electromagnetic surface waves supported at the interface of two dissimilar media is then discussed and structuring of surfaces to increase binding of these waves will also be covered.

2.2 Frequency Selective Screens

2.2.1 Response of Electrons to an External Field

In order to understand the transmission and reflection response of a structured metal surface one must consider how the 'free' electrons respond to an external electric field.

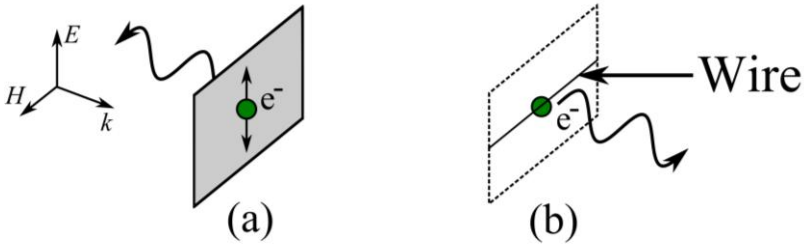

***Figure 2.2.1**. (a) Induced oscillations, low transmittance. (b) Electrons confined to a wire, no induced oscillations, high transmittance*

Consider a plane wave incident on a metal sheet as in *Figure 2.2.1a,* electrons in the sheet will oscillate in the direction of the incident electric field. Accelerating charges emit radiation and so the electrons reradiate like an electric dipole. The radiation emitted by the electrons is 180° out of phase with the incident radiation and so the reradiated and incident radiation destructively interferes resulting in a very small level of transmission. The radiation re-emitted by the oscillating electron into the incident medium is the reflected wave[40].

In *Figure 2.2.1b* electrons are confined to a wire running perpendicular to the incident electric field. Since the electrons are geometrically confined to this wire very limited oscillations can occur in the direction of the electric field. This results in large transmission of the incident electromagnetic wave.

It is these basic principles which determine the transmission response of frequency selective screens (FSSs). Utilising various geometries and restricting the oscillations of the free electrons can produce tailor made frequency selective responses.

2.2.2 Capacitive and Inductive Filters

2.2.2.1 Capacitive Strip Filter

An array of long (>> λ) thin metallic strips as in *Figure 2.2.2,* orientated such that the strips are perpendicular to the incident electric field behaves as a capacitive, low-pass filter[41]. It can be described as having a capacitive surface impedance due to the capacitance between the neighbouring strips. The surface impedance, Z_s is described by *Equation 2.2.1* where E_{surf} and H_{surf} are the electric and magnetic fields at the surface.

$$Z_s = \frac{E_{surf}}{H_{surf}}$$ *Equation 2.2.1*

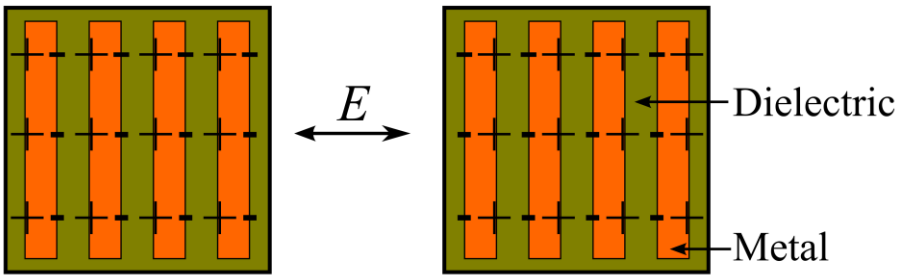

***Figure 2.2.2**. Metallic lamellar grating on a substrate. The alternating 'edge' charges produce a capacitive response.*

The electron cloud at the surface of the conducting regions of the filter oscillates in response to the incident electric field resulting in a net charge build up at the edges of the strips. If a high frequency, short wavelength source is incident on the array these regions of net charge oscillate as indicated in *Figure 2.2.2*. The oscillation of the electrons and subsequent re-emission of the electromagnetic energy leads to high reflection and low transmission. When low frequency, long wavelength radiation is incident on the array the electrons oscillate with a lower frequency and because they are confined in the direction of the electric field due to the edges of the strip, they remain stationary for a larger proportion of the temporal cycle of the electromagnetic wave, during this time they cannot respond to the electric field and so the transmission is high.

2.2.2.2 Inductive Strip Filter

The array of metallic strips discussed in the previous section may also be used as a high-pass inductive filter[41], having an inductive surface impedance when the strips are orientated parallel to the incident electric field as in *Figure 2.2.3*. It is inductive as the strips can support the flow of current due to being much longer than the incident wavelength in the direction of the polarisation of the incident electric field.

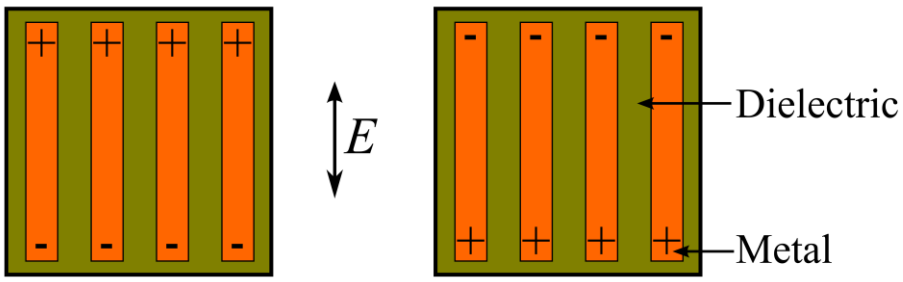

***Figure 2.2.3**. Metallic lamellar grating on a substrate. The electric field oscillates between two states resulting in an inductive, high-pass filtering response.*

The electron cloud oscillates along the length of the strips in response to the incident electric field. In the long wavelength, low frequency limit the electron cloud is able to travel a long distance before it is forced to change direction, allowing a large amount of energy to be transferred to the electrons and re-emitted out of phase with the incident radiation, resulting in low transmission and high reflection. For the short wavelength, high frequency limit the electron cloud oscillates at high frequency but with a much smaller displacement. This interaction transfers less energy so the filter is less efficient and transmission is higher.

2.2.2.3 Mesh Filters

The geometrical properties of the inductive and capacitive strip filters discussed in the previous sections can be utilised in order to make two-dimensional filters with high or low-pass filtering properties. The inductive mesh and its complementary structure the capacitive mesh or patch array, can be seen in *Figure 2.2.4*.

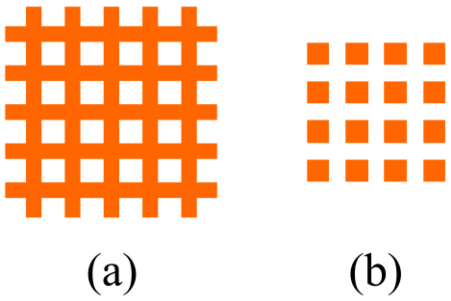

***Figure 2.2.4**.(a) An inductive mesh filter (High pass) (b) A capacitive mesh filter (Low pass)*

The mesh filters shown in *Figure 2.2.4* behave in a similar manner to the filters shown in the *Section 2.2.2* but with the added benefit that they are polarisation independent. The inductive mesh allows the electrons in the metal to travel across the whole geometry of the filter and a low frequency source is again able to induce large scale motion of electrons leading to strong reflection and poor transmission.

The complementary structure of the inductive mesh is the capacitive mesh shown in *Figure 2.2.4b*. The behaviour of filters can be predicted by Babinet's principle[16] (see *Section 2.3*) if the response of its complement is known. The capacitive mesh behaves as a low pass filter because the electrons are confined to the metal patches and respond to the electric field when switched rapidly between two different charged states due to a high frequency source.

It is well known that metallic inductive meshes filter out low frequencies because they are commonly used to reflect microwaves, for example on the glass door of a microwave oven or on a satellite dish. Whereas the capacitive mesh is very poor at reflecting microwave radiation.

2.3 Babinet's Principle

M. Babinet formulated a principle in 1837[15] relating the diffraction from a screen and its complement to that of no screen; this is known as Babinet's principle. Let $U_1(P)$ and $U_2(P)$ be the complex amplitude of the diffracted signal when screen 1 or its complement, screen 2 is placed between the source and point of observation, *P*. These amplitudes are related to the amplitude in the presence of no screen, $U(P)=1$ by *Equation 2.3.1*.

$$U(P)=1=U_1(P)+U_2(P) \qquad \textit{Equation 2.3.1}$$

The sum of the diffraction patterns caused by screens one and two is equal to that of the undisturbed beam. This is the scalar form of Babinet's principle however an analogous theorem extending its use to that of electromagnetic radiation was derived by H. G. Booker[16] in 1946.

2.3.1 Electromagnetic form of Babinet's Principle

This derivation of Babinet's principle is adapted from *Principles of Optics, Born and Wolf, p559*[42].

Consider a two-dimensional (zero thickness) perforated perfect electrical conductor (PEC) (*Figure 2.3.1*), with an electromagnetic wave incident in the negative *z* direction

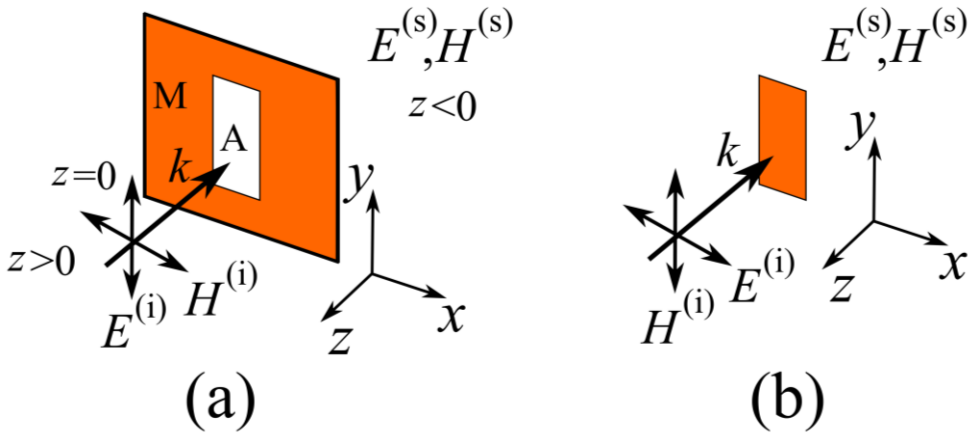

Figure 2.3.1. *Schematic illustration of a complementary pair of metal structures showing coordinate system, incident and scattered fields., (a) Hole in a PEC sheet and (b) PEC patch.*

On the conducting regions (M) the boundary conditions state that the tangential components of the electric field must equal zero.

$$E_x^{(i)} + E_x^{(s)} = E_y^{(i)} + E_y^{(s)} = 0\,, \qquad \textit{Equation 2.3.2}$$

where $\underline{E}^{(i)}$ and $\underline{E}^{(s)}$ are the incident and scattered electric fields respectively.

The boundary conditions on the aperture region are such that the scattered tangential magnetic *H* fields are zero since no currents are induced in this region.

$$H_x^{(s)} = H_y^{(s)} = 0 \qquad \textit{Equation 2.3.3}$$

Consider the polarisation of the electric vector of the incident radiation on the patch to be rotated by 90° with respect to that incident on the aperture. This is equivalent to a transformation of $E \rightarrow H$.

The fields on screen 1 can be represented in the following form:

$$\underline{E}_1^{(i)} = \underline{F}^{(i)}, \qquad \textit{Equation 2.3.4}$$

here $\underline{E}_1^{(i)}$ is the electric field incident on screen 1.

On region M, *Equation 2.3.5* and *Equation 2.3.6* apply.

$$E_{1x}^{(s)} = -F_x^{(i)} \qquad \textit{Equation 2.3.5}$$

$$E_{1y}^{(s)} = -F_y^{(i)} \qquad \textit{Equation 2.3.6}$$

On region A, *Equation 2.3.7* is applicable.

$$H_{1x}^{(s)} = H_{1y}^{(s)} = 0 \qquad \textit{Equation 2.3.7}$$

Similarly the fields on screen 2 can also be represented in this manner.

$$\underline{H}_2^{(i)} = \underline{F}^{(i)} \qquad \textit{Equation 2.3.8}$$

Where $\underline{H}_2^{(i)}$ is the magnetic field incident on screen 2.

$$E_{2x}^{(s)} = E_{2y}^{(s)} = 0 \qquad \textit{Equation 2.3.9}$$

$$H_{2x}^{(s)} = F_x^{(i)} \qquad \textit{Equation 2.3.10}$$

$$H_{2y}^{(s)} = F_y^{(i)} \qquad \textit{Equation 2.3.11}$$

Maxwell's equations are invariant in free space under the transformation, $E \rightarrow H,\ H \rightarrow -E$.

Combining *Equation 2.3.5* - *Equation 2.3.11*:

$$\underline{H}_2 = -\underline{E}_1^{(s)} \qquad \textit{Equation 2.3.12}$$

$$\underline{E}_1 = \underline{E}_1^{(i)} + \underline{E}_1^{(s)} \qquad \textit{Equation 2.3.13}$$

$$\underline{E}_1 = \underline{F}^{(i)} - \underline{H}_2 \qquad \textit{Equation 2.3.14}$$

Therefore,

$$E_1 + H_2 = F^{(i)} \qquad \textit{Equation 2.3.15}$$

Hence the sum of the electric fields transmitted through screen 1 and the magnetic fields (equivalent to a 90° rotation of incident polarisation) through screen 2 is equal to the incident field. This implies that the transmitted fields through a structure will be equal to the reflected fields from its complement. This is only true for a two-dimensional perfect electrical conductor with no substrate, but in the microwave regime where metals are near perfectly conducting and substrates are typically sub-wavelength, it can be a useful principle to predict the response of structures.

2.4 Surface Waves

2.4.1 Introduction

Electromagnetic surface waves are longitudinal charge oscillations which are supported at the interface between two different media. Between a conducting and insulating medium, these waves are non-radiative, and require a momentum enhancement technique for coupling to occur to incident plane waves. On a planar metallic surface, a surface wave is transverse magnetic (TM) and can only be coupled to with TM polarised radiation since a normal component of electric field is required to generate the necessary polarisation surface charge. The dispersion of a surface wave is asymptotic to the light line at low frequencies and is often considered to be 'grazing photon – like'. Metals at these low frequencies are often considered to be perfectly conducting due to their large conductivity and therefore large imaginary permittivity. These surface waves are therefore often referred to as surface currents having a long propagation length. In this regime the wave is loosely bound to the surface and has fields that extend many wavelengths into the surrounding media. At higher frequencies the mode is asymptotic

to the surface plasma frequency that lies in the ultraviolet. At these higher frequencies the dispersion of the mode generally curves away from the light line as the frequency dependent permittivity of the metal surface plays a dominant role. Metals are considered to be 'plasmonic' in this frequency regime close to the plasma frequency with their permittivities dominated by its negative real component. Surface waves in this regime are commonly referred to as 'surface plasmons'.

Introducing structure to a metal surface allows the electromagnetic properties of the surface to be altered allowing the properties of the surface waves supported to be tailored. This allows many of the properties of surface plasmons at optical frequencies to be reproduced at lower frequencies.

2.4.1.1 Background

Electromagnetic surface waves have been extensively studied over the last century, initially they were investigated by Uller[5] in 1903. Later, Zenneck[6] and Sommerfeld[7] individually developed theories proposing the propagation of electromagnetic waves across the surface of a conducting material. Zenneck realised that there was the possibility of utilising surface waves for radio communication across the Earth. Around the same time Wood[43] observed light and dark bands in reflection from a ruled metallic grating when illuminated with light. It was found that these two types of 'Wood anomalies' were dependent on the geometrical properties of the grating and were only observed when the electric field was polarised perpendicular to the grating grooves. Rayleigh[44] proposed that these reflection features were a result of a diffracted order going from being propagating to evanescent and its energy being distributed into all other orders. Later experiments confirmed this theory (Wood (1912)[45], (1935)[46], Ingersoll (1920)[47]) for one type of Woods anomaly but not the other. Strong (1935)[48] also observed the same phenomena but noticed that the position of the second type of anomaly, a reflectivity minimum, was also dependent on the metal chosen for the grating fabrication. Fano[49] in 1941 proposed that the second Wood anomaly was in fact a special case of the surface waves discussed by Zenneck and Sommerfeld and was a result of a diffracted order becoming evanescent and producing a pair of superficial waves that cannot leave the surface. He considered the grating equation by Fraunhoffer (1821)[42] (*Equation 2.4.1*).

$$\lambda_g\left(\sin\theta_N - \sin\theta\right) = N\lambda_0 \qquad \textit{Equation 2.4.1}$$

Where λ_g is the grating pitch, θ_N is the angle between the diffracted order and the normal to the surface, θ is the angle of incidence, N is an integer and λ_0 is the incident wavelength. When $\sin\theta_N > 1$ the diffracted order, N, becomes evanescent and diffracts into a pair of surface waves that are trapped on the surface as their fields are exponentially decaying normal to the surface.

Later in 1952 Pines and Bohm[50] suggested that electrons in a metal could be treated as a plasma which in 1958 led Ferrell[51] to propose that if a metal film were bombarded with a beam of electrons it would emit radiation at a plasma frequency, this was later observed by Steinmann[52] in 1960. The emitted radiation was found to have two characteristic energies of $h\omega_p/2\pi$ and $h\omega_p/\left(\sqrt{2}2\pi\right)$. It is the latter which is the surface plasmon. Meanwhile Barlow and Cullen (1953)[9,10], Rotman (1951)[53] and Goubau (1950)[54,55] found that structuring of surfaces allowed enhanced binding of low frequency electromagnetic surface waves by changing the effective properties of the surface. Introducing resonant behaviour to a surface increased the inductive part of the surface impedance therefore increasing the binding of waves to the surface.

Palmer in 1952[56] observed reflectivity features for s-polarised radiation incident on a deep grating showing that Rayleigh's theory was incomplete and only valid for shallow gratings. Teng and Stern (1967)[57] suggested that optical gratings were imparting additional momentum to allow coupling to the surface plasmon and were able to map out its dispersion. Later studies by Ritchie (1968)[58] and Beaglehole (1969)[59] provided comprehensive studies of grating-coupled surface plasmon polaritons.

In more recent studies, particularly since the emergence of metamaterial research, structuring surfaces in order to create 'designer' plasmonic surfaces has become popular. Pendry et al. (2004)[2] proposed that an array of sub-wavelength holes in a metal substrate can be considered to have an effective permittivity such that the cutoff of the holes acts as an 'effective' plasma frequency. This was experimentally verified by Hibbins et al. (2005)[3]. This designer surface allows the effective plasma frequency to be chosen and the dispersion of the modes tuned by careful selection of the hole size.

Another new surface which has been designed to support bound surface waves is the Sievenpiper high impedance surface[11]. This sub-wavelength resonant system uses a 'mushroom-like' structure that possesses capacitive and inductive components, designed so that the structure is very thin ($<<\lambda$). Below its resonant frequency the surface can be described as having an inductive surface impedance and supports bound surface waves.

2.4.1.2 Surface Wave Derivation

Surface waves can be supported at the interface between two dissimilar media. Consider the case in *Figure 2.4.1*, where there is an interface between two media, in the *x-y* plane. Medium 1 has a dielectric constant ε_1 and extends in the +*z* direction. Medium 2 has a dielectric constant ε_2 and extends in the –*z* direction.

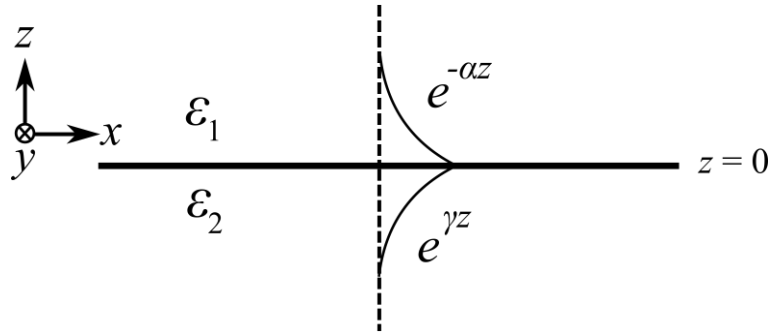

Figure 2.4.1. *Interface between two dissimilar materials, ε_1 and ε_2, and the exponentially decaying fields that are characteristic of a surface wave. α and γ are the decay constants into the media ε_1 and ε_2 respectively.*

For a wave to be bound to the surface its fields must decay exponentially into both media with a decay constant α into the first medium and γ into the second. The dispersion of a transverse magnetic (TM) surface wave will be derived. (Derivations adapted from *Field Theory of Guided Waves, Collin*[60]). The derivations in this thesis assume a time dependence term $e^{i\omega t}$ which is the general convention used in the microwave engineering textbooks from which they have been adapted. Physics textbooks often use $e^{-i\omega t}$ to describe the time dependence. The use of $e^{i\omega t}$ results in a negative ε_i for lossy materials whereas using $e^{-i\omega t}$ leads to a positive value. Since the physics is unchanged by using the $e^{i\omega t}$ convention, this has been left intact in the

derivations however material properties have been quoted throughout the thesis with the physics convention of lossy materials possessing a positive ε_i.

The components of the electric field in medium 1 take the following form (note that the time-dependence $e^{i\omega t}$ has been omitted for clarity):

$$E_x = Ae^{-ikx-\alpha z} \qquad \textit{Equation 2.4.2}$$

$$E_y = 0 \qquad \textit{Equation 2.4.3}$$

$$E_z = Be^{-ikx-\alpha z} \qquad \textit{Equation 2.4.4}$$

where *A* and *B* are constants.

In medium 2 the fields also take the following form:

$$E_x = Ce^{-ikx+\gamma z} \qquad \textit{Equation 2.4.5}$$

$$E_y = 0 \qquad \textit{Equation 2.4.6}$$

$$E_z = De^{-ikx+\gamma z} \qquad \textit{Equation 2.4.7}$$

Using Maxwell's equations:

$$\nabla \times \underline{B} = \frac{\varepsilon}{c^2}\frac{\partial \underline{E}}{\partial t} \qquad \textit{Equation 2.4.8}$$

$$\nabla \times \underline{E} = -\frac{\partial \underline{B}}{\partial t} \qquad \textit{Equation 2.4.9}$$

$$\nabla \times \nabla \times \underline{E} = \frac{-\varepsilon}{c^2}\frac{\partial^2 \underline{E}}{\partial t^2} \qquad \textit{Equation 2.4.10}$$

Expanding with $E_y = 0$,

$$\hat{x}\left(\frac{-\partial^2 E_x}{\partial z^2} + \frac{\partial^2 E_z}{\partial x \partial z}\right) + \hat{z}\left(\frac{\partial^2 E_x}{\partial x \partial z} - \frac{\partial^2 E_z}{\partial x^2}\right) = \varepsilon\frac{\omega^2}{c^2}\left(\hat{x}E_x + \hat{z}E_z\right) \qquad \textit{Equation 2.4.11}$$

Inserting expressions for *E* in medium 1,

$$k^2 A + ik\alpha B = \varepsilon_1 \frac{\omega^2}{c^2} A$$ *Equation 2.4.12*

$$ik\alpha A - \alpha^2 B = \varepsilon_1 \frac{\omega^2}{c^2} B$$ *Equation 2.4.13*

Applying the same logic below the surface leads to another pair of equation:

$$k^2 C + ik\gamma D = \varepsilon_1 \frac{\omega^2}{c^2} C$$ *Equation 2.4.14*

$$-ik\gamma C - \gamma^2 D = \varepsilon_1 \frac{\omega^2}{c^2} D$$ *Equation 2.4.15*

The tangential electric field and normal electric displacement must be continuous across the interface, hence:

$$A = D$$ *Equation 2.4.16*

$$\varepsilon_1 B = \varepsilon_2 D$$ *Equation 2.4.17*

Combining all of the above gives expressions for the wavevector, *k* and the decay constants, α and γ:

$$k = \sqrt{\frac{\varepsilon_1 \varepsilon_2}{\varepsilon_1 + \varepsilon_2}} \frac{\omega}{c}$$ *Equation 2.4.18*

$$\alpha = \sqrt{\frac{-\varepsilon_1^{\,2}}{\varepsilon_1 + \varepsilon_2}} \frac{\omega}{c}$$ *Equation 2.4.19*

$$\gamma = \sqrt{\frac{-\varepsilon_2^{\,2}}{\varepsilon_1 + \varepsilon_2}} \frac{\omega}{c}$$ *Equation 2.4.20*

If the incident medium is air ($\varepsilon_1 = 1$) these equations show that TM surface waves only exist on materials with $\varepsilon_2 < -1$, for example metals. If ε_2 is positive then α and γ are imaginary and the waves are not decaying from the surface but are simply propagating plane waves. If ε_2 is negative and < -1 then a bound surface wave is supported.

The solution for TE surface waves can also be derived by the same method through the principle of duality if the electric and magnetic fields are exchanged and μ is substituted for ε. For a TE surface wave to be supported the interface must be between media with different permeabilities. At high frequencies however, $\mu \approx \mu_0$ for most materials so this is not readily realised for a planar interface.

2.4.1.3 Drude Model

The dispersion of surface modes and the binding of the fields to the surface are dependent on the dielectric properties of the media. If we assume an air-metal interface such that medium 1 is air ($\varepsilon_1 = 1$) and medium 2 is a metal that can be described using the Drude model[61], then its complex permittivity ($\varepsilon = \varepsilon_r + \varepsilon_i i$) and the dispersion of the surface mode at the interface can be calculated. *Equation 2.4.21* and *Equation 2.4.22* define the real part of the permittivity, ε_r and imaginary part of the permittivity, ε_i respectively. Note the negative value for the imaginary component of the permittivity, this is due to the choice of sign for the time dependence ($e^{i\omega t}$) so a negative value indicates a medium exhibiting loss.

$$\varepsilon_r = 1 - \frac{{\omega_p}^2 \tau^2}{1 + \omega^2 \tau^2} \qquad \textit{Equation 2.4.21}$$

$$\varepsilon_i = \frac{-{\omega_p}^2 \tau}{\omega(1 + \omega^2 \tau^2)} \qquad \textit{Equation 2.4.22}$$

Here τ is the mean collision time of the electrons, $\omega_p = \sqrt{ne^2/m\varepsilon_0}$ is the plasma frequency, with n the electron density, e the charge of an electron, m the mass of an electron and ε_0 the permittivity of free space.

The values of $\omega_p = 1.93\times10^{16}\text{s}^{-1}$ and $\tau = 5.07\times10^{-15}\text{s}$ for aluminium [Bohren and Huffman[62]] have been used to calculate the values in *Figure 2.4.2*. Aluminium does not perfectly fit the Drude model due to interband transitions at ~ 1.5 eV ~ 830 nm. However at low frequencies the Drude model provides a good fit to aluminium and most other metals.

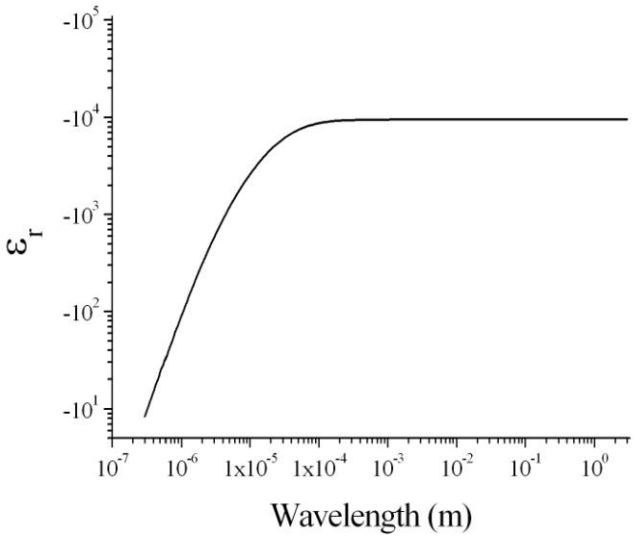

(a)

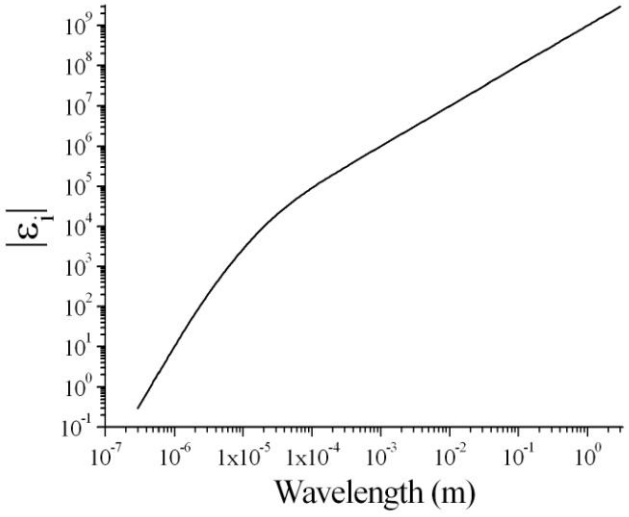

(b)

Figure 2.4.2. *Real and imaginary components of the dielectric function of aluminium calculated from the Drude model using* $\omega_p = 1.93\times10^{16}\,s^{-1}$ *and* $\tau = 5.07\times10^{-15}\,s$. ***(a)*** *Plot of* ε_r *as a function of wavelength.* ***(b)*** *Plot of* ε_i *as a function of wavelength.*

The dielectric properties of aluminium and metals in general are frequency dependent. For long wavelength radiation such as radio waves and microwaves the permittivity is large and dominated by its imaginary component. At shorter wavelengths, such as in the visible regime, the permittivity is dominated by its negative real component for 'plasmonic' metals such as gold and silver.

The permittivity can also be expressed as a function of conductivity, σ (*Equation 2.4.23*).

$$\varepsilon = 1 - \frac{i\sigma}{\omega\varepsilon_0} \qquad \textit{Equation 2.4.23}$$

Where,

$$\sigma = \frac{nq^2\tau}{m(1+i\omega\tau)} \qquad \textit{Equation 2.4.24}$$

Therefore when $\omega << 1/\tau$, i.e. in the radiowave and microwave regime the conductivity is primarily real and a large number. This leads to a permittivity which is large and imaginary.

2.4.1.4 Surface Wave Dispersion Curve

Through substitution of *Equation 2.4.21* and *Equation 2.4.22* into *Equation 2.4.18*, the dispersion of a surface wave may be calculated. The dispersion of a surface wave on a planar metal is schematically illustrated in *Figure 2.4.3*.

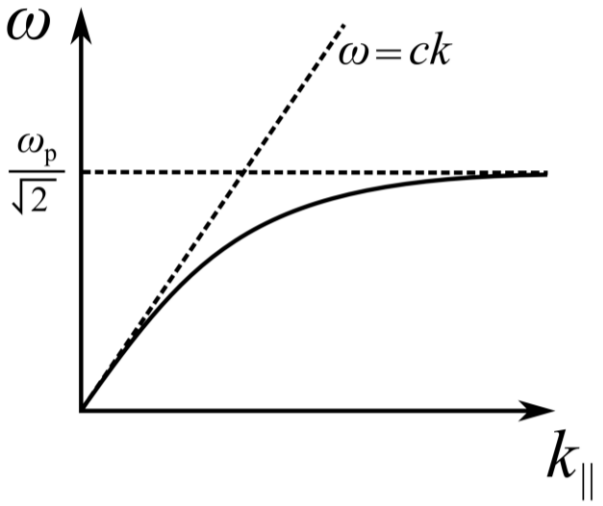

Figure 2.4.3. *Dispersion of surface waves on a planar metal/air interface.*

The dispersion of a surface wave lies outside of the radiative light line which represents the maximum in-plane wavevector ($k_{\parallel}$) available to an incident photon (i.e. a grazing photon). At low frequencies, $k \approx \omega/c$, i.e. the surface mode lies near to the light line and propagates at close to the speed of light. These modes are loosely bound and extend for many wavelengths into the surrounding media. Hence these modes are often referred to as surface currents and are the same as AC currents on a wire. At high frequencies the surface waves are asymptotic to the surface plasma frequency ($\omega_{SP} = \omega_p / \sqrt{1+\varepsilon_1}$) which lies in the ultraviolet region. Above the surface plasma frequency the surface mode is cut-off and cannot propagate. In the visible frequency regime, below ω_{SP} the surface waves are strongly bound to the surface, and are hence often referred to as surface plasmons.

The penetration of the surface wave fields into the metal may be calculated by combining *Equation 2.4.23* and *Equation 2.4.20* :

$$\gamma = \frac{\omega}{c}\sqrt{\frac{-\varepsilon_2^{\,2}}{1+\varepsilon_2}} \approx \frac{\omega}{c}\sqrt{-\varepsilon_2} = \frac{\omega}{c}\sqrt{-\left(1-\frac{i\sigma}{\omega\varepsilon_0}\right)} \approx \frac{\omega}{c}\sqrt{\left(\frac{i\sigma}{\omega\varepsilon_0}\right)} = (i+1)\frac{\omega}{c}\sqrt{\frac{\sigma}{\omega\varepsilon_0}} = (i+1)\sqrt{\mu_0\omega\sigma}$$

$$\approx \frac{(i+1)}{\delta} \qquad \textit{Equation 2.4.25}$$

Here $\delta = \sqrt{\frac{2}{\omega\mu_0\sigma}}$ is the skin depth. At microwave frequencies metals typically have a skin depth of ~ 1 μm, i.e. much less than the wavelength of the radiation.

The current and electric field decay into the metal,

$$J_x(z) = \sigma E_x(z) = \sigma E_0 e^{-z(i+1)/\delta} \qquad \textit{Equation 2.4.26}$$

The magnetic field can be calculated by integration of the current density,

$$H_0 = \int_0^\infty J_x(z)dz = \frac{\sigma\delta}{i+1}E_0 \qquad \textit{Equation 2.4.27}$$

Thus allowing the surface impedance, Z_s to be defined:

$$Z_s = \frac{E_x}{H_y} = \frac{i+1}{\sigma\delta} \qquad \textit{Equation 2.4.28}$$

Hence, we can see that the impedance of the surface has equal real and imaginary parts; therefore the resistance and inductance are equal in magnitude for a planar metal/air interface. Since a $e^{i\omega t}$ time dependence has been used in this derivation, an inductive surface will have a positive imaginary impedance whereas a capacitive surface will have a negative imaginary impedance. If $e^{-i\omega t}$ had been used the sign of the imaginary component of the impedance would have been reversed.

2.4.1.5 Surface Impedance of a General Surface

2.4.1.5.1 TM Surface Wave

Assuming the geometry in *Figure 2.4.1*, a surface wave propagates in the *x* direction with fields decaying in the *z* direction. A TM surface wave will have fields such that $E_y = H_x = H_z = 0$. The *x* component of the electric field, E_x will be of the following form:

$$E_x = Ce^{-ikx-\alpha z} \qquad \textit{Equation 2.4.29}$$

The magnetic field component, H_y can be derived from Ampere's law:

$$\underline{\nabla} \times \underline{H} = \varepsilon \frac{\partial \underline{E}}{\partial t} \qquad \textit{Equation 2.4.30}$$

The non-zero magnetic field component can then be found:

$$i\omega\varepsilon E_x = \frac{\partial H_y}{\partial z} \qquad \textit{Equation 2.4.31}$$

Substituting *Equation 2.4.29* into *Equation 2.4.31* and integrating to solve for H_y gives,

$$H_y = \frac{-i\omega\varepsilon}{\alpha} Ce^{-ikx-\alpha z}. \qquad \textit{Equation 2.4.32}$$

The surface impedance of a TM surface wave is therefore:

$$Z_s = \frac{E_x}{H_y} \qquad \textit{Equation 2.4.33}$$

$$Z_s(TM) = \frac{i\alpha}{\omega\varepsilon} \qquad \textit{Equation 2.4.34}$$

The impedance of a surface that supports a TM surface wave has a positive reactance and is therefore inductive.

2.4.1.5.2 TE Surface Wave

If we assume that the electric fields of the surface wave are transverse, i.e. lie in the *y* direction the magnetic field will be in the *x* direction. The magnetic field will take the following form:

$$H_x = Ce^{-ikx-\alpha z} \qquad \textit{Equation 2.4.35}$$

With use of Faraday's law, the electric field can be found,

$$\underline{\nabla} \times \underline{E} = -\mu \frac{\partial \underline{H}}{\partial t}. \qquad \textit{Equation 2.4.36}$$

Derivatives of the field components give:

$$\frac{\partial E_y}{\partial z} = -i\omega\mu H_x \qquad \textit{Equation 2.4.37}$$

Substitution of *Equation 2.4.35* into *Equation 2.4.37* and integrated to solve for E_y.

$$E_y = \frac{i\omega\mu}{\alpha} C e^{-ikx-\alpha z}$$ *Equation 2.4.38*

The surface impedance is again the ratio of the electric and magnetic fields however there is a negative sign in the equation to ensure that the correct sign is obtained.

$$Z_s = \frac{-E_y}{H_x}$$ *Equation 2.4.39*

The negative sign ensures that the surface will be absorbing and therefore always have a positive resistance. Since for the TE surface wave the electric and magnetic fields are interchanged with respect to a TM surface wave this is equivalent to a 90° rotation about the *z* axis, $Y \rightarrow X$, $X \rightarrow -Y$.

Therefore,

$$Z_s(TE) = \frac{-i\omega\mu}{\alpha}$$ *Equation 2.4.40*

TE surfaces modes are therefore supported on surfaces which have a negative reactance and are therefore capacitive.

2.4.1.6 Corrugated Surfaces

The properties of surface waves supported on a surface can be altered by introducing corrugation or structure. One common example[9,60,63] of this is the introduction of grooves that are λ/4 in length into a metal substrate (*Figure 2.4.4*).

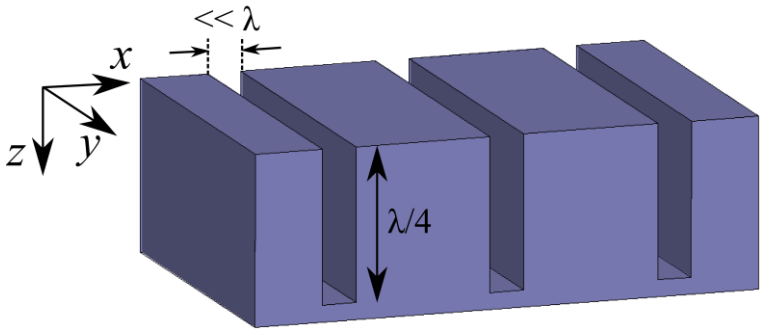

Figure 2.4.4*. Schematic illustration of a section of an array of grooves in a metallic substrate.*

Reflections at $z = 0$ and $z = +\lambda/4$ interfere to form a standing wave. The electric and magnetic fields can be represented by forward and backward waves inside the grooves:

$$E(z) = E_f e^{-ikz} + E_b e^{ikz}$$ *Equation 2.4.41*

$$H(z) = H_f e^{-ikz} + H_b e^{ikz}$$ *Equation 2.4.42*

The impedance at the surface is defined as the ratio of the electric and magnetic fields:

$$Z = \frac{E_{total}(z=0)}{(-)H_{total}(z=0)}$$ *Equation 2.4.43*

The impedance inside the groove, η, can also be defined as such:

$$\eta = \left|\frac{E_f(z)}{H_f(z)}\right| = \left|\frac{E_b(z)}{H_b(z)}\right|$$ *Equation 2.4.44*

Since the groove is terminated by a short, the impedance at $z = -\lambda/4$ is zero as the electric field is zero at the boundary. This leads to the electric field being reversed on reflection.

$$E_b(z=0) = -E_f(z=0)$$ *Equation 2.4.45*

The impedance at the surface can be expressed as a function of the distance from the short by combining *Equation 2.4.41* and *Equation 2.4.42*.

$$\frac{E_{total}(d)}{H_{total}(d)} = \frac{E_f e^{ikd} - E_f e^{-ikd}}{H_f e^{ikd} + H_f e^{-ikd}}$$ *Equation 2.4.46*

$$Z(d) = i\eta \tan(kd)$$ *Equation 2.4.47*

If $d > \lambda/4$, then $\tan kd < 0$, leading to a negative impedance, i.e. a capacitive surface and TM surface waves are cut-off. When $d < \lambda/4$, $\tan kd > 0$ and the surface is inductive allowing TM surface waves to be supported. The surface impedance will be a maximum as *d* approaches $\lambda/4$ due to the discontinuity in the tangent function.

The surface impedance of a corrugated surface can also often be described by a lumped circuit model composed of an inductor and capacitor in a parallel resonant circuit. The frequency dependent surface impedance is described by *Equation 2.4.48*.

$$Z = \frac{i\omega L}{1-\omega^2 LC}$$ *Equation 2.4.48*

The resonant frequency is determined by *Equation 2.4.49*.

$$\omega_0 = \frac{1}{\sqrt{LC}}$$ *Equation 2.4.49*

This type of circuit analysis is useful if the inductance and capacitance values of the structure can be calculated, allowing complex systems to be characterised.

2.4.1.6.1 Dispersion of Surfaces Waves on Corrugated Surfaces

By changing the impedance of a surface, the dispersive properties of the surface modes supported are also changed.

Using Ampere's Law (*Equation 2.4.30*) and Faraday's Law (*Equation 2.4.36*) and assuming that E_x takes the form used in *Equation 2.4.29* the non-zero field components can be found:

$$i\omega\varepsilon_0 E_x = \frac{\partial H_y}{\partial z} \qquad \textit{Equation 2.4.50}$$

$$i\omega\varepsilon_0 E_z = \frac{-\partial H_y}{\partial x} \qquad \textit{Equation 2.4.51}$$

$$-i\omega\mu_0 H_y = \frac{\partial E_z}{\partial x} - \frac{\partial E_x}{\partial z} \qquad \textit{Equation 2.4.52}$$

These equations may be solved to find H_y and E_z:

$$H_y = \frac{-i\omega\varepsilon_0}{\alpha} Ce^{-ikx-\alpha z} \qquad \textit{Equation 2.4.53}$$

$$E_z = \frac{-ik}{\alpha} Ce^{-ikx-\alpha z} \qquad \textit{Equation 2.4.54}$$

Combining these equations, an expression for the wave vector *k* may be derived:

$$k^2 = \mu_0\varepsilon_0\omega^2 + \alpha^2 \qquad \textit{Equation 2.4.55}$$

If *Equation 2.4.55* is combined with *Equation 2.4.34*:

$$Z = \frac{i}{\omega\varepsilon_0}\sqrt{k^2 - \mu_0\varepsilon_0\omega^2}\,, \qquad \textit{Equation 2.4.56}$$

$$Z^2 = \frac{-\left(k^2 - \mu_0\varepsilon_0\omega^2\right)}{\omega^2{\varepsilon_0}^2}, \qquad \textit{Equation 2.4.57}$$

$$\frac{k^2}{\omega^2{\varepsilon_0}^2} = \frac{\mu_0\varepsilon_0\omega^2}{\omega^2{\varepsilon_0}^2} - Z^2, \qquad \textit{Equation 2.4.58}$$

$$k^2 = \omega^2\varepsilon_0\left(\mu_0 - \varepsilon_0 Z^2\right), \qquad \textit{Equation 2.4.59}$$

$$k^2 = \omega^2\varepsilon_0\mu_0\left(1 - \frac{\varepsilon_0 Z^2}{\mu_0}\right), \qquad \textit{Equation 2.4.60}$$

$$k^2 = \frac{\omega^2}{c^2}\left(1 - \frac{Z^2}{{Z_0}^2}\right) \text{ and} \qquad \textit{Equation 2.4.61}$$

$$k_{TM} = \frac{\omega}{c}\sqrt{\left(1 - \frac{Z^2}{{Z_0}^2}\right)} \qquad \textit{Equation 2.4.62}$$

An equivalent expression can be found for the dispersion of TE surface waves:

$$Z_s(TE) = \frac{-i\omega\mu_0}{\alpha}, \qquad \textit{Equation 2.4.63}$$

$$Z^2 = \frac{\omega^2 \mu_0^{\ 2}}{k^2 - \mu_0\varepsilon_0\omega^2}, \text{ and} \qquad \textit{Equation 2.4.64}$$

$$k_{TE} = \frac{\omega}{c}\sqrt{\left(1 - \frac{Z_0^{\ 2}}{Z^2}\right)}. \qquad \textit{Equation 2.4.65}$$

At the resonant frequency *Equation 2.4.48* has a pole and therefore the surface impedance goes to infinity. Below the resonant frequency the surface impedance is negative, therefore inductive and able to support a TM surface wave. Above the resonant frequency the surface impedance is positive, therefore capacitive and able to support a TE surface wave as the electromagnetic properties of the surface have now changed to allow the fields of a TE mode to be supported (2.4.1.5.2). The dispersion of these surface waves is schematically shown in *Figure 2.4.5*.

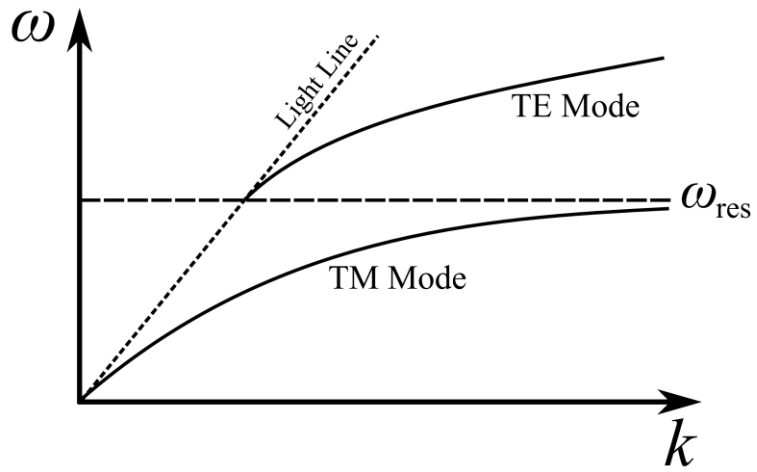

Figure 2.4.5*. Schematic illustration of the dispersion of TM and TE surface waves on a corrugated surface whose surface impedance is described by a parallel inductor-capacitor lumped circuit model.*

Close to the asymptotic frequency the surface mode is more closely bound to the surface, this is schematically shown in *Figure 2.4.6*.

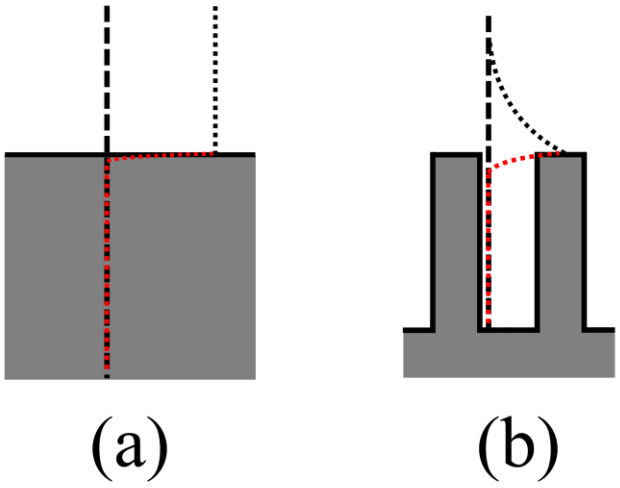

Figure 2.4.6*. Schematic illustration of the spatial extent of the electric fields of a surface wave. Red dotted line indicates field magnitude below the surface, black dotted line indicates field magnitude above the surface for (a) Planar metal/dielectric interface. (b) Resonant high impedance surface.*

For the planar metal/dielectric interface (*Figure 2.4.6a*) the electric field penetrates only a minimal distance into the metal and extends for many wavelengths into the dielectric. If the surface is corrugated (*Figure 2.4.6b*), close to the resonant frequency the electric fields are more closely bound to the surface and bear closer resemblance to that of surface wave (SPP) in the visible regime.

2.4.2 Coupling Mechanisms

The dispersion of a surface wave is such that its momentum is always greater than that available to an incident photon and as such requires a coupling mechanism in order for coupling to occur. Grating coupling is the mechanism used in this thesis to excite surface waves; however prism coupling will also be discussed as it is another common technique.

2.4.2.1 Prism Coupling

Prism coupling is often used to couple incident radiation to surface waves on planar metal films in the optical regime[64,65]. However in recent times[26] this technique has also be used to excite surface waves on structured metal surfaces.

The refraction of an electromagnetic wave is determined by Snell's law (*Equation 2.4.66*).

$$n_1 \sin\theta_1 = n_2 \sin\theta_2 \qquad \textit{Equation 2.4.66}$$

Here n_1 and n_2 are the refractive index of medium 1 and 2, θ_1 and θ_2 are the incident and refracted angles at the interface of medium 1 and medium 2. If a wave is incident from a high index to a low index there will be an angle at which the transmitted wave will graze the surface, this is known as the critical angle and is determined by setting θ_2 equal to 90° in *Equation 2.4.66*.

$$\theta_c = \sin^{-1}\left(\frac{n_2}{n_1}\right) \qquad \textit{Equation 2.4.67}$$

Beyond the critical angle there is no transmitted wave and therefore total internal reflection (TIR) occurs. This is due to conservation of momentum since the wave in the high index medium has greater in-plane momentum than that supported in the lower index medium. A propagating wave is not formed and only an evanescent field is produced that decays away from the surface. Since the evanescent fields in the low index medium have greater in-plane momentum than that of any propagating fields they can be used to couple to a surface wave on a planar metal, this is illustrated in *Figure 2.4.7*. The extra region of the dispersion diagram that can be coupled to is shaded grey, this region is limited by the light line in the prism medium, and includes part of the surface wave dispersion curve.

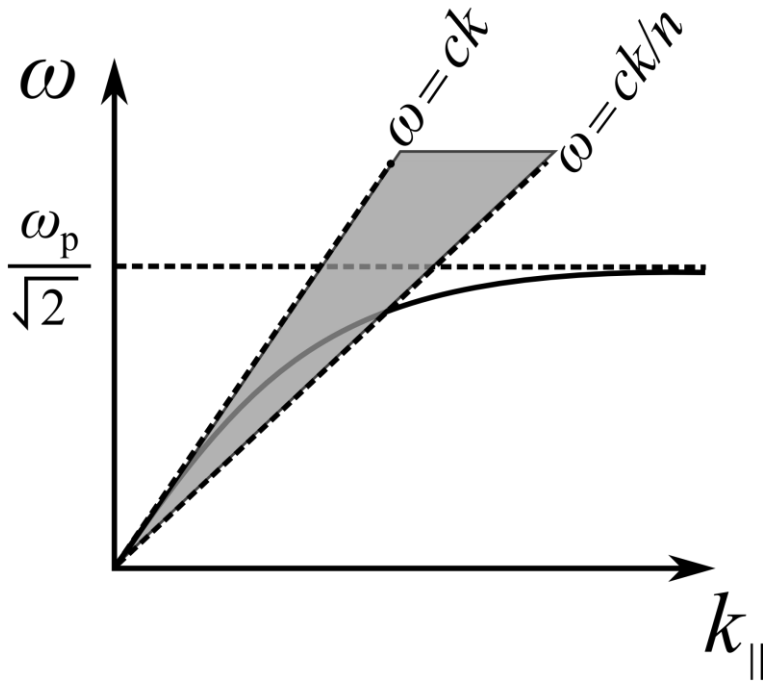

Figure 2.4.7. *Schematic illustration of the dispersion of a surface wave on a metal/air interface and the light lines associated with the air and a medium of refractive index, n.*

There are two typical configurations for prism coupling, one set-up is the Otto[64] configuration whereby the metal surface on which the surface wave will be excited is placed less than a few wavelengths from the prism. This air gap ensures that the dispersion of the surface wave is not altered significantly by the exponential decay of the fields of the surface wave into the prism dielectric while also allowing coupling to the surface wave. The coupling strength decreases with increasing separation and an ideal (100%) coupling separation is ~ λ, as at this separation the radiative and non-radiative losses will be equal. The Otto configuration may be difficult to implement at optical frequencies due to the small gap required between the prism and metal surface as any non-uniformity or dust particles in the gap region may cause weak coupling to the surface mode. The other commonly used configuration for prism coupling is the Kretschmann-Raether[65] set-up, whereby an optically thin metal film is attached to the prism, typically by thermal deposition. The exponential fields from the prism surface decay through the metal film and excite a surface wave on the air/metal interface; this method eliminates the gap problems experienced with the Otto configuration and is therefore more commonly used.

2.4.2.2 Grating Coupling

Another method for coupling to surface waves is grating coupling, which uses the periodicity of a surface and the resultant scattering to enhance the momentum of an incident photon. This technique is used throughout the work described in this thesis to couple to surface modes. The periodicity of the surface can scatter incident radiation by an integer number of grating vectors, $\left|\underline{k}_{\mathrm{g}}\right| = 2\pi/\lambda_{\mathrm{g}}$ where λ_g is the periodicity of the grating (*Equation 2.4.68*).

$$k_{sw} = n_1 k_0 \sin\theta \pm N k_g \qquad \textit{Equation 2.4.68}$$

Scattering from the grating periodicity is the origin of propagating diffracted orders, when the wavelength of the incident radiation is such that a diffracted order is no longer propagating it is considered to be evanescent. It is the utilisation of these evanescent fields in grating coupling which have greater in-plane momentum than the incident wavevector that allows coupling to surface waves.

Figure 2.4.8 illustrates the coordinate system used throughout this section, if the azimuth angle is non-zero (i.e. the grating vector is not in the incident plane then *Equation 2.4.68* becomes:

$$k_{sw}{}^2 = n_1{}^2 k_0{}^2 \sin^2\theta + N^2 k_g{}^2 \pm 2 n_2 N k_g k_0 \sin\theta\cos\varphi \qquad \textit{Equation 2.4.69}$$

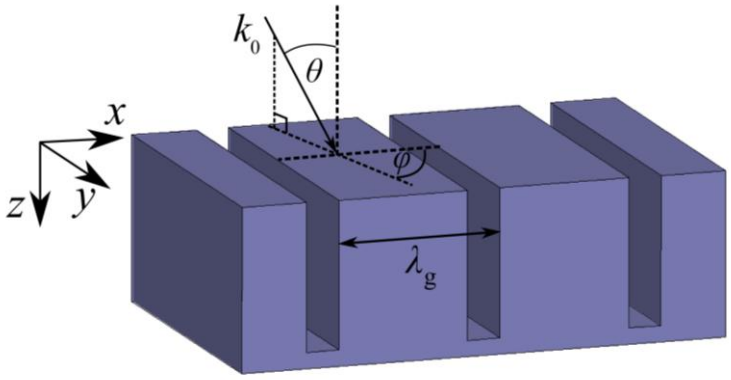

***Figure 2.4.8**. Schematic illustration of a section of a grating showing the coordinate system, grating pitch, λ_g, incident wave vector, k_0, polar angle, θ, and azimuth angle, φ.*

The dispersion of surface waves as the result of diffraction for a periodic surface is schematically shown in *Figure 2.4.9*.

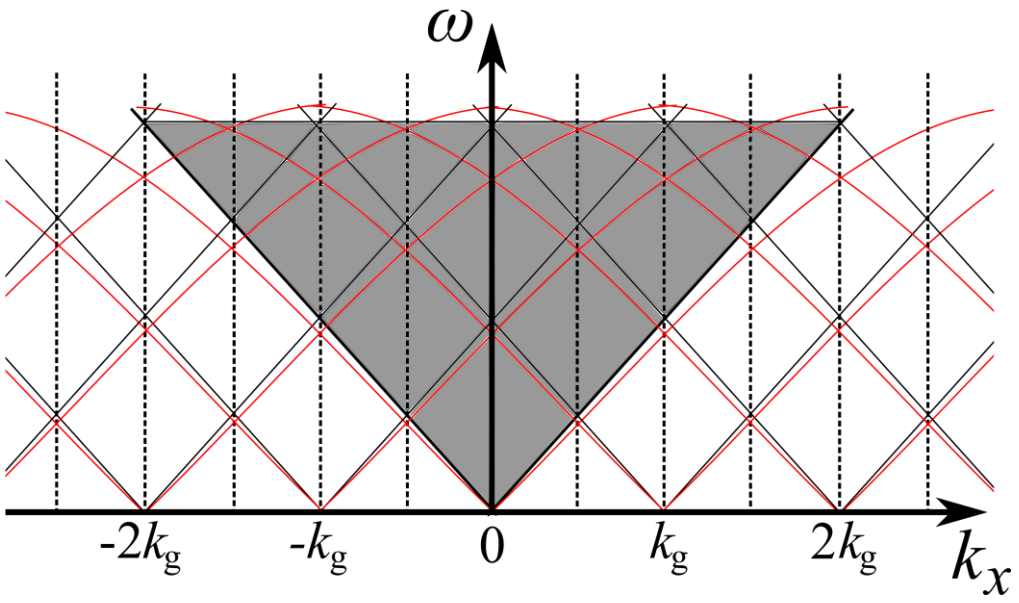

Figure 2.4.9. *Dispersion diagram showing the zeroth order and diffracted light lines (black lines). Surface waves are illustrated by red lines and are reflected at the Brillouin zone boundaries* $(k_g/2)$. *Grey area represents the radiative light cone.*

The grating is represented by a series of points in reciprocal space all separated by $|k_g|$. The zero-order light lines and surface modes associated with them may be scattered by an integer number of k_g therefore creating a series of diffracted light lines and diffracted surface modes. The grey area represents the light cone and as a result of diffraction from the grating periodicity, surface modes can now be coupled to radiatively. This discussion is only a simple representation, as in reality band gaps will form at the intersection of surface waves (discussed in *Section 2.4.3*).

A 2D reciprocal space representation of the solutions to *Equation 2.4.69* is illustrated in *Figure 2.4.10*.

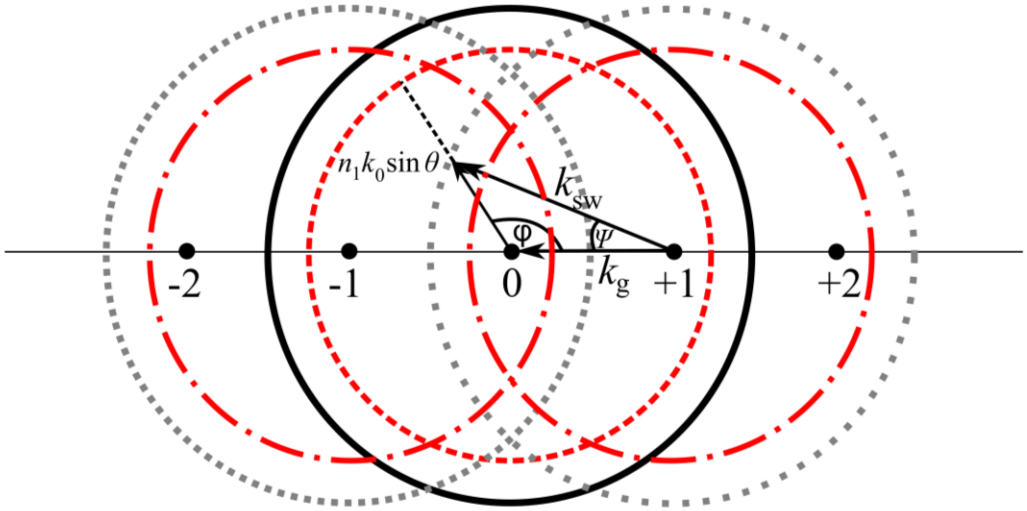

Figure 2.4.10. *2D-Reciprocal space representation of a one dimensional grating. Solid black circle indicates the momentum of a zero-order surface wave. Dashed red circle indicates the maximum momentum available to an incident photon (grazing incidence). Dot-dash red circle indicates momentum available to a photon that has undergone a k_g scatter. Dotted grey circle indicates the momentum of surface waves that have been diffracted by the grating periodicity. k_g is the grating vector, θ is the polar angle of incidence and φ the azimuth angle. The surface wave propagates at an angle ψ ($\neq \varphi$) relative to the grating vector.*

This representation is a slice through the light cones in the $k_x k_y$ - plane at a fixed value of frequency. The black circle centred on the origin is the momentum of a zero order surface wave, inside this is a red dashed circle which is the in-plane momentum of a grazing photon. Since the surface wave lies outside the light circle direct coupling cannot occur. The other two pairs of circles (dot-dash red and solid grey) in the figure are the diffracted light circles and surface waves associated with the $+|k_g|$ and $-|k_g|$ scattering centres. The diffracted surface waves (grey circles) overlap with the zero order light circle and can therefore give a solution to *Equation 2.4.69*.

2.4.3 Band Gaps in the Dispersion of Grating Coupled Surface Waves

Photonic band gaps exist much like electron band gaps in solid state physics. One such example of a common structure exhibiting band gaps is that of a dielectric stack with periodic refractive index modulations in either two or three dimensions. Such a

structure is commonly referred to as a photonic crystal[66]. Diffraction gratings may also be considered as 1D-photonic crystals and exhibit band gaps in their dispersion[58,67].

The origin of band gaps in the dispersion of grating coupled surface waves can be understood by considering a simple one-dimensional grating whose amplitude is described by a series of sinusoidal harmonics (*Equation 2.4.70*).

$$A(x) = a_1 \sin(k_g x + \phi_1) + a_2 \sin(2k_g x + \phi_2) + ...a_n \sin(nk_g x + \phi_n) + ... \qquad \textit{Equation 2.4.70}$$

Here $a_1, a_2, ...a_n$ are the amplitudes of the harmonic components of the surface profile and $\phi_1, \phi_2, ...\phi_n$ are their relative phases. A $2k_g$ scattering process results in forward and backward travelling waves that interfere to form a standing wave at $k_x = 0$. There are two standing wave solutions (*Equation 2.4.71* and *Equation 2.4.72*).

$$\psi_1 = \exp(ik_g x) + \exp(-ik_g x) = 2\cos(k_g x) \qquad \textit{Equation 2.4.71}$$

$$\psi_2 = \exp(ik_g x) - \exp(-ik_g x) = 2i\sin(k_g x) \qquad \textit{Equation 2.4.72}$$

There are two possible field solutions for these standing waves, one solution has the charges located at the peaks and troughs of the grating modulation and the other has the charges at the mid-points between the peaks and troughs (*Figure 2.4.11*).

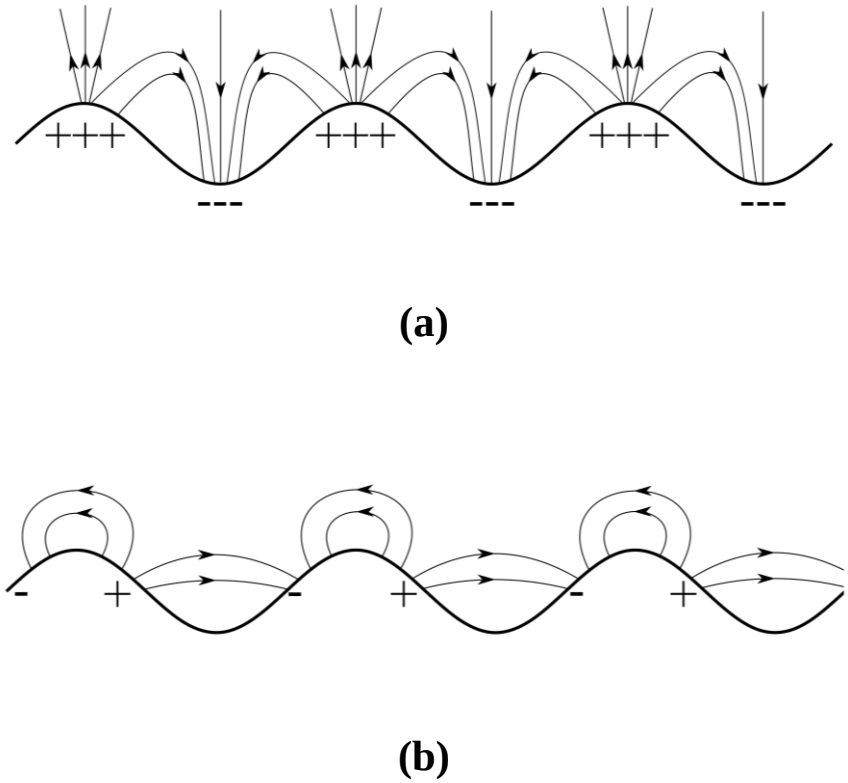

Figure 2.4.11. *Schematic illustration of standing wave field solutions for (a) low frequency solution (b) high frequency field solution.*

The solution in *Figure 2.4.11b* requires a greater amount of energy to set up its field profile due to the high curvature of the fields therefore resulting in it having a higher frequency[68]. The two field solutions having different energies results in a band gap in the dispersion of the surface modes illustrated in *Figure 2.4.12*.

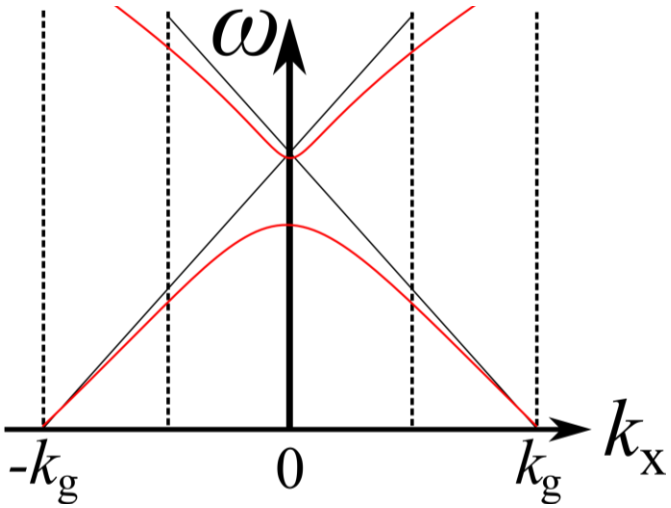

Figure 2.4.12. *Schematic illustration of a band gap formed at $k_x = 0$ in the dispersion of the surface modes scattered from k_g and $-k_g$. Black lines are the first order diffracted light lines and the red lines are the surface waves.*

A band gap in the dispersion of a surface wave will form whenever two modes intersect, i.e. every $k_g/2$. Chen et al.[67] have observed band gaps in surface plasmon dispersions that have required up to 5 k_g scattering. The size of the band gap is determined by the grating profile and curvature of the mode's dispersion[69]. A purely sinusoidal grating that has no higher order harmonics will still exhibit a band gap at $k_x = 0$, however the gap will be much smaller because the process requires two consecutive k_g scattering events which is less probable than a single 2 k_g scatter.

2.4.4 Coupled Surface Waves on Planar Structures

Surface waves supported on metal-dielectric interfaces have been discussed in *Section 2.4.1.2*. Structures with multiple interfaces can support surface waves on each interface. These surface waves are then able to couple together through the metal if it is thinner than a few skin depths. If the film is symmetrically clad by dielectric, these modes will be degenerate and couple together forming two resonances with different field profiles and energies, similar to the standing surface waves on gratings discussed earlier.

The field profiles for coupled surface waves can be seen in *Figure 2.4.13*. The modes are termed symmetric or anti-symmetric depending on their charge and field distribution. The symmetric mode has a charge distribution that is symmetric about the interface and the anti-symmetric mode has an anti-symmetric charge distribution.

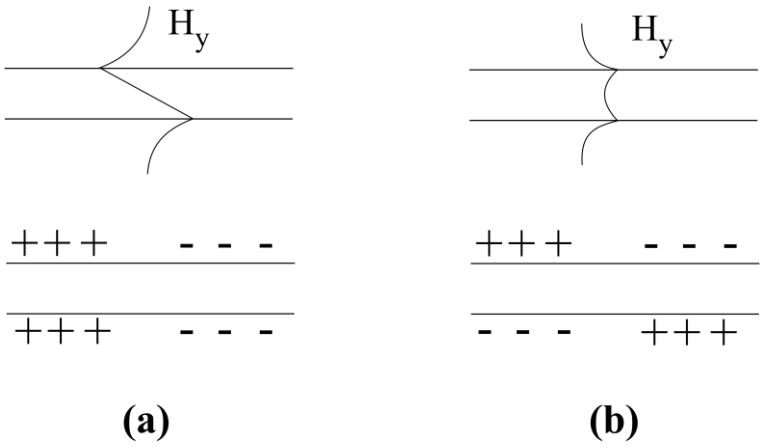

Figure 2.4.13*. Magnetic H field and surface charge distributions for the (a) symmetric and (b) anti-symmetric coupled surface modes.*

The schematic representation of the dispersion of these coupled surface waves is seen in *Figure 2.4.14*. The low frequency mode has a symmetric charge distribution and is asymptotic to the light line at low values of k_x. At high values of k_x it is asymptotic to the surface plasmon frequency. The high frequency mode has an anti-symmetric charge distribution and is also asymptotic to the light line at low values of k_x. However at higher values of k_x the mode approaches the bulk plasmon frequency of the metal. As k_x is further increased the momentum perpendicular to the surface of the film, k_z is reduced. This leads to weaker coupling between the two surface waves and the coupled mode reduces to the surface plasmon frequency as the film begins to behave more like a single interface[70].

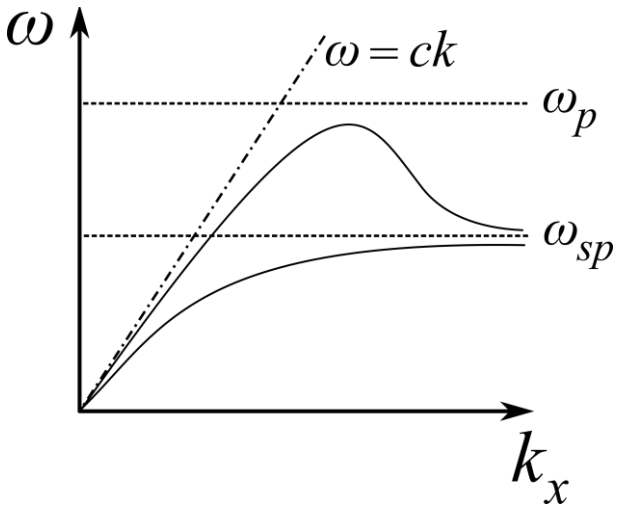

Figure 2.4.14. *Schematic representation of the dispersion of coupled surface plasmon polaritons on a thin metal film.*

At microwave frequencies metals behave as near perfect electrical conductors and hence the electric field has minimal penetration into the metal. Coupled surface waves however can be supported on structured surfaces such as hole arrays where evanescent fields can be supported inside the holes. A schematic representation of coupled surface waves on a hole array at microwave frequencies is shown in *Figure 2.4.15*.

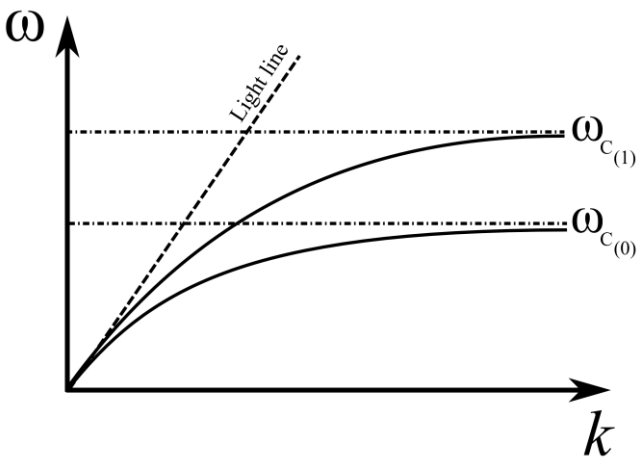

Figure 2.4.15. *Schematic dispersion of coupled surface waves on a hole array at microwave frequencies. Asymptotic frequencies are the resonances of the hole array. Subscript indicates the quantisation of the electric field longitudinally through the hole.*

In this scenario the surface plasmon and bulk plasmon frequencies lie much higher than the frequency regime of interest. The cut-off of the holes acts as an effective surface plasmon frequency to which the lowest frequency mode asymptotes. The lowest

frequency mode has a symmetric charge distribution such that the electric field within the hole has no nodes and is symmetric. This is similar to the coupled mode excited on a thin metal film at visible frequencies. The higher frequency mode is asymptotic to the cut-off frequency for a mode with longitudinally quantised electric fields and therefore has an anti-symmetric charge distribution.

2.4.5 Enhanced Transmission Phenomena

In 1998 Ebbesen[12] observed enhanced optical transmission (EOT) through an array of sub-wavelength holes in an optically thick metal film that was many orders of magnitude greater than that predicted by Bethe's aperture theory[13] (Bethe's theory suggests than the transmission through a single sub-wavelength hole will scale as $\propto (r/\lambda)^4$). This enhanced transmission phenomena was later attributed to the excitation of surface plasmon polaritons[14] (SPPs) as the transmission maxima recorded occurred close to the onset of diffraction. Further theoretical[71,72] and experimental[73] studies agreed with the SPP excitation theory. There are three possible mechanisms through which transmission can occur in this scenario. Without the excitation of SPPs the fields inside the metal film will exponentially decay with very little penetration into the metal. Therefore there will be a very small probability of tunnelling occurring and transmission will be very low unless the film is very thin. If a SPP is excited on a single interface there will be an increased probability of tunnelling as the resonant fields at the surface will be enhanced over that of a non-resonant photon electron interaction. If SPPs are excited on both interfaces they can couple together to give significant transmission enhancement if the system is symmetric.

At microwave frequencies although penetration of the electric field into the metal is assumed to be negligible, enhanced transmission phenomena through hole arrays can however still be observed. There is a substantial body of work that has explored hole arrays (inductive meshes) in the long wavelength limit (Munk et al.[1] and references therein). Resonant behaviour can be observed[19,21,74] as a transmission peak for the hole array or a reflection minimum for the patch array when the incident wavelength, λ_0, is close to the grating pitch, λ_g. This resonant behaviour has been predicted by equivalent circuit theories[21,75,76], where capacitive and inductive components determine the resonant frequency and resistive components determine the loss. The resonances

observed in these structures are essentially identical to those observed in EOT being a result of diffractively coupled surface waves due to the periodicity of the array. García de Abajo et al.[77] have provided further discussion on this resonant behaviour from periodically perforated PEC layers, illustrating that complete transmission is possible close to the onset of diffraction regardless of hole size. They attribute the resonance to the accumulation of long-distance in-phase coherent multiple scattering from the holes in the array which can be described as being equivalent to a coupled surface wave description. This has been experimentally verified in thick (~1 mm) hole arrays by Hou et al[78]. Other studies in the microwave regime have also been performed by Beruete et al.[79,80]

2.5 Summary

In this chapter, methods to control microwave transmission with the use of patterned metallic surfaces have been briefly discussed. There are many ways in which one may structure a surface to produce a frequency dependent response. Frequency selective surfaces utilise metallic elements whose shape can be used to restrict the response of electrons to an incident electromagnetic field. Simple capacitive and inductive filters which exhibit low-pass and high-pass frequency selective behaviour have been discussed. Babinet's principle has been derived which predicts the response of a PEC screen if the behaviour of its complement is known. Metallic surfaces are able to support surface waves which can also be utilised to control microwave transmission. In this chapter electromagnetic surface waves have been discussed and the dispersion equation derived. The properties of surface waves in both the microwave and higher frequency regimes have been covered. At low frequencies surface modes are loosely bound to the surface and propagate at close to the speed of light whilst at higher frequencies these waves are tightly bound to the surface and have a near-zero group velocity for frequencies close to the surface plasma frequency. Altering of a surface's impedance to enhance binding of low-frequency surface waves and mimic the behaviour observed at higher frequencies has been covered. Coupling to surface modes by prism and grating coupling has been discussed. The affect of band gaps in the dispersion of surface waves as a result of grating coupling has also been briefly discussed. Finally a brief background into coupled surface waves and their role in enhanced transmission phenomena in the low (microwave) and high frequency (visible) regimes has been given.

3 Experimental Methods and Modelling

3.1 Introduction

In the experimental chapters of this thesis, modelling is presented with experimental data to provide a greater understanding of the underlying physics. In this chapter the methods used to acquire the experimental data and to perform the computational modelling are discussed.

All experiments in this thesis were performed in the microwave regime with a free-space incident plane wave set-up. This set-up utilises source and detector horns that act as approximate point sources, directed at spherical collimating mirrors to form a plane wave. The frequency range available for use was $5.4 \leq f_0 \leq 110$ GHz ($\sim 55 \geq \lambda_0 \geq 3$ mm).

Modelling allows the response of structures to be predicted and tuned for exact requirements and reduces the financial and time costs that a trial and error experimental approach would entail. The majority of the modelling for this thesis has been performed with a commercial finite-element method (FEM) modelling software package; Ansoft's High Frequency Structure Simulator[17] (HFSS, versions 10-12). When HFSS was not a suitable modelling option other techniques were employed.

Modal matching[2,81-85] is used in chapter 6 to predict the response of arrays of holes in a PEC substrate. This analytical technique allowed more control over how the modelled responses were achieved, particularly when considering the number of diffracted orders that would be included in the calculation. This allowed the dispersion of surface modes and their asymptotic frequencies to be more clearly understood without the perturbation caused by band folding and the resulting band gaps introduced by inclusion of diffracted orders.

The Fourier Modal Method is used briefly in chapter 7 to model the response of a resonant cavity in which a thin metal film is placed. Due to the small dimensions of the film relative to other dimensions in the model and the incident wavelength this structure could not be modelled for very small film thicknesses with a finite-element method.

This is one of the limitations of the finite element method and will be discussed later in this chapter.

In this chapter a review of the specific FEM models used to predict responses for the structures in the experimental chapters will also be discussed in detail, highlighting any problems or issues encountered with them.

3.2 Transmission Measurements

A typical setup for performing transmission measurements can be seen in Figure 3.2.1.

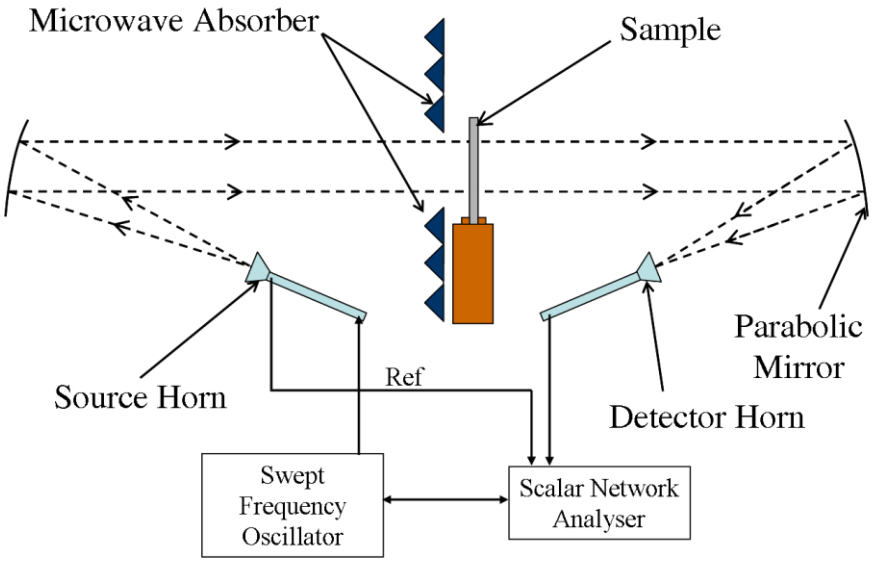

***Figure 3.2.1**. Schematic illustration of experimental set-up used for transmission measurements.*

Microwave radiation is generated by an *Agilent PSG CW* swept frequency oscillator which drives a horn antenna through a coaxial waveguide or flexible waveguide. Before the signal is emitted from the horn a reference signal is taken via a directional coupler and crystal detector, which is received by an *Agilent 8757D* scalar network analyser to take account of any fluctuations of the signal. The horn is assumed to produce a radiation pattern similar to that of a point source and therefore is placed at the focal point of a 2 m radius of curvature spherical mirror to form a collimated beam. The mirrors are mounted on wooden structures (not shown) which allow their rotation about

the vertical and horizontal axis as well as height to be adjusted. The whole setup also sits on a wooden bench, this ensures that any unwanted diffraction and scattering is minimised. The experiments are performed in a normal laboratory environment as opposed to an anechoic chamber, the kit is positioned away from nearby walls such that any reflections are minimised at the wavelengths under study (~ 60 mm – 3 mm). Spherical mirrors are used due to the ease of manufacture although parabolic mirrors would produce a more collimated beam due to the absence of spherical aberration. The mirrors are bigger than the beam to reduce scattering from their edges however if required the beam size can be reduced further by putting absorbing material around the edge of the mirror. The beam is directed at the sample which is placed in an aperture formed from microwave absorbing material. A second spherical mirror collects the transmitted radiation which is focused into a detector horn. The detector horn has a crystal detector attached; the measured signal from this detector is then received by a spectrum analyzer which is interfaced with a PC through a General Purpose Interface Bus (GPIB) card and a *LabView* program. A stepper motor driven rotating turntable is also synchronised into the PC and analyzer allowing the incident polar angle to be varied.

The polarisation of the incident and the detected radiation is set by the orientation of the waveguides and horns. This allows p-polarised (TM) and s-polarised (TE) responses to be measured, i.e. T_{pp} and T_{ss}. (Cross polarised responses, T_{ps} and T_{sp} can also be measured although this is not used in this thesis.)

3.3 Modelling

The main method used to perform modelling for this thesis was the finite element method (FEM). This numerical technique was chosen to be used instead of other modelling methods due to the flexibility that is offered for different geometries to be modelled. In contrast many analytical modelling techniques are designed to solve a particular geometry and cannot be easily modified to solve more complex systems. The main drawback with FEM modelling is however the computation time required for solving a model. Since FEM modelling performs a full wave analysis, no approximations are made leading to modelling times that may be orders of magnitude longer than a simple analytical approach.

Another numerical technique that could have been used was the finite-difference time domain (FDTD) method[86,87]. This method is similar to the FEM method in that they both utilise a mesh to describe the volume space being modelled, however with the FDTD method Maxwell's equations are discretized in both space and time. The input source is a pulse of radiation as opposed to a plane wave; this means that the response from a large range of frequencies from one simulation is readily achieved by using a Fourier transform. The evolution of a model with time can also be represented which can sometimes provide useful information. Other methods that could have been used include a variation of FDTD that starts with Maxwell's equations in integral form as opposed to the differential form, known as the finite integration method[88] (FIT). Another time domain technique is the transmission line matrix (TLM) method[89] which uses the analogy between the electromagnetic field and a mesh of transmission lines. The model space to be solved is filled with a mesh of transmission lines which intersect at nodes, the transmission and reflection is then calculated from the impedance of the combination of transmission lines. The finite volume method (FVM) is another volume discretisation method in which the volume integrals in the partial differential equations governing the behaviour of the system are converted to surface integrals through the use of the divergence theorem. The terms in the solution are evaluated as fluxes at the surfaces of each finite volume; this technique is popular in the study of fluid dynamics. Another numerical method is the Boundary Element Method (BEM), sometimes known as the Method of Moments (MoM)[90]. This technique uses given boundary conditions to fit boundary values into the integral equation. The integral equation is an exact solution to the governing partial differential equations. This technique can be more efficient than volume discretisation methods (FEM, FVM, FDTD) when the surface/volume ratio of the problem is small. Overall the FEM method was considered to be the best technique for the majority of the systems under study in this thesis due to being very flexible and able to cope with many different complex geometries.

3.3.1 Finite Element Method

3.3.1.1 Background

The FEM technique is a modelling method which uses volume discretisation, dividing the three dimensional modelling space into smaller geometrical regions with tetrahedral elements such as that seen in *Figure 3.3.1*.

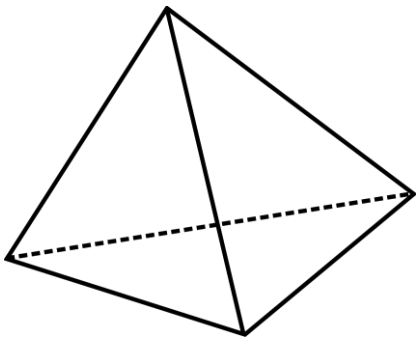

Figure 3.3.1. *Tetrahedral element used to represent fields in three dimensional space.*

The tetrahedral elements have flat faces and so cannot accurately represent a curved surface, however if sufficient numbers of elements are used a good approximation can be achieved (elements with curved edges were introduced in HFSS version 12, this improves this approximation but also increases computation time). Maxwell's equations are transformed into a matrix form and then solved numerically for each mesh element. The field components tangential to the edges are stored at the vertices of the tetrahedral elements and the fields tangential to the faces are stored at the edges. The *E* and *H* fields within the tetrahedral elements are determined by interpolating these stored values. The accuracy of the field solutions depends on the number and density of the tetrahedral elements in the model with the greatest number needed where the gradient of the fields is largest.

There are three solution types that can be chosen in HFSS, driven modal, driven terminal and eigenmode. The driven modal solution calculates the response of a structure to a user-defined excitation such as an incident plane wave, at specified frequencies. This is the option used for all of the modelling in this thesis as it is a good representation of the experiments that have been performed. The driven terminal solution calculates terminal based S parameters of passive structures driven by a source. This produces a terminal based description in terms of voltages and currents. The eigenmode solution calculates the resonances of a structure, providing the resonant frequencies and their corresponding fields. Since no incident wave is used for this solution type, no information with regard to coupling of radiation to a resonant mode can be inferred. This does have the advantage however, that modes that exist beyond

the light cone and therefore cannot be coupled to radiatively can be found and their fields examined.

3.3.1.2 Representing Sample and Assigning Materials

HFSS uses a computer aided design (CAD) interface to allow input of the model geometry. Numerous tools allow 2D and 3D objects to be drawn and edited; this allows almost any geometry to be represented. Once an object has been created within HFSS material parameters can be assigned, either chosen from the HFSS library which contains a large number of material parameters for microwave frequencies or defined manually by the user. Metals are defined by their conductivity and by default, materials with conductivity higher than 10^5 siemens/m do not have a mesh generated inside them but utilise a surface impedance approximation. Objects using this approximation are meshed on the surface only and the decay of the fields is approximated by the skin depth. At the boundary of a conductor *Equation 3.3.1* applies:

$$\underline{E}_{\tan} = Z_s\left(\hat{n} \times \underline{H}_{\tan}\right), \qquad \textit{Equation 3.3.1}$$

here $Z_s = \left((1+i)/\delta\sigma\right)$ is the surface impedance and $\delta = \sqrt{2/\omega\sigma\mu}$ is the skin depth of the conductor.

Other materials are defined by their relative permittivity, ε_r, relative permeability, μ_r, dielectric loss tangent, $\varepsilon_i/\varepsilon_r$ and magnetic loss tangent, μ_i/μ_r. Other properties such as magnetic saturation, Landé G factor and delta *H* values can be entered to describe magnetic materials. These material properties can be made frequency dependent by importing a table of values from which HFSS will interpolate across the frequency range modelled. This function has not been used in this thesis as the material properties have been assumed to be non-dispersive, this is however vital for predicting the optical response of structures where material properties are often known to be dispersive.

3.3.1.3 Boundaries

HFSS provides a range of boundaries that can be applied to surfaces; boundaries are used on the outside of a model to provide a termination but can also be used on internal

surfaces where necessary. The most common boundary condition used in this thesis is a periodic master/slave boundary condition. These boundaries ensure that fields on the master/slave are identical to that on the corresponding slave/master to ensure accurate representation of an infinite array. Using these types of boundary conditions enables the modelling of an array to be reduced to a unit cell, reducing the volume of the model and therefore computation time accordingly. A requirement of the master/slave boundaries is that the unit cell must be selected so that there is no discontinuity from one boundary to the other, i.e. if the master boundary has a metal region in contact with it in a particular area then its corresponding slave boundary must also have metal in the same region, this is illustrated in *Figure 3.3.2*. *Figure 3.3.2* shows an array of metal patches with the unit cell selected by placement of master and slave boundaries through the centre of the gap region, this, or placement of them through the metal regions, is acceptable. If there is a discontinuity the fields cannot be matched from one unit cell to the next and an accurate modelling result cannot be guaranteed.

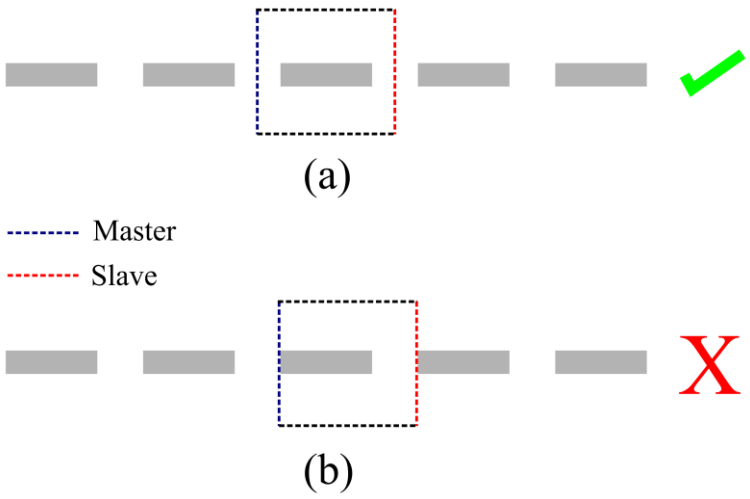

***Figure 3.3.2**. Assignment of master and slave boundaries to define unit cell of model.*
***(a)** Continuity across boundary **(b)** Discontinuity across boundary*

A radiation boundary is commonly used to terminate a model on its input or exit face, this boundary absorbs radiation incident onto it simulating the effect of the boundary being infinitely far away from the structure. At the radiation boundary surface, the second-order radiation boundary condition is used (*Equation 3.3.2*).

$$\left(\nabla \times \underline{E}\right)_{\tan} = ik_0 \underline{E}_{\tan} - \frac{i}{k_0}\nabla_{\tan} \times \left(\nabla_{\tan} \times \underline{E}_{\tan}\right) + \frac{i}{k_0}\nabla_{\tan}\left(\nabla_{\tan} \cdot \underline{E}_{\tan}\right), \qquad \textit{Equation 3.3.2}$$

here $\underline{E}_{\tan}$ is the component of the electric field tangential to the surface. The second order boundary condition is an approximation of free space. The accuracy of the approximation is dependent on the distance from the radiating object.

Another boundary used for terminating models is a perfectly matched layer (PML), this is a box that has material parameters that are fictitious but are designed to be absorbing in the direction perpendicular to the surface. PMLs perform a similar function to the radiation boundaries but are more efficient at absorbing waves that strike the boundary at non-normal angles of incidence such as diffracted waves and transmitted and reflected waves in models where the structure is illuminated at a non-normal angle of incidence. They are more efficient at non-normal angles due to the material properties of the PML being anisotropic. The real parts of the permittivity and permeability values of the PML are chosen so that they are close to that of free space to keep the optical density of the layer close to that of the region of the model at the PML interface. This ensures that the mesh in the PML is of a similar density and helps maintain continuity across the boundary. The size of the PML will be determined by the material parameters used and the expected angle at which the radiation is likely to strike the boundary. If the PML is defined to have a low optical density the PML will need to be large to be effective at absorbing the radiation incident on the boundary. If the radiation is expected to be striking the boundary at a large angle the PML will also need to be large as it is only absorbing perpendicular to the interface. The boundaries that are used to terminate models are typically placed at a distance $(\lambda/2 \to \lambda)$ away from the radiating structure to ensure that they are far enough away to not interfere with the decay of the fields near the structure but not too far that they make the model volume larger than necessary. PMLs can fail to be perfectly absorbing close to the onset of diffraction since at the onset of diffraction, the diffracted orders are propagating at a grazing angle. These grazing diffracted orders are not well absorbed since the PML is set to only absorb in the direction normal to its surface. It requires a very large PML to produce accurate results, therefore making the model volume significantly larger.

In *Figure 3.3.3* the typical HFSS unit cell of an array and the location of boundaries are shown for radiation incident along the *z* axis. The model is terminated on the incident and exit faces typically by a PML or radiation boundary however if a port excitation is

used these are not needed as a port represents a semi-infinite waveguide which can both emit and detect radiation. The sides of the model are bounded by pairs of master and slave boundaries.

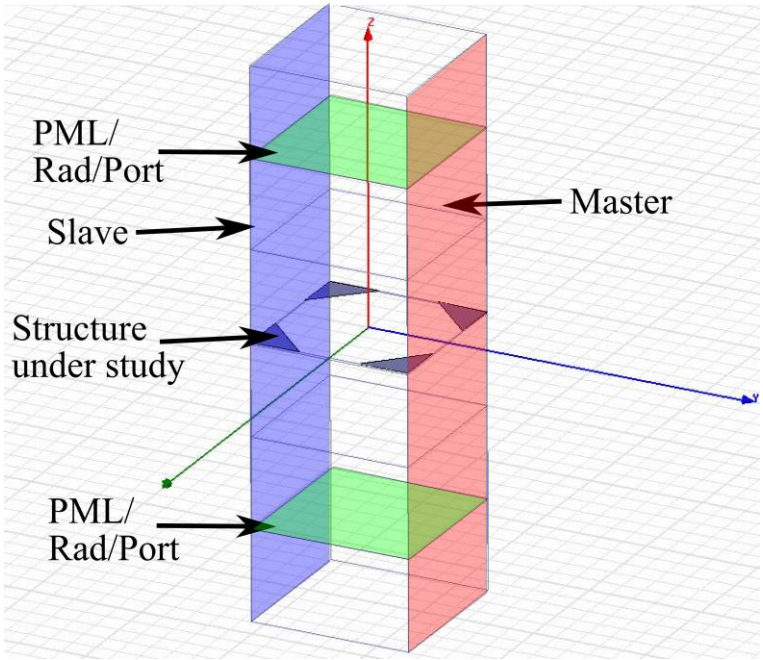

Figure 3.3.3*. Illustration of the unit cell of an array modelled in HFSS and locations of boundaries.*

Perfect *E* and perfect *H* boundaries are also used in this thesis; they act as perfect electrical and perfect magnetic conductors respectively in that they force the tangential field (*E* or *H*) to be zero at the boundary. When applied to a 2D object (zero thickness sheet) the perfect *E* boundary will make the object behave as a perfect conductor, this can be a good approximation to use when describing screens that can be considered to have a very small thickness relative to the incident wavelength.

Other boundaries in HFSS that are not used in this thesis include finite conductivity boundaries which can be used to represent a surface which is not a perfect conductor. Impedance boundaries can be used to represent a resistive surface, the fields at the surface and losses generated in the resistor are calculated via analytical formulae. Lumped RLC boundaries can be used to represent a boundary as a combination of resistors, inductors and capacitors. Layered impedance boundaries which represent multiple thin layers as a single layer with the impedance calculated by the values entered by the user are also available. *E* and *H* symmetry boundaries can be used to reduce the size of a problem where planes of electric or magnetic symmetry exist, for example reducing a waveguide cross section to half its size.

3.3.1.4 Sources

When using a driven model solution type a source has to be defined to allow the model geometry to be driven. Most of the modelling in this thesis has used a plane wave as the source as this best describes the free-space measurements that are performed. The plane wave can be described in spherical or Cartesian coordinates allowing the incident angle and polarisation angle to be varied. Other incident waves are available such as Gaussian beams and near field and far field waves.

Another modelling tool which is particularly useful for driving periodic structures that are in the diffractive regime is a 'Floquet port'. A Floquet port can only be used with periodic structures as the fields are defined in terms of diffracted orders. The Floquet ports are defined on the incident and exit faces of the unit cell and radiation is injected into the model as plane waves that are comprised of a series of Floquet modes. These Floquet modes are the diffracted fields from the periodic structure. This excitation does not need a PML to terminate which means that an improvement in the modelled transmission and reflection values close to the onset of diffraction can be achieved. Floquet ports were used when accurate modelling was needed close to the onset of diffraction to overcome this problem.

3.3.1.5 Meshing

HFSS creates an initial mesh in the model space according to the model's spatial resolution and the refractive index of the media. The fields are then calculated within these tetrahedral elements for the solution frequency defined. An adaptive process is then performed where the number of mesh elements is increased by a user defined percentage (typically 30%) with the new elements being injected into the regions where the field gradient is largest and more resolution is needed in order to accurately represent the electromagnetic response. This adaptive process continues until a specified convergence target has been achieved or the maximum number of defined adaptive passes has been reached. Reaching a converged solution can require a very large mesh depending on the model geometry and material parameters. The computation time is proportional to the numbers of elements comprising the mesh and for large models can run to many hours depending on the specification of the computer.

An example of a mesh plotted on a plane through the centre of a unit cell of a hole array is shown in *Figure 3.3.4*.

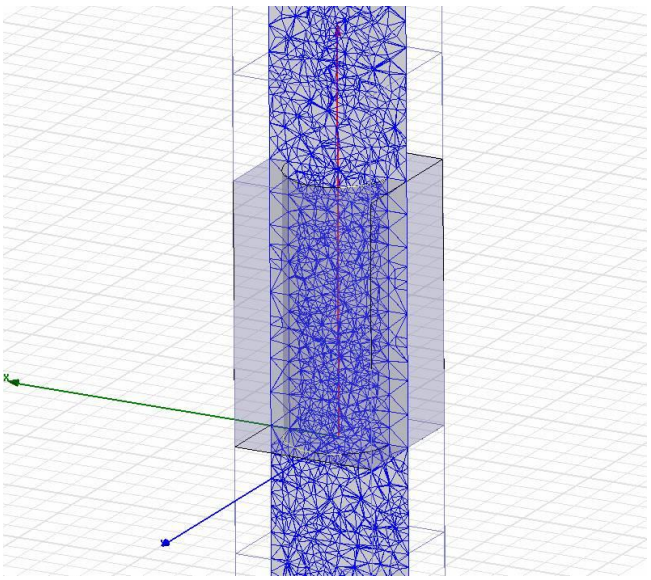

Figure 3.3.4*. A two dimensional representation of a mesh through the centre of the unit cell of a hole array.*

Mesh operations can be applied to particular regions of a model's geometry where it is known that a high resolution will be needed. These mesh operations will be applied on the initial mesh and this helps the adaptive meshing process converge to the correct solution. Like most modelling techniques it is possible for the model to converge on an incorrect solution if there are simply not enough tetrahedra in the initial mesh and therefore information about the fields in a particular region of the model. If this is the case the adaptive process does not have enough information about where the additional resolution is needed to improve the solution.

A frequency sweep can be added to a model which will solve the fields for a range of frequencies using the mesh generated at the solution frequency. Since the adaptive processing only occurs at the single solution frequency and is applied to the whole of the frequency sweep it is often not appropriate to use the same mesh across a large frequency band as the mesh won't be appropriate particularly for multiple resonance models. This occurs as the regions where the gradient of the EM fields is largest will change with frequency and therefore the original mesh is no longer suitable. When this is the case a new mesh should be generated to provide more accurate solutions.

The convergence is checked by exploring the change in the magnitude of the scattering matrix (*S*-matrix) values between each adaptive pass. This can be plotted to determine at what point there is no significant improvement by adding more tetrahedral elements, i.e. the change in the *S*-matrix is just due to numerical noise. The convergence can also be checked by examining the values of the transmission and reflection coefficients to see if they alter significantly between adaptive passes

3.3.1.6 Post Processing

After analysis of the model is completed, the solution data can be used in a number of ways. The electric, magnetic and other derived field quantities such as Poynting vector can be plotted across a user defined plane or volume. The incident fields, total fields and scattered fields can all be plotted separately. The incident fields are the plane-wave fields that would exist in the absence of the model. The total fields are the fields that exist within the model with a non-zero incident field. The scattered fields are the fields formed from subtraction of the incident fields from the total fields. Fields can be plotted in scalar form or vector form and animated with changing parameters such as frequency, phase and user-defined parameters. HFSS also has a built-in field calculator which allows a multitude of operations to be performed on these complex field quantities with respect to geometrical regions of the model, for example a field quantity can be integrated over a plane in the model that has been defined by the user. The number of operations and calculations possible are numerous and as such will not be fully discussed here.

3.3.1.7 Scripting

HFSS can be driven by scripts written in Microsoft Visual Basic (VB) a commonly used programming language. These scripts can be used to perform tasks that may need to be repeated such as calculating values from field solutions and drawing models. Scripts were used to generate models which are composed of a unit cell with a random structure factor discussed in chapter 4. Further detailed information about the use of these scripts can be found later in this chapter (*Section 3.4.2*).

3.4 Thesis Specific Modelling

3.4.1 Regular Hole/Patch Arrays

Chapter 4 presents a transmission study of square patch and square hole arrays that were fabricated from aluminised Mylar composed of 60 nm thickness aluminium on Mylar of 75 μm thickness. The model (*Figure 3.4.1*) is assumed to be infinite in the plane of the sample so a square unit cell of dimensions 7.02 mm × 7.02 mm was defined and assigned master and slave boundaries to give the required periodic boundary conditions.

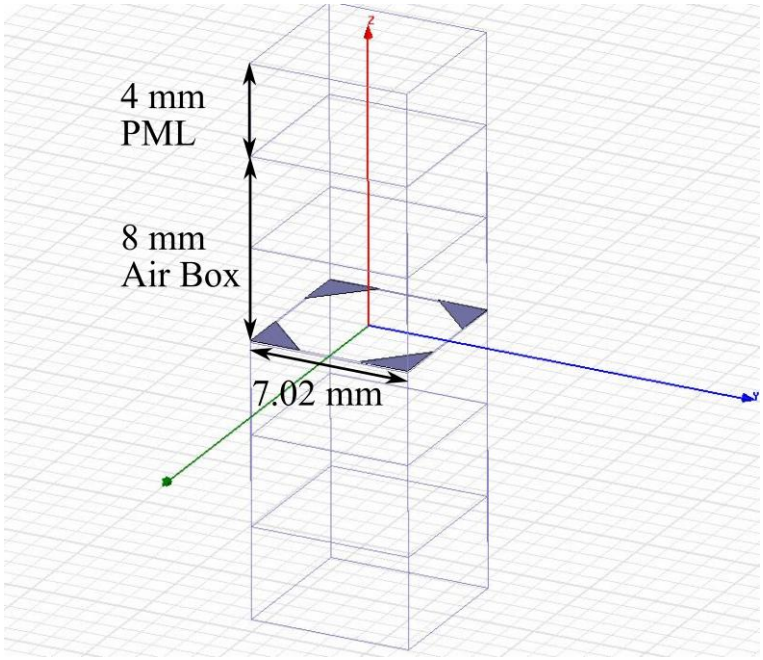

***Figure 3.4.1**. HFSS unit cell used to model square patch and hole arrays.*

The sheet tool was used to draw a square in the centre of the unit cell with its edges at 45° with respect to the coordinate axes. The side length was defined as a variable allowing it to be easily changed later and the square defined as a PEC boundary. A split operation was used to divide the square into four quadrants and these quadrants then moved to the corners of the unit cell. This allows the side length of the metal to be changed and therefore the filling fraction through the whole range of 0 to 100 % metal occupancy to be studied. When the side length reaches $\sqrt{(7.02)^2/2}$, i.e. 50 % occupancy electrical connectivity is formed across the unit cell and what was a patch array has now evolved into a hole array. A dielectric layer of 75 μm was added below the PEC sheets to represent the Mylar. This layer was defined with $\varepsilon_r = 2.6$ and

$\varepsilon_i/\varepsilon_r = 0.003$. Air boxes of height 8 mm were then added above and below the structure to allow terminating boundaries to be placed away from the near field of the structure. The model is terminated with a PML of height 4 mm on the incident and exit faces to absorb any transmitted or reflected rays at the boundary. Mesh operations were assigned to the air boxes and dielectric layer to ensure that the initial mesh had a sufficient number of tetrahedra to generate a good enough solution such that adaptation of the mesh would converge to the correct answer.

3.4.2 Random Array Modelling

Modelling of truly random structures is not a feasible task for a finite-element method modelling code such as HFSS due to not being able to reduce the problem to a unit cell. The whole structure would need to be modelled which is computationally intensive and not practical without very expensive powerful computers. In chapter 4 modelling of structures with periodic boundary conditions and a random structure factor was performed to try to produce a simplistic approximation to a random system. As drawing a complex random structure within HFSS would have been very time consuming to do manually, a script was written to automate the process. The random structure was produced by initially recording a Visual Basic macro in HFSS to draw a circle. This produces the necessary lines of code to interface with HFSS which could then be modified to perform more complex tasks. This piece of code was then modified to define the radius and spatial coordinates with a random number and executed with a loop to produce a series of random elements of various sizes and spatial coordinates. The size of the elements was given a Gaussian distribution and the spatial distribution was defined to be uniformly random. Visual Basic cannot natively produce a Gaussian distribution and therefore a Box-Muller transformation (discussed in *Section 3.4.2.1*) was implemented to generate a Gaussian distribution from a uniformly random distribution.

3.4.2.1 Box-Muller Transformation

There are two forms of the Box-Muller transformation the basic method which utilises trigonometric identities and the polar form.

3.4.2.1.1 Basic Method

If two uniform random numbers between 0 and 1, x_1 and x_2 are generated, *Equation 3.4.1* and *Equation 3.4.2* can be used to transform these numbers into a Gaussian distribution with a mean of zero and a standard deviation of one:

$$y_1 = \sqrt{-2\ln(x_1)}\cos(2\pi x_2)$$ *Equation 3.4.1*

$$y_2 = \sqrt{-2\ln(x_1)}\sin(2\pi x_2)$$ *Equation 3.4.2*

This method is not typically used for generating a Gaussian distribution since the use of trigonometric functions in computing is slower when compared to other operations and there is also potential for numerical instability when one of the numbers x_1 and/or x_2 is close to zero.

However the Box Muller transformation can also be performed using the polar form (*Section 3.4.2.1.2*) which helps to eliminate these problems.

3.4.2.1.2 Polar Form

The polar form of the Box-Muller transformation is a type of rejection sampling which generates random numbers and discards those that do not fit the desired criteria. This method is faster than the basic method as long as random numbers can be generated rapidly as it avoids the use of trigonometric functions. The method was first developed by Bell[91] and then modified by Knop[92]. The section of VB code below shows the algorithm used.

```
Do
        Randomize()
        x1=2*Rnd()-1
        Randomize()
        x2=2*Rnd()-1
        w=x1*x1+x2*x2
Loop While w>=1.0
w=Sqr((-2*Log(w))/w)
```

*y1=x1*w*

*y1=x2*w*

A pair of random numbers $x1$ and $x2$ are generated with a value between −1 and 1, these numbers are then checked to ensure that the sum of their squares is equal to or less than one. This ensures that these points lie on or within a circle of unit radius thus allowing trigonometric identities to be replaced by their ratio equivalents. Therefore the equations from the basic method can then be simplified to:

$$y_1 = x_1\sqrt{\frac{-2\ln w}{w}}$$ Equation 3.4.3

$$y_2 = x_2\sqrt{\frac{-2\ln w}{w}}$$ Equation 3.4.4

The final code was used to generate a random pattern of discs duplicated over an area of four 30 mm × 30 mm unit cells. The centre of this area was used as the unit cell with everything else removed from the model. An example unit cell is shown in *Figure 3.4.2*.

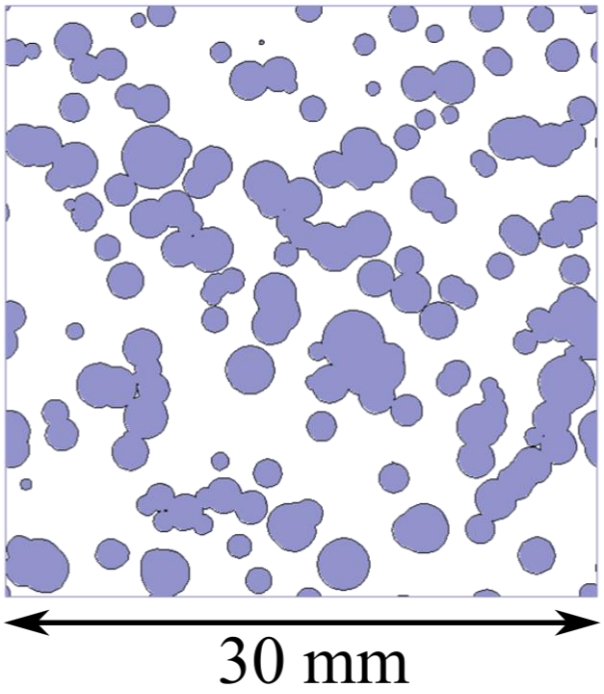

***Figure 3.4.2**. A HFSS unit cell with random structure factor produced using VB script.*

Taking the centre of four identical unit cells ensures that continuity is maintained across the boundaries of the unit cell, i.e. if metal/void is present on one boundary there will be metal/void on the opposite boundaries. 30 mm × 30 mm was at the upper limit of the size of the unit cell that could be modelled with the computing power available.

3.4.3 Multi-Modal Transmission of Microwaves through Hole Arrays

In chapter 6 the transmission response of arrays of large holes (cutoff below the onset of diffraction and arrays of small holes (cutoff above the onset of diffraction) is presented. The FEM modelling of these arrays was performed by creating a unit cell of dimensions 5.5 mm × 5.5 mm with two pairs of master/slave boundaries. A slab of aluminium was placed in the model which then had a 64 segment polyhedron removed from the centre. A polyhedron was used to represent the hole as the default cylinder is only represented by a limited number of segments around the periphery whereas the polyhedron tool allows the number to be specified. Initial modelling using the cylinder tool produced results that were misleading as all features appeared too high in frequency relative to the experimental data; this was due to the holes being effectively smaller than if they had a perfect circular cross-section. Increasing the number of segments composing the polyhedron increases the accuracy of the solution but also increases the solution time due to the higher resolution mesh needed. A polyhedron comprised of 64 segments was chosen as this appeared to give a good convergence in the results with increasing numbers of segments, beyond this number showed very little improvement in the result. The unit cell of the model is shown in *Figure 3.4.3*.

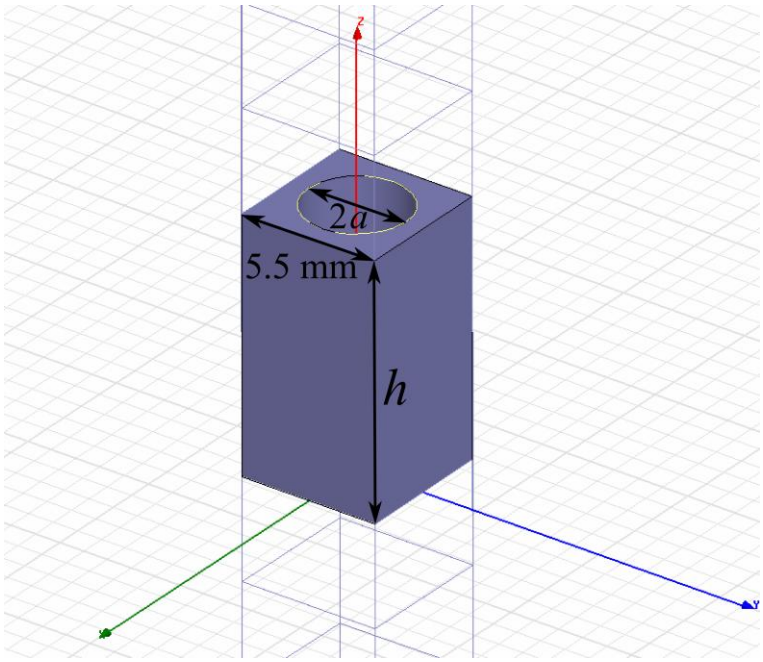

***Figure 3.4.3**. HFSS unit cell used for the modelling of multi-modal transmission of microwaves through hole arrays.*

Air boxes were added either side of the unit cell and the model terminated on the incident and exit face with a PML. Mesh operations were assigned to the hole and surrounding air boxes.

3.4.3.1 Modal – Matching Method

In chapter 6 a modal matching technique is employed to calculate the dispersion of surface modes on a square array of cylindrical holes in a PEC substrate. The modal matching technique has been used previously by many authors to study arrays of square holes[2,81-85]. This method allows the dispersion of surface waves to be calculated on periodic surfaces and the influence of diffraction to be studied by variation of the number of diffracted orders to be included in the calculation. This allows the asymptotic frequencies of surface modes to be found without any band gaps in the dispersion being created. The eigenmode solver within HFSS could calculate the dispersion of a zero order surface mode that lies beyond the light line however it would not be able to remove the effect that diffraction has on the dispersion therefore exhibiting band-gaps at the Brillouin zone boundaries.

The code used in this thesis was written by E. Hendry and is an adaptation of the technique described by W. C. Gibon[84]. The electromagnetic fields within three regions are considered, incident medium (I), within the holes (II) and the transmitted medium (III), illustrated in *Figure 3.4.4*.

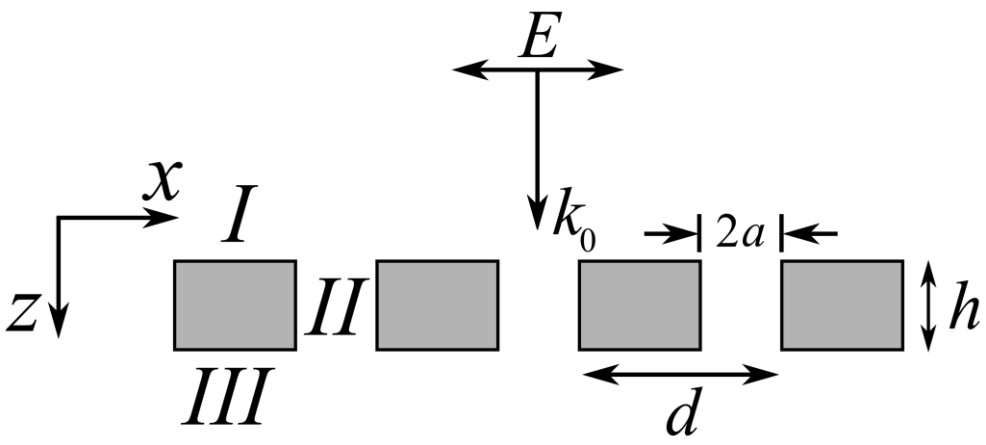

Figure 3.4.4*. Cross-section of the hole array geometry described by the modal matching method.*

The fields within the incident medium are represented as the sum of a plane wave and a Fourier-Floquet expansion of diffracted orders (*Equation 3.4.5*). Likewise in the transmitted medium the fields are also expanded as a Fourier-Floquet expansion of diffracted orders (*Equation 3.4.6*), the time dependent component $\exp(i\omega t)$ has been omitted for clarity:

$$E_x^{\ I} = \exp\left(ik_x x + ik_z^{\ 0,0} z\right) + \sum_{m_1,m_2} r^{m_1,m_2} \psi_1^{\ m_1,m_2} \exp\left(-ik_z^{\ m_1,m_2} z\right) \qquad \textit{Equation 3.4.5}$$

$$E_x^{\ III} = \sum_{m_1,m_2} t^{m_1,m_2} \psi_1^{\ m_1,m_2} \exp\left(ik_z^{\ m_1,m_2} (z-h)\right) \qquad \textit{Equation 3.4.6}$$

Where, $\psi_1^{\ m_1,m_2} = \exp\left(i(k_x + \frac{2m_1\pi}{d})x\right) \cdot \exp\left(i\frac{2m_2\pi}{d} y\right)$

m_1 and m_2 are the diffracted orders, k is the wavevector associated with a diffracted order, d is the grating pitch and h is the height of the array. t^{m_1,m_2} and r^{m_1,m_2} are the complex transmission and reflection coefficients for each diffracted order.

Inside the holes the fields are represented by the lowest order cylindrical waveguide mode, the TE_{11} and the walls of the waveguide are assumed to be PEC.

$$E_\rho^{II} = B\frac{J_1(k_c\rho)}{\rho}\cos(\phi)\exp(iq_z z) - C\frac{J_1(k_c\rho)}{\rho}\cos(\phi)\exp(-iq_z z) \qquad \textit{Equation 3.4.7}$$

$$E_\phi^{II} = -B\frac{\partial J_1(k_c\rho)}{\partial\rho}\sin(\phi)\exp(iq_z z) + C\frac{\partial J_1(k_c\rho)}{\partial\rho}\sin(\phi)\exp(-iq_z z) \qquad \textit{Equation 3.4.8}$$

q_z is the propagation constant which is defined by *Equation 3.4.9*.

$$q_z = \sqrt{\varepsilon_h {k_0}^2 - {k_c}^2} = \sqrt{\varepsilon_h {k_0}^2 - \left(\frac{1.841}{a}\right)^2} \qquad \textit{Equation 3.4.9}$$

The Cartesian components of these fields can be found from *Equation 3.4.10* and *Equation 3.4.11*.

$$E_x = E_\rho\cos\phi - E_\phi\sin\phi \qquad \textit{Equation 3.4.10}$$

$$E_y = E_\rho\sin\phi + E_\phi\cos\phi \qquad \textit{Equation 3.4.11}$$

The *z*-component of the incident and transmitted wavevectors is:

$$k_z^{m_1,m_2} = \sqrt{{k_0}^2 - \left(k_x + \frac{2m_1\pi}{d}\right)^2 - \left(\frac{2m_2\pi}{d}\right)^2}, \qquad \textit{Equation 3.4.12}$$

The *z* components of the electric field and the components of magnetic *H* field are found from Maxwell's equations. The boundary conditions at the interface are such that the tangential electric field must be continuous, being zero on the PEC regions, whilst the perpendicular component may be discontinuous. The perpendicular magnetic field

must be continuous on all regions; the tangential magnetic field must be continuous in the region of the hole due to the absence of currents but may be discontinuous on the PEC regions. The fields are then matched at the interfaces using overlap integrals, this leads to an expression for the transmission function. The dispersion of surface modes can then be inferred from the points of divergence in the transmission function. The dispersion of the surface waves is influenced by the number of diffracted orders as the strength of evanescent diffraction is important in the calculation[84]. This means that although band-folding is removed when diffraction is not included in the calculation the approximation is poorer leading to small changes in the dispersion of the modes.

3.4.4 Enhanced Transmission through a Continuous Metal Film

In chapter 7 a structure designed to give resonant microwave transmission through a thin continuous metal film is presented. Modelling for this structure is very challenging for an FEM code due to the parameters of the metal film as discussed for the patch and hole array structures. The modelling however cannot be approximated by a 2D PEC layer since fields must penetrate into and through the film in order to give any transmission. A diagram of the model is shown in *Figure 3.4.5*.

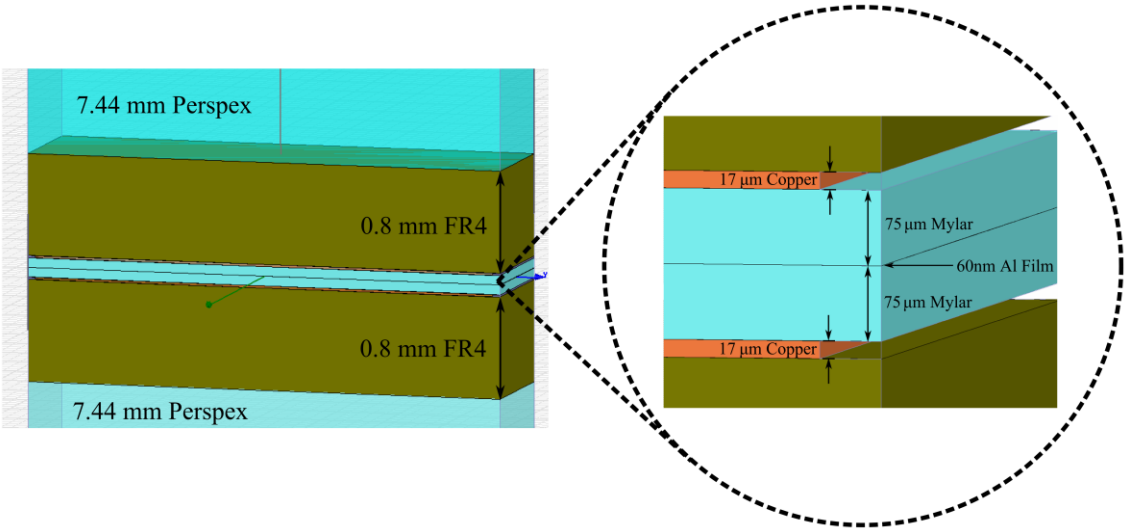

Figure 3.4.5. *HFSS unit cell for the modelling of enhanced transmission through a continuous thin metal film.*

Due to the structure being a mono-grating and only periodic in one direction (i.e. strips of metal) the unit cell can be defined as much smaller than that of the hole and patch

array structures. This allows modelling of the film with a finite thickness and conductivity to be possible.

The unit cell is defined as 3.8 mm × 0.1 mm. The dimension in the non-periodic direction was set to be a small value in order to reduce the size of the problem but not reduced too small such that the mesh elements would be forced to have a very irregular, long and thin shape as these would have difficulty in accurately representing the geometry of the model. A rectangular box was drawn to fit across the unit cell and have a depth of 60 nm; this represents the thin metal film. The material properties were defined as $\varepsilon_r = -10^4$ and $\varepsilon_i/\varepsilon_r = -10^3$, i.e. the approximate Drude parameters for a metal at microwave frequencies. This box was then split into four in the plane in order to reduce the aspect ratio of the layer (*Figure 3.4.6*); this is required in order to help the HFSS mesher so that the tetrahedra are not required to have such a large aspect ratio.

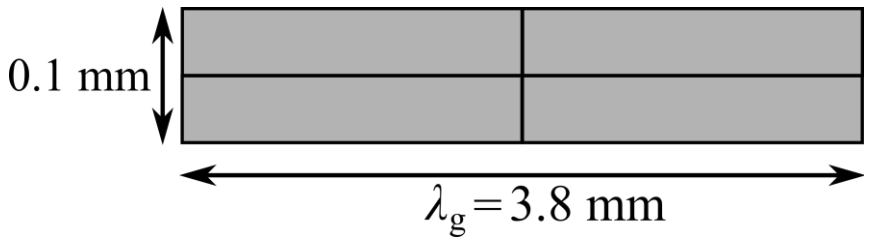

Figure 3.4.6*. Schematic illustration showing the plan view of the splitting of the thin metal film to aid meshing.*

Boxes of thickness 75 μm were then added either side of the metal film layer and assigned dielectric properties of $\varepsilon_r = 2.6$ and $\varepsilon_i/\varepsilon_r = 0.003$ to represent the Mylar layers. Rectangular boxes of thickness 17 μm and width 3.68 mm were then added either side to represent the grating structure, these boxes were assigned with copper properties from the HFSS materials library, having an electrical conductivity of 5.8×10^7 siemens/m and a relative permeability, $\mu_r = 0.999991$. A pair of boxes of thickness 0.8 mm was then added on the outside of the grating structures to represent the FR4 circuit board layers. These layers had dielectric properties of $\varepsilon_r = 4.1$ and $\varepsilon_i/\varepsilon_r = 0.02$. Finally a pair of boxes was used on the outside of the circuit board to represent the Perspex layers. These layers had a thickness of 7.44 mm and dielectric properties of

$\varepsilon_r = 2.6$ and $\varepsilon_i/\varepsilon_r = 0.00577$. An air box of height 32 mm was then drawn around the model with the edges in the direction of the grating assigned as master and slave boundaries to provide repeat boundary conditions in that direction. The other faces were defined as perfect *H* boundaries as the tangential magnetic field is always zero at these walls due to the incident electric field always being in the plane made by $\underline{k}_g$ and the normal to the surface. The incident and transmitted faces of the model are terminated by a PML.

Model resolution mesh operations with a resolution of 10 nm were applied to the four segments of the thin metal film. This keeps the length of the mesh elements at 10 nm and above, helping the HFSS mesher form a continuous mesh across the metal film/Mylar boundary. The elements would otherwise be very small in the metal layer due to the very high refractive index, if a continuous mesh is not formed across the interface this will cause the model to not solve or give erroneous results as a slowly varying element size is required.

3.4.4.1 Fourier Modal Method

In chapter 7 a structure is investigated composed of a resonant cavity containing a thin metal film (~ 60 nm thickness). Due to the very small dimensions of the film relative to the incident wavelength and dimensions of other components of the sample, this is a very complex model for a finite element method model. Mesh elements within the film need to be small enough to accurately represent the field, this high resolution needed however cannot be applied across the whole of the model as it would be computationally inhibiting. The mesh needs to be graded in density throughout the regions of differing dimensions so that the model can be solvable. The limit at which this is practical is about the dimensions of the sample studied, however in order to model films with a smaller thickness another method needed to be employed.

The Fourier Modal Method code used in this thesis was written by M. R. Gadsdon[93] and so only a brief outline of the method will be described. The Fourier Modal Method[94], like HFSS is also a numerical method however it does not use a mesh and so the limitations on the spatial dimensions described above are not as severe. The Fourier Modal Method is similar to the Exact Modal Method[95,96] but with the permittivity of the

grating region being represented by a Fourier series as opposed to being treated analytically. These modal methods use differential techniques similar to those employed in coordinate transform methods such as the Chandezon method[97], whereby Maxwell's equations are solved in their differential form. The Chandezon method however transforms the grating profile onto a flat plane which means that only continuous gratings can be represented.

The fields in the homogeneous regions are described by a Rayleigh expansion of the diffracted eigenmodes whereas the fields in the grating regions are described by a Fourier series related to the grating profile. Maxwell's equations can be reduced to the Helmholtz equation and this can be expanded as a 2-fold Fourier series representation which leads to an infinite set of second-order coupled differential equations. These equations can be reduced to two infinite sets of first order differential equations whose eigenvalues and eigenvectors can be calculated. The field coefficients are then calculated by applying the appropriate boundary conditions to the eigenvectors at each interface with the eigenvalues describing the phase change through each layer.

3.4.5 Metallic Crosses

In chapter 8 the microwave transmission through an array of metallic crosses is investigated. The FEM modelling for this structure was performed by creating a 4.21 mm × 4.21 mm unit cell in the centre of which a cross was placed. The cross was generated by drawing two rectangular boxes of 0.2 mm width, 35 μm thickness and 3.45 mm length and uniting them to form a single object. The cross was assigned as copper from the material library, having electrical conductivity of 5.8×10^7 siemens/m and a relative permeability, $\mu_r = 0.999991$. A 0.762 mm thickness box was placed above the cross to represent the Nelco NX9255 substrate, the dielectric properties were assigned to be $\varepsilon_r = 2.51$ and $\varepsilon_i/\varepsilon_r = 0.0018$. It was later found that the dielectric response of the substrate appeared to be frequency dependent and so for higher frequencies ε_r needed to be increased to 2.99 to achieve a reasonable fit to data. Air boxes of height 8 mm were then added either side of this substrate layer and the cross subtracted from the air boxes. The incident and exit faces of the model were terminated with radiation boundaries; the unit cell is shown in *Figure 3.4.7*.

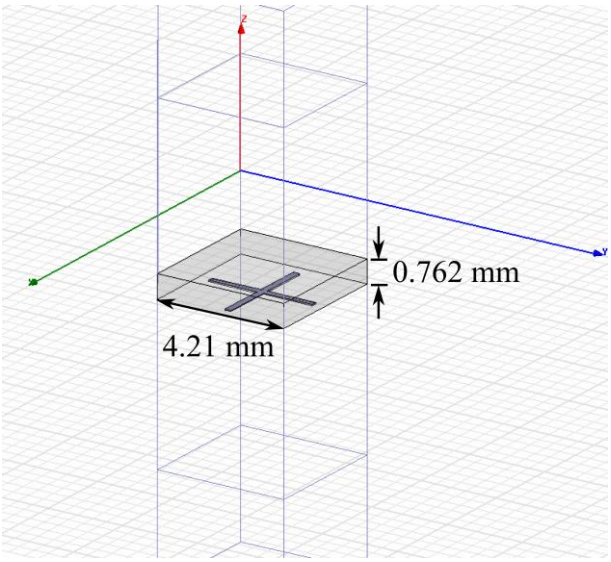

Figure 3.4.7*. HFSS unit cell for the cross array.*

A mesh operation was applied to the surface of the crosses as it was known that large field gradients would be expected in this region. Mesh operations were also applied within the air boxes and dielectric substrate.

In chapter 8 a sample comprising a Fabry Perot cavity from two layers of arrays of crosses was explored, to generate the unit cell for this, the model just described was copied and modified. The Duplicate-along-a-Line tool was used to produce a second layer of crosses a small distance, *d*, below the original. The distance, *d* was defined as a variable so it could be easily changed. The move tool was then used to move the cross from the top side of the second layer to the lower side, making the cavity symmetrical about its centre.

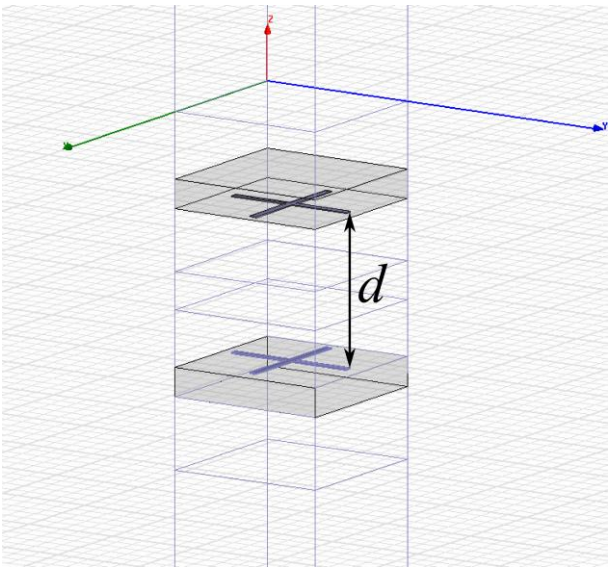

***Figure 3.4.8**. HFSS unit cell of the Fabry Perot cavity composed of arrays of crosses separated by a distance d.*

The air boxes in the lower half of the model were defined such that they move when the separation between the two layers is increased in size, i.e. the second layer of crosses never gets too close to the boundary on the exit face of the model.

3.5 Summary

In this chapter a description of the experimental apparatus used to record microwave transmission measurements has been discussed. Transmission measurements were performed in a free space environment with a collimating mirror setup. Source and detector horns are placed within the focal point of spherical mirrors to form a plane wave which is directed at the sample under study.

A summary of the modelling techniques discussed in this thesis has been presented. FEM was the chosen modelling technique for the majority of the modelling within this thesis due to the flexibility offered for various geometries. The basic principles of the FEM software, HFSS, have been covered along with the advantages and disadvantages of this method. Representation of samples, assigning material parameters and meshing has been discussed. A description of the finite element models used for the experimental chapters in this thesis is also given.

The principle of the modal matching method has been described in this chapter. This analytical technique allows the dispersion of surface waves on hole arrays to be calculated by representing the fields in the incident and transmitted regions as a Fourier Floquet expansion of diffracted orders, these fields are then matched with the fields in the holes which are represented as waveguide modes. Use of this analytical technique allows the dispersion of the surface waves to be calculated without the inclusion of diffracted orders in the calculation thus allowing the asymptotic frequencies to be observed without the complication of band-folding and band gaps forming in the mode dispersion.

The Fourier Modal Method has also been briefly discussed in this chapter. This numerical technique allows the response of one-dimensional gratings to be predicted but unlike FEM it does not use a mesh and as such the limitations on spatial dimensions are not as severe. This technique was used in chapter 7, where the responses of very thin metallic films in a resonant cavity were to be predicted.

4 Microwave transmission of regular and random arrays of patches and holes

4.1 Introduction

In this first experimental chapter the microwave transmissive properties of patterned metallic thin films are investigated. Over recent years there has been substantial interest in the electromagnetic properties of patterned metal surfaces and thin films. Much of this work[12,71,98] has focused on the transmissive properties of films in the visible region but there is also a long history of radar related research[99-102]. Metallic structure has been utilised in the control of microwave transmission for many years particularly in the area of frequency selective filters[1]. These filters are typically formed from periodic arrays of metallic elements which, due to their structure and connectivity, transmit or reflect selectively (chapter 2). Another established research field that measures the electromagnetic properties of arrays of metallic elements is the study of D.C. and A.C. electrical properties of random metallic-dielectric composites[103-106]. Studies in this field are often focused on the region of the percolation threshold, i.e., the metallic occupancy at which a connected conducting pathway is formed across the system, thus drastically altering the conductive properties. This changing behaviour across percolation will lead to significant changes in a structure's microwave transmissive properties similar to how a patch array and a hole array have very different properties due to their differing connectivity.

Regular and random metallic structures are distinctly different in that a regular array has a well defined periodicity and corresponding diffraction features associated with trapped evanescent waves becoming propagating and being able to leave the surface. These diffracted orders will each have surface waves associated with them and due to band folding (discussed in chapter 2) coupling to these modes will be possible. Random arrays however, have no defined periodicity and therefore will have no well defined diffraction feature or strongly coupled surface modes.

The first experimental section within this chapter investigates square arrays of square patches and square arrays of square holes whose edges are orientated at 45° with respect to the lattice. This enables the dependence of the microwave transmission on the metal occupancy either side of the connectivity threshold (when the metal patches switch from disconnected to connected) to be fully explored. If the edges of the patches and holes were orientated parallel to the lattice vectors connectivity would not be achieved until 100 % metal occupancy.

Conventional wisdom would have it that the high microwave transmissivity of a regular array of patches will switch off on increase of the metal occupancy through the connectivity threshold. However, the remarkable result presented here is that, for frequencies close to the diffraction edge, the existence of the resonance previously discussed causes the microwave transmittance to go from zero to unity through this threshold – a complete reversal of the expected behaviour at lower frequencies.

The second experimental section of this chapter investigates the microwave response of random arrays of metallic discs and its complement; a random array of holes in a metal film. The transmission response of these arrays is remarkably different to that of the regular arrays due to the lack of a well-defined periodicity. Since there is no well defined periodicity, no resonant behaviour is observed and therefore this reversed transmission threshold is not observed. Also no sudden change in transmission is observed between samples containing metallic connectivity and samples that are disconnected, i.e. where one would observe a D.C. percolation threshold. Measurements on the complementary structure (random array of holes in a metal film) however show that it is the structure that is dominant in defining the transmission response and not just the metal occupancy.

4.2 Background

4.2.1 Regular Arrays

The patches and holes considered in many previous studies[19,21,74] have been aligned so that their sides lie parallel to those of the unit cell. However, relatively few studies[107,108] have investigated square patches (or holes) that are rotated compared to the

conventional geometry, giving connectivity between neighbouring patches in the 45° rotation case at 50 % metal occupancy (
Figure **4.2.1**).

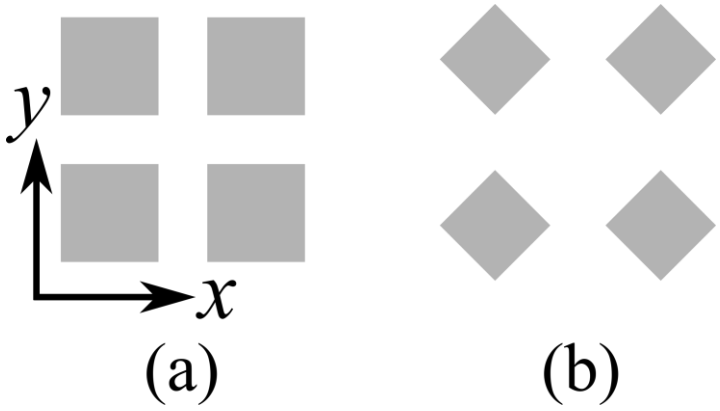

Figure 4.2.1.(a) *Conventional patch/hole array geometry.* ***(b)*** *45° rotated geometry.*

While this perhaps seems quite incidental, it crucially enables the dependence of the microwave transmission on the metal occupancy either side of the connectivity threshold (when the metal patches switch from disconnected to connected) to be fully explored. Arrays of patches and arrays of holes exhibit suppressed or enhanced transmission phenomena mediated by the resonant excitation of surface waves. A discussion of surface waves and their role in transmission through patch/hole arrays is discussed in chapter 2.

4.2.2 Percolation

The concept of percolation was first conceived by Flory[109] and Stockmayer[110] during the Second World War in relation to gel formation in polymers but the terminology and mathematical treatment was first dealt with by Broadbent and Hammersley (1957)[111] (also Hammersley[112]).

Percolation theory is used to describe the behaviour of a system when one component of the system is increased relative to another, when one of the components exhibits a physical property which changes the behaviour of the composite system. In particular it describes the important behaviour when one of the components has formed a connection spanning the whole of the system[113]. For example, percolation theory is used in fluid

dynamics to determine whether a fluid will flow from one side of a perforated material to the other as the number of holes in the layers increases. Another example is the growth of a metal film during thermal deposition. As metal is deposited clusters will form and the metallic filling fraction will increase with metallic connectivity across the system achieved at and beyond the percolation threshold. At the percolation threshold there will be a large increase in the DC conductivity as current can now flow across the system. *Figure 4.2.2* shows a scanning electron microscope image of a gold film which is discontinuous showing typical cluster forming behaviour.

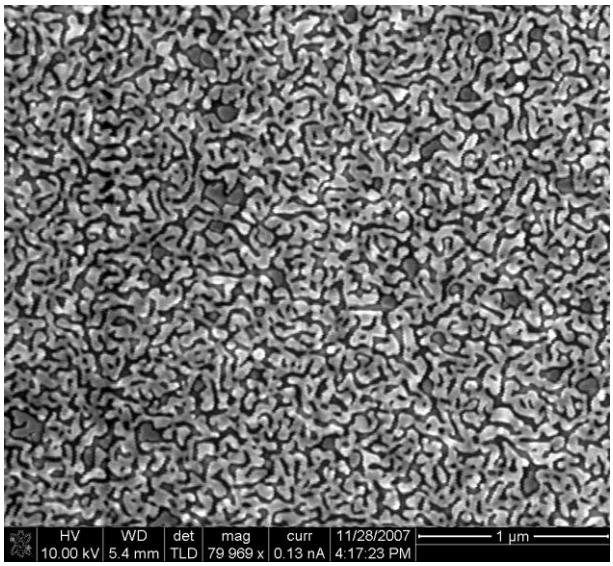

***Figure 4.2.2**. Scanning electron microscope (SEM) image of a discontinuous gold film formed by thermal deposition on a glass substrate. Cluster formation clearly visible. (image courtesy of C. P. Burrows)*

The sub-units considered in the discrete modelling description of a percolation problem can be the lattice vertices; this is known as **site percolation**. The lattice edges connecting neighbouring points can also be used and this is known as **bond percolation**, shown in *Figure 4.2.3*.

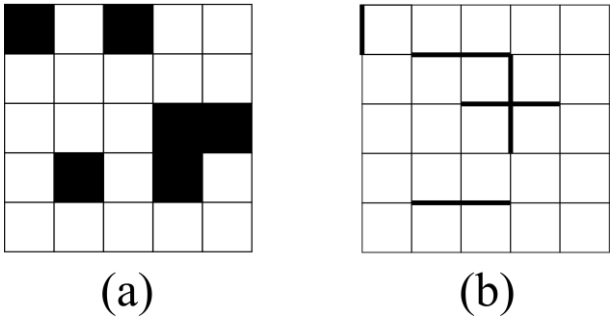

***Figure 4.2.3**. Sub-units used in percolation theory (a) Site percolation (b) Bond percolation*

Site percolation will be discussed in this thesis as it is this particular type of percolation that is closest to the behaviour of our random thin metal films. Also when the site occupancy reaches 100 % the total occupancy will also be 100 % whereas for bond percolation this will not necessarily be the case and occupancy will be related to the width of the bond relative to its period.

If p defines the probability of a site being occupied and neighbouring occupied sites are considered to be connected, then, when $p = 0$, all sites are isolated from all other sub-units. When $p = 1$, all sites are connected to the maximum number of neighbouring sub-units. There will be value of p at which there will exist a cluster which will traverse the system, this is known as an infinite cluster as the system is assumed to be infinite, this occurs at the percolation threshold, p_c. Below p_c only isolated clusters will exist. It is at the percolation threshold that the phase transition will be observed. In this thesis this phase transition corresponds to a transition from a non-conducting system to that of a conducting system.

For a 1D system, i.e. a linear chain of sites there will not be a connection from one side of the system to the other unless all of the sub-units are connected to one another, therefore $p_c = 1$. For a 2D square lattice $p_c = 0.593$, so when 59.3% of the sites are occupied there will then be an infinite cluster present. The percolation threshold depends on the lattice type of the system. Values of the percolation threshold for various lattices calculated by Galam and Maugar[114] can be seen in *Table 4.2.1*.

Lattice Type	**Dimensionality**	$p_c - \text{site}$	$p_c - \text{bond}$
Linear Chain	1	1	1
Honeycomb	2	0.6962	0.65271
Square	2	0.592746	0.500000
Triangular	2	0.50000	0.34729
Diamond	3	0.430	0.388
Simple Cubic	3	0.311605	0.248812

***Table 4.2.1**. Percolation thresholds for various lattices[114].*

4.2.2.1 Previous Percolation Studies

There have been numerous electrical percolation studies performed on 2D and 3D systems at D.C., many of which are published within material science journals. One of the earliest studies was by J. Gurland (1966)[115] who measured the conductivity of silver balls dispersed in Bakelite powder and found a threshold to occur at 30 % volume occupancy of conducting balls. The results from this experiment were later shown by A. Mallaris and D. T. Turner (1971)[116] to be sensitive to the preparation method. A 2D percolation study was performed by B. J. Last and D. J. Thouless (1971)[106] in which they randomly punched holes in a square lattice into conducting colloidal graphite paper and then measured the resistance. They found that the conductivity is not proportional to the size of the infinite cluster, $P(p)$ as one may initially anticipate. This is due to dead ends in the infinite cluster contributing to its size but not its electrical conductivity.

Youngs et al.[104] investigated the AC conductivity of a composite composed of silver microspheres embedded in paraffin wax showing that a clear percolation threshold is observed in the material properties (*Figure 4.2.4*).

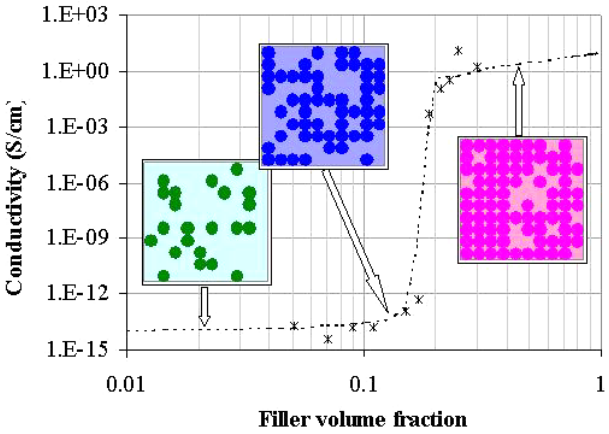

Figure 4.2.4*. Behaviour of the conductivity at 1 Hz with increasing filler volume fraction for a silver microsphere – paraffin wax composite*[105]*. Points are experimental data, dotted line is a fit is from McLachlan effective medium theory*[117]*.*

There are many D.C. and low frequency electrical percolation studies however there have been very few percolation studies focused on the transmission and/or reflection of microwaves. The work by Antonets et al[99,118] showed experimentally that the D.C. conductivity of thin films deposited by thermal evaporation differs substantially from that of bulk samples as expected from theory[119-121]. Surface scattering and grain boundary[122] scattering reduces the conductivity of thin films when the thickness and metal grains are smaller than the mean free path of electrons. The conductivity of the thin films was found to be several orders of magnitude smaller than the corresponding bulk samples. They measured the microwave reflectivity of thin metal films of differing metal thicknesses formed by thermal deposition. Their experiments showed a sharp increase in reflection and therefore conductivity as the film thickness was increased beyond the percolation threshold[99], as shown in *Figure 4.2.5.*

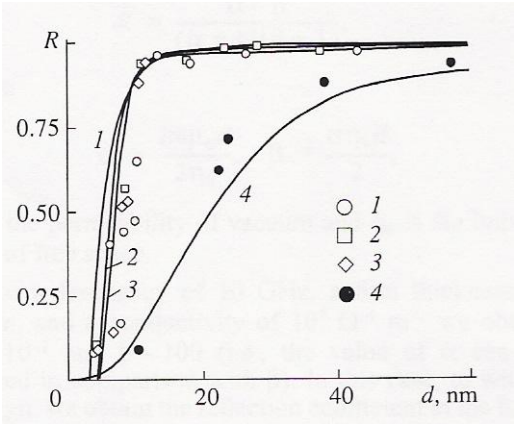

Figure 4.2.5*. Dependence of the reflection coefficient, R of a 10 GHz microwave signal on the film thickness, d* [99]*. Solid lines represent theory, the points are experimental data. (1) Silver, (2) Copper, (3) Gold, (4) Iron.*

Lagarkov et al.[102] measured the 12 GHz microwave transmission and reflection of arrays of copper spots randomly distributed on a fibre-glass substrate and found that a wide absorption band was present around the percolation threshold. Field probe measurements of the electric field of a sample near the percolation threshold, found that the field showed strong localised enhancement in some regions leading to the observed absorption.

4.3 Experimental

4.3.1 Samples

Samples were produced by wet-etching aluminised Mylar® of 75 μm thickness, the aluminium being 60 nm thick. The array designs were drawn in Inkscape[123], a freeware vector graphics program and printed out on an A1 (841 mm × 594 mm) sheet. This A1 pattern was then used in an Agfa-Gevaert reprographic camera to produce a reduced size exposure on photographic paper. This exposure is used as a mask for the etching process. Reducing the size of the original design allows a greater resolution to be achievable and the photographic paper ensures the highest contrast between features on the mask. Development and fixing of the exposed mask is then performed with standard photographic chemicals. The aluminised Mylar is coated with dry film negative photoresist which is exposed through the mask inside an ultraviolet light box. The sample is then placed in a chemical tank containing photoresist developer which

dissolves all of the unexposed photoresist; this leaves the aluminium to be removed exposed. After development of the photoresist the sample is placed in an etchant composed of phosphoric acid, nitric acid and acetic acid. The remaining photoresist is then removed with a stripping agent to leave the final sample.

4.3.1.1 Regular Arrays

Samples were produced using a square array geometry of pitch, $\lambda_g = 7.02$ mm with a square patch of side length *a* on each lattice point (*Figure 4.3.1*).

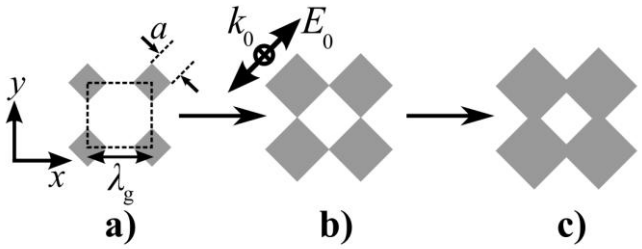

Figure 4.3.1*. Schematic illustrating the increase of patch size with fixed pitch to form a fully connected conducting network. (Grey represents aluminium and the dotted line indicates a unit cell of the array.) Orientation of the incident electric vector illustrated.*

Each square patch is orientated with its sides at 45° to the primary lattice vectors. Note that while the thickness of the aluminium layer is much less than the skin depth at the frequency range studied (~ 1 μm), it is essentially completely opaque to microwaves due to its Drude - like dielectric function $\mathrm{Im}(\varepsilon) \to \infty$ manifested as a large impedance mismatch. A series of samples were fabricated with metal occupancy, $0 \le X \le 100\%$ (no metal to continuous aluminium) by variation of the patch side length, *a*, (*Figure 4.3.1*) while maintaining the pitch, λ_g. Any sample with $a > 4.965$ mm ($X > 50\,\%$) results in overlapping patches to form a conducting mesh network (hole array).

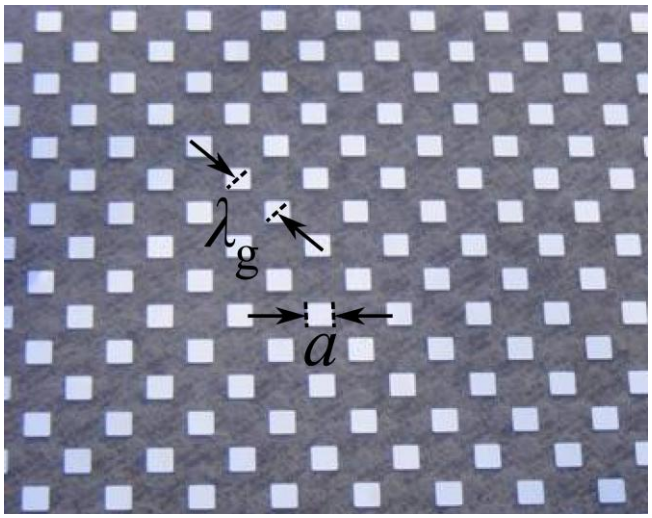

***Figure 4.3.2**. Photograph of an array of square metallic patches, fabricated by etching aluminised Mylar. Patch side length, a and fundamental grating pitch, λ_g illustrated.*

4.3.1.2 Random Arrays

The initial idea for an experimental study of a random percolating system was to fabricate thin metal films through thermal evaporation, of varying thickness across the percolation threshold. This would have allowed a study similar to that performed by Antonets et al.[99] to be performed but with frequency dependence also investigated. A few samples composed of aluminium deposited on glass were fabricated. However due to limited fabrication facilities a large enough uniform metal thickness area for a free space measurement could not be achieved. The metal is evaporated from a fixed point leading to an approximately Gaussian distribution in the deposition of metal leaving a much greater thickness of metal in the centre than around the edges, particularly noticeable over large areas. Since this was not going to be practical another technique was sought and it was decided that the technique used to fabricate the arrays in *section 4.3.1* could be combined with a random pattern generator to fabricate random arrays from aluminised Mylar. This technique is also repeatable since the etching mask can be used again allowing samples with known clusters and percolating networks to be fabricated if needed.

In order to produce random array geometries for fabrication using the technique in *4.3.1* a code was written in *R*, a statistical programming language. The user inputs a number of required particles/elements, the code then produces a random set of *x* and *y*

coordinates confined to an A1 layout. Each set of coordinates is assigned a value based on a Gaussian distribution; this value determines the size of the disc placed at these coordinates. The discs are allowed to overlap with one another without restriction allowing connectivity and percolating networks to form as the number of discs is increased. The black and white image formed can be outputted as a file, printed and used to generate a photomask for etching. Sections of outputted patterns of increasing filling fraction are shown in *Figure 4.3.3*.

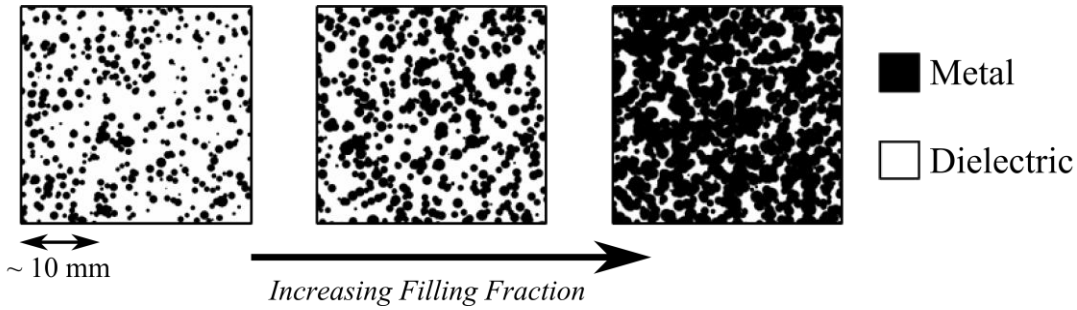

***Figure 4.3.3**. Schematic illustration of sections of random arrays produced using the computer code.*

The area filling fraction occupied by the discs is determined by analysing the image in *imagej* a freeware image analysis program which counts the number of black pixels relative to the pixels that comprise the whole image. A section of a final sample fabricated from aluminised Mylar® can be seen in *Figure 4.3.4*.

***Figure 4.3.4**. Image of a random array fabricated from aluminised Mylar®.*

A series of samples with metallic filling fractions ranging from zero to 100 % were fabricated allowing transmission measurements across the percolation threshold to be

performed. Each structure has its own unique set of spatial coordinates and therefore is not an incremental progression from the samples with a lower filling fraction; this allows systematic error to be reduced. If an unusual distribution of discs were generated that produced strikingly different results from the other samples this would be apparent as other arrays would not contain similar conducting networks.

The complementary structure of each of the random arrays was also fabricated to study the effect of removal of metal disks from a continuous film on its transmissive properties.

The samples were supported on a 3 mm thick sheet of expanded polystyrene (refractive index ~ 1 at these frequencies) and placed behind a 100 mm × 100 mm aperture formed from microwave-absorbing material. Transmission measurements in the frequency range $12.4 \leq \nu \leq 60$ GHz were performed with a series of matched source and detector horns, and normalised to transmission through the aperture and polystyrene sheet without a sample.

4.4 Results and Discussion

4.4.1 Regular Arrays

Typical normal incidence transmission results are shown in *Figure 4.4.1*. First order diffraction occurs at 42.7 GHz due to the 7.02 mm periodicity.

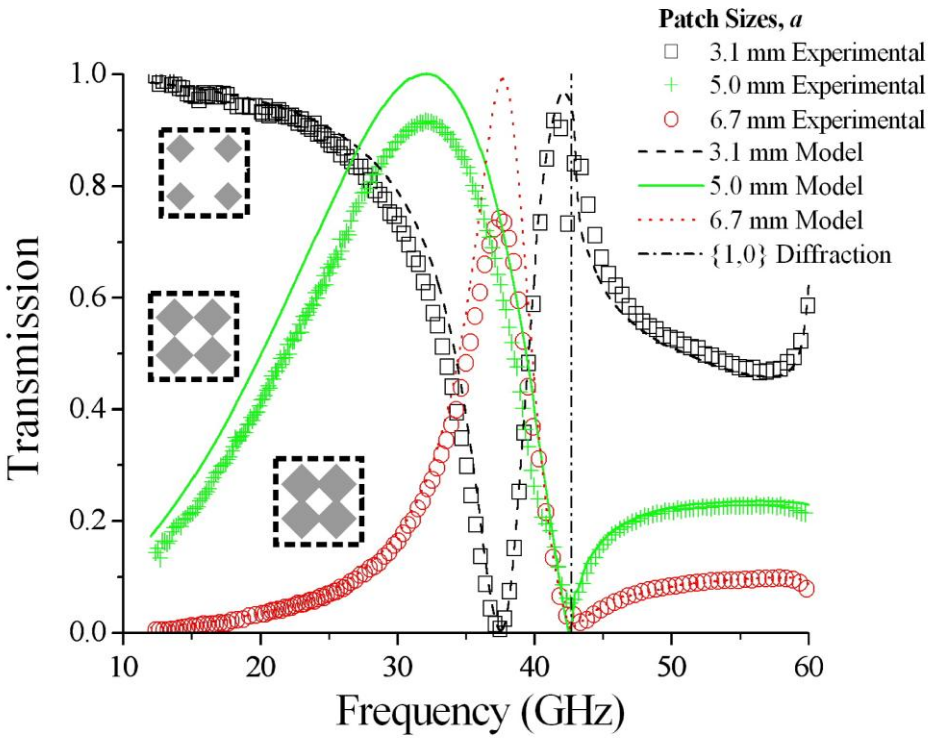

Figure 4.4.1. *Transmission measurements for three patch sizes on a square array of pitch 7.02 mm. Normal incidence, electric-field vector polarised parallel to patch side. Schematic diagrams illustrate the connectivity of the structures.*

Modelled responses are obtained with a finite element method (FEM) model[17] (discussed in chapter 3), using the unit cell illustrated in *Figure 4.3.1*, together with periodic boundary conditions. We assume that the sample is infinite in extent in the *xy*-plane and that a perfect plane wave is incident. In reality of course, both the sample and beam spot are finite. There is also a small incident angle spread of ~ 1 – 2° inherent in the experimental technique and this spread accounts for the small discrepancy between the data and the model near to the diffraction edge where an extra mode is observed in the data. This arises from a band gap close to the diffraction edge and the consequential existence of a mode associated with each band edge. At normal incidence, field symmetry prevents coupling to the upper frequency mode. However at other angles of incidence the symmetry is broken and the wave can couple to both the upper and lower branch. Then, because of the finite angle spread in the incident beam, this higher frequency mode is seen for normal incidence resulting in an extra minimum in transmission (more information on band gaps can be found in chapter 2). This is evident from modelling shown in *Figure 4.4.2*.

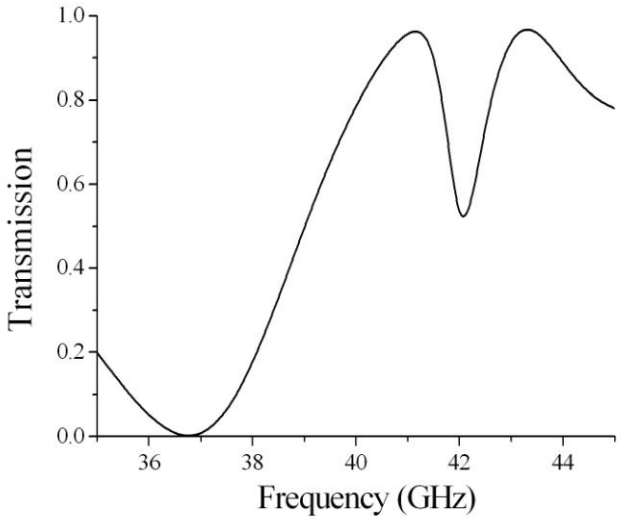

***Figure 4.4.2**. Modelled response of 3.1 mm patches in a square array of pitch 7.02 mm, $\theta = 2°$, p-polarised incident radiation.*

Electric fields for the mode present at 42 GHz in *Figure 4.4.2* are shown in *Figure 4.4.3*.

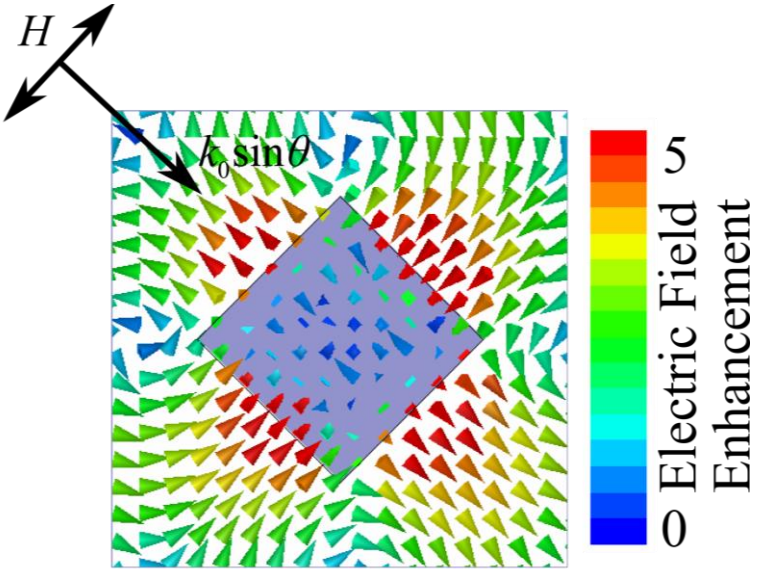

***Figure 4.4.3**. Vector electric fields plotted at 42 GHz at a phase corresponding to maximum field enhancement for an array of 3.1 mm square patches in a square array of pitch 7.02 mm. $\theta = 2°$.*

The electric fields show that the mode cannot be coupled to at normal incidence due to the symmetry of the fields and therefore configuration of the charges. A phase variation across the patches is required to excite this mode.

The dielectric properties of the Mylar® were found by forming a Mylar®-filled slit between two metallic plates. On resonance a TEM mode is supported between the plates with the resonant frequency dependent on the slit geometry and the Mylar dielectric properties. The resonant transmission peaks were fit to an FEM model by varying the real part of the Mylar® permittivity. The imaginary part of the permittivity was set to that of polyester due to having similar low-loss properties and the difficulty in guaranteeing the same normalisation between the model and experiment. The dielectric properties of the Mylar® were determined to be $\varepsilon = 2.62 + 0.01i$ across the frequency range of interest. Further the thin metal patches have been represented as two-dimensional (*i.e.*, zero thickness) objects and defined as PEC in the model. While this is generally a good approximation for the microwave regime it does lead to other discrepancies between the model and data since the finite loss in the thin metal layer is not accounted for. This is apparent in the data for the 5.0 mm and 6.7 mm patch side samples close to the resonant peak. Better agreement between model and data can be achieved by introducing finite thickness and loss within the metal but such FEM modelling is computationally intensive. Metals in the microwave regime have very large refractive indices (~ 10^3) and the thickness of our film is very sub-wavelength $\left(\sim \lambda/10^5\right)$. Then to maintain sensible aspect ratios of the finite element model tetrahedra, a very dense mesh in the metal relative to that in the incident medium is required to accurately describe the fields. In addition, the mesh in the incident medium has to be graded in density in order to match with the mesh in the metal at the metal-air interface. This requires a large amount of computer memory and many hours of computing time to solve the fields within these elements. Therefore the simple two-dimensional, PEC approximation has been employed throughout the remainder of this study.

At low frequencies the disconnected arrays of patches ($a < 4.965$ mm) exhibit low-pass frequency filtering behaviour commonly seen for a regular capacitive patch array[1] (discussed in chapter 2). This is simply because long wavelengths cannot drive currents around the system. The connected arrays ($a < 4.965$ mm) exhibit high-pass frequency

filtering behaviour associated with inductive meshes[1] (discussed in chapter 2) since currents are able to propagate in the continuous network of metal. Samples of a given metal occupancy (X %) are the inverse of those with an occupancy of $(100-X)$ %. Thus, using Babinet's principle[15] (chapter 2) and assuming a zero-thickness perfect conductor, samples with X % occupancy will have a normal incidence transmissivity T_X, while $(100-X)$ % samples have a transmissivity of $1-T_X$.

Each of the samples exhibits a resonance near the diffraction edge that can be seen as a **minimum** in transmission for the disconnected samples and a **maximum** in transmission for the connected patch samples. These resonances are similar to those reported by García de Abajo et al.[77,124], being of geometrical nature, associated with the periodicity of the array, and are hybridised with the dipolar mode of each patch/hole, similar to the surface waves on textured metals discussed in chapter 2. Indeed, one may examine the modelled fields to more fully understand their origin (*Figure 4.4.4* and *Figure 4.4.5*).

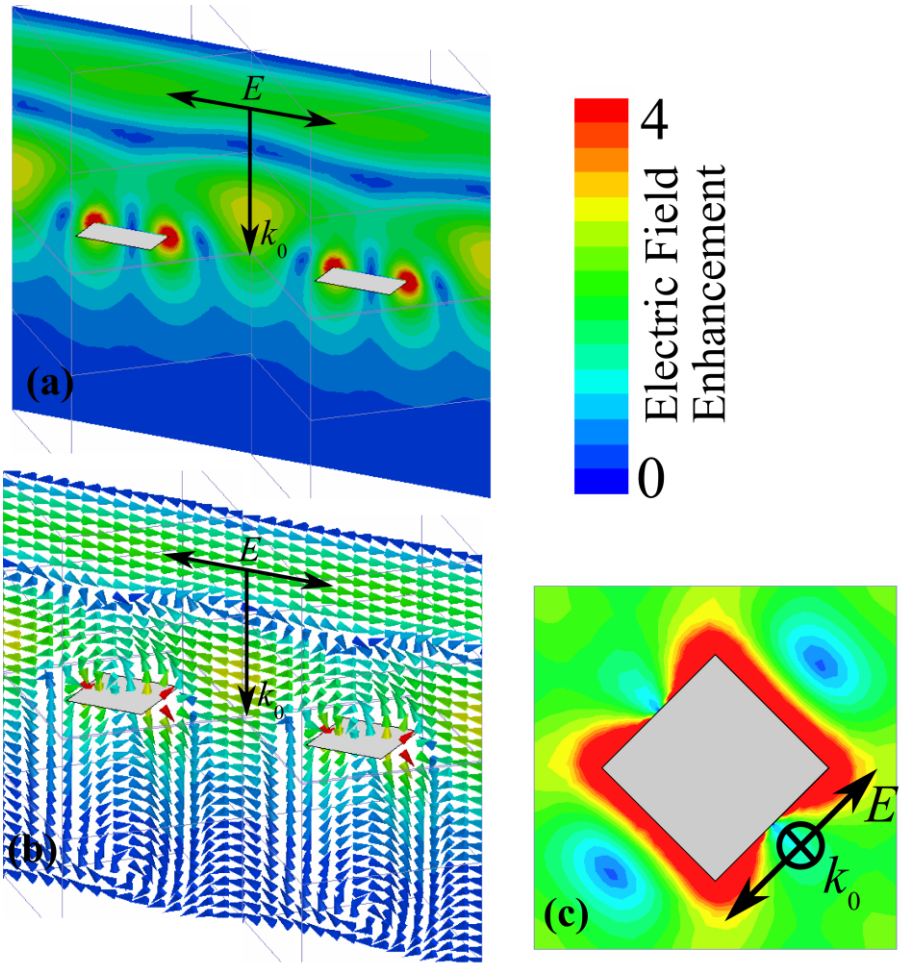

Figure 4.4.4. *Electric field plots from FEM modelling of two neighbouring unit cells of the a = 3.1 mm patch array on resonance. (a) Time-averaged electric field plotted through the middle of the unit cell in the $E_0 – k_0$ plane. (b) Instantaneous vector electric fields plotted through the middle of the unit cell in the $E_0 – k_0$ plane at a phase corresponding to maximum local field enhancement. (c) Time-averaged electric field plotted in the plane of the sample. Light grey indicates PEC regions.*

For the disconnected patch array (*Figure 4.4.4*), there exists a standing wave across the patch edge along the direction of polarisation with the fields showing dipolar character. The complementary structure (*Figure 4.4.5*) also shows dipolar behaviour in its field profile with large fields in the holes. Fields within the holes (*Figure 4.4.5c*) have similar character to that of the first order rectangular waveguide mode, TE_{10} [125].

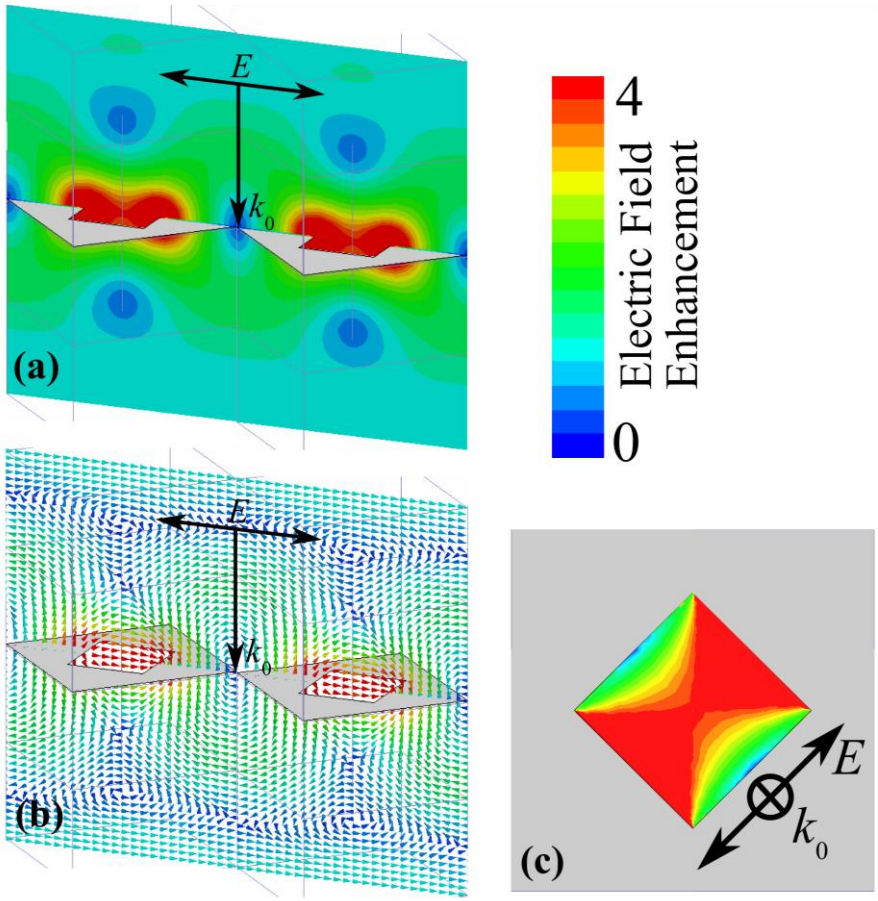

***Figure 4.4.5**. Electric field plots from FEM modelling of the a = 6.7 mm hole array on resonance. (a) Time-averaged electric field plotted through the middle of the unit cell in the $E_0 – k_0$ plane. (b) Instantaneous vector electric fields plotted through the middle of the unit cell in the $E_0 – k_0$ plane at a phase corresponding to maximum local field enhancement. (c) Time-averaged electric field plotted in the plane of the sample. Light grey indicates PEC regions.*

Near-field interaction between neighbouring patches and holes can be seen on the field plots. Since the patches are disconnected the linkages between unit cells are supported by displacement currents whereas the connected array can support propagating currents. The strength of the evanescent diffracted orders is greatest closest to the onset of the first propagating diffracted order and it is these evanescent fields that lead to the resonant interaction between neighbouring patches/holes. There are two transmission channels present: a resonant and a non-resonant contribution and it is the interference between these two channels that leads to the characteristic Fano-resonance[126] shape (*Figure 4.4.4*). The transmission minimum/maximum reduces in frequency as the patch/hole size is increased. This is due to the changing relative contributions from the resonant and non-resonant transmission channels. For small holes the non-resonant

contribution is minimal and transmission is mediated by the resonant excitation of surface waves. As the size of the holes is reduced and the structure approaches the limit of a planar metal/air interface this resonance will approach the diffraction edge. For large holes the non-resonant contribution is greater than previously, leading to a broader resonance at lower frequencies. As discussed in the work of Bravo-Abad et al.[83], the diffraction due to scattering from small holes (hole size < λ_{cutoff}) induces narrow resonances close to the diffraction edge which are a result of the collective electromagnetic interaction between the holes. Diffraction from larger holes (hole size $\approx \lambda_{cutoff}$) induces a broadening of the resonance and a shift to lower frequencies as the interaction between the holes reduces and transmission is mediated by grazing diffracted orders. This is illustrated by further experimental data for various patch and hole sizes in *Figure 4.4.6*.

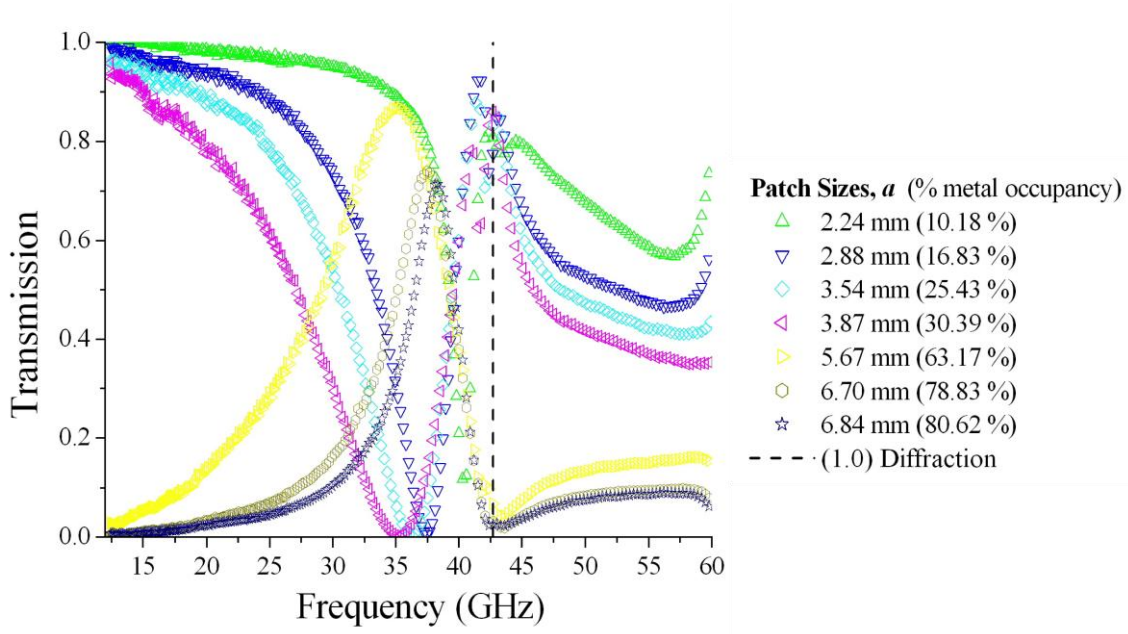

Figure 4.4.6. *Experimental normal incidence transmission for square arrays of various patch/hole sizes rotated by 45° with respect to the lattice.*

The transmission as a function of metal occupancy at a series of fixed frequencies is plotted in *Figure 4.4.7*.

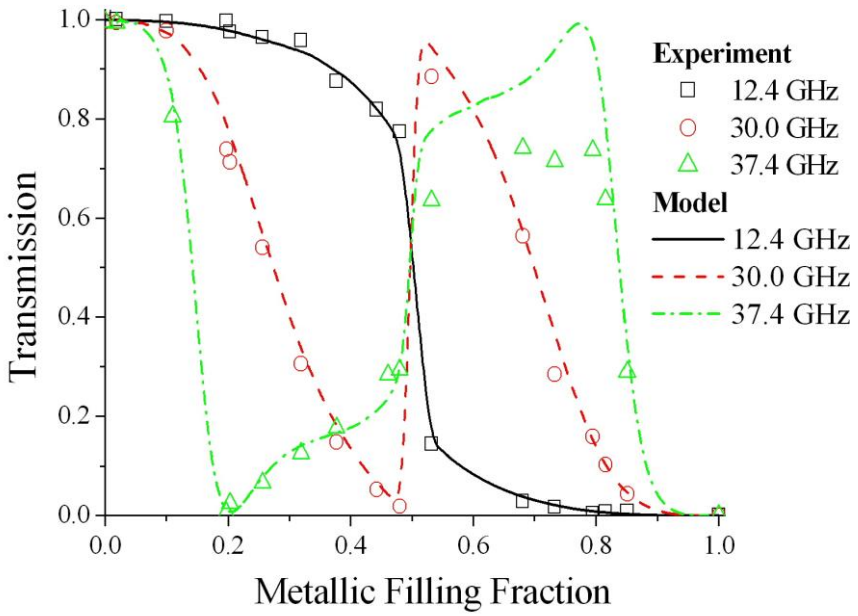

Figure 4.4.7*. Normal incidence transmission measurements as a function of metal occupancy for a square array of square patches orientated at 45° with respect to the unit cell. The model is for PEC metal. Diffraction onset at 42.7 GHz.*

At DC the transition with increasing metal occupancy from full transmission to zero transmission would be expected to take the form of a perfect step function at 50 % occupancy with an infinite negative gradient. However for a finite frequency the transition takes a different form. At 12.4 GHz the transition still exhibits an edge but it is less sharp due to the finite frequency of the incident radiation restricting the movement of the electrons on the arrays. Since the incident wavelength is now closer to the grating pitch, λ_g, the perturbation due to the resonance is also becoming increasingly important. This results in a smoothing of the dependence on metal occupancy through the connectivity point.

At frequencies closer to the onset of diffraction, the perturbation due to the resonance results in a strikingly different transition profile. Transmission for 30.0 GHz shows the effect is sufficiently strong such that the gradient of the transmission function on passing through 50 % occupancy is of opposite sign. The transmission no longer continually decreases across the whole of the metal occupancy range since the structure is strongly resonant close to the connectivity threshold. At 37.4 GHz the transition profile is further perturbed. Approximate 180° rotation symmetry of the transmission

spectrum is visible about the 50 % occupancy condition, T = 0.5 point, due to Babinet's principle[15]. However it is apparent that while the resonant transmission is reduced to T = 0 at about 20 % metal occupancy, the maximum at 80 % occupancy reaches only T = 0.8. This, as previously discussed, is due to the dissipation in the metal, which on resonance may be substantial and is not accounted for in the PEC model.

4.4.1.1 Modelling

Modelling allows further understanding of the response of structures without the need to fabricate numerous samples. *Figure 4.4.8* shows the effect of changing the periodicity of an array of 3.1 mm patches on the resonant mode seen in the transmission spectrum.

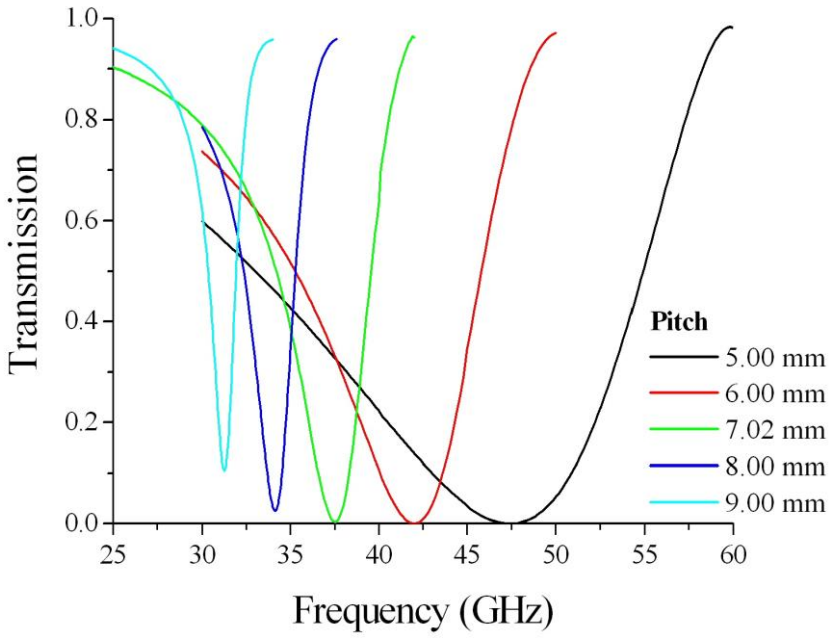

***Figure 4.4.8**. Normal incidence modelled transmission response for a square array of patches, orientated at 45° with respect to the unit cell. Modelling for different lattice periodicities illustrated.*

The modelling shows that the mode position is strongly dependent on the periodicity of the array and always appears on the low frequency side of the onset of diffraction. As the pitch is increased the mode shifts down in frequency with the onset of diffraction. This confirms the diffractive nature of the coupling to this mode and its surface wave nature as the periodicity has a more significant influence than the hole/patch size on the

resonant frequency of the mode. The width of the resonance is also dependent on the periodicity, the closer the mode lies to the diffraction edge the higher the Q factor of the mode. For the larger pitch modelling (8 mm and 9 mm) it can be seen that the depth of the mode is also affected, by changes in pitch, this is due to the now much lower metallic occupancy of the array, therefore lower amount of scattering for each unit cell and hence weaker coupling to the mode.

Further modelled transmission responses as a function of filling fraction are shown in *Figure 4.4.9*. The effect of the resonant behaviour on the transmission can be clearly seen with deep features in the spectrum and complex behaviour across the connectivity threshold at 50 % occupancy.

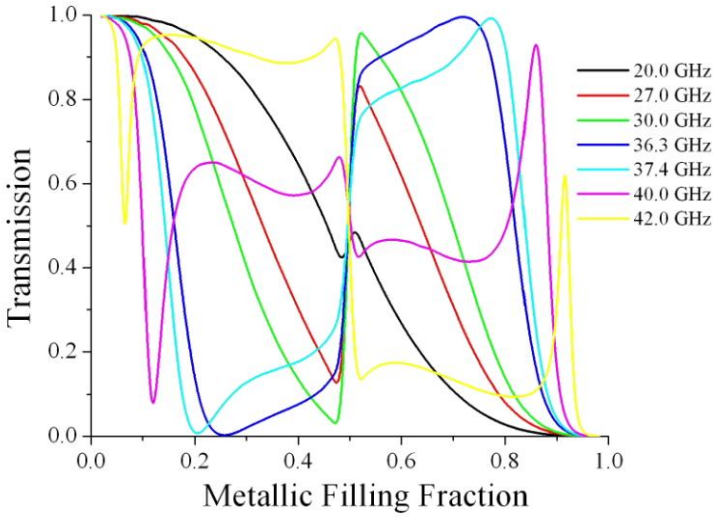

Figure 4.4.9. *Modelled normal incidence transmission as a function of metallic filling fraction for a series of frequencies.*

Another interesting phenomenon is seen in *Figure 4.4.10*, where the transmission response as a function of filling fraction is shown for a number of frequencies near the diffraction edge. There is a frequency at which a large range of filling fraction gives a transmission response which is close to 50 %.

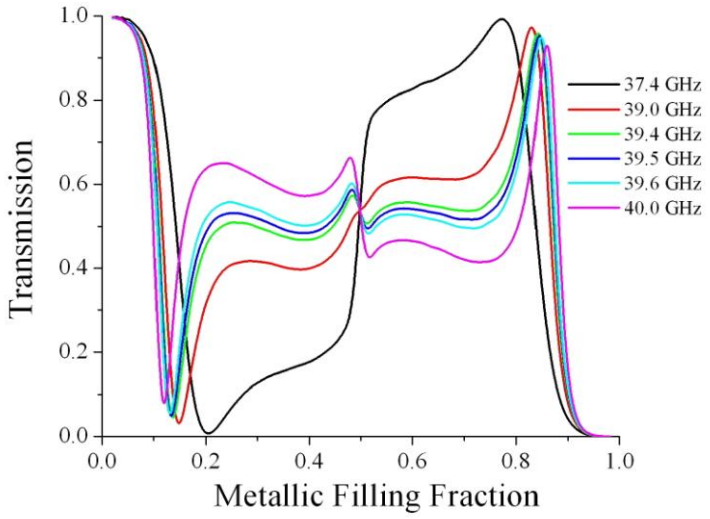

***Figure 4.4.10**. Modelled normal incidence transmission as a function of filling fraction for a series of frequencies close to the onset of diffraction.*

This effect is due to the diffractively coupled nature of the modes and their pinning to frequencies near the diffraction edge. Looking back at *Figure 4.4.6* shows the transmission responses for these filling fractions all passing the region of 50 % transmission at approximately the same frequency leading to a frequency where the metallic occupancy can be changed significantly without any significant difference in transmissivity.

4.4.2 Random Arrays

A series of random arrays of metallic overlapping discs were fabricated with metallic filling fraction from 0 to 100 %. The DC resistance was checked with a voltmeter across the arrays with the test leads positioned at various points around the edges. For each of the arrays there were either no conducting pathways across the sample or there was enough connectivity that conduction was possible wherever the leads were placed on the metallic regions. Electrical connectivity is present across the samples that have metallic filling fraction of 64.6 % or greater. The samples with occupancy of 54.7 % or less do not have connectivity across the whole sample. This indicates that the percolation threshold has been reached between 54.7 % and 64.6 % metallic occupancy.

Transmission results for a series of random arrays of varying metallic filling fraction can be seen in *Figure 4.4.11*.

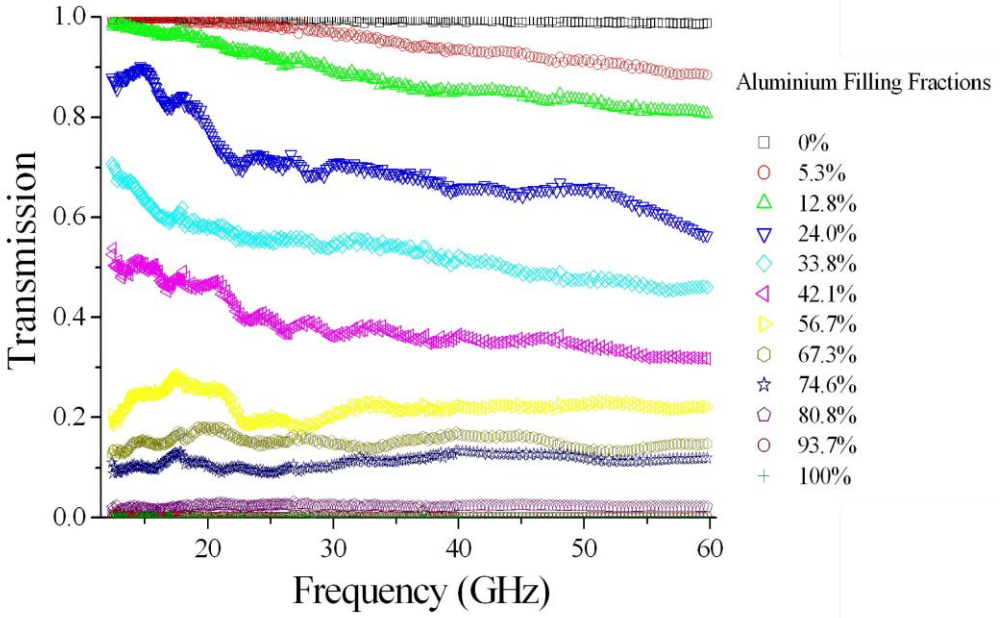

Figure 4.4.11. *Experimental transmission measurements as a function of frequency for random arrays of 1.5 mm mean diameter aluminium discs on a 75 μm Mylar® substrate. Various filling fractions.*

At low frequencies the transmitted intensity is high for samples containing disconnected conducting pathways as the electrons in the small clusters of metal cannot respond efficiently to the incident electric field. This is similar behaviour to that seen for the regular arrays and common behaviour for structures lacking metallic connectivity at long wavelengths (discussed in chapter 2). This is evident for the samples with metallic filling fraction of 42.1% or less. For samples containing a higher metallic concentration, larger clusters are formed and greater connectivity is present. These larger networks which provide longer conducting pathways are more responsive to an incident electric field and therefore are less transmissive. This behaviour is similar to the frequency selective behaviour seen in metallic meshes.

The transmission response as a function of varying filling fraction for the random arrays is plotted in *Figure 4.4.12*.

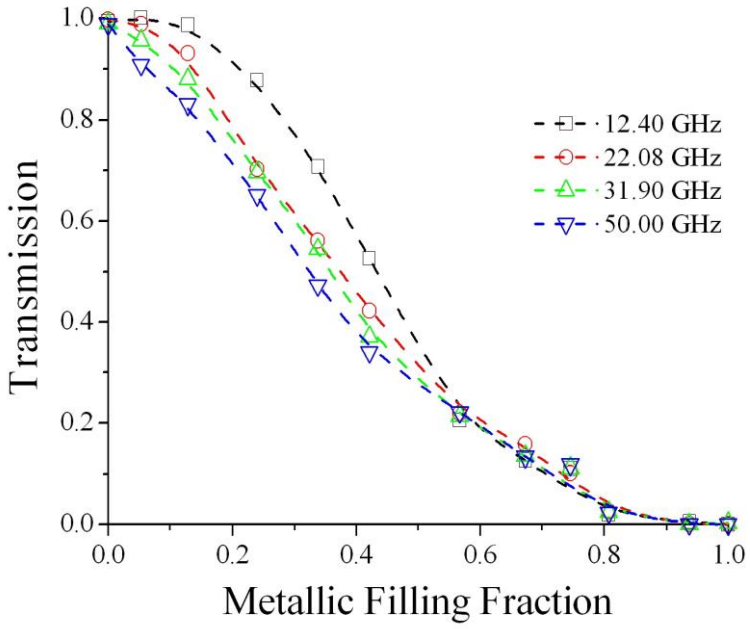

***Figure 4.4.12**. Experimental transmission measurements for various frequencies as a function of filling fraction for random arrays of 1.5 mm mean diameter aluminium discs on a 75 μm Mylar substrate.*

The transmission is close to 100 % for small metallic filling fractions and near zero for high filling fractions as expected but there is no substantial evidence of a percolation threshold. The transmission does not drop off suddenly at a particular value of filling fraction but continuously falls almost linearly for much of the range of values. At low frequencies (12.4 GHz) there is some evidence of a change in this behaviour with high transmission being maintained for a wider range of filling fractions leading to a sharper gradient near the 50 % occupancy region. The behaviour observed here for these random arrays is very different to that observed for the regular arrays due to the lack of a resonant response.

4.4.3 Random Arrays of Holes in a Metal Film

The complementary structures to those discussed in *Section 4.4.2* were fabricated to study the effect of differing connectivity on the transmissivity of the thin metal films. Being the complement, these films are random discs of metal removed from a continuous thin film.

Transmission spectra from 10 - 60 GHz for a range of filling fractions can be seen in *Figure 4.4.13*.

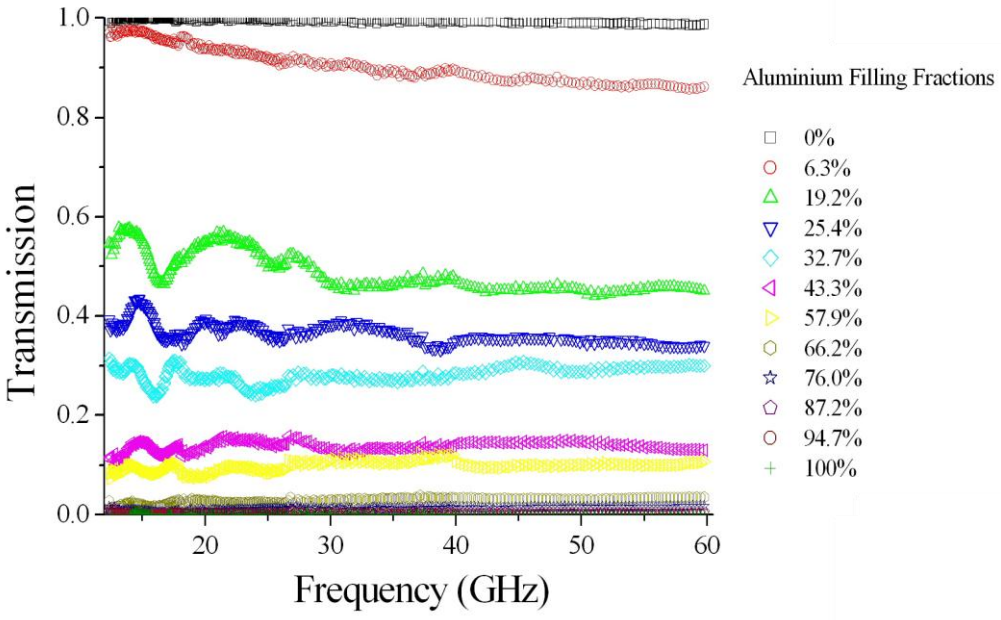

***Figure 4.4.13**. Experimental transmission measurements as a function of frequency for the complement of the arrays in Figure 4.4.11.*

Initially the transmission measurements do not appear too dissimilar to that recorded for the original structures with high/low transmission seen for the low/high metallic occupancy structures respectively. The responses however do appear much less frequency dependent with all structures apart from the low metal content (6.3 % occupancy) producing a very flat frequency response. The transmission also drops off much quicker with increasing filling fraction than for the original structures; this can be more clearly seen in *Figure 4.4.14*.

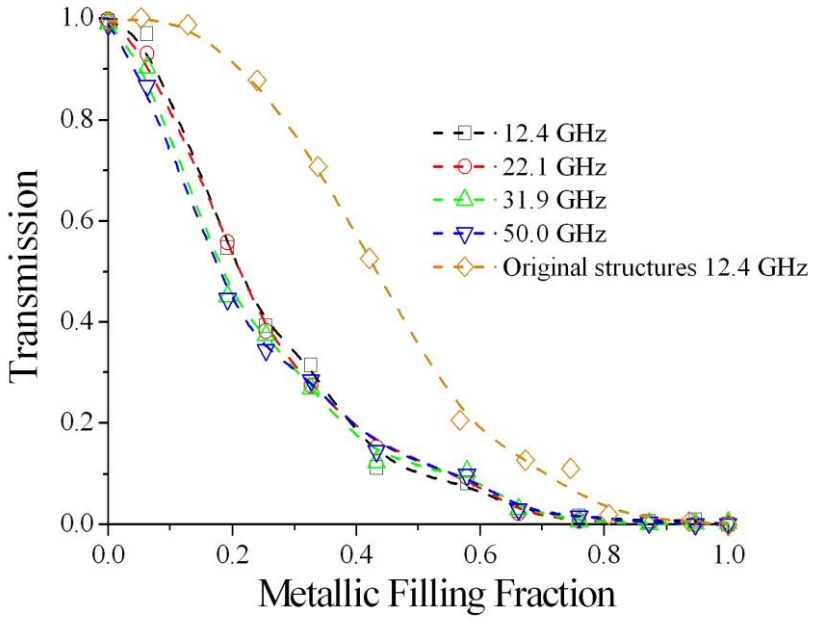

***Figure 4.4.14**. Transmission measurements as a function of metallic filling fraction for the complement of the arrays in Figure 4.4.12.*

It can be seen that the filling fraction dependence of the transmission differs vastly from that of the original structures. The transmission falls off much more quickly suggesting that the percolation threshold has been reached at a lower metallic occupancy. This differing behaviour for the same filling fractions is due to the very different metallic structure these samples possess. Removing discs from a metal film can lead to a structure that has many thin conducting channels that provide connectivity but do not occupy a large area; this cannot happen with the original random disc arrays since the discs have a defined mean size.

If the transmission through the random arrays and their complement is added the sum is not always equal to unity (*Figure 4.4.15*). If the samples could be considered as perfectly conducting this sum should be equal to unity across all frequencies.

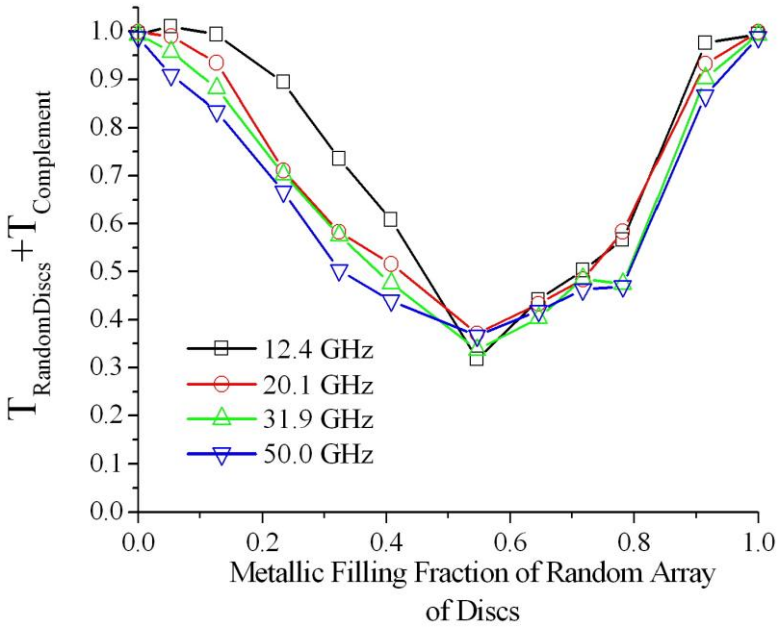

***Figure 4.4.15**. Sum of the transmission through a random array of metal discs and its complement.*

This shows that there is power that is being either absorbed or scattered which is not being collected in the zero order measurements. This minimum in the sum of transmission through the two arrays (i.e. maximum in absorption/scattering) occurs in the region where the percolation threshold occurs. This is expected as any absorption into the metal will be greatest when the metal clusters are in closest proximity, this will be due to enhanced electric fields between them. Maximum scattering will also be expected in this particular scenario as this will be when disorder within the arrays is greatest. This however cannot be easily confirmed because of the difficulty in modelling a random system due to not being able to reduce the problem to a unit cell. The whole random system would need to be modelled which would be too computationally intensive.

4.4.3.1 Vector Network Analyser (VNA) Measurements

Although many of the measurements made for this thesis were performed with a scalar microwave setup which only measures the intensity of the microwave signal, access to an Anritsu VectorStar Vector Network Analyzer (VNA) became available towards the end of the study. A VNA allows measurement of the amplitude and phase of the microwave signal giving another dimension to the measurements that can be made.

This extra measurement allows more information about wave propagation in the sample to be determined. Due to the sub-wavelength nature of the random structures, effective parameters can be determined which describe the properties of a homogeneous layer that would produce the same response.

The VNA must be calibrated to define the reference plane for the phase measurements. The calibration or 'error correction' used was a 2 port Short-Open-Load-Through (SOLT) calibration to eliminate the frequency dependent response of the connecting coaxial cables and adapters. This process consists of connecting calibration standards from a calibration kit to the ends of the cables and performing an error correction. The calibration kit information has to be installed onto the VNA as each calibration kit is unique with its own specification. Each calibration standard is attached in turn to the end of the cables and an error correction performed. The 'short' standard mimics a metal plate, i.e. resulting in a perfect reflection with a 180° phase change. The 'open' standard gives a 0°/360° phase change on reflection. The 'load' standard acts as a perfect absorber resulting in no reflection. With a 'load' standard attached to the end of each cable an 'isolation' error correction can be performed, this takes into account internal leakages within the VNA however this is very minimal in modern VNAs and is not a significant part of the calibration. The ends of the cables are then connected together, i.e. connecting port 1 to port 2 and a 'through' error correction performed. Once all of these calibration steps have been performed the transmission *S* parameters, S_{12} and S_{21} are equal to unity and their phase component is equal to zero for all calibrated frequencies when the cables are connected together. The cables are then attached to the horns and measurements performed with collimating mirrors as was done for the scalar measurements. Normalisation was performed by subtracting the background transmission and phase, i.e. a fall in transmission below 100 % or any phase change is purely a result of introducing the sample.

4.4.3.2 Effective Refractive Index Retrieval of Random Arrays

Knowledge of the transmission magnitude and phase response of a bulk composite with sub-wavelength structure allows an effective refractive index to be calculated. This effective index describes what value of refractive index a homogeneous medium would have to reproduce the transmission and phase response of the structured material. Since the random arrays studied only have two-dimensional structure, the effective

permeability has been assumed to be that of free space as no magnetic resonances or current loops are expected to be generated out of the plane of the structure to produce a magnetic response.

The transmission magnitude and phase were fitted to the recursive Fresnel transmission formula (*Equation 4.4.1*) which calculates the transmission and phase across a three layer system (i.e. two interfaces).

$$t_{13} = \frac{t_{12}t_{23}e^{\beta}}{1 + r_{12}r_{23}e^{2\beta}}$$ *Equation 4.4.1*

Where t_{mn} and r_{mn} are the complex transmission and reflection coefficients across the interface between medium *m* and medium *n*. $\beta = ik_z d$, where $i = \sqrt{-1}$, $k_z = 2\pi/\lambda$ and *d* is the thickness of the medium.

Equation 4.4.1 can be rewritten in terms of complex refractive index of the medium, *n* (*Equation 4.4.2*), assuming that the incident and transmitted media are free space $(n_1 = n_3 = 1)$.

$$t_{13} = \frac{\left(\frac{4}{(n+1)^2}\right)e^{\beta}}{1 - \left(\frac{n-1}{n+1}\right)^2 e^{2\beta}}$$ *Equation 4.4.2*

The complex permittivity, $\varepsilon = \varepsilon_r + \varepsilon_i i$ can be written in terms of the complex refractive index, $n = n_r + n_i i$ by using *Equation 4.4.3* and *Equation 4.4.4*.

$$\varepsilon_r = n_r^{\,2} - n_i^{\,2}$$ *Equation 4.4.3*

$$\varepsilon_i = 2n_r n_i$$ *Equation 4.4.4*

The frequency dependent real and imaginary components of the permittivity for a disconnected (5.3 % metal occupancy) random array are shown in *Figure 4.4.16*. For

the purpose of the fitting the thickness of the sample is assumed to be just that of the metal, i.e. 60 nm, as the dielectric substrate has a low refractive index and is very sub-wavelength ($\sim \lambda/1000$) therefore it is not expected to significantly alter the transmission magnitude or phase. It must be noted that the values determined from this parameter extraction are only valid for normal incidence since this was how the measurements were taken and therefore no knowledge about other angles of incidence can be inferred. Care must also be taken when considering the magnitude of the values determined from this extraction method as they are highly dependent on the value for the thickness of the array entered into *Equation 4.4.2*. The physical thickness of the metal was used to calculate the values however there is a large amount of debate in the literature over the applicability of effective parameters for thin metamaterial layers. Refractive index, permittivity and permeability are bulk (macroscopic) properties which describe how polarisable the material is to incident electric and magnetic fields and therefore these values shouldn't change with the thickness of the composite structure. It has been found that the use of the transmission and reflection coefficients to extract effective parameters of a thin layer does not always accurately describe the polarisation properties[127]. This is due to the thickness of the structure needing to include a large number of metallic inclusions in order for it to be truly represented by effective parameters and for these values to be independent of the thickness of the material. This problem has been investigated in a number of studies[128-130]. Due to the uncertainty of the validity of these extracted values only the general trend can be relied upon as there is a potential for the values to be easily inflated.

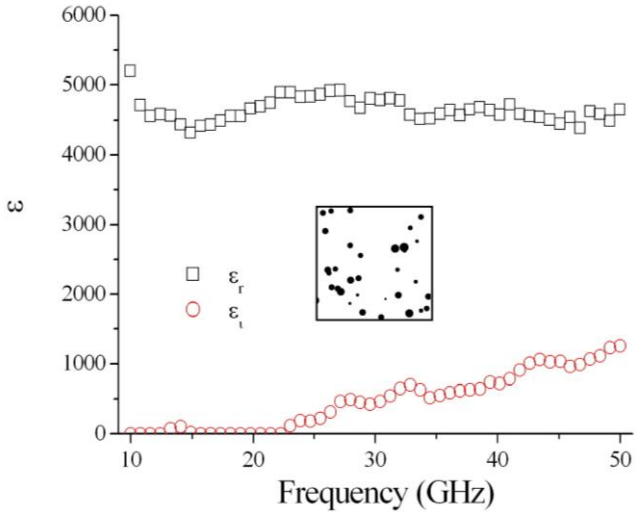

***Figure 4.4.16**. Real and imaginary components of the permittivity of a 5.3 % metal occupancy random array of discs, extracted by fitting experimentally measured transmission and phase to the Fresnel equation. Schematic inset illustrates sample geometry.*

The real part of the permittivity, ε_r was determined to be approximately 4500 and shows very little frequency dependence. The imaginary part of the permittivity, ε_i appears to be tending towards zero at low frequencies and rising at higher frequencies. This trend is expected for a low occupancy disconnected array as the transmission also shows similar frequency dependent behaviour, being highly transmissive at low frequencies and slowly falling at higher frequencies.

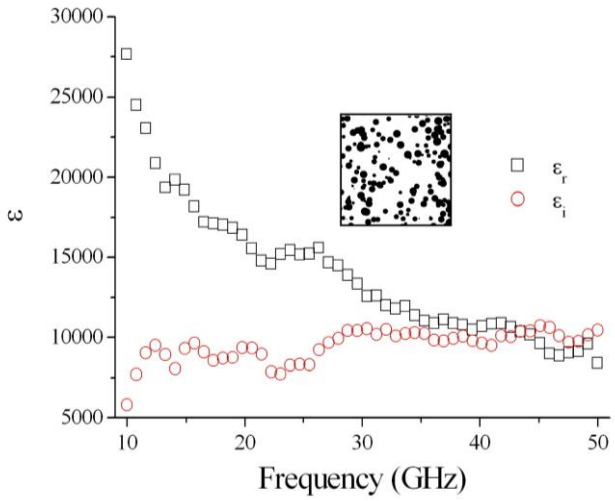

Figure 4.4.17*. Real and imaginary components of the permittivity of a 23.4 % metal occupancy random array of discs, extracted by fitting experimentally measured transmission and phase to the Fresnel equation. Schematic inset illustrates sample geometry.*

The frequency dependent real and imaginary components of the permittivity for a disconnected (23.4 % metal occupancy) random array are shown in *Figure 4.4.17*. At this level of occupancy no connected pathway across the system is present however larger clusters are being formed from overlapping discs introducing localised connectivity. The real part of the permittivity, ε_r is now much larger with this higher level of metallic content, ~ 27000 at 10 GHz and now showing a frequency dependent behaviour falling to ~10000 at 50 GHz. The imaginary part of the permittivity, ε_i appears to still have a similar frequency dependent behaviour to that of the array in *Figure 4.4.16* but now having a much higher value and becoming comparable to the real part at higher frequencies.

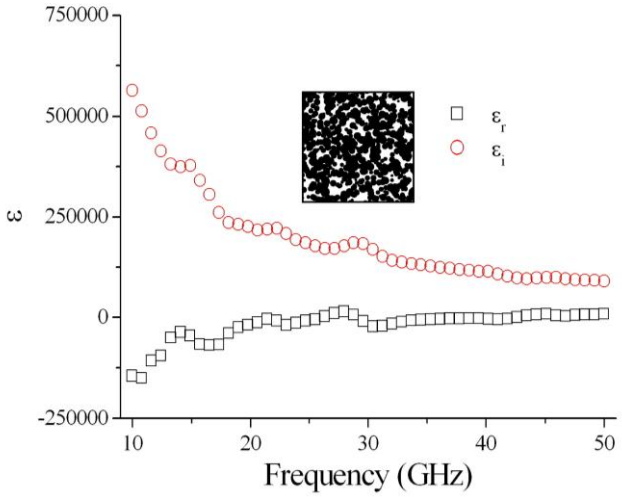

***Figure 4.4.18**. Real and imaginary components of the permittivity of a 71.8 % metal occupancy random array of discs, extracted by fitting experimentally measured transmission and phase to the Fresnel equation. Schematic inset illustrates sample geometry.*

The frequency dependent real and imaginary components of the permittivity for a connected (71.8 % metal occupancy) random array are shown in *Figure 4.4.18*. The majority of the clusters in this array have now connected together allowing current to flow. This change in structure has also lead to a change in the effective parameters. The imaginary component of the permittivity is now dominant and very large, being >500000 at low frequencies. The real part of the permittivity now goes from negative to positive across the frequency range studied with the composite array acting as though it has an effective plasma frequency now in the GHz regime. This could potentially allow support of bound surface waves on this structure.

The real component of the effective permittivity is shown in *Figure 4.4.19* for a series of metallic occupancies and frequencies. Only one sample was made for each value of metallic occupancy therefore the three data points for the different occupancies are from the same structure.

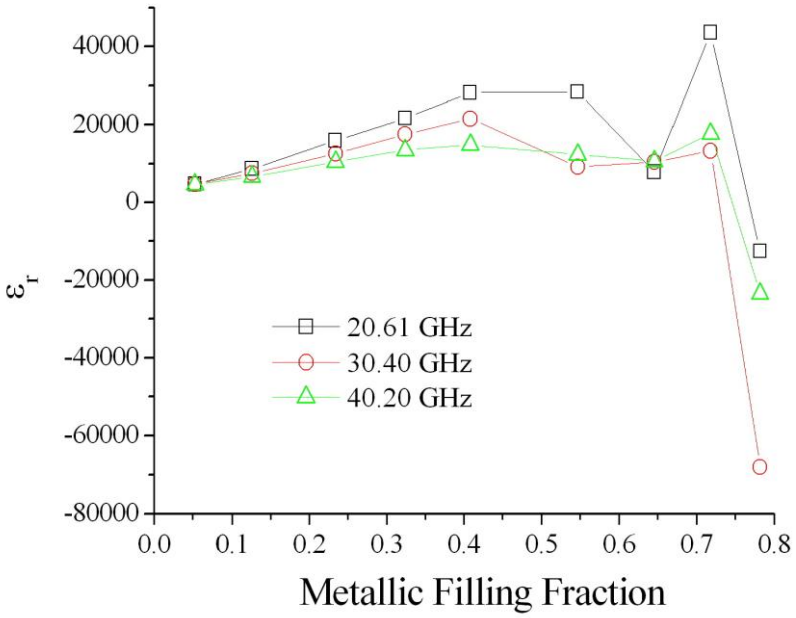

***Figure 4.4.19**. Real component of the effective permittivity as a function of metal occupancy for different frequencies.*

The real part of the permittivity appears to initially rise as the metal occupancy is increased before appearing to fall quickly to a large negative value.

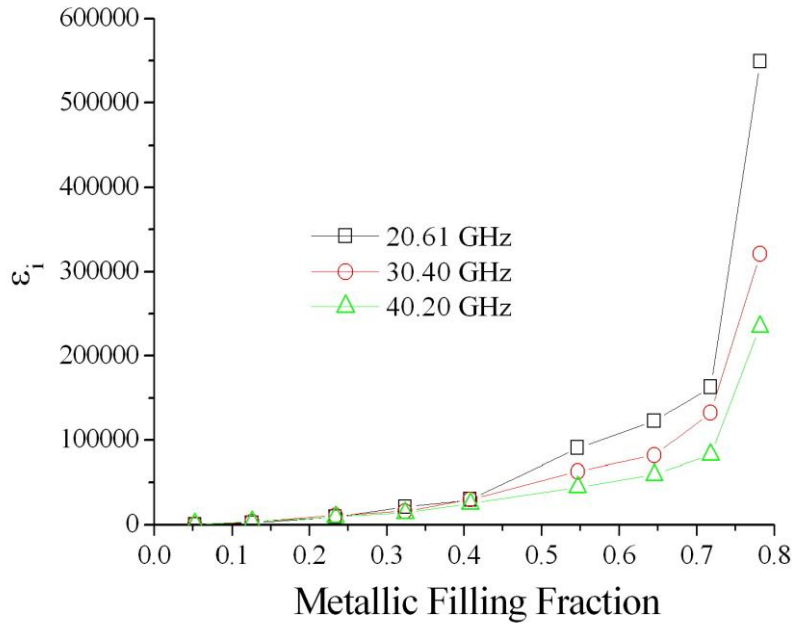

***Figure 4.4.20**. Imaginary component of the effective permittivity as a function of metal occupancy for different frequencies.*

The imaginary part of the permittivity (*Figure 4.4.20*) appears to rise strongly as the metal occupancy is increased. It is thought that this behaviour in permittivity values is due to geometrical resonant behaviour of the clusters which causes a resonant response of the permittivity. As the size of the clusters increases the resonant behaviour will fall in frequency just as the resonant frequency of an antenna falls as its length is increased. *Figure 4.4.21* shows schematically the real and imaginary components of the permittivity of a typical resonant system.

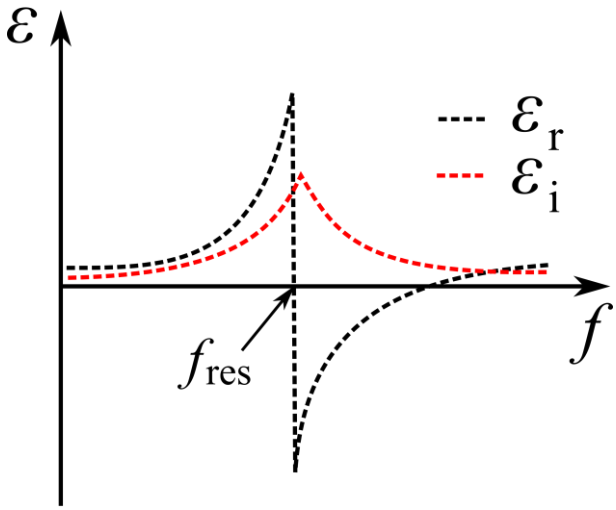

Figure 4.4.21. *Schematic illustrating the typical behaviour of the real and imaginary components of the permittivity for a resonant system.*

The low frequency behaviour that is shown in *Figure 4.4.21* exhibits an increasing ε_r and then a sudden decrease to negative values at the resonant frequency before returning to positive values at high frequencies. ε_i increases with frequency and is a maximum at the resonant frequency before falling at higher frequencies. The resonant frequency will move to lower frequencies as the metallic content and cluster size increases.

Effective parameters were also retrieved for the random array of holes, the real and imaginary components of the permittivity for an 8.5 % metallic occupancy structure can be seen in *Figure 4.4.22*. The behaviour of the permittivity is similar to that seen for the low occupancy disc samples with the real component dominating over the imaginary component with the two becoming comparable at higher frequencies.

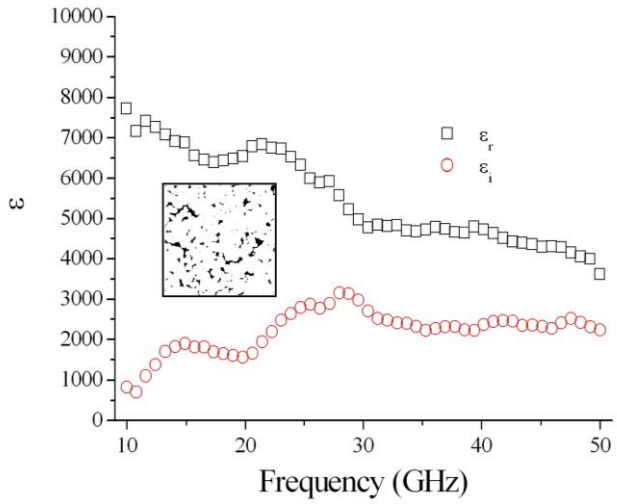

***Figure 4.4.22**. Real and imaginary components of the permittivity of a 8.5 % metal occupancy random array of holes in a metal film, extracted by fitting experimentally measured transmission and phase to the Fresnel equation. Schematic inset illustrates sample geometry.*

Extracted parameters for a 21.8 % metal occupancy sample are shown in *Figure 4.4.23*. The imaginary component has now exceeded the value of the real component, this happens with the disc structures but at a much higher metallic occupancy. This highlights how the details of the structure are very important in defining the response, not just the occupancy. As can be seen in the inset of *Figure 4.4.23*, the metallic shapes formed by the complementary structure are very different to that of the original structure. Many cusps are formed by overlapping circular holes due to their curved edges. If a different initial shape with straight edges such as a square had been chosen to create the arrays the complementary structures would have had a structure not too dissimilar from itself, possibly resulting in a similar response to the original structure.

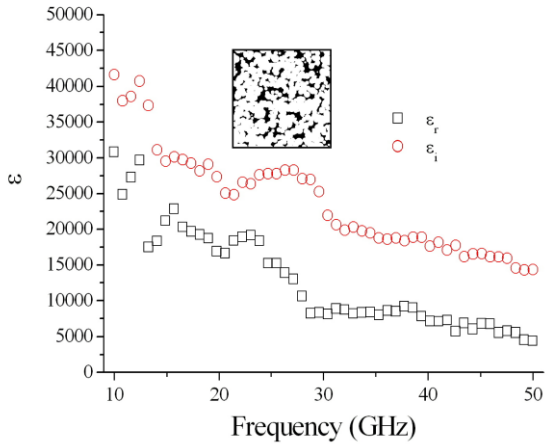

***Figure 4.4.23**. Real and imaginary components of the permittivity of a 21.8 % metal occupancy random array of holes in a metal film, extracted by fitting experimentally measured transmission and phase to the Fresnel equation. Schematic inset illustrates sample geometry.*

The permittivity values extracted for a 67.6 % metal occupancy array of holes that consists of a highly connected structure can be seen in *Figure 4.4.24*.

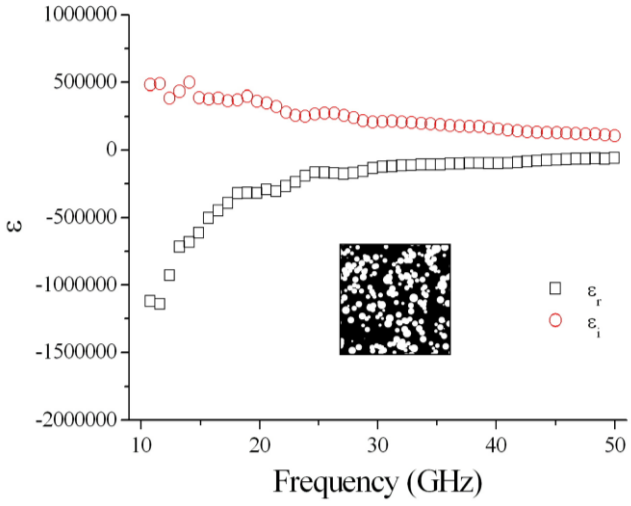

***Figure 4.4.24**. Real and imaginary components of the permittivity of a 67.6 % metal occupancy random array of holes in a metal film, extracted by fitting experimentally measured transmission and phase to the Fresnel equation. Schematic inset illustrates sample geometry.*

The frequency dependence of the permittivity appears to be similar to that of a plasmonic metal at visible frequencies, the real part being large and negative at low frequencies and tending towards zero at higher frequencies. The imaginary part of the permittivity is large at low frequencies and falls at higher frequencies. The ratio of the real part of the permittivity to the imaginary part is plotted in *Figure 4.4.25* as this allows the properties of the surface to be compared easily with that of a plasmonic metal.

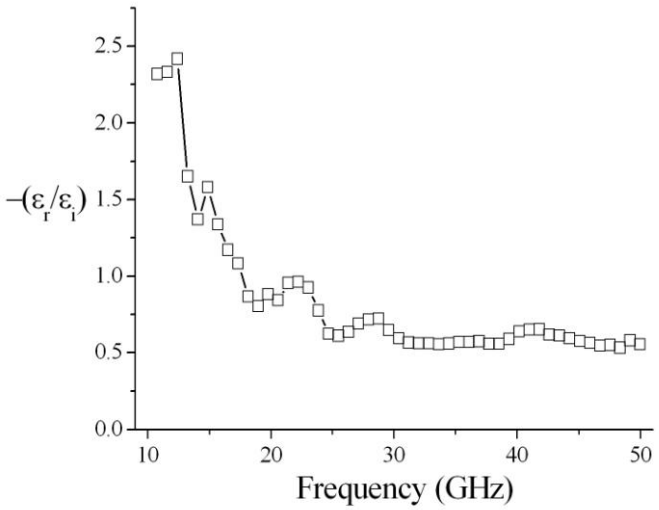

Figure 4.4.25*. Negative ratio of real component of permittivity to imaginary component for the structure in Figure 4.4.24.*

Good plasmonic metals at visible frequencies typically have a ratio of 10, e.g. the permittivity of gold $\approx -10+i$ at 650 nm which provides good binding of surface waves[131], often referred to as surface plasmon polaritons at those frequencies. Poorer plasmonic metals such as aluminium have a smaller ratio, $\varepsilon(Al) \approx -56+23i$ at 650 nm, i.e. a ratio of ~ 2.6. The low frequency measurements on this sample suggest that this structure has a ratio $-(\varepsilon_r/\varepsilon_i)$ similar to that of a non-structured metal film at visible frequencies.

The real part of the permittivity is plotted for all of the random hole arrays in *Figure 4.4.26.*

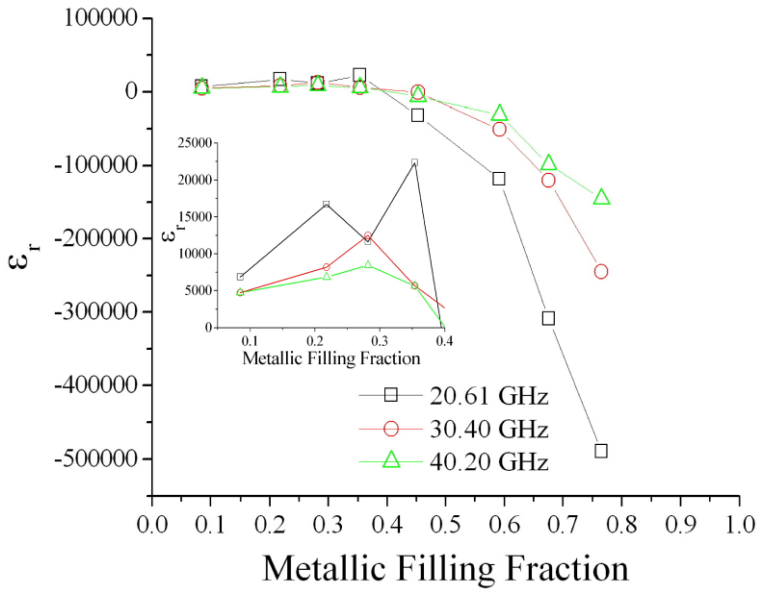

Figure 4.4.26*. Real component of the effective permittivity for a series of random arrays of holes in a metal film. Inset shows values for low metallic filling fraction on an expanded scale.*

The real component of the permittivity exhibits similar behaviour to that seen for the original structures in *Figure 4.4.19*, increasing with increasing filling fraction and then falling to a large negative value. The main difference appears to be that the transition from positive to negative values of ε_r occurs at a much lower value of metallic filling fraction. This also appears to be consistent with the earlier fall in transmission exhibited by these structures.

The imaginary component of the permittivity (*Figure 4.4.27*) also shows very similar behaviour to that in *Figure 4.4.20*, rapidly increasing as the metal occupancy increases.

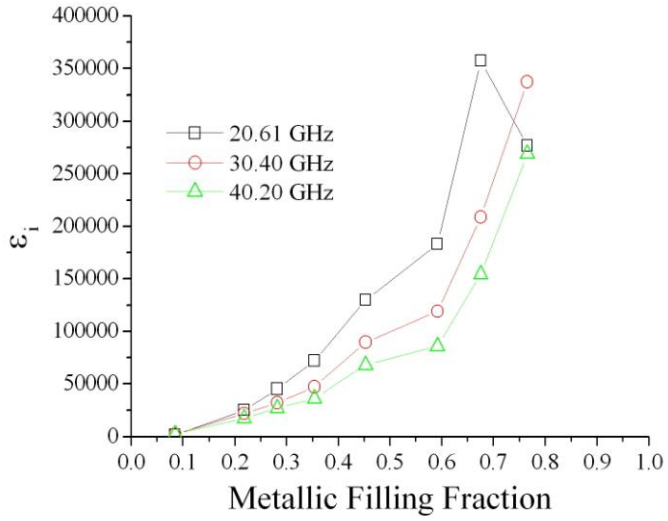

***Figure 4.4.27**. Imaginary component of the effective permittivity for a series of random arrays of holes in a metal film.*

Being able to measure phase information and determine effective parameters for these films has shown a large amount of information that could not be obtained from just the intensity measurements. Due to time limitations this could not be pursued further, however these results do suggest that one could utilise these types of structure to mimic the behaviour of plasmonic metals at microwave frequencies. Depending on the permittivity values for other angles of incidence such a structure could then be possibly corrugated to form a diffraction grating to allow coupling to tightly bound surface waves similar to those observed at optical frequencies[131]. Coupling to these modes could also be possible through a frustrated total internal reflection (FTIR) coupling mechanism such as prism coupling (chapter 2).

In order to fully understand the response of these random composites a full analysis of the effect of changing every parameter of the system would need to be performed. Without a theoretical model this would be very much a trial and error process experimentally. The effect of changing the size of the initial discs/holes may shift the frequency dependent response. It would be reasonable to expect the response of the arrays to shift up/down in frequency if the discs/holes are decreased/increased in size as the clusters of metal are acting similar to antennas that have a resonant response dependent on their length. The standard deviation of the Gaussian distribution of the sizes may also have an effect but it is not clear what that is at this stage. This is also true for the randomness of the spatial distribution of the discs/holes. The degree of

disorder has not been fully investigated in this study but it is a very complex aspect of the system. The spatial coordinates have been generated randomly but they could have been created similar to a quasi-periodic structure, according to a set of criteria which has a degree of randomness. This would have created a regime which lies between the regular and random arrays discussed in this chapter. Adjusting the randomness of the structure is discussed further in the future work section of chapter 9.

4.4.3.3 Modelling of Random Structures

A description of the modelling codes used in this thesis can be found in chapter 3. Modelling of a random structure is not a simple problem; unlike a regular array that can be represented by a unit cell with repeat boundary conditions, a truly random structure will have no repeat periodicity. Therefore in order to accurately predict the response of such a structure the whole structure must be modelled. This is not possible with the finite-element modelling code, *HFSS* and computing resources available. An attempt was made to approximate a random structure by modelling a periodic structure with a random structure factor. A 30 mm × 30 mm unit cell was used as this is at the upper limit of the capabilities of the computer due to the sheer volume within the model that requires meshing. In the unit cell a random distribution of discs was created with a Gaussian distribution of diameters with a mean diameter of 1.5 mm and a standard deviation of 0.5 mm. The discs were then assigned as PEC boundaries. The unit cells were designed in such a way that continuity was maintained across the boundaries of the cells (see chapter 3). Transmission measurements for a number of different cells with the same number of discs are plotted in *Figure 4.4.28*.

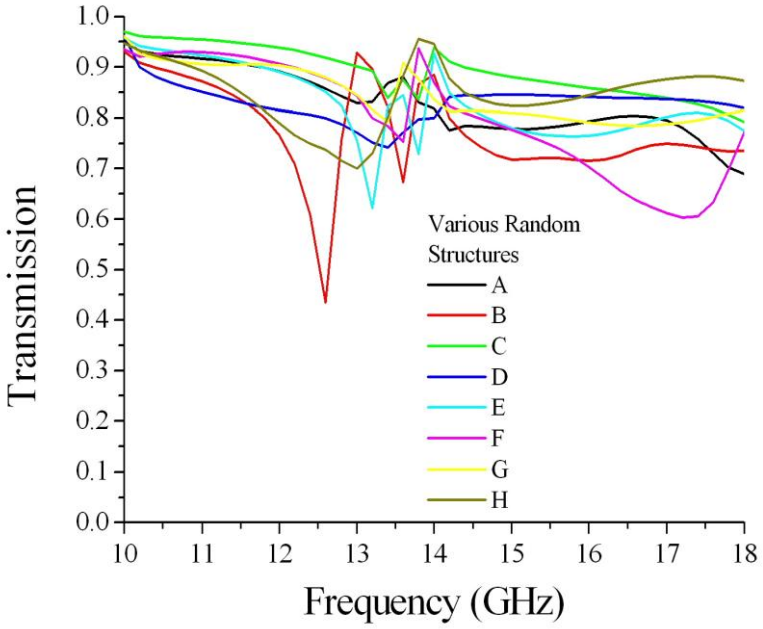

Figure 4.4.28*. Normal incidence transmission through an infinite square array composed of a 30 mm pitch unit cell containing 200 randomly distributed PEC discs. Gaussian distribution of diameters, 1.5 mm mean, 0.5 mm standard deviation.*

The arrays (A–H) in *Figure 4.4.28* do not have exactly the same filling fraction due to the random nature of the distribution, sizes and overlap of the discs. The mean occupancy is 36% and the filling fractions of individual unit cells are close enough that any differences in response are due to structural differences as opposed to a significant difference in occupancy. As previously with the experimental samples the filling fractions are calculated by analysis of an image of the array.

The transmission results for the arrays (A–H) differ significantly from one another given the similar metallic filling fractions. This effect is due to having a repeat periodicity within the modelling. Any differences between structures of unit cells which produce transmission features will be magnified since it is infinitely periodic and therefore determines the transmission of the whole structure. The statistical nature of these structures is completely different to truly random structures as the size of the clusters is restricted to the size of the unit cell. This means that the biggest possible linear cluster within a sample is just under $\sqrt{18} = 42.4$ cm (diagonal length of unit cell); at 4.24 cm the cluster will be infinite in length due to the repeat boundary conditions. This however does not mean that longer clusters aren't possible within the unit cell if

they are non-linear (i.e. do not form a straight chain) but the restriction significantly limits their creation. There are many sharp features in the transmission response. Electric fields for the sharp minimum seen in the transmission response for array B of *Figure 4.4.28* are shown in *Figure 4.4.29*.

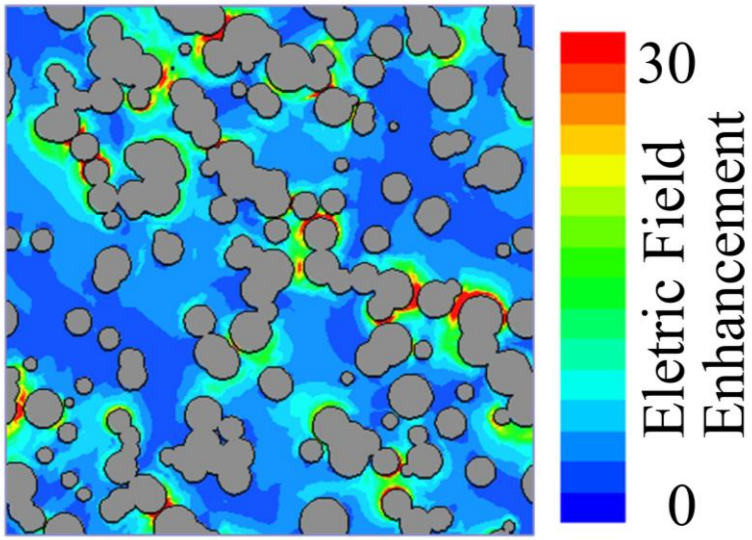

***Figure 4.4.29**. Time-averaged electric field magnitude plotted at 12.6 GHz through the plane of the unit cell of random array B (Figure 4.4.28).*

Field enhancement is observed in the regions between some but not all of the metal clusters. The field enhancement appears to be greatest when the gap between clusters is small and the clusters are of comparable size. The feature in the transmission response is strong because any local arrangement of the metal discs that produce a particular transmission characteristic will are repeated across the whole sample. If the model were truly random there would be a large averaging effect as each 30 mm × 30 mm region would have different structure and contribute differently to the overall response of the array.

Diffraction is also a significant issue with the long order periodicity in a model such as that discussed since at the frequencies under study the periodic surface will be in the diffracting regime. This means that power will be lost into diffracted orders which wouldn't exist if the structure were truly random. For simplicity the transmission plotted from the modelling shows the sum of all the transmitted orders. Since this

modelling technique doesn't provide a good comparison with the experiments performed this technique was not pursued any further.

4.5 Summary

In summary a transmission study through a series of square patch/hole arrays with various connectivity and metal occupancies has been presented. It has been found that the variation of transmission with metal occupancy does not take the form of a step function as may be anticipated but is heavily frequency dependent. This frequency dependence is due to the periodicity of the array and the associated resonances. The elements that comprise the arrays are able to interact by means of evanescent diffracted orders in the near field to give resonant transmission/reflection causing strong perturbation to the metal occupancy dependent transmission. Most strikingly at frequencies close to the diffraction edge, the expected decrease in transmission on crossing the 50 % occupancy (the connectivity) threshold is completely reversed.

A transmission study of arrays of random metallic discs and random arrays of holes in a metal film has been discussed. The random arrays produce vastly different transmission responses to that of the regular arrays since no strongly resonant behaviour is observed in the transmission. Possibly surprisingly the random arrays show very little evidence of a percolation threshold in their transmission response in contrast to the conductivity thresholds measured in previous studies. Effective permittivity values for the random arrays have been extracted and show that by careful choice of structure one can design a surface which has tailored electromagnetic properties. These properties can be much different to those generally found in this frequency regime such as high refractive index materials exhibiting low loss or 'plasmonic-like' surfaces with a dominant large and negative real permittivity.

The results from the two regimes investigated (random and regular) are very different due to the presence or lack of a well defined periodicity, however one potential area for future study could be that of systems possessing some partial degree of disorder. Quasi-random systems which could have small amounts of randomness in pitch, size of patches/holes or rotation may offer an electromagnetic response between the two extremes observed in this work offering potentially greater levels of material parameter control.

5 Dispersion of Surface Modes on Hole and Patch Arrays and the Role of Babinet's Principle

5.1 Introduction

In chapter 4 the microwave transmission response of arrays of holes in a metallic film, and the complementary system of an array of metallic patches, were studied. These arrays were found to support diffractively coupled electromagnetic surface waves due to the regular metallic periodicity of the structure. In this experimental chapter the dispersion of electromagnetic surface waves on metallic patch arrays and their inverse, hole arrays is characterised experimentally. The dispersion of the modes supported on the two types of structure is found to be different for the same incident polarisation. For p-polarised (TM) incident polarisation the surface mode excited on the hole array appears to follow the in-plane linear diffracted light lines while s-polarised (TE) incident polarisation follows the out-of-plane parabolic diffracted light lines. For the complementary structure, the patch array, the reverse is true; this is predicted by Babinet's principle as there is a requirement for a 90° rotation of the polarisation for a complementary response to be expected. These results validate the application of Babinet's principle in the microwave regime; however it is not obvious 'a priori' which incident polarisation experiences dominant coupling to which grating vector. In this chapter, experimental results, combined with the predictions of the field solutions from numerical modelling, illustrate that periodicity in the electric and magnetic fields determines the form of the dispersion of these surface modes.

5.2 Background

5.2.1 Dispersion of Surface waves on bi-gratings

Grating coupling was introduced in chapter 2 as a means of coupling incident photons to surface modes on periodically textured metallic surfaces. This was introduced for the simple case of a one-dimensional (or mono) grating where periodicity is only present in

one direction. Another common form of diffraction grating is that of a two-dimensional (or bi) grating (*Figure 5.2.1*).

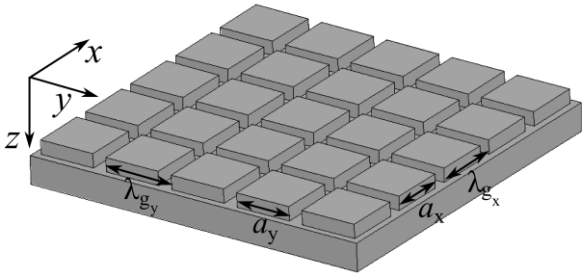

Figure 5.2.1. *Schematic of a bigrating illustrating grating period, λ_g and feature size, a.*

The grating has two periods λ_{g_x} and λ_{g_y} in the corresponding directions. If these two periods are equal, the grating will have four-fold rotational symmetry and the onset of first order diffraction in the *x* and *y* directions will occur at the same frequency $\left(c/\lambda_g\right)$ at normal incidence. If the grating is rectangular then it will only have two-fold rotational symmetry and the frequency of the onset of diffraction in *x* and *y* directions will no longer be degenerate. The presence of two grating vectors, k_{g_x} and k_{g_y} provides an additional set of mechanisms for coupling to a surface wave. The reciprocal space representation of a two-dimensional grating will be a repeat of that for the one dimensional grating but also repeated in the k_y direction (*Figure 5.2.2*).

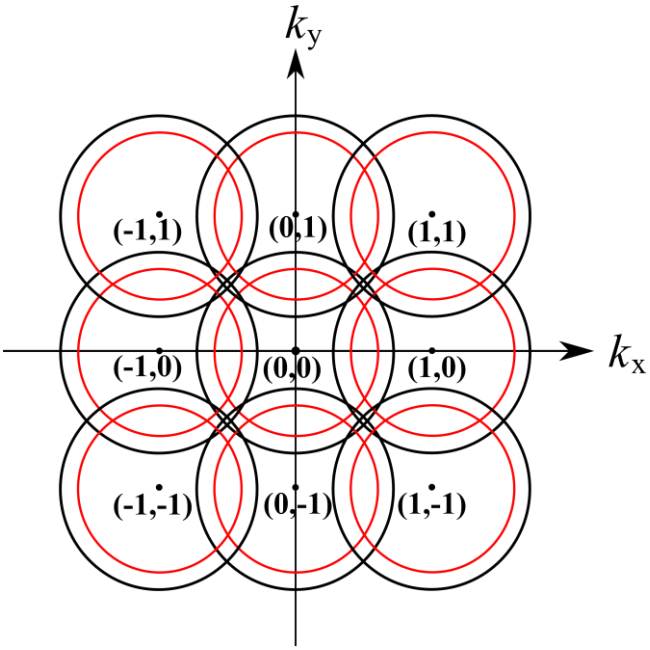

***Figure 5.2.2**. 2D reciprocal space representation of a square bigrating at a fixed frequency, points illustrate scattering centres, the black circles show the momentum of the surface modes whilst the red circles illustrate the range of momentum available from an incident photon.*

If the incident wave lies in the *x*-*z* plane then scattering can occur out of the plane of incidence via the k_{g_y} grating vector and also in the plane of incidence via the k_{g_x} grating vector. A surface wave that is coupled to via a k_{g_y} scattering will disperse in a similar manner to that of a surface wave excited on a one-dimensional grating in the conical mount ($\varphi = 90°$) as shown in *Figure 5.2.3*.

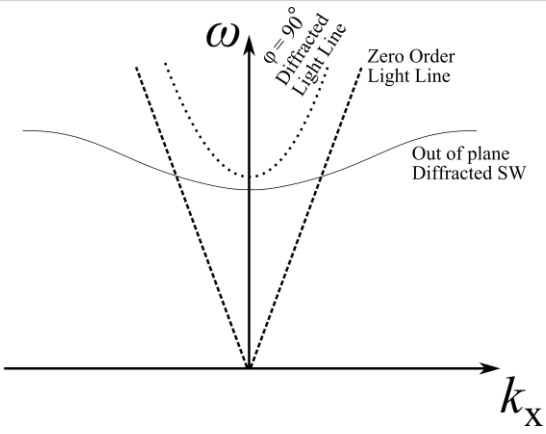

***Figure 5.2.3**. Dispersion of a surface wave that has been scattered by an out of plane $(0,k_g)$ grating vector.*

The light line associated with out of plane diffraction is parabolic as it is formed from the intersection of the light cones centred on (0,0) and $(0,k_g)$ projected onto the k_x axis, this is illustrated in *Figure 5.2.4*.

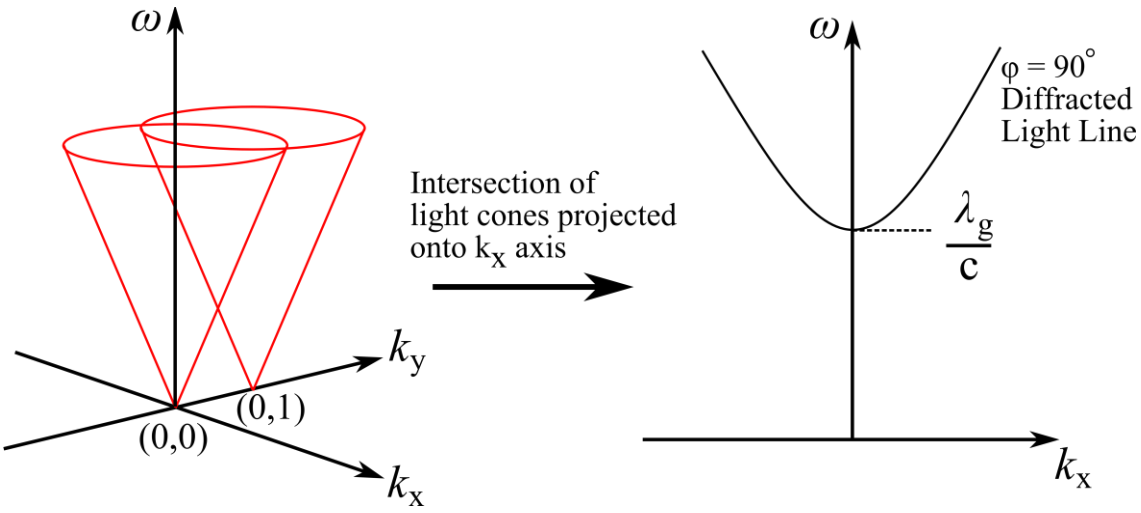

***Figure 5.2.4**. Illustration of the intersection of the light cones centred on (0,0) and (0,1) forming a parabolic diffracted light line.*

The dispersion of the surface mode is generated by the intersection of two horn shaped cones. As seen in *Figure 5.2.3* a region of the $(0,k_g)$ scattered surface mode lies within the light cone and therefore can be coupled to radiatively.

Clearly the dispersion of the in-plane and out-of plane diffractively coupled surface waves is very different, therefore it is not obvious 'a priori' which of these modes is coupled to most strongly for a grating with four-fold symmetry (i.e. $\lambda_{g_x} = \lambda_{g_y}$).

5.2.2 Dispersion of surface waves on gratings with metallic connectivity

Many previous studies of diffractively coupled surface waves on gratings at microwave, infrared or visible frequencies have often been confined to gratings composed of continuous metal such as grooves[1-10] in a metal substrate or continuous in one-dimension such as slits[56,132-136]. There is also a substantial body of work concerning the enhanced transmission properties of arrays of holes[12,71,78,79,137-142] (also the work of Garcia de Abajo[22] and references therein). These types of arrays support real propagating currents due to the metallic connected nature of their structure. The dispersion of surface modes on these surfaces has also been extensively studied, particularly more recently in the context of enhanced transmission through sub-wavelength hole arrays[12,14,73,143]. The surface modes on these square arrays which mediate the transmission are found to be associated with in-plane diffraction (i.e., the dispersion of the surface modes follow the $k_g \hat{\mathrm{k}}_x$ diffracted light lines) for p-(TM) polarised incident radiation, and the orthogonal grating wave vector, (i.e., the out-of-plane, $k_g \hat{\mathrm{k}}_y$ diffraction) when s-(TE) polarised radiation is incident[73]. There are relatively few studies from the photonics community of the analogous enhanced resonant reflection phenomenon exhibited by arrays of metal patches. However it is important to note that the resonant features recorded in the transmission and/or reflection spectra from both connected (holes) and disconnected (patches/particles) arrays, have been associated with excitation of diffractively coupled surface waves, as demonstrated by the work of Minhas et al[144]. However the electromagnetic response of inductive and capacitive grid FSSs (frequency selective surfaces) away from resonance is well studied[19,21,74], but their response is generally not discussed in detail around the resonance, presumably due to the fact that FSSs have only been of interest in the subwavelength regime (i.e. not in the proximity of the onset of diffraction). The surface impedance of a periodic metallic array, in particular the reactance, determines the character of the surface wave supported (chapter 2). An inductive surface will support a

TM surface mode, as typically observed on hole arrays in enhanced transmission studies. A capacitive surface such as an array of patches will support a TE surface mode.

In this chapter, the transmission through a pair of complementary thin arrays of perfectly conducting elements as a function of the polar angle of incidence θ, the frequency ν_0 and polarisation is experimentally recorded. The experimental transmission data illustrate the band structure of the resonances supported, which are attributed to diffractively-coupled surface waves. The results validate this application of Babinet's principle in the microwave regime. Furthermore, these experimental results, combined with the predictions of the field solutions from numerical modelling, illustrate that periodicity in the electric and magnetic fields determines the form of the dispersion of these surface modes.

5.3 Experimental

Samples were fabricated by etching a square array (pitch, λ_g = 7.02 mm) of square patches (side length a), orientated at 45° with respect to the lattice unit vectors, into aluminised Mylar® (75 μm thickness, $\varepsilon_r \sim 2.6$). The aluminium layer is ~ 60 nm thick (determined from scanning electron microscopy (SEM) measurements), which is much less than the skin depth at the frequency range studied (~1μm). Note however that the layer is almost completely electromagnetically opaque at these wavelengths (T < 1%) due to the large impedance mismatch presented at the metal-air interface. The 45° rotated element geometry has been specifically chosen to allow for the study of self-complementary structures (chapter 4). For arrays in which the patch side length is greater than 4.965 mm, neighbouring patches overlap, forming a conducting mesh network (a hole array), which is the complementary structure to the patch array.

Figure 5.3.1a is representative of the connected structure experimentally studied, with square holes of 3.23 mm side length. Similarly, *Figure 5.3.1b* shows the near-complementary disconnected array, of 3.10 mm side length patches. The arrays are not exact complements of one another due to inaccuracies inherent in the method of fabrication.

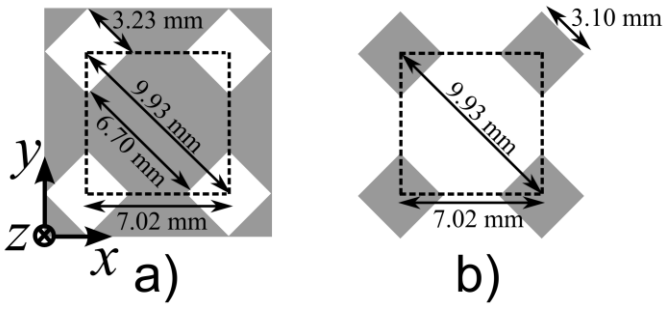

Figure 5.3.1*. Schematic representation of the experimental samples. The dotted lines indicate the unit cell of the* ***(a)*** *hole array and* ***(b)*** *disconnected patch array. The shaded area represents aluminium occupancy and the unshaded regions dielectric.*

5.4 Results and Discussion

The samples were mounted for support on a sheet of expanded polystyrene (refractive index ~ 1) and placed behind an aperture formed from microwave absorbing material. A collimated microwave beam is incident normal to the surface of the samples. Transmission data for frequencies in the range 26.5 – 60.0 GHz were obtained by normalising the transmission through the sample, to that of the aperture and polystyrene sheet alone. The polar angle, θ in the plane of incidence (*xz*-plane) was varied from –60° to 60°.

Figure 5.4.1 shows the normal incidence transmission spectra for both the 3.23 mm hole array and its near complementary 3.10 mm patch array structure.

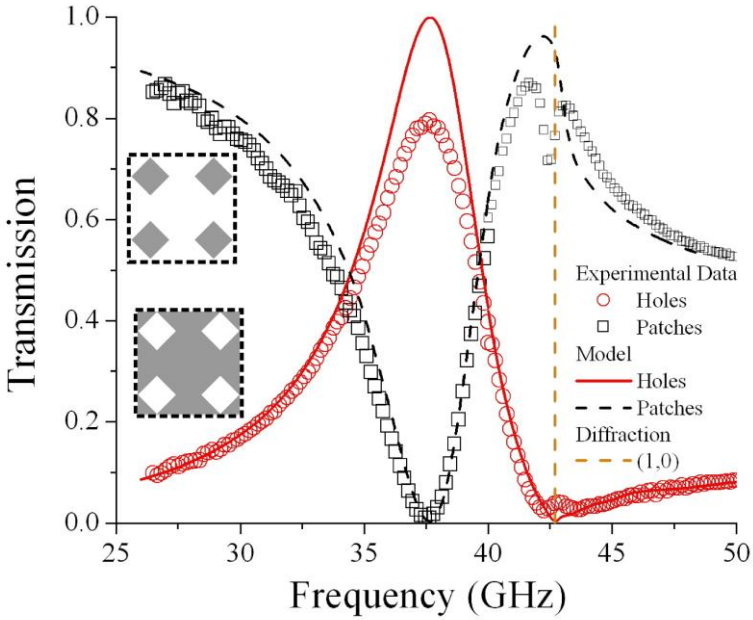

Figure 5.4.1. *Zero order transmission measurements for patches and holes on a square array of pitch 7.02 mm. Normal incidence, electric-field vector polarised across the diagonal of the patches. Schematic diagrams illustrate the connectivity of the structure.*

As discussed previously in chapter 4, these periodic arrays of holes/patches exhibit resonant behaviour close to the diffraction edge. This resonant behaviour is associated with diffractively coupled surface waves. The arrays of patches and holes exhibit complementary behaviour as predicted by Babinet's principle[16].

Figure 5.4.2 shows the transmission for the 3.23 mm hole array for both p- and s-polarised radiation. The intensity of the transmission efficiency is plotted on a logarithmic greyscale to improve clarity of the features close to the onset of diffraction. The transmission responses for p- and s-polarised radiation at normal incidence $(k_0 \sin\theta = 0)$ are identical due to the symmetry of the sample.

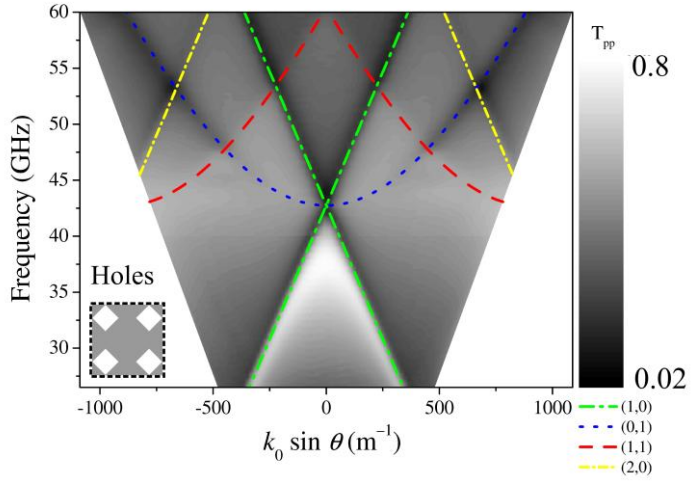

(a)

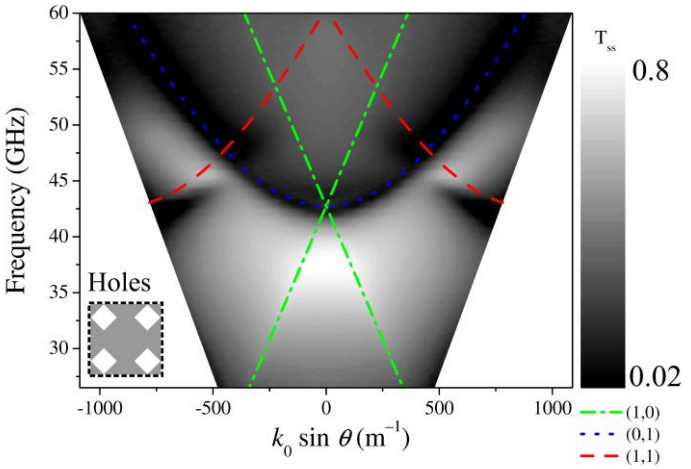

(b)

Figure 5.4.2. *Zero-order transmission for the 3.23 mm square hole array sample as a function of in-plane momentum, k_x, for* ***(a)*** *p-polarised and* ***(b)*** *s-polarised radiation. Lines indicate sets of diffracted light-lines due to grating periodicities. The schematic in the bottom left corner illustrates connectivity of the sample.*

The angle-dependent transmission data of the hole array structure illuminated with p-polarised radiation, shows that the resonant features observed are associated with diffraction from the grating vectors that lie in the plane of incidence. The dispersion of the surface waves strongly follows the in-plane diffracted light lines. These straight diffracted light lines arise from the intersection of the light cones centred on $k_x = \pm k_g$

with the $k_y = 0$ plane, they intersect at $f = c/\lambda_g \approx 42.7\,\text{GHz}$. There is also evidence of much weaker coupling into the diffracted orders associated with the orthogonal (0,1) periodicity. Conversely, for s-polarised incident radiation (*Figure 5.4.2b*) scattering from the grating vectors that lie out of the plane of incidence is dominant. The surface mode follows the parabolic diffracted light line generated from the intersection of the light cone centred on $k_y = \pm k_g$ with the y = 0 plane. This disparity between the coupling efficiency of p- and s-polarised radiation to the surface modes supported on hole arrays and bigratings has also been reported by other authors[73,143].

Figure 5.4.3 shows the dispersion of the resonance for p- and s-polarised radiation for the 3.10 mm patch array, the near complementary structure to the 3.23 mm hole array.

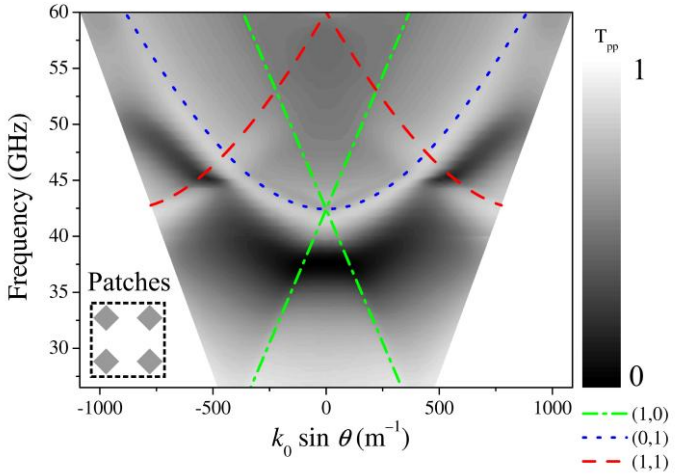

(a)

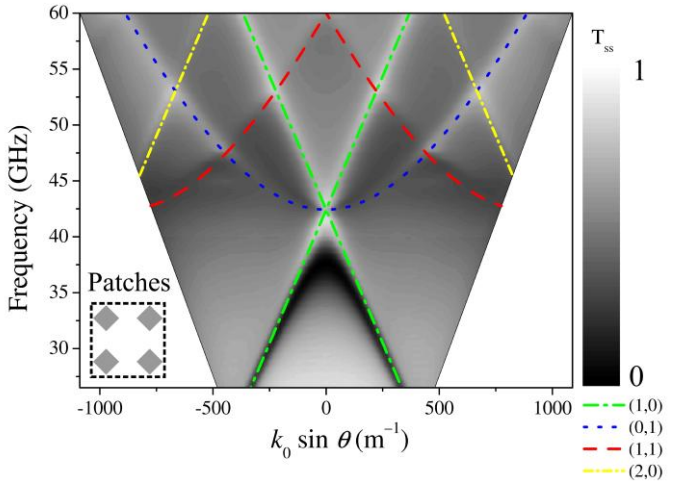

(b)

Figure 5.4.3*. Zero-order transmission for the 3.10 mm square patch sample as a function of in-plane momentum, k_x, for* ***(a)*** *p-polarised and* ***(b)*** *s-polarised radiation. Lines indicate sets of diffracted light-lines due to the grating periodicities. The schematic in the bottom left corner illustrates connectivity of the sample.*

For $k_0 \sin\theta \neq 0$ the dispersion of these modes is reversed in polarisation with respect to the response of the complementary structure, i.e. the dispersion of the modes on the patch structure for p-polarised incident radiation, associated with the $\pm k_g \hat{\mathbf{k}}_y$ diffraction (*Figure 5.4.3a*), are complementary to that of the hole structure for s – polarised

radiation (*Figure 5.4.2b*), and vice versa. This verifies the requirement of a 90° rotation of polarisation in order to satisfy Babinet's principle. Note that the magnitude of transmission for the pair of experimental structures on resonance is not perfectly complementary since there is absorption inside the metal layer which is not accounted for by Babinet's principle. There are also small differences in sample geometry. This mode dispersion can be further explained by examining the resonant fields from FEM modelling (*Figure 5.4.4* and *Figure 5.4.5*) using perfect electrical conductor (PEC).

Figure 5.4.4 shows the time-averaged magnitude and instantaneous vector surface current density for the 3.23 mm hole array at a frequency associated with the resonant transmission peak.

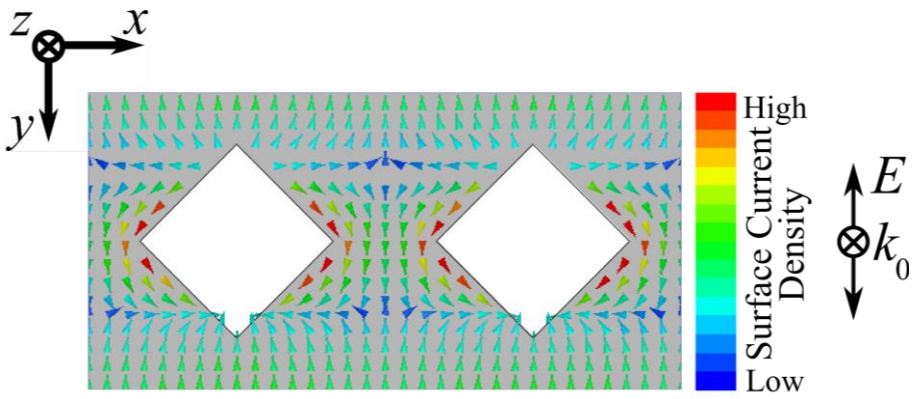

***Figure 5.4.4**. Surface current density magnitude plotted on the surface of the PEC hole array on resonance (37.6 GHz) for two unit cells, θ = 0°. The incident electric field is polarised along the y-axis. Arrows represent the direction of the surface current at a phase corresponding to maximum surface current density.*

The hole array is a connected structure and therefore supports real surface currents. The surface currents run parallel to the incident E-field, but due to the rotated geometry of the holes, there is enhancement of the surface current density at the narrowest point, i.e. between the corners of the holes at their nearest point. This results in enhanced magnetic field loops in the orthogonal direction to the surface current. *Figure 5.4.5* shows the instantaneous vector magnetic (***H***) field plot for the 3.23 mm hole array on resonance. Again the fields are plotted at a phase corresponding to maximum field enhancement.

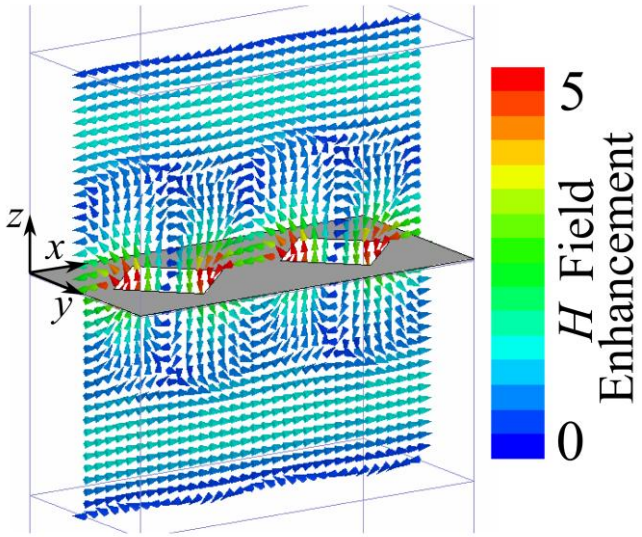

***Figure 5.4.5**. Time-averaged magnetic field enhancement plotted on resonance(37.6 GHz) through the centre of two holes with arrows representing the direction of the field at a phase corresponding to maximum field enhancement, θ = 0°. Grey represents the metal. The incident electric field is polarised along the y-axis.*

Magnetic field loops are present between neighbouring holes that lie in the *xz*-plane, i.e., parallel to the incident magnetic field. The dominant periodicity of the structure that influences the dispersion of the surface mode can be determined by examining the fields away from the sample in the transmitted half space. This allows the transmitted fields to be considered without the influence of near-field evanescent effects close to the structure. *Figure 5.4.6* shows the time-averaged magnetic fields on resonance parallel to the incident magnetic vector at a distance 3 mm below the surface of the sample.

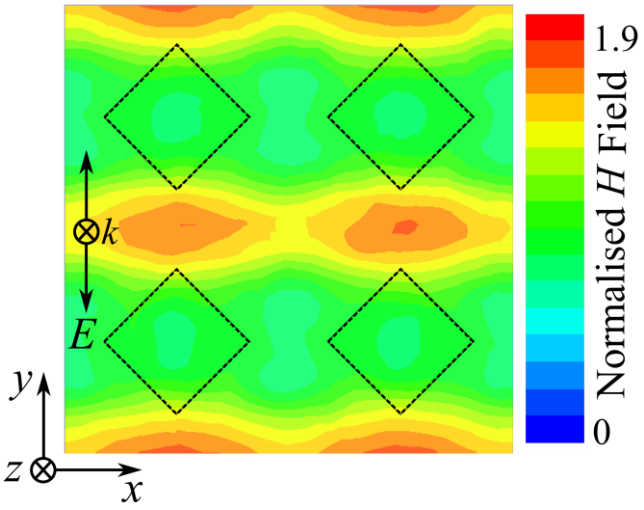

***Figure 5.4.6**. Time-averaged magnetic fields on resonance (37.6 GHz) parallel to the direction of the incident magnetic vector (in the x-direction) 3 mm below the hole array, $\theta = 0°$. The field is plotted across four unit cells for clarity. Black dashed lines indicate the position of the holes.*

The magnetic fields show periodicity in the direction of the incident electric field (y – direction) resulting in dominant scattering from the $k_g \hat{\mathrm{k}}_y$ grating vector. Since the coupling efficiency into these diffracted orders is most dominant, the surface wave disperses along the parabolic out-of-plane diffracted light lines (*Figure 5.4.2b*) for non-zero angles of incidence. A similar description can be used to describe the response for the orthogonal polarisation with the scattering from the $k_g \hat{\mathrm{k}}_x$ grating vector leading to the linear dispersion seen in *Figure 5.4.2a*.

Field plots from the finite-element method modelling for the 3.10 mm patch array are plotted in *Figure 5.4.7*.

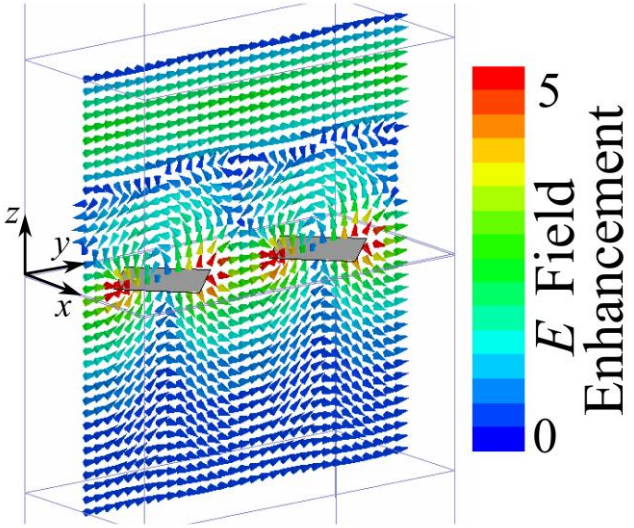

***Figure 5.4.7**. Electric field enhancement on resonance (37.4 GHz) plotted through the centre of two patches at a phase corresponding to maximum field enhancement, $\theta = 0°$. Grey represents the metal. The incident electric field vector is polarised along the y axis.*

On resonance loops of electric field are present between neighbouring patches in the *yz*-plane, i.e. there are components of electric field present in the direction of the incident electric field. Again the dominant periodicity can be determined by examining the fields below the surface of the sample. *Figure 5.4.8* shows the time-averaged electric fields on resonance parallel to the incident electric vector 8 mm below the surface of the sample.

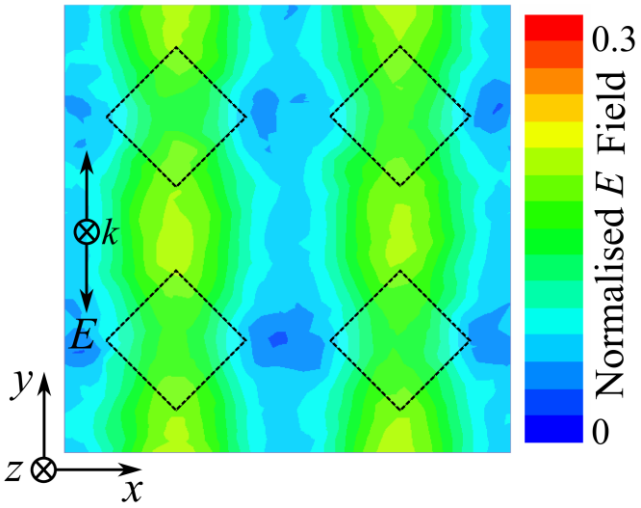

***Figure 5.4.8**. Time – averaged resonant electric fields on resonance (37.4 GHz) parallel to the direction of the incident electric vector (in the y - direction) 8 mm below the patch array, θ = 0°. Fields plotted across four unit cells for clarity. Black dashed lines indicate the position of the patches.*

The electric fields show periodicity in the direction orthogonal to the incident electric field (*y*-direction) resulting in dominant scattering from the $k_g \hat{\mathrm{k}}_x$ grating vector. Since the coupling efficiency into these diffracted orders is most dominant, the surface wave disperses along the linear in-plane diffracted light lines (*Figure 5.4.3b*). A similar description can be used to explain the response for the orthogonal polarisation with the scattering from the $k_g \hat{\mathrm{k}}_y$ grating vector leading to the parabolic dispersion seen in *Figure 5.4.3a*.

The band structures of surface wave resonances on disconnected arrays are clearly reversed with respect to their polarisation response from those observed on a grating of continuous metal[12,14,73,143]. This interchange in behaviour of the electric and magnetic fields is however completely predicted by Babinet's principle to describe the nature of complementary structures.

5.5 Summary

In this chapter the dispersion of surface modes on two near complementary thin metallic gratings in the microwave regime have been studied, showing the well known enhanced transmission, or the corresponding, lesser studied, enhanced reflection phenomena. The

modes for a given linear polarisation are found to closely follow the light lines associated with $\pm k_g \hat{\mathbf{k}}_x$ or $\pm k_g \hat{\mathbf{k}}_y$ diffraction, depending on the connectivity of the structure, with a near identical dispersion being observed for the array's complementary structure if the polarisation of the incident microwaves is rotated by 90°. The results accord well with the electromagnetic form of Babinet's principle. FEM modelling shows that for the disconnected patch arrays, strong electric fields are present between neighbouring patches and there is strong modulation in the electric field perpendicular to the plane of incidence. By contrast the holes in the complementary structure have strong loops of magnetic field between them with strong modulation in the magnetic field in the plane of incidence.

6 Multi-modal transmission of microwaves through hole arrays

6.1 Introduction

In chapter 2 the excitation of diffractively coupled surface waves and their role in the enhanced transmission phenomena seen with below cut-off metallic hole arrays is discussed. Surface waves on the metal/air interfaces couple together via evanescent fields in the holes leading to two possible modes of oscillation, an in-phase mode and an out-of-phase mode. These modes have symmetric and anti-symmetric charge distributions respectively. This coupled oscillator system is analogous to masses on a spring or bonding/anti-bonding atomic pairs. The coupling between these surface waves, and therefore their resonant frequency is strongly dependent on the depth and size of the holes. Few studies have focused on the anti-symmetric resonance due to its high Q factor and proximity to the diffraction edge[145-147]. Kirilenko and Perov[145] and Lomakin and Michielsen[146] used analytical and numerical modelling techniques to study the symmetric and anti-symmetric modes supported on hole arrays observing that the anti-symmetric mode has a very high Q-factor. Suckling et al.[147] experimentally studied a hexagonal array of holes with the expectation of observation of the anti-symmetric mode but due to sample inhomogeneities the mode was not observed. Many previous studies of coupled surface waves supported on hole arrays have focused on the symmetric oscillation[12,71,78-80,137-142].

Above the waveguide cut-off, propagating fields are supported in the hole, this allows coupling together of diffractively coupled surface waves through oscillatory waveguide modes when the depth of the holes is such that discrete longitudinally quantised electric fields can be supported.

In this study two arrays of holes in the two distinct regimes have been experimentally explored and their differences highlighted and explained. One array of holes has a cut-off above the onset of diffraction, the other a cut-off below the onset of diffraction. Their transmission responses show that these two cases are very different, with the

number of modes supported being dependent on both the depth of the holes and their diameter.

6.2 Background

6.2.1 Electromagnetic Waveguides

The cut-off frequency of a hole in a metallic substrate and thereby the frequency above which propagating fields are supported is determined by waveguide theory. Electromagnetic waveguides are structures that allow guiding of electromagnetic waves. The propagation through a waveguide was first considered by Heaviside[148] in 1893 however he thought that propagation through a hollow tube was not possible and that two conductors would be needed to transfer electromagnetic energy. Shortly after, propagation was mathematically proven by Lord Rayleigh[149] for circular and rectangular waveguides and he discovered that there are an infinite number of transverse electric (TE) and transverse magnetic (TM) modes which exist above a cut-off frequency. Waveguides were then briefly forgotten until rediscovered independently by George C. Southworth[150,151] and W. L. Barrow[152] in 1936, with the latter providing experimental evidence of propagation through a circular waveguide.

In this section the cut-off frequencies for TE and TM modes of a circular waveguide will be derived. These derivations are adapted from *Microwave Engineering*[125] by *D. M. Pozar*.

6.2.1.1 Fields at a Perfectly Electrically Conducting (PEC) Boundary

The derivation for the propagation through a waveguide assumes that it is infinitely long and has perfect electrically conducting (PEC) boundaries. Therefore the following conditions apply at the boundaries.

Since the walls are considered to be PEC the skin depth, δ will be zero as all fields will be excluded from the walls, as the conductivity, $\sigma \to \infty$, $\delta \to 0$. Therefore,

$$\hat{n}.\underline{D} = \rho_s \qquad \textit{Equation 6.2.1}$$

$$\hat{n}.\underline{B} = 0 \qquad \textit{Equation 6.2.2}$$

$$\hat{n} \times \underline{E} = 0 \qquad \textit{Equation 6.2.3}$$

$$\hat{n} \times \underline{H} = J_s \qquad \textit{Equation 6.2.4}$$

Here $\hat{n}$ is a unit vector normal to the surface, $\underline{D}$ is the electric displacement field, ρ_s is the surface charge density, $\underline{B}$ is the magnetic field, and J_s is the surface current density.

6.2.1.2 General Waveguide Solutions

There are three types of possible waveguide modes, transverse magnetic (TM), transverse electric (TE) and transverse electromagnetic (TEM) modes. The TM and TE modes have no longitudinal component of magnetic and electric field respectively. Whereas the TEM mode has neither longitudinal electric or magnetic components since all fields lies transverse to the axis of the waveguide.

The field components for an arbitrary cross-section waveguide will be derived and then used to derive the solutions for specific geometries.

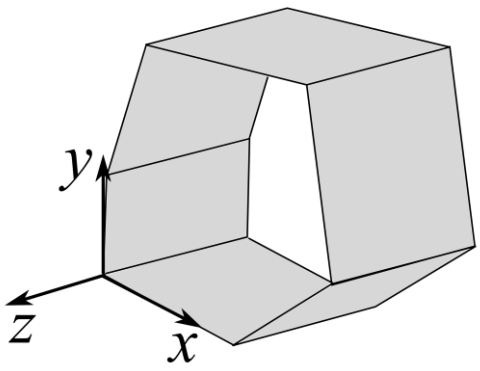

Figure 6.2.1. *Schematic illustration of a closed waveguide of arbitrary cross-section, coordinate system illustrated.*

Figure 6.2.1 shows the coordinate system used for these derivations. The cross-section is arbitrary but continuous through the length of the waveguide, i.e. through the *z* axis. The electric, *E* fields and magnetic *H* fields can be represented by the following:

$$\underline{E} = \left[\overline{E}(x,y) + \hat{z}E_z(x,y)\right]e^{-ikz} \qquad \textit{Equation 6.2.5}$$

$$\underline{H} = \left[\overline{H}(x,y) + \hat{z}H_z(x,y)\right]e^{-ikz} \qquad \textit{Equation 6.2.6}$$

Where $\overline{E}(x,y)$ and $\overline{H}(x,y)$ are the transverse fields, E_z and H_z are the axial fields. The time dependence, $e^{i\omega t}$ has been omitted for clarity. If the waveguide is assumed to be source free, then:

$$\underline{\nabla} \times \underline{E} = -i\omega\mu\underline{H} \qquad \textit{Equation 6.2.7}$$

$$\underline{\nabla} \times \underline{H} = i\omega\varepsilon\underline{H} \qquad \textit{Equation 6.2.8}$$

Where μ and ε are the permeability and permittivity of the waveguide cavity. The electric and magnetic fields have e^{-ikz} axial dependence so the field components can be reduced to:

$$\frac{\partial E_z}{\partial y} + ik_z E_y = -i\omega\mu H_x \qquad \textit{Equation 6.2.9}$$

$$-jk_z E_x - \frac{\partial E_z}{\partial x} = -i\omega\mu H_y \qquad \textit{Equation 6.2.10}$$

$$\frac{\partial E_y}{\partial x} - \frac{\partial E_x}{\partial y} = -i\omega\mu H_z \qquad \textit{Equation 6.2.11}$$

$$\frac{\partial H_z}{\partial y} + ik_z H_y = -i\omega\varepsilon E_x \qquad \textit{Equation 6.2.12}$$

$$-jk_z H_x - \frac{\partial H_z}{\partial x} = i\omega\mu E_y \qquad \textit{Equation 6.2.13}$$

$$\frac{\partial H_y}{\partial x} - \frac{\partial H_x}{\partial y} = -i\omega\mu E_z \qquad \textit{Equation 6.2.14}$$

These equations are then solved to obtain the transverse field components:

$$H_x = \frac{i}{k_c^{\,2}}\left(\omega\varepsilon\frac{\partial E_z}{\partial y} - k_z\frac{\partial H_z}{\partial x}\right)$$ *Equation 6.2.15*

$$H_y = \frac{-i}{k_c^{\,2}}\left(\omega\varepsilon\frac{\partial E_z}{\partial x} - k_z\frac{\partial H_z}{\partial y}\right)$$ *Equation 6.2.16*

$$E_x = \frac{-i}{k_c^{\,2}}\left(k_z\frac{\partial E_z}{\partial x} + \omega\mu\frac{\partial H_z}{\partial y}\right)$$ *Equation 6.2.17*

$$E_y = \frac{j}{k_c^{\,2}}\left(k_z\frac{\partial E_z}{\partial y} + \omega\mu\frac{\partial H_z}{\partial x}\right)$$ *Equation 6.2.18*

Here $k_c^{\,2}$ is the cut-off wavevector:

$$k_c^{\,2} = \omega^2\varepsilon\mu - k_z^{\,2} = k_0^{\,2} - k_z^{\,2}$$ *Equation 6.2.19*

Therefore if $k_0 < k_c$, k_z will be complex and therefore no propagating fields are supported.

6.2.1.3 Transverse Electric (TE) Modes

The transverse electric (TE) modes are defined as having no axial component of electric field but do have an axial component of magnetic field, therefore:

$$E_z = 0$$ *Equation 6.2.20*

$$H_z \neq 0$$ *Equation 6.2.21*

The transverse components of the fields can be simplified accordingly:

$$H_x = \frac{-ik_z}{k_c^{\,2}}\frac{\partial H_z}{\partial x}$$ *Equation 6.2.22*

$$H_y = \frac{-ik_z}{k_c^{\,2}}\frac{\partial H_z}{\partial y}$$ *Equation 6.2.23*

$$E_x = \frac{-i\omega\mu}{k_c^{\,2}}\frac{\partial H_z}{\partial y}$$ *Equation 6.2.24*

$$E_y = \frac{i\omega\mu}{k_c^{\,2}}\frac{\partial H_z}{\partial x}$$ *Equation 6.2.25*

The axial component of the magnetic field, H_z, may be found using the Helmholtz wave equation:

$$\nabla^2 \underline{H} + \omega^2 \mu\varepsilon \underline{H} = 0 \qquad \textit{Equation 6.2.26}$$

Since,

$$H_z(x,y,z) = h_z(x,y)e^{-ikz} \qquad \textit{Equation 6.2.27}$$

This can be reduced to a 2D wave equation:

$$\left(\frac{\partial^2}{\partial x^2} + \frac{\partial^2}{\partial y^2} + k_c{}^2\right) H_z = 0 \qquad \textit{Equation 6.2.28}$$

6.2.1.4 Transverse Magnetic (TM) Modes

The transverse magnetic (TM) modes are defined as having no axial component of magnetic field but do have an axial component of electric field, therefore:

$$E_z \neq 0 \qquad \textit{Equation 6.2.29}$$

$$H_z = 0 \qquad \textit{Equation 6.2.30}$$

The transverse components of the fields can be simplified accordingly:

$$H_z = \frac{i\omega\varepsilon}{k_c{}^2}\frac{\partial E_z}{\partial y} \qquad \textit{Equation 6.2.31}$$

$$H_y = \frac{-i\omega\varepsilon}{k_c{}^2}\frac{\partial E_z}{\partial x} \qquad \textit{Equation 6.2.32}$$

$$E_x = \frac{-ik_z}{k_c{}^2}\frac{\partial E_z}{\partial x} \qquad \textit{Equation 6.2.33}$$

$$E_y = \frac{ik_z}{k_c{}^2}\frac{\partial E_z}{\partial y} \qquad \textit{Equation 6.2.34}$$

E_z can then be reduced to a 2D wave equation:

$$\left(\frac{\partial^2}{\partial x^2} + \frac{\partial^2}{\partial y^2} + k_c{}^2\right) E_z = 0 \qquad \textit{Equation 6.2.35}$$

6.2.1.5 Transverse Electromagnetic (TEM) Modes

The TEM waveguide modes are defined as having no axial component of electric or magnetic field.

$$E_z = H_z = 0 \qquad \textit{Equation 6.2.36}$$

Using the equations derived previously (*Section 6.2.1.2*), the transverse fields are also zero unless the cut-off wave vector, $k_c = 0$. This results in TEM modes propagating without cut-off and with $k_z = k_0$, i.e. in an air filled waveguide the mode will propagate at the speed of light, *c*.

$$\left(\frac{\partial^2}{\partial x^2} + \frac{\partial}{\partial y^2}\right) E_x = 0 \qquad \textit{Equation 6.2.37}$$

Equation 6.2.37 is also satisfied by E_y, therefore,

$$\nabla_t^{\,2} \overline{E}(x,y) = 0 \qquad \textit{Equation 6.2.38}$$

Where $\overline{E}(x,y)$ are the transverse electric field components and $\nabla_t^{\,2} = \frac{\partial^2}{\partial x^2} + \frac{\partial^2}{\partial y^2}$ is the Laplacian operator in transverse dimensions.

The fields of a TEM waveguide mode satisfy Laplace's equation similar to the case of two conductors in the electrostatic limit.

The electric field can be expressed as a gradient of the scalar potential:

$$\overline{E}(x,y) = -\nabla_t \Phi(x,y) \qquad \textit{Equation 6.2.39}$$

Where $\nabla_t = \underline{\hat{x}}\left(\frac{\partial}{\partial x}\right) + \underline{\hat{y}}\left(\frac{\partial}{\partial y}\right)$ is the transverse gradient operator.

$$\nabla \cdot \underline{D} = \nabla \cdot \varepsilon \overline{E}(x,y) = 0 \qquad \textit{Equation 6.2.40}$$

$$-\nabla_t^{\,2} \Phi(x,y) = 0 \qquad \textit{Equation 6.2.41}$$

Where $\Phi(x,y)$ satisfies Laplace's equation, therefore a closed conductor cannot support a TEM waveguide mode since $\Phi(x,y)$ would be constant and $\overline{E}(x,y)$ would be zero.

6.2.1.6 Circular Waveguides

Consider a waveguide with circular cross section as illustrated in *Figure 6.2.2*.

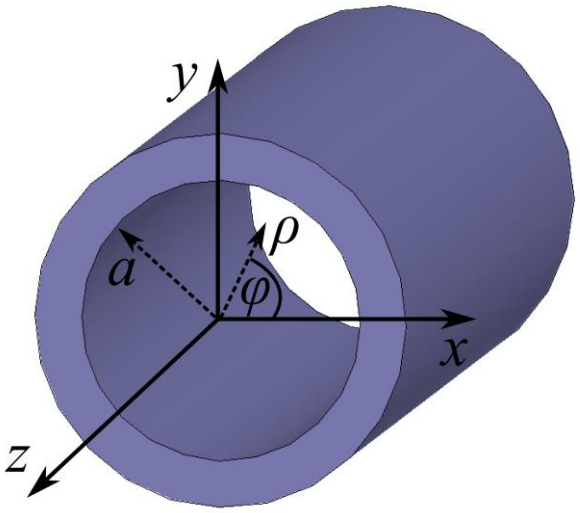

Figure 6.2.2. *Cross-section of a circular waveguide illustrating coordinate system for Cartesian and cylindrical polar coordinates.*

The transverse field components, in cylindrical polar coordinates can be expressed in terms of the longitudinal field components.

$$E_\rho = \frac{-i}{k_c^{\,2}}\left(k_z \frac{\partial E_z}{\partial \rho} + \frac{\omega\mu}{\rho}\frac{\partial H_z}{\partial \varphi}\right) \qquad \textit{Equation 6.2.42}$$

$$E_\varphi = \frac{i}{k_c^{\,2}}\left(\frac{k_z}{\rho}\frac{\partial E_z}{\partial \varphi} - \omega\mu \frac{\partial H_z}{\partial \rho}\right) \qquad \textit{Equation 6.2.43}$$

$$H_\rho = \frac{i}{k_c^{\,2}}\left(\frac{\omega\varepsilon}{\rho}\frac{\partial E_z}{\partial \varphi} - k_z \frac{\partial H_z}{\partial \rho}\right) \qquad \textit{Equation 6.2.44}$$

$$H_\varphi = \frac{-i}{k_c^{\,2}}\left(\omega\varepsilon \frac{\partial E_z}{\partial \rho} - \frac{k_z}{\rho}\frac{\partial H_z}{\partial \varphi}\right) \qquad \textit{Equation 6.2.45}$$

These expressions can then be used to find solutions for the TE and TM modes supported.

6.2.1.6.1 TE Modes

As discussed previously there is no longitudinal electric field component for a TE mode,

$$E_z = 0 \qquad \textit{Equation 6.2.46}$$

Therefore,

$$\left(\frac{\partial^2}{\partial\rho^2}+\frac{1}{\rho}\frac{\partial}{\partial\rho}+\frac{1}{\rho^2}\frac{\partial^2}{\partial\varphi^2}+k_c{}^2\right)h_z(\rho,\varphi)=0 \qquad \textit{Equation 6.2.47}$$

Where,

$$H_z(\rho,\varphi,z)=h_z(\rho,\varphi)e^{-ikz} \qquad \textit{Equation 6.2.48}$$

This equation can be solved using the separation of variables method:

$$h_z(\rho,\varphi)=R(\rho)P(\varphi) \qquad \textit{Equation 6.2.49}$$

$$\frac{\rho^2}{R}\frac{d^2R}{d\rho^2}+\frac{\rho}{R}\frac{dR}{d\rho}+\rho^2k_c{}^2=\frac{-1}{P}\frac{d^2P}{d\varphi^2} \qquad \textit{Equation 6.2.50}$$

The left hand side of the equation is dependent on ρ whereas the right hand side is dependent on φ. Therefore each side is equal to a constant which we shall define as $k_\varphi{}^2$.

$$\frac{d^2P}{d\varphi^2}+k_\varphi{}^2P=0 \qquad \textit{Equation 6.2.51}$$

$$\rho^2\frac{d^2R}{d\rho^2}+\rho\frac{dR}{d\rho}+\left(\rho^2k_c{}^2-k_\varphi{}^2\right)R=0 \qquad \textit{Equation 6.2.52}$$

The general solution to *Equation 6.2.52* is *Equation 6.2.53*.

$$P(\varphi)=A\sin(k_\varphi\varphi)+B\cos(k_\varphi\varphi) \qquad \textit{Equation 6.2.53}$$

H_z must be periodic in φ and k_φ must be an integer, n, therefore:

$$P(\varphi) = A\sin(n\varphi) + B\cos(n\varphi) \qquad \textit{Equation 6.2.54}$$

If n is substituted for k_φ in *Equation 6.2.52* then a Bessel differential equation is formed. This will have a solution of the type:

$$R(\rho) = CJ_n(k_c\rho) + DY_n(k_c\rho) \qquad \textit{Equation 6.2.55}$$

Where $J_n(x)$ and $Y_n(x)$ are Bessel functions of the first and second kind respectively, C and D are constants.

As $Y_n(k_c\rho) \to 0$, $\rho \to 0$ therefore this term is not applicable to situations of circular symmetry so $D = 0$.

Then,

$$h_z(\rho,\varphi) = (A\sin(n\varphi) + B\cos(n\varphi))J_n(k_c\rho) \qquad \textit{Equation 6.2.56}$$

The tangential electric field must fall to zero at the walls of the waveguide therefore:

$$E_\varphi(\rho,\varphi) = 0 \text{ at } \rho = a \qquad \textit{Equation 6.2.57}$$

The transverse fields can then be found:

$$E_\rho(\rho,\varphi,z) = \frac{-i\omega\mu n}{k_c{}^2\rho}(A\cos(n\varphi) + B\sin(n\varphi))J_n(k_c\rho)e^{-ik_z} \qquad \textit{Equation 6.2.58}$$

$$E_\varphi(\rho,\varphi,z) = \frac{i\omega\mu n}{k_c}(A\sin(n\varphi) + B\cos(n\varphi))J_n{}'(k_c\rho)e^{-ik_z} \qquad \textit{Equation 6.2.59}$$

$$H_\rho(\rho,\varphi,z) = \frac{-ik_z}{k_c}(A\sin(n\varphi) + B\cos(n\varphi))J_n{}'(k_c\rho)e^{-ik_z} \qquad \textit{Equation 6.2.60}$$

$$H_\varphi(\rho,\varphi,z) = \frac{-ik_z n}{k_c{}^2}(A\cos(n\varphi) + B\sin(n\varphi))J_n(k_c\rho)e^{-ik_z} \qquad \textit{Equation 6.2.61}$$

Where $J_n'(k_c\rho)$ is the first derivative with respect to its argument. At $\rho = a$, $E_\varphi(\rho,\varphi) = 0$ therefore $J_n(k_c\rho) = 0$. The *m*th root of $J_n(k_c\rho)$ will be defined as p_{nm}'. The cut-off wavenumber for the TE_{mn} may then be defined as:

$$k_{c(m,n)} = \frac{p'_{nm}}{a}, \qquad \textit{Equation 6.2.62}$$

where *m* is the number of radial nodes and *n* is the number of circumferential nodes in the electric field.

The propagation constant k_z for the TE_{mn} mode is then defined as:

$$k_z = \sqrt{k_0^{\,2} - k_c^{\,2}} = \sqrt{k_0^{\,2} - \left(\frac{p'_{nm}}{a}\right)^2} \qquad \textit{Equation 6.2.63}$$

Also the cut-off wavelength can be defined:

$$\lambda_{c(m,n)} = \frac{2\pi a}{p'_{nm}} \qquad \textit{Equation 6.2.64}$$

The values for p'_{nm} are shown in *Table 6.2.1*.

n	p'_{n1}	p'_{n2}	p'_{n3}
0	3.832	7.016	10.174
1	1.841	5.331	8.536
2	3.054	6.706	9.970

Table 6.2.1. *Values of p'_{nm} for the lowest order TE modes in a cylindrical waveguide.*

The lowest order waveguide mode is the one which has the lowest value of p'_{nm}, i.e. the first mode to propagate will be the TE_{11}. The cut-off frequency of the TE_{11} waveguide mode is therefore:

$$f_c = \frac{1.841c}{2\pi a} \qquad \textit{Equation 6.2.65}$$

Modelled fields for the TE_{11} mode are shown in *Figure 6.2.3*.

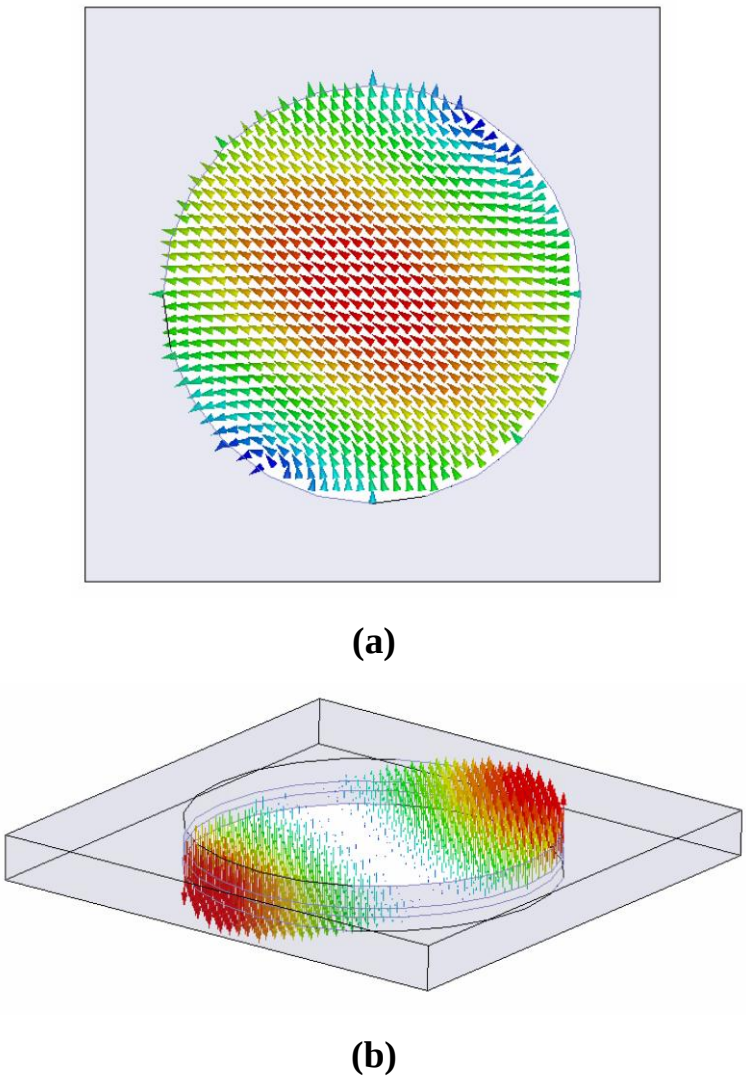

***Figure 6.2.3**. Modelled fields for the TE_{11} cylindrical waveguide mode. Holes modelled as having a uniform cross-section and infinite in length. Fields plotted across an x-y plane. Electric **(a)** and magnetic **(b)** vector fields plotted at a phase corresponding to maximum field enhancement.*

Equation 6.2.65 is derived on the basis of a waveguide of infinite length, however for a mode to be supported in a waveguide of finite length the field must also be quantised longitudinally. This introduces an extra momentum term, $k_z = N\pi/L$ leading to the cut-off of the *N*th longitudinally quantised TE_{11} waveguide mode, $f_{c(1,1,N)}$ being given approximately by:

$$f_{c(1,1,N)} \approx \frac{c}{2\pi}\sqrt{\left(\frac{1.841}{a}\right)^2+\left(\frac{N\pi}{L}\right)^2} \qquad \textit{Equation 6.2.66}$$

6.2.1.6.2 TM Modes

Similar to the TE modes, the longitudinal fields can be expressed in cylindrical polar coordinates and solved using the separation of variables method:

$$E_z(\rho,\varphi,z) = e_z(\rho,\varphi)e^{-ikz} \qquad \textit{Equation 6.2.67}$$

$$\left(\frac{\partial^2}{\partial\rho^2}+\frac{1}{\rho}\frac{\partial}{\partial\rho}+\frac{1}{\rho^2}\frac{\partial^2}{\partial\varphi^2}+k_c{}^2\right)e_z = 0 \qquad \textit{Equation 6.2.68}$$

$$e_z(\rho,\varphi) = (A\sin(n\varphi)+B\cos(n\varphi))J_n(k_c\rho) \qquad \textit{Equation 6.2.69}$$

The longitudinal component of the electric field must fall to zero at the walls of the waveguide, therefore:

$$e_z(\rho,\varphi) = 0 \text{ at } \rho = a \qquad \textit{Equation 6.2.70}$$

$$J_n(k_c a) = 0 \qquad \textit{Equation 6.2.71}$$

$$k_{c(n,m)} = \frac{p_{nm}}{a} \qquad \textit{Equation 6.2.72}$$

Where p_{nm} is the *m*th root of the Bessel function $J_n(p_{nm}) = 0$. The values for p_{nm} are shown in
Table **6.2.2** .

n	p_{n1}	p_{n2}	p_{n3}
0	2.405	5.520	8.654
1	3.822	7.016	10.174
2	5.135	8.417	11.620

Table 6.2.2*. Values of* $p_{nm}{}'$ *for the lowest order TM modes in a cylindrical waveguide.*

The transverse fields can then be expressed as:

$$E_\rho(\rho,\varphi,z)=\frac{-ik_z}{k_c^{\,2}}\left(A\sin(n\varphi)+B\cos(n\varphi)\right)J_n'(k_c\rho)e^{-ik_z} \qquad \textit{Equation 6.2.73}$$

$$E_\varphi(\rho,\varphi,z)=\frac{-ik_z n}{k_c}\left(A\cos(n\varphi)-B\sin(n\varphi)\right)J_n(k_c\rho)e^{-ik_z} \qquad \textit{Equation 6.2.74}$$

$$H_\rho(\rho,\varphi,z)=\frac{-i\omega\varepsilon n}{k_c^{\,2}\rho}\left(A\cos(n\varphi)-B\sin(n\varphi)\right)J_n(k_c\rho)e^{-ik_z} \qquad \textit{Equation 6.2.75}$$

$$H_\varphi(\rho,\varphi,z)=\frac{-i\omega\varepsilon}{k_c}\left(A\sin(n\varphi)+B\cos(n\varphi)\right)J_n'(k_c\rho)e^{-ik_z} \qquad \textit{Equation 6.2.76}$$

The lowest order propagating TM mode is the TM_{01}, fields for this mode are shown in *Figure 6.2.4*.

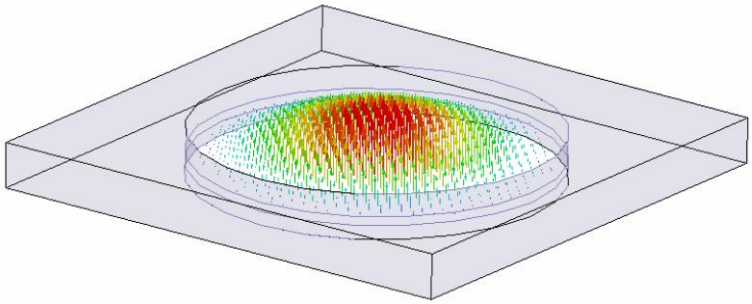

(a)

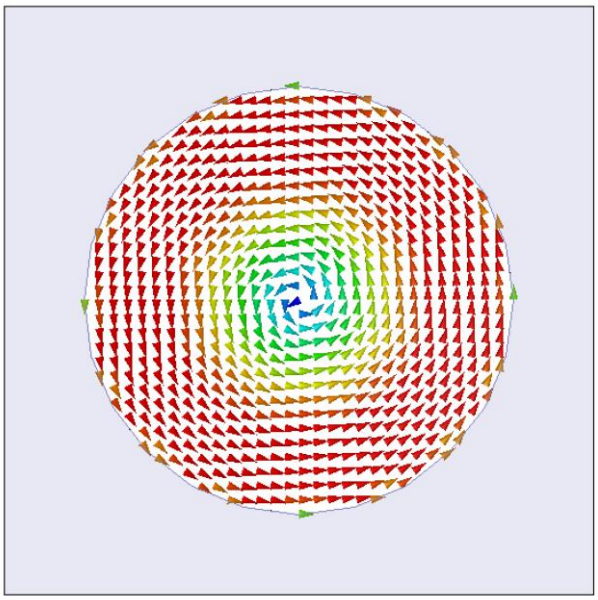

(b)

Figure 6.2.4*. Modelled fields for the TM_{01} cylindrical waveguide mode. Holes modelled as having a uniform cross-section and infinite in length. Fields plotted across an x-y*

*plane. Electric **(a)** and magnetic **(b)** vector fields plotted at a phase corresponding to maximum field enhancement.*

Since the lowest order waveguide mode for a circular waveguide is the TE_{11}, it is the cut-off frequency of the TE_{11} mode that will be significant in the experimental study within this chapter. This cut-off frequency determines when propagating fields can be supported within the holes of the arrays under study and therefore it will be this mode's cut-off that will be referred to for the rest of the chapter.

6.3 Experiment and Methods

The structure under study is that of an array of unfilled cylindrical holes in a metallic plate, arranged in a square lattice of 5.5 mm pitch. *Figure 6.3.1* illustrates the unit cell of the array and the coordinate system used in all of the modelling and experiments discussed in this chapter.

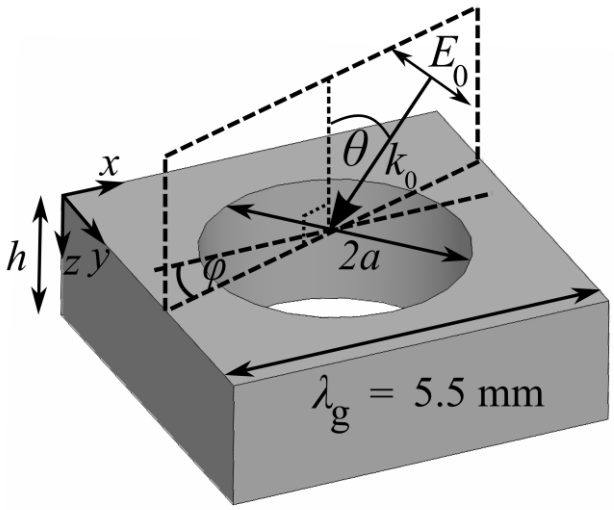

***Figure 6.3.1**. Unit cell of the sample and coordinate system illustrating the plane of incidence, polar angle, θ, azimuth angle, φ, hole diameter, a, and hole depth, h.*

Samples were fabricated using computer numerical control (CNC) milling of stacked aluminium plates. This allowed many samples to be produced of different thicknesses

but identical hole size. These samples can then be arranged to form many combinations.

Two stacks of plates were milled, both sets have pitch 5.5 mm but have different hole sizes. One set of plates has holes of diameter 4 mm, these holes having a cut-off frequency of 43.95 GHz, according to *Equation 6.2.65* which lies below the onset of diffraction at 54.55 GHz. The second set of plates has holes of diameter 3.1 mm and therefore a cut-off frequency of 56.71 GHz, i.e. above the onset of diffraction.

A single-mode-approximation, modal matching technique has been employed to calculate the dispersion of surface modes on perfect electrically conducting (PEC) cylindrical hole arrays. This modelling code was written by *E. Hendry* and is discussed in further detail in chapter 3. This technique is based on the work of McPhedran et al.[84,153] The electric fields in the vacuum regions either side of the holes are represented as a two-dimensional Fourier-Floquet expansion of diffracted orders. Inside the holes the fields are represented by the lowest order cylindrical waveguide mode, the TE_{11}. The number of diffracted orders included in the calculation can be varied allowing the dispersion of modes with and without diffraction to be calculated. This allows the origin of any modes, their asymptotic frequencies and the result of band folding to be qualitatively understood.

Finite-element method (FEM) modelling has also been used to provide a fit to experimental data and produce field plots. This additional modelling technique has been used as the single-mode-approximation modal matching technique is not exact and therefore can only be used qualitatively. Without the inclusion of higher order waveguide modes the modal matching code cannot fully reproduce experimental data.

Transmission measurements have been performed using a free-space microwave set-up using matched microwave source and detector horns from 40 – 60 GHz. Collimating mirrors are used to form a plane wave. The sample sits on a rotating turntable which allows the polar angle of incidence, θ to be varied (More detail on the experimental set-up can be found in chapter 3).

6.4 Results and Discussion

6.4.1 Cut-off Below Onset of Diffraction ($f_c < f_{diff}$)

For an array of large holes the cut-off frequency, f_c, may be set below the onset of diffraction, f_{diff}, i.e. ($f_c < f_{diff}$). In order to investigate this regime an array of holes with 4 mm diameter in a square array with pitch of 5.5 mm will be considered.

Figure 6.4.1 shows modal-matching modelling without inclusion of diffracted orders in the expansion of the electric fields for 4 mm diameter holes in a square array of 5.5 mm pitch and 10 mm depth, i.e. the reflected and transmitted electric fields are defined as only containing a specular component.

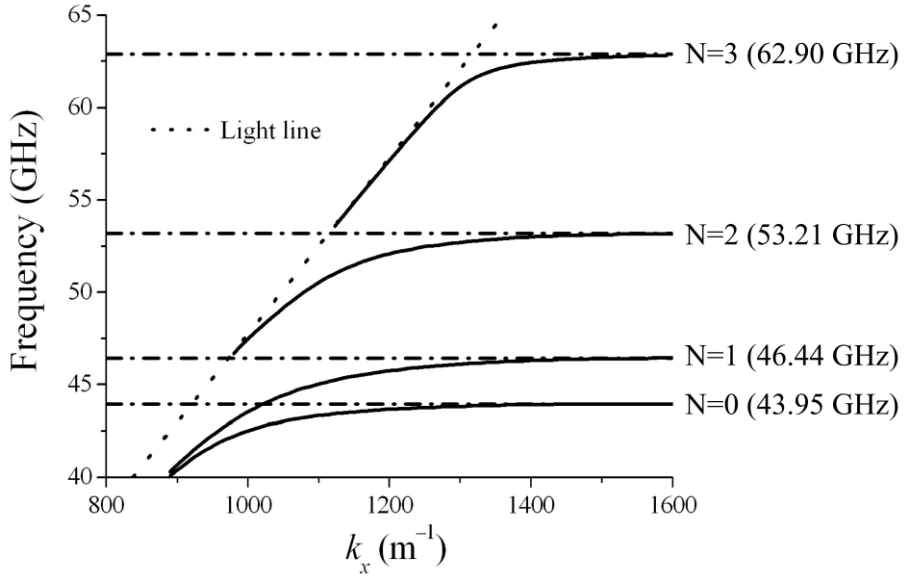

Figure 6.4.1. *Modal matching eigenmode solutions without inclusion of diffracted orders for 4 mm diameter holes in a square array of 5.5 mm pitch and 10 mm depth. Solid lines indicate position of the modes supported. Dash-dot lines indicates the asymptotic frequencies. N indicates the longitudinal quantisation of the electric field in the z direction. Light line also illustrated.*

The two lowest frequency modes supported on the hole array have a dispersion that is similar to that of a surface wave on a planar plasmonic metal/dielectric interface (discussed in chapter 2). At small values of k_x the modes are asymptotic to the light line and at large values of k_x tend towards a limit frequency. At large values of k_x the lowest order mode is asymptotic to the cut-off (43.95 GHz) frequency of the holes

($N = 0$) which is acting as an effective or 'spoof' plasma frequency[2,3]. The second mode asymptotes at large values of k_x to the cut-off frequency of the first order waveguide mode (N = 1) with quantised field in the longitudinal direction (46.44 GHz). The third mode seen in *Figure 6.4.1* is asymptotic to the cut-off frequency of the second order waveguide mode with quantised field in the longitudinal direction (53.21 GHz); this mode however **starts from, but is not asymptotic to the light line**. This is due to the modes requiring the holes to be able to support propagating fields in order to be excited, this can only occur above the corresponding cut-off frequency. There will an infinite number of these higher order longitudinally quantised modes all starting from the light line above their corresponding cut-off frequency.

The influence of diffraction can be considered by taking into account the scattering from the periodicity of the array and representing these modes in a reduced zone representation. This can be done by folding the modes back into the first Brillouin zone at the Brillouin zone boundary $(k_g / 2)$. This simple approach ignores any band gaps that may open at the Brillouin zone boundaries but gives a qualitative picture of which modes may be coupled to by an incident photon.

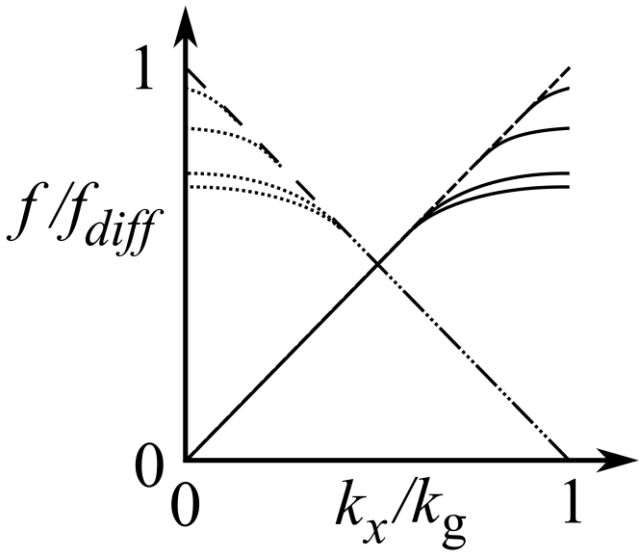

***Figure 6.4.2**. Schematic representation of dispersion of surface modes when $f_c < f_{diff}$, where f_{diff} is the frequency of the onset of diffraction. Modes folded into the first Brillouin zone to represent the effect of first order diffraction. Long dash line illustrates diffracted light line, dotted lines illustrate diffracted modes.*

Figure 6.4.2 shows the modes that have been folded back into the first Brillouin zone. All four of the modes that were in the dispersion plot without diffraction occur below f_{diff} = 54.55 GHz and are band folded back into the radiative light cone with possibility of coupling with an incident photon.

In order to measure experimentally the behaviour of the modes supported when the cut-off lies below the diffraction edge, cylindrical holes of 4 mm diameter were drilled into five 400 mm × 400 mm sheets of aluminium of various thicknesses in a square array of 5.5 mm pitch (4761 holes). This allows arrays of different thicknesses to be assembled by bolting the arrays together in various combinations. The holes have an infinite thickness cut-off at 42.77 GHz. The samples were mounted perpendicular to a collimated microwave beam and transmission measurements were performed from 40 – 60 GHz, normalised to transmission without the sample.

Figure 6.4.3 shows normal incidence transmission measurements and a FEM model for a sample of 9.94 mm deep holes. Below the cut-off (42.77 GHz) transmission is near zero as predicted by waveguide theory[125]. A series of surface modes which manifest themselves as peaks in the transmitted signal are supported between the cut-off frequency and the onset of diffraction at 54.55 GHz. The modes that are present at the edge of the transmission band close to the diffraction edge have a high Q factor. These modes are sensitive to angle and as such are greatly affected by any beam spread (~ 1 – 2° for this experimental setup), this accounts for the reduced visibility of the mode at 54.50 GHz in the experiment. The modes close to the cut-off of the holes are also very sensitive in frequency to the hole size. Consequently, because of some non-uniformity in the diameter of the holes the modes are broadened and weakened. This effect manifests itself most strongly in the loss of intensity of the first order mode. Furthermore there is a degree of roughness in the cross-section of the holes which results in a mean diameter of 4.05 mm.

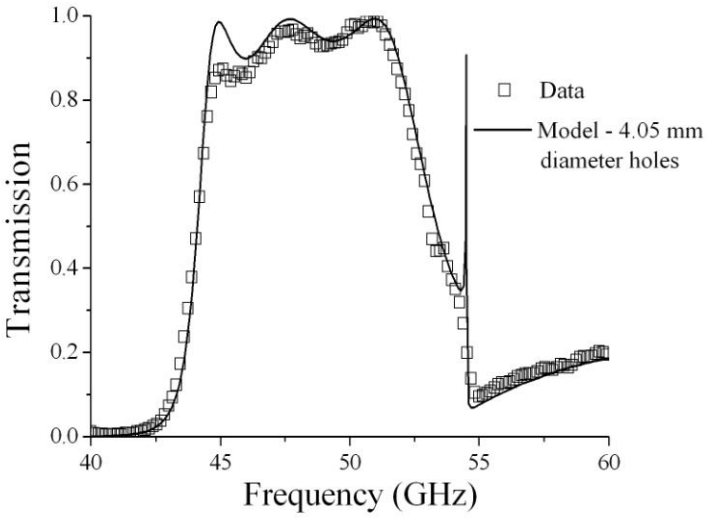

***Figure 6.4.3**. Normal incidence transmission measurements for 4 mm diameter holes in a square array of 5.5 mm pitch, 9.94 mm thick aluminium. Fit achieved using FEM modelling also illustrated.*

The *x*-component of the electric fields (parallel to the incident electric field) are shown in *Figure 6.4.4* for the four transmission maxima in *Figure 6.4.3*.

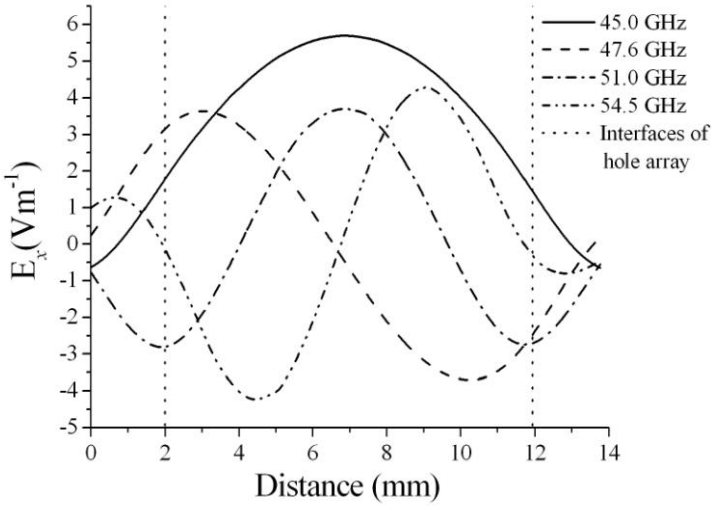

***Figure 6.4.4**. FEM model predictions of the x-component of the electric field (parallel to the incident electric field). Amplitude plotted through the centre of the 4 mm diameter, 9.94 mm deep holes (θ=0°).*

The two lowest order modes have similar field profiles to that seen for coupled surface waves on thin metal films[70,154-157] with symmetric and anti-symmetric fields that have

hyperbolic cosine (45 GHz) and hyperbolic sine (47.6 GHz) character. As a result of diffraction the boundary conditions at the entrance of the holes is altered leading to the frequency of the lowest order mode being higher than the cut-off frequency predicted by *Equation 6.2.66* which assumes a single isolated waveguide. Since these modes are above the cut-off frequency of the lowest order waveguide mode, the holes can support a mixture of propagating and evanescent fields. This results in the fields appearing to have some oscillatory character. The two higher frequency modes are oscillatory and have cosine (51 GHz) and sine (54.5 GHz) solutions as these modes are Fabry Perot-like resonances inside the holes. This explains their dispersion starting from the light line above the cut-off frequencies. Due to the proximity of the fourth mode to the diffraction edge, strong evanescent near-fields have resulted in the two nodes near the interface being forced outside of the holes.

The 9.94 mm depth sample was mounted on a stepper motor driven turntable to allow the incident angle, θ, to be varied while the transmission was measured. The dispersion of the modes was experimentally measured for p-polarised (transverse magnetic) radiation (*Figure 6.4.5*).

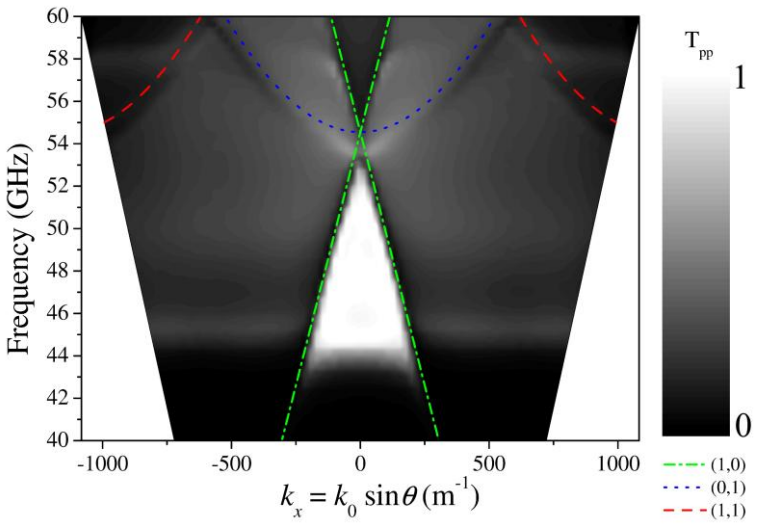

(a)

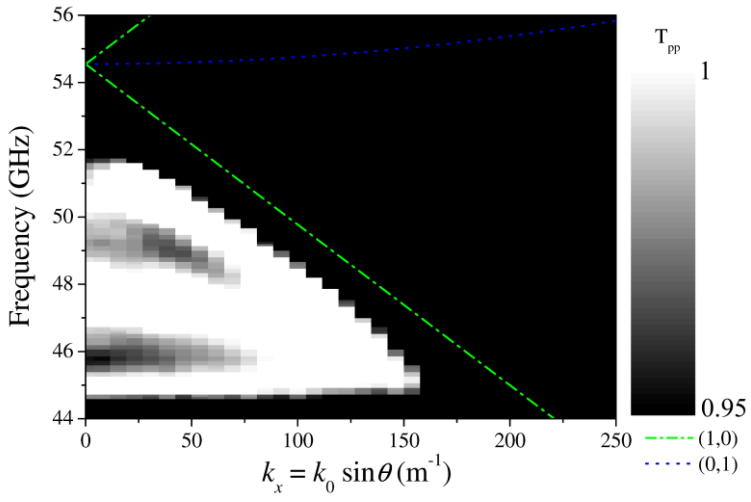

(b)

Figure 6.4.5*. (a) Experimental zero order transmission measurements for the 9.94 mm thick square array of 4.05 mm diameter holes, 5.5 mm pitch, as a function of in-plane momentum, k_x. Diffracted light lines illustrated. (b) Detailed plot of resonant transmission maxima.*

Figure 6.4.5a shows that the modes are dispersive, following the (±1,0) diffracted light lines suggesting that it is the in-plane $\pm k_g \hat{k}_x$ diffraction that is the dominant mechanism in the coupling to these modes. This type of dispersion is characteristic of coupled surface waves on hole arrays[12,14,73,143,158] due to the metallic connectivity of the structure (see chapter 5). *Figure 6.4.5b* shows the transmission in more detail so that the lowest three modes can be clearly distinguished. The modes closest to the diffraction edge are strongly incident angle dependent, a common characteristic of surface waves.

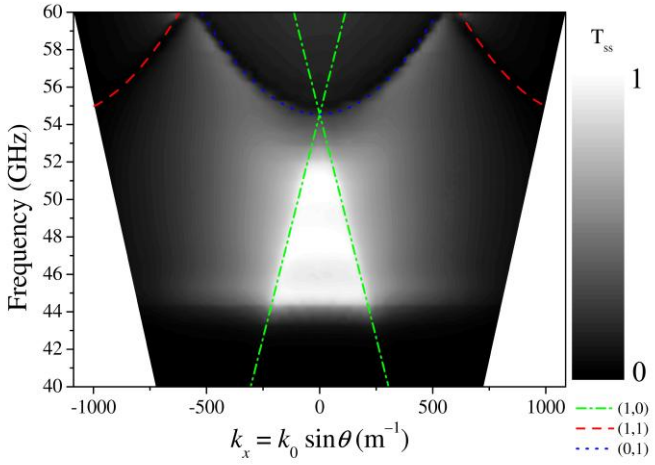

Figure 6.4.6*. Experimental zero order s-polarised transmission measurements for the 9.94 mm thick square array of 4.05 mm diameter holes, 5.5 mm pitch, as a function of in-plane momentum, k_x. Diffracted light lines illustrated.*

Figure 6.4.6 shows the s-polarised transmission response as a function of in-plane momentum and frequency. For this incident polarisation the modes now have a different dispersion, being more influenced by the parabolic out-of-plane diffracted light lines than previously for the p-polarised case, this is similar to the study on complementary arrays seen in chapter 5. The differences between *Figure 6.4.5* and *Figure 6.4.6* are not as large as that observed in chapter 5 which investigated the dispersion of surface modes on hole arrays for different incident polarisations. This is due to the modes being further away from the diffraction edge and thus being less influenced by the form of the diffracted light lines. Transmission measurements are shown in *Figure 6.4.7* for $\varphi = 45°$. Since the grating vector responsible for first order diffraction is now at 45° to the incident wave vector the diffracted light lines ((1,0) and (-1,0)) are now parabolas that intersect on the $k_x = 0$ axis. The dispersion characteristics of the modes has also changed to closer to that of these diffracted light lines further indicative of surface wave behaviour.

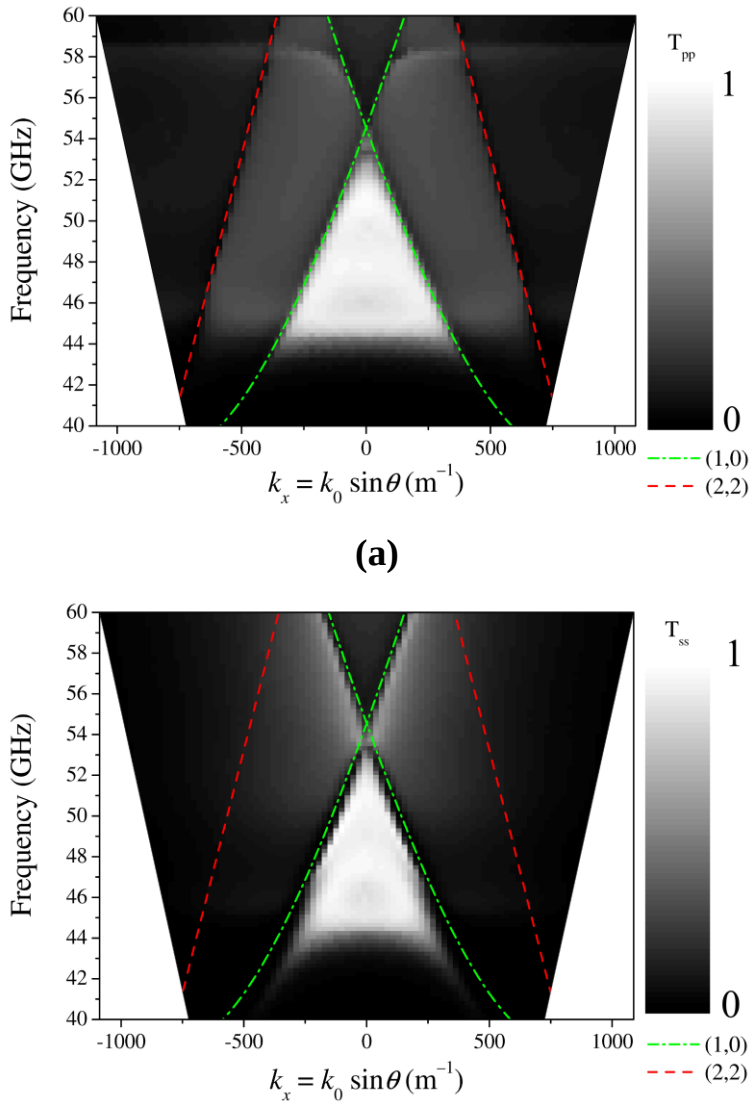

Figure 6.4.7*. Experimental zero order transmission measurements for the 9.94 mm thick square array of 4.05 mm diameter holes, 5.5 mm pitch, as a function of in-plane momentum,* k_x, $\varphi = 45°$. ***(a)*** *p-polarised* ***(b)*** *s-polarised incident radiation. Diffracted light lines illustrated.*

Experimental and modelled transmission maxima for arrays of various thicknesses are shown in *Figure 6.4.8*. Samples with small hole depths only support two modes, the lower frequency symmetric and anti-symmetric coupled surface modes close to the diffraction edge. As the hole depth is increased higher order modes with the electric field quantised longitudinally become supported. These modes appear from the diffraction edge as they are diffractively coupled modes and reduce in frequency as the hole depth is increased, asymptotically approaching the cut-off frequency for an infinite

length waveguide. Increasing the hole depth reduces the longitudinal momentum component, k_z, i.e. *Equation 6.2.66* will tend to that of *Equation 6.2.65* reducing the cut-off of these modes to that of an infinite waveguide. Since the arrays are bolted together to make even deeper holes there are inevitably small non-uniform gaps between the layers of the holes in some of the samples. This results in a loss of intensity in the background level of the transmission, accounting for some of the discrepancy between the model and experiment. The high frequency mode maxima are also lowered in frequency due to the 1 - 2° angle spread present in the incident beam.

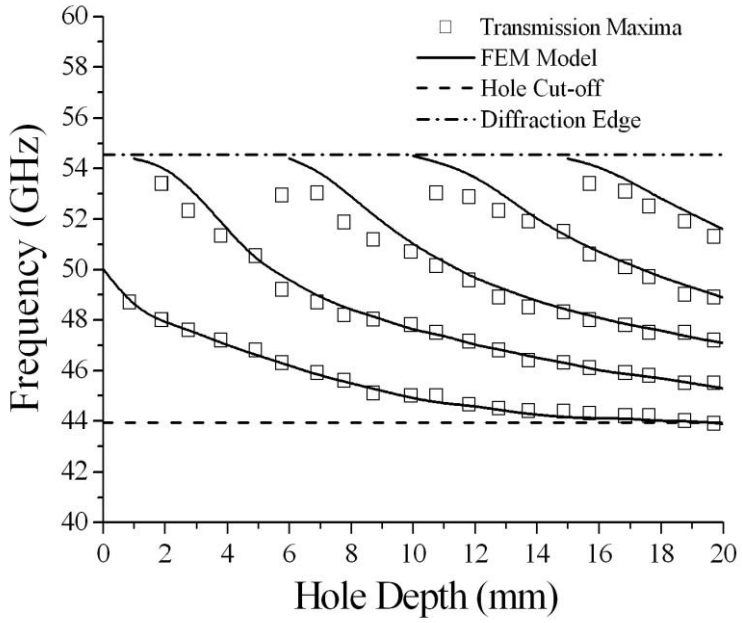

Figure 6.4.8*. Experimental and modelled normal incidence transmission maxima as a function of hole depth for an array of 4.05 mm diameter holes, 5.5 mm pitch.*

6.4.2 Cut-off Above Onset of Diffraction ($f_c > f_{diff}$)

Figure 6.4.9 shows the dispersion of the modes supported by 3 mm diameter holes in a square array of 5.5 mm pitch and 2 mm depth calculated by the modal matching method.

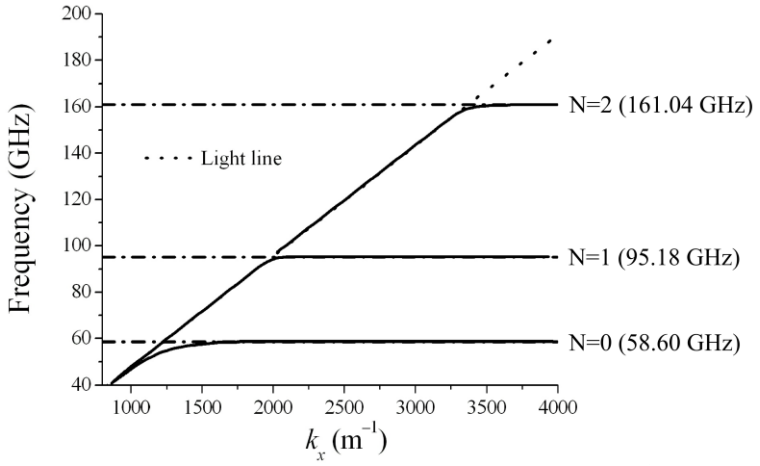

***Figure 6.4.9**. Calculated eigenmode solutions without inclusion of diffracted orders for 3 mm diameter holes in a square array of 5.5 mm pitch and 2 mm depth. Solid lines indicate position of the modes supported. Dash-dot lines show the asymptotic frequencies. N indicates the longitudinal quantisation number for the electric field in the z direction.*

The surface of small holes supports a series of modes with surface wave character similar to that seen for the large holes. At large values of k_x the lowest order mode is asymptotic close to the infinite cut-off (58.6 GHz) frequency of the holes which is acting as an effective plasma frequency. Again, the second mode also asymptotes at large values of k_x to the cut-off frequency of the first order waveguide mode with quantised field in the longitudinal direction (95.18 GHz). The third mode seen in *Figure 6.4.9* is asymptotic to the cut-off frequency of the second order waveguide mode with quantised field in the longitudinal direction (161.04 GHz); but again starts from the light line rather than being asymptotic to it.

The effect of diffraction and band-folding can be qualitatively introduced by reflecting the dispersion of the modes back into the first Brillouin zone. All of the modes at a frequency below f_{diff} = 54.55 GHz are folded back into the light cone allowing radiative coupling to them. *Figure 6.4.10* shows the eigenmodes inside the radiative light cone. Since we are considering the case when the cut-off frequency is above f_{diff} only the two lowest order modes ($\mathrm{N}=0, \mathrm{N}=1$) will appear in the normal incidence transmission spectra as the higher order modes are not asymptotic to the light line.

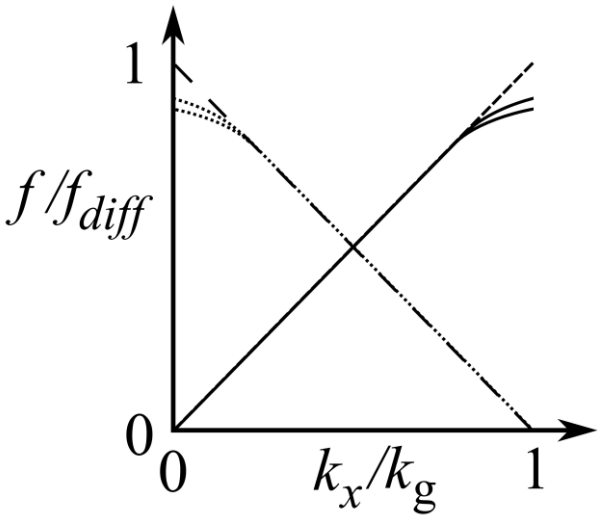

Figure 6.4.10*. Schematic representation of dispersion of surface modes when* $f_c > f_{diff}$*. Modes folded into the first Brillouin zone to represent the effect of first order diffraction.*

A similar experiment to that used for the large holes was performed to observe the behaviour with small holes. Cylindrical holes of 3.1 mm diameter were drilled into 400 mm × 400 mm sheets of aluminium of various thicknesses in a square array of 5.5 mm pitch (4761 holes). This allows arrays of different thicknesses to be assembled by bolting the arrays together in various combinations. The holes have an infinite thickness cut-off at 56.71 GHz. The samples were mounted perpendicular to a collimated microwave beam, transmission measurements performed from 40 – 60 GHz and normalised to transmission without the sample.

Figure 6.4.11 shows the normal incidence transmission response for the 3.1 mm diameter holes. Only the two lowest order evanescent transmission modes are present as predicted. Also shown is a finite element method model fit to the data. As seen previously for the arrays with the larger holes the hole diameter in the model has to be increased by 50 μm to account for a spread in hole size. The two modes are observed very close to the onset of diffraction as expected. Due to proximity to the diffraction edge the modes are very sensitive to the incident angle. The anti-symmetric mode has a high Q-factor and angle-spread in the beam as well as sample inhomogenities have resulted in its intensity of its peak being significantly reduced.

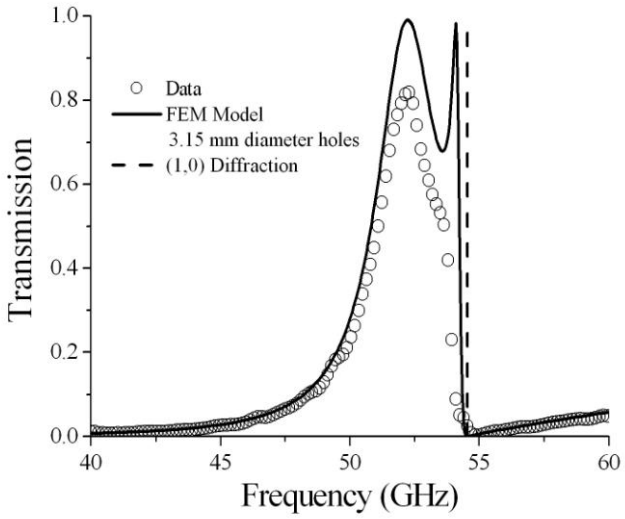

Figure 6.4.11. *Experimentally measured normal incidence transmission for 3.1 mm diameter holes in a square array of 5.5 mm pitch and 1.905 mm depth.*

The *x*-component of the electric fields (parallel to the incident electric field) for the two modes is plotted in *Figure 6.4.12*. The lower frequency mode (52.9 GHz) has an electric field distribution that is symmetric with peak electric field in the centre of the hole. The electric fields for the higher frequency mode can also be seen in *Figure 6.4.12* and shows that the mode is anti-symmetric in character. These field profiles can be represented with hyperbolic cosine and hyperbolic sine functions respectively. The electric fields for the anti-symmetric mode reverse in the centre of the hole, this rapid reversal of the electric field means that more energy is stored in the fields resulting in a higher resonant frequency.

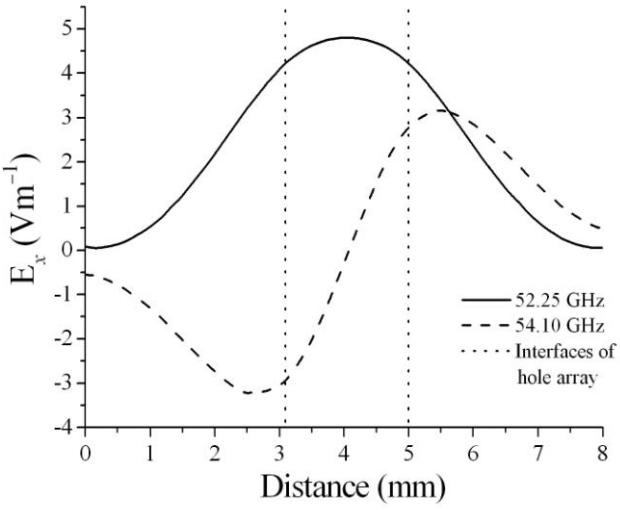

***Figure 6.4.12**. FEM model predictions of the electric field tangential to the plane of the array and parallel to the incident electric field. Amplitude plotted through the centre of the 3.15 mm diameter, 2 mm deep holes. Interfaces illustrated by dotted lines.*

Figure 6.4.13 shows the angle dependent transmission response for p- and s-polarised incident radiation of the array of small holes. The measured responses are vastly different and typical of that seen for surface waves on hole arrays (chapter 5). The in-plane scattering appears to be the dominant coupling mechanism to the surface modes for p-polarised incident radiation leading to the modes following the linear in-plane diffracted light lines. For s-polarised radiation the out-of-plane scattering is most dominant leading to a parabolic dispersion of the modes.

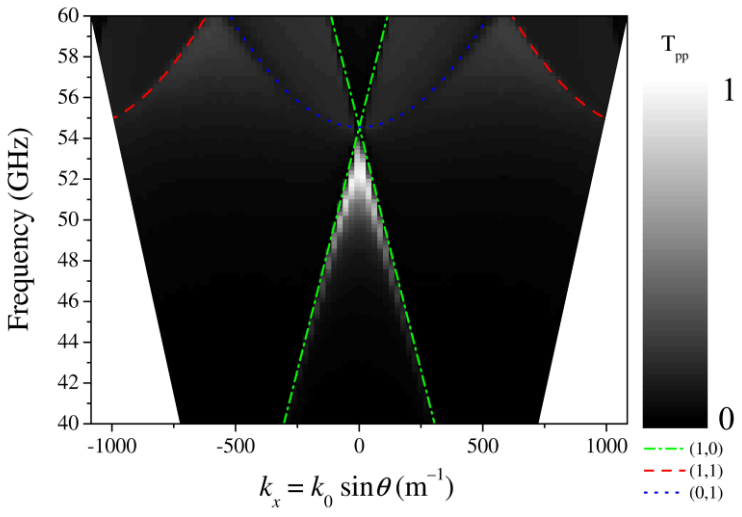

(a)

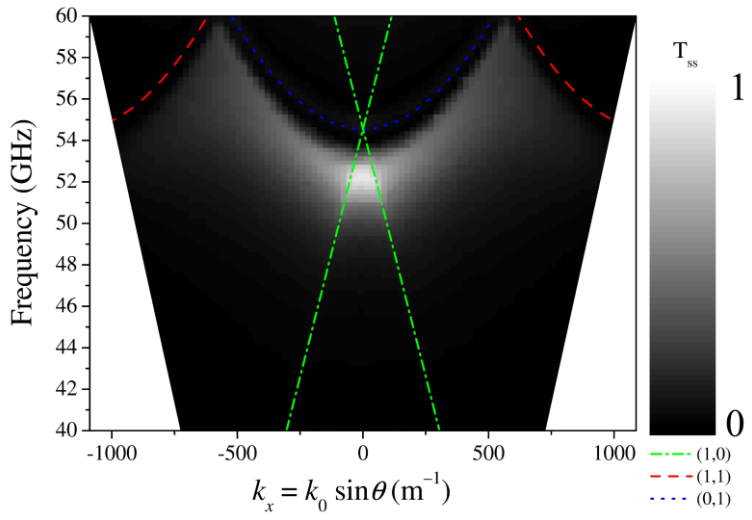

(b)

Figure 6.4.13*. Experimental zero order transmission measurements for the 1.905 mm thick square array of 3.05 mm diameter holes, 5.5 mm pitch, as a function of in-plane momentum, k_x, $\varphi = 0°$. Diffracted light lines illustrated.* ***(a)*** *p-polarised incident radiation.* ***(b)*** *s-polarised incident radiation*

Figure 6.4.14 shows the angle dependent response of the hole arrays for p and s polarised incident radiation at an incident azimuth angle of 45°. The modes coupled to for p and s polarised radiation both still follow the diffracted light lines associated with the fundamental grating periodicity however these light lines now have a similar dispersion. The coupling to the modes is however clearly very different, at large angles the modes are not observed for p-polarised radiation but they are still very prominent in the s-polarised response. This occurs since the electric field is invariant with incident angle for s-polarised radiation allowing coupling strength to be maintained for larger angles. Coupling to a mode that follows the (1,1) diffracted light lines that results from in-plane scattering is observed for p-polarised radiation, this is consistent with the $\varphi = 0°$ scenario. It is likely that a mode can be coupled to due to (-2,2) diffraction out of the plane of incidence for s-polarised incident radiation however this mode would be out of the measured frequency range since the diffracted light line would be a parabola centred on 77.14 GHz.

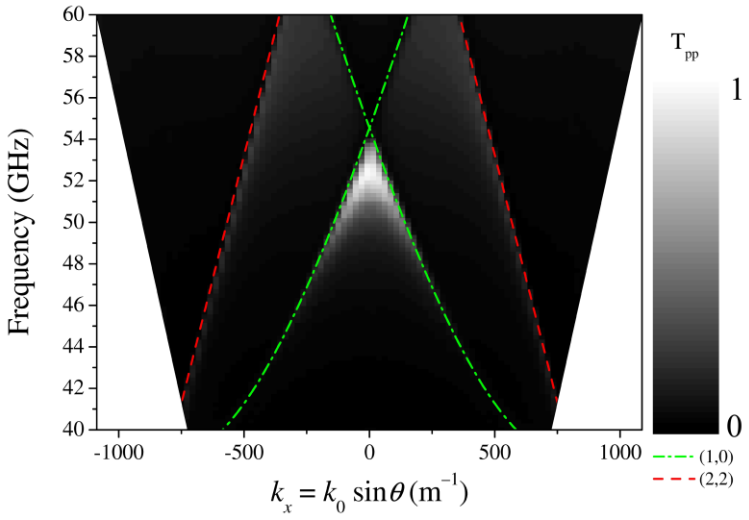

(a)

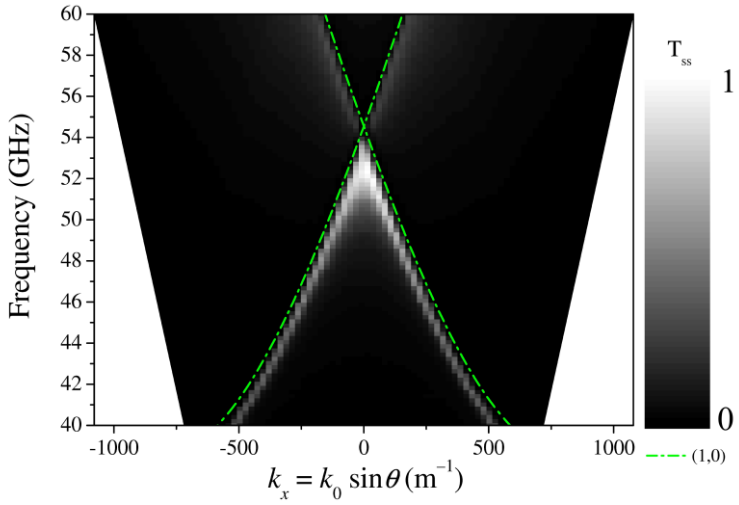

(b)

Figure 6.4.14*. Experimental zero order transmission measurements for the 1.905 mm thick square array of 3.05 mm diameter holes, 5.5 mm pitch, as a function of in-plane momentum,* k_x, $\varphi = 45°$. *Diffracted light lines illustrated.* ***(a)*** *p-polarised incident radiation.* ***(b)*** *s-polarised incident radiation.*

Figure 6.4.15 shows the depth dependence of the normal incidence transmission maxima for 3.1 mm diameter holes in a square lattice of 5.5 mm pitch for various hole depths.

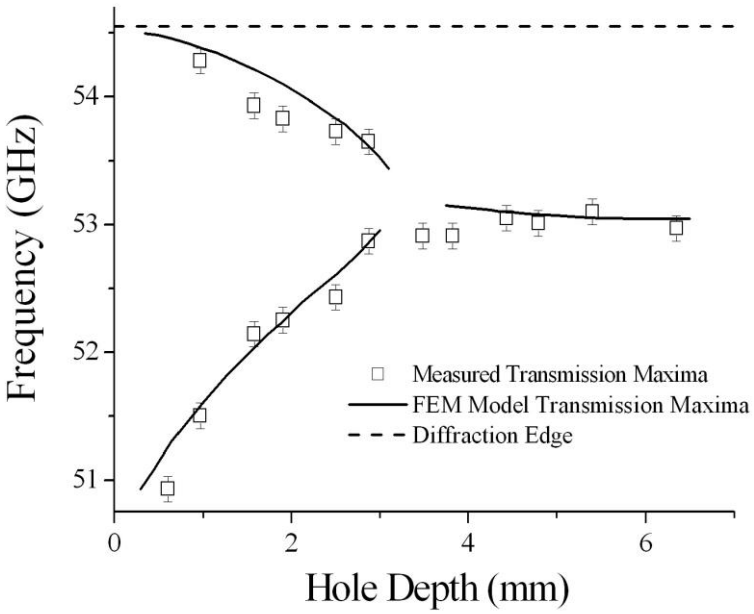

Figure 6.4.15*. Experimental and modelled (FEM) normal incidence transmission maxima for 3.15 mm diameter holes in a square array of 5.5 mm pitch for various hole depths. Error bars represent the approximate error in determining the resonant frequency.*

For small hole depths the surface waves excited on the front and back interface of the holes are strongly coupled resulting in the symmetric/anti-symmetric modes being well separated in frequency. As the depth of the holes is increased the coupling between the modes decreases and their resonant frequencies converge with the structure acting as a single interface in the limit of infinitely deep holes with only one mode supported. The anti-symmetric mode position appears too low in frequency relative to the model, this is due to the effect of beam spread and non-planar sample as any non-normal component of the incident wavefront will result in the mode being reduced to a lower frequency. The error bars represent the error in determining the peak positions from the transmission spectra. They are small relative to the scatter in the data and deviation from the model, as the main source of error is sample and experimental uncertainties. In the region where the two modes converge, the position of the modelled transmission maxima are not plotted as the modes cannot be clearly distinguished.

6.4.3 Cavity Modes

As a result of the method of sample fabrication there were inevitably small gaps present in samples that were composed of two or more layers of holes. These gaps form

metallic cavities that allow radiation to diffractively couple into a mode between the two layers leading to extra features being observed in the transmission response. This is evident in *Figure 6.4.16* where four plates have been screwed together to form a sample with thickness close to that of the original single layer sample used for the measurements in *Figure 6.4.5*. A deep feature can be seen in the transmission response at around 54 GHz that is absent in the single layer sample.

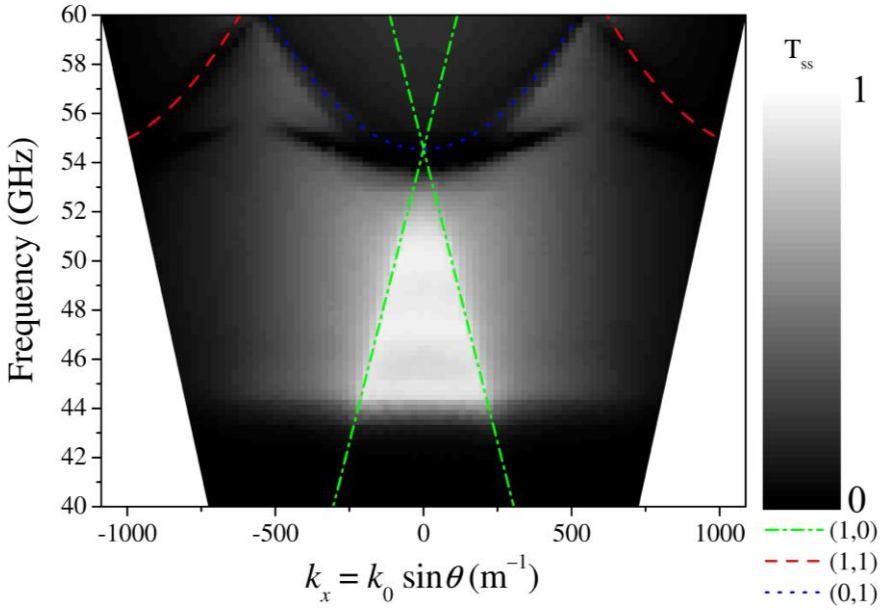

***Figure 6.4.16**. Experimental zero order s-polarised transmission measurements for the 9.58 mm thick square array of 4.05 mm diameter holes composed of 4 separate plates, 5.5 mm pitch, as a function of in-plane momentum, k_x, $\varphi = 0°$. Diffracted light lines illustrated.*

This extra mode appears to be influenced by diffraction following the out-of-plane diffracted light lines ((0,1) and (1,1)). The mode can be seen more clearly by taking a line plot up through the two dimensional dispersion map at a fixed angle of incidence, θ as shown in *Figure 6.4.17*. The transmission response at an angle of 20° has been chosen as at this angle the mode is more clearly distinguishable from the transmission features resulting from diffraction.

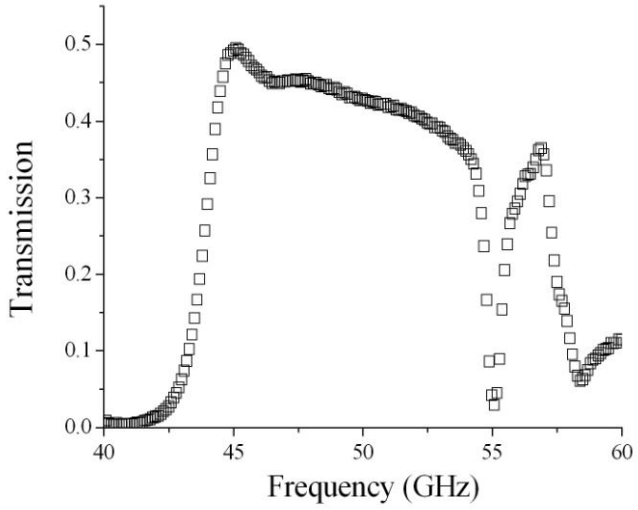

Figure 6.4.17*. Experimental zero order transmission measurements for the 9.58 mm thick square array of 4.05 mm diameter holes composed of 4 separate plates, 5.5 mm pitch,* $\theta = 20°$, $\varphi = 0°$.

The origin of this mode at 55 GHz can be explained with the aid of finite element modelling. Since the gap between the plates will be non-uniform and cannot be measured easily a simple assumption has been used. The model assumes that two 5 mm plates are separated by a small uniform gap. The transmission response is shown in *Figure 6.4.18*, despite the model only being a simple representation of the sample a mode is still clearly observed at close to 55 GHz. The mode appears to shift up in frequency, broaden and become deeper as the gap is increased. As the gap is increased it becomes easier for radiation to couple into the mode leading to the increased coupling strength. For small gaps the resonance has a high Q factor since the electric fields will be compressed into a much smaller volume. The electric fields for this mode for a gap of 0.5 mm are shown in *Figure 6.4.19* and *Figure 6.4.20*.

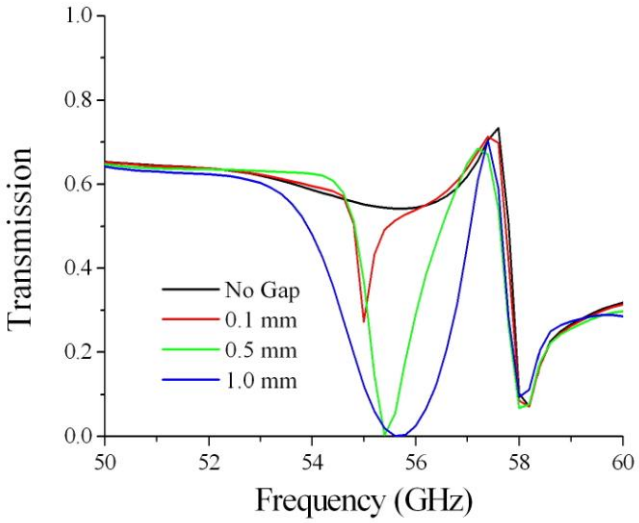

***Figure 6.4.18**. Modelled transmission measurements for two 4 mm diameter, 5 mm depth hole arrays separated by a 0.5 mm air gap, $\theta = 20°$, $\varphi = 0°$ s-polarised incident radiation.*

The electric field distribution in *Figure 6.4.19* shows that there is clear interaction between the two hole arrays in the form of strong vertical electric fields between the metal regions of the arrays. These electric fields reverse across the metal region between neighbouring holes (at the edges of the unit cell in *Figure 6.4.19*) forming a standing wave oscillation.

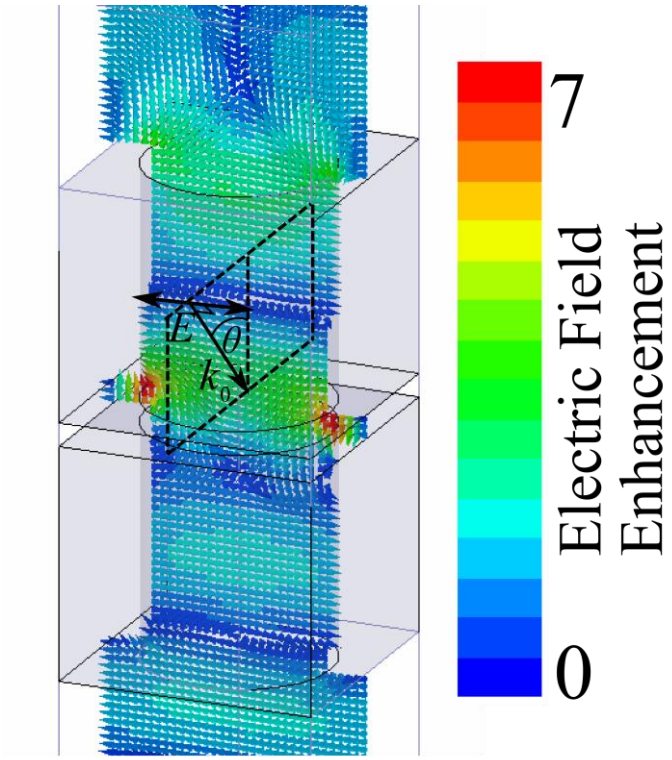

***Figure 6.4.19**. Instantaneous scattered electric field magnitude and direction predictions plotted at a phase corresponding to maximum local field enhancement through the centre of two 4 mm diameter, 5 mm depth hole arrays separated by a 0.5 mm air gap, $\theta = 20°$, $\varphi = 0°$ s polarised incident radiation.*

Fields in the gap between the arrays, viewed from above can be seen in *Figure 6.4.20*.

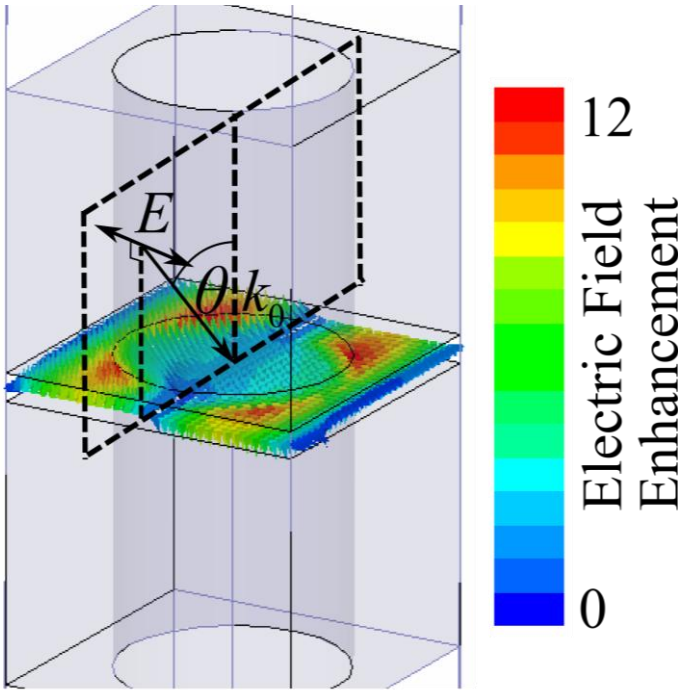

Figure 6.4.20*. Instantaneous scattered electric field magnitude and direction predictions plotted at a phase corresponding to maximum local field enhancement through the middle of the gap between two 4 mm diameter, 5 mm depth hole arrays separated by a 0.5 mm air gap,* $\theta = 20°$ *,* $\varphi = 0°$ *s polarised incident radiation.*

Since the fields of this mode are concentrated in the region around the hole and are quantised across the unit cell of the array its position in frequency is largely determined by the pitch of the array.

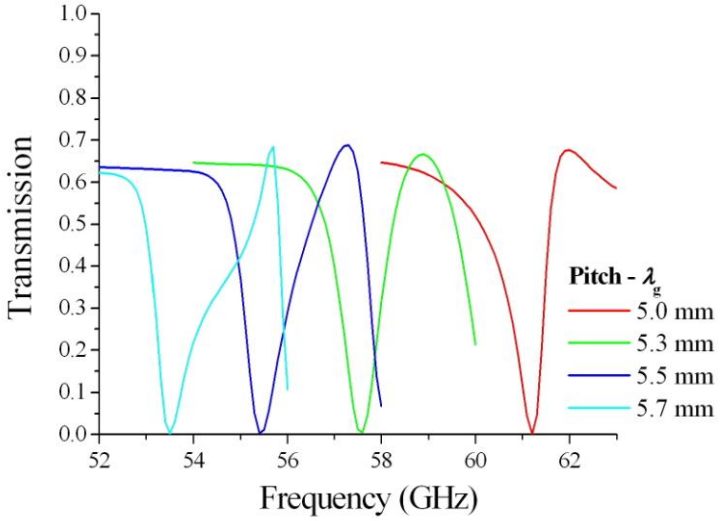

Figure 6.4.21. *Transmission through two 4 mm diameter, 5 mm depth aluminium hole arrays separated by a 0.5 mm air gap,* $\theta = 20°$, $\varphi = 0°$ *s polarised incident radiation, various array periodicities.*

Figure 6.4.21 shows the effect of changing the pitch of the hole arrays on the mode supported within the gap. The mode position is very sensitive to the pitch due to the standing wave nature of the mode across the unit cell.

Extra features are also observed in the p-polarised transmission response with the presence of a gap between two plates. The experimental transmission response for p-polarised incident radiation on the stack of four metal plates is shown in *Figure 6.4.22*. Differences in the transmission response are also observed for this incident polarisation. The mode discussed previously is present but has a different dispersive character. At normal incidence $(k_x = 0)$ the responses for p and s polarisation are identical due to the rotational symmetry of the sample. At finite angles of incidence the coupling to the mode weakens for p-polarised incident radiation as the in-plane component of the electric field required to excite the mode is angle-dependent, this leads to very weak coupling at large angles. Another cavity mode is present in the p-polarised response at lower frequencies within the band of high transmission. A narrow dark band can be seen to appear at non-zero values of k_x at ~ 46 GHz. This feature appears to become more prominent at larger angles of incidence.

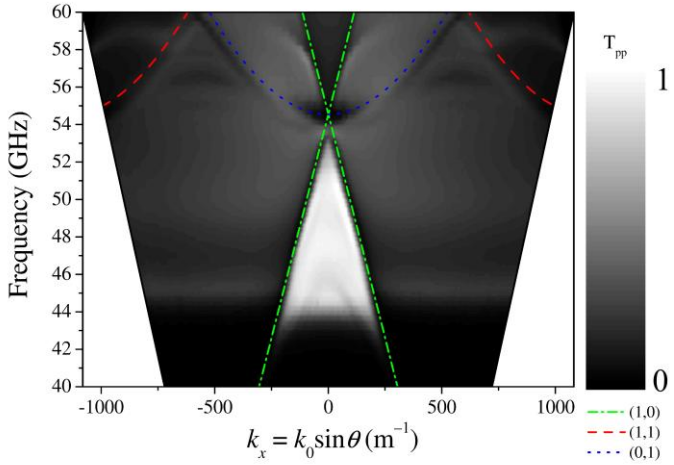

Figure 6.4.22*. Experimental zero order p-polarised transmission measurements for the 9.58 mm thick square array of 4.05 mm diameter holes composed of 4 separate plates, 5.5 mm pitch, as a function of in-plane momentum, k_x, $\varphi = 0°$. Diffracted light lines illustrated.*

Modelling for two 5 mm deep hole arrays separated by an air gap of 0.5 mm for various angles of p-polarised incident radiation is shown in *Figure 6.4.23*.

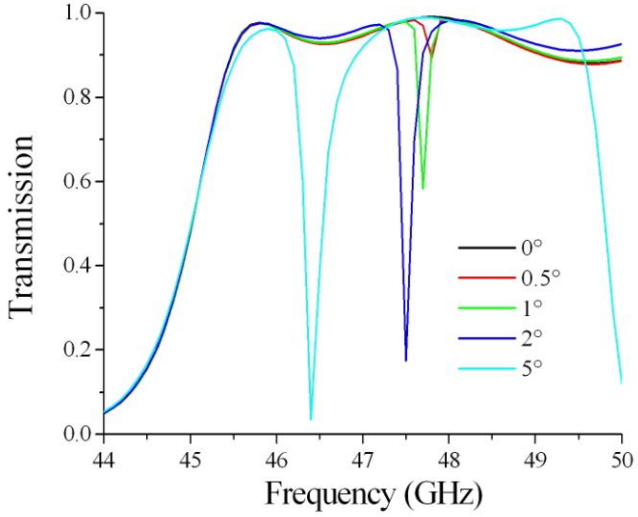

Figure 6.4.23*. Modelled transmission response for two 4 mm diameter, 5 mm depth hole arrays separated by a 0.5 mm air gap, various angles of incidence, p-polarised incident radiation.*

A mode is excited at non-zero angles of incidence with the coupling to this mode increasing as the angle is increased. The mode position falls in frequency as the angle is

increased, appearing to follow the in-plane diffracted light line. The origin of this mode can be understood by examining the modelled electric fields (*Figure 6.4.24*).

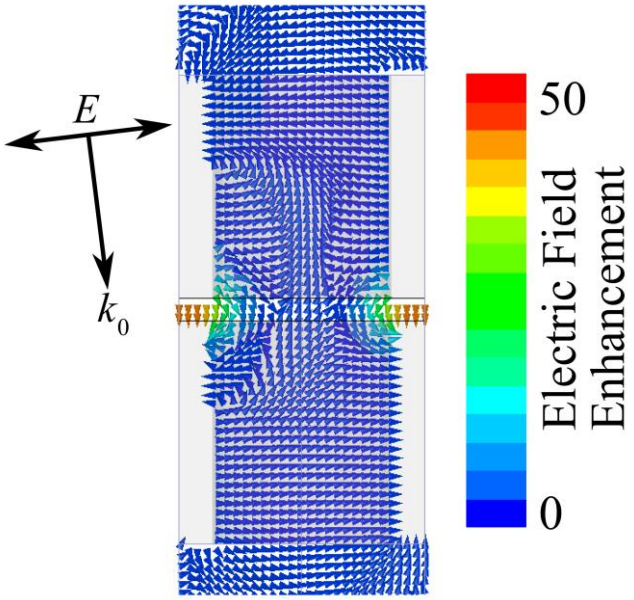

***Figure 6.4.24**. Modelled electric field predictions for two 4 mm diameter, 5 mm depth hole arrays separated by a 0.5 mm air gap, θ=5°, p-polarised incident radiation. Fields plotted through the centre of the hole in the plane of polarisation.*

The fields of this mode are also concentrated in the region between the two hole arrays but the fields in the plane of incidence are in phase across the metal region. This means that this mode cannot be coupled to at normal incidence as a phase difference in the incident electric field across the hole array is needed to set up this charge distribution. As the angle of incidence is increased the phase difference across the unit cell is increased therefore increasing the coupling to this mode. Since there is no reversal of the field across the metal region the mode is almost D.C. in character. This can be further observed from viewing the fields in the plane of the sample (*Figure 6.4.25*).

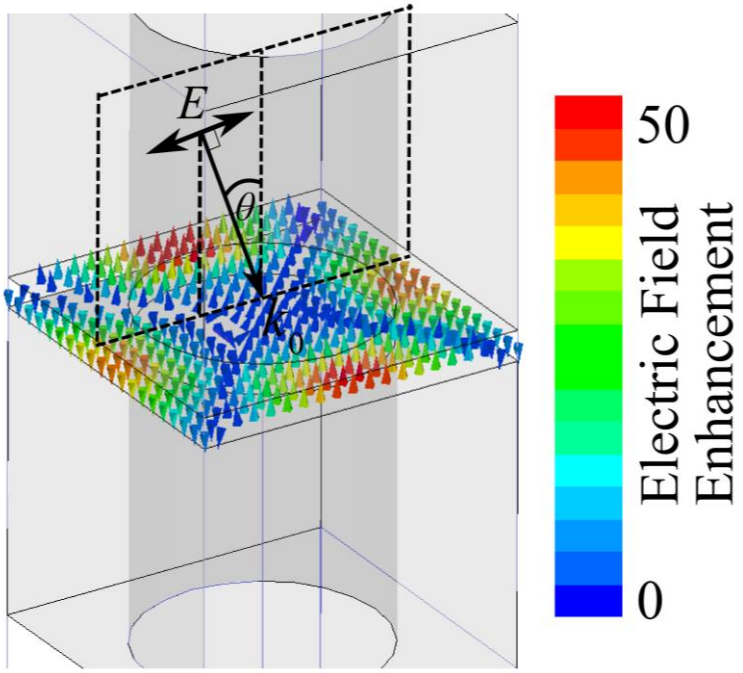

***Figure 6.4.25**. Modelled electric field predictions for two 4 mm diameter, 5 mm depth hole arrays separated by a 0.5 mm air gap, θ=5°, p-polarised incident radiation. Fields plotted through the centre of the gap in the plane of the array.*

The effect of changing the gap size on the transmission response is shown in *Figure 6.4.26.*

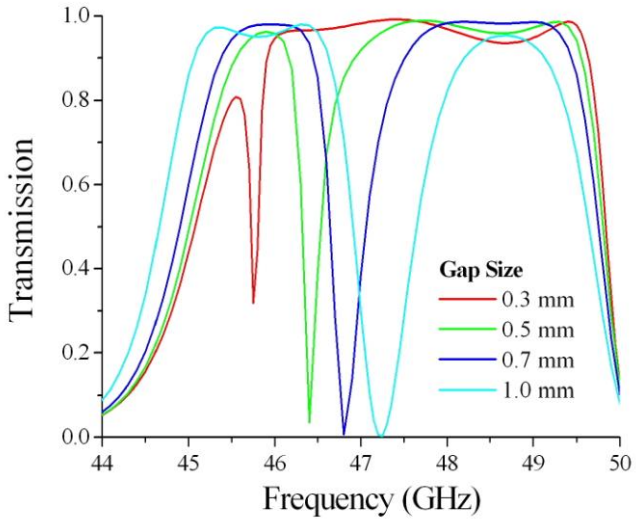

***Figure 6.4.26**. Modelled transmission response for two 4 mm diameter, 5 mm depth hole arrays separated by various air gaps, $\theta = 5°$, p-polarised incident radiation.*

The mode width, depth and position are, as previously seen for the higher frequency mode dependent on the gap size. The position of the mode falls in frequency at an increasing rate as the gap size is reduced as shown in *Figure 6.4.27*.

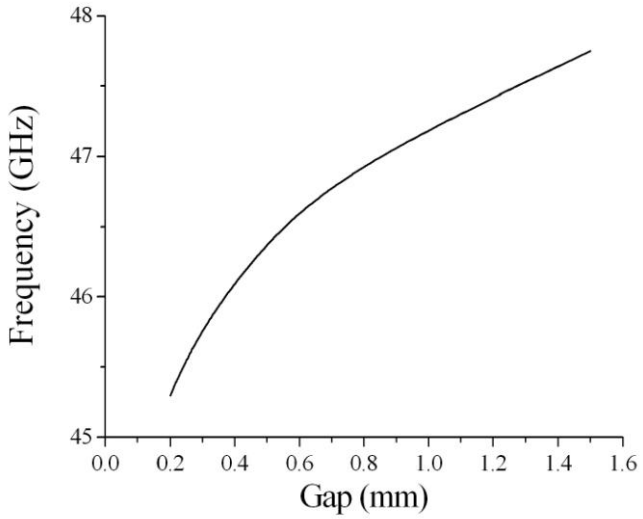

***Figure 6.4.27**. Modelled resonant frequencies of the lowest order cavity mode as a function of gap size.*

This rapid fall in resonant frequency is due to the D.C. character of the fields, since as the gap closes the fields will appear to become more uniform. The resonant frequency will therefore tend to zero as the gap tends towards zero.

6.5 Summary

In summary, a transmission study of metallic hole arrays of large holes with the cut-off below diffraction, and small holes where the cut-off lies above the onset of diffraction has been presented. The large holes support a series of modes, if the depth of the holes is sufficient to support a longitudinally quantised field solution. The two lowest order modes have evanescent field character whereas the fields of the higher order modes are propagating much like those of a Fabry Perot cavity. The small holes however can only support two modes regardless of the depth of the holes. Only evanescent fields are supported resulting in a symmetric/anti-symmetric pair of coupled surface waves. The symmetric mode is the often observed enhanced transmission mechanism and the anti-symmetric mode is the higher Q mode often neglected in these types of study. The

fundamental difference between these two cases is that only the two lowest-order coupled surface waves are asymptotic to the light line whereas the higher order modes start from the light line above the cut-off frequency as they have non evanescent fields within the holes. Cavity modes excited between two metallic hole arrays have also been investigated showing the presence of two modes, a symmetric mode only excited with p-polarised radiation at non-zero angles of incidence and a higher frequency anti-symmetric mode.

7 Enhanced microwave transmission through a continuous thin metal film

7.1 Introduction

In this chapter the microwave transmission through a thin continuous metal film is considered. At microwave frequencies metals have a high conductivity, hence a large complex refractive index and therefore are often considered as nearly perfectly conducting. This results in a large impedance mismatch being present across a dielectric/metal interface[159]. This large impedance mismatch leads to metals being highly reflective and very poor transmitters. A thin metal film of only 60 nm thickness $\sim 10^{-6}\lambda$ transmits $< 0.1\%$ of all incident microwave radiation when modelled using the Fourier Modal Method[93] and representing the metal layer by the approximate Drude parameters for a metal at microwave frequencies ($\varepsilon = -10^4 + 10^7 i$).

Transmission enhancement has been observed through metal structures perforated with sub-wavelength holes in previous chapters of this thesis and in many studies within the scientific community[12,14,73,143]. In this study however the metal film is continuous with no perforations or corrugation. The transmission enhancement is achieved experimentally with the use of a resonant cavity. The cavity is composed of two arrays of metallic slits separated by a dielectric. A similar structure has been studied previously by Hibbins et al.[18] and shown to support a series of standing wave resonances in the plane of the structure resulting in a series of transmission maxima. The placement of a metallic layer in the centre of the cavity can be thought of as being analogous to the inclusion of a tunnel barrier in a quantum mechanical system[160]. On resonance the whole structure is impedance matched allowing the electric and magnetic fields to penetrate inside the metal film. The structure is symmetric with a cavity either side of the metal film, on resonance coupling between these cavities allows power to be transferred across the layer therefore enabling transmission on resonance of ~ 35%.

7.2 Background

7.2.1 Resonant Slit

A metallic slit can support standing wave transverse electric magnetic (TEM) waveguide modes[60,133] (*Figure 7.2.1a*) similar to those supported by a Fabry-Perot etalon[161] (*Figure 7.2.1b*) with field quantisation along the length of the cavity. The standing wave electric and magnetic field solutions are however exchanged such that the electric field is a maximum at the cavity entrance and exit and the magnetic field is zero.

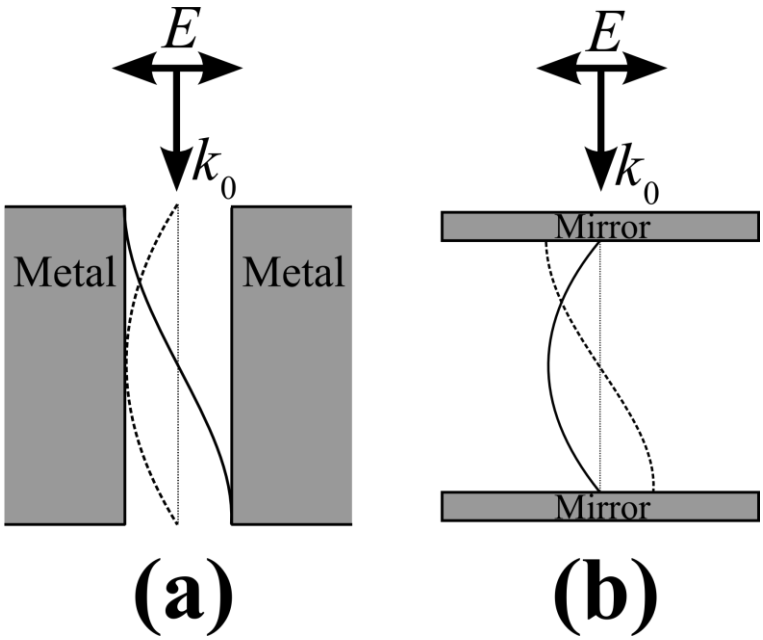

Figure 7.2.1. *Schematic illustration of the electric (solid line) and magnetic (dashed line) field solutions on resonance for the fundamental mode supported within* ***(a)*** *Metallic slit,* ***(b)*** *Fabry-Perot etalon*

The resonant frequencies can be approximated by *Equation 7.2.1*, the typical half wavelength quantisation condition for a Fabry-Perot resonator.

$$f \sim \frac{Nc}{2nl} \qquad \textit{Equation 7.2.1}$$

Where N is the mode number, c is the speed of light, n is the refractive index of the slit medium and l the length of the slit. Typically the resonant frequency is lower than this approximation since a finite distance is required for the fields in the cavity to match the fields in free space beyond the length occupied by the slits[162,163]. This resonant mode

can also be considered to be a coupled surface mode. Diffraction at the slit opening allows excitation of a surface wave on each of the metal/air interfaces inside the slit; these waves can then couple together across the air gap. Since it is a coupled surface mode, when the slit width, *w*, is very small a correction to the resonant frequency also has to be considered due to the finite conductivity of the metal[163], resulting in a lower resonant frequency.

7.2.2 Resonant Groove

A slit that is shorted at one end (i.e. a groove in a metal substrate) can similarly support a TEM mode. On resonance, since the electric field must be zero at the closed end, the short circuit is transformed by the length of the groove into an open circuit at the top. The top surface therefore has large impedance as seen previously in chapter 2 and hence the propagation of surface waves is prohibited. The resonant frequency can be approximated by *Equation 7.2.2*, a quarter wavelength quantisation condition.

$$f \sim \frac{Nc}{4nl} \qquad \textit{Equation 7.2.2}$$

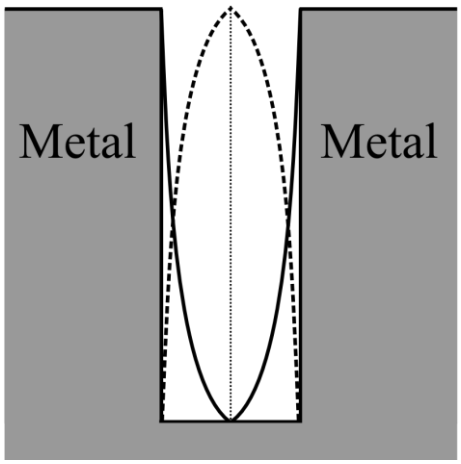

***Figure 7.2.2**. Schematic illustration of the electric (solid line) and magnetic (dashed line) field solutions on resonance for the fundamental mode supported within a groove in a metallic substrate.*

When filled with a lossy dielectric these resonant grooves can be used as effective absorbers, however their thickness requirement of λ/4 of the wavelength to be absorbed means they can be very impractical. For radar frequencies this could mean a thickness

of several centimetres which adds a substantial amount of weight to the object being shielded. One alternative is to fill the grooves with a high refractive index medium effectively making them appear longer to the incident radiation. The other option is to introduce a bend in the groove, shown in *Figure 7.2.3*.

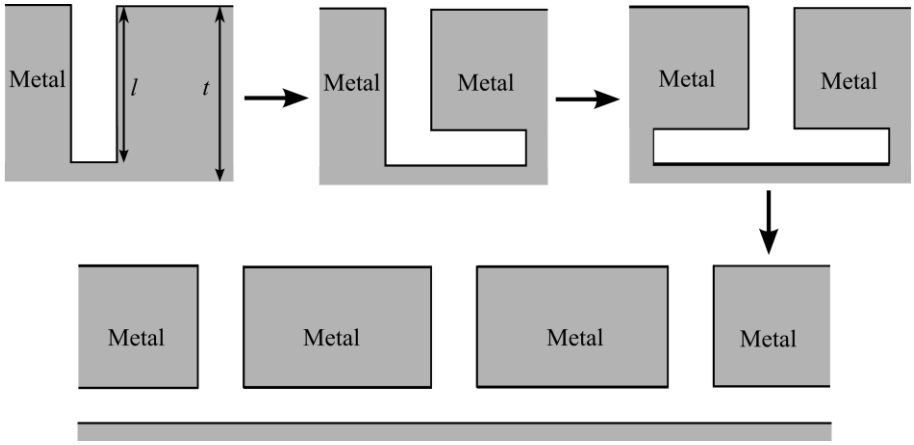

Figure 7.2.3*. Introduction of 90° bends in a groove and joining them to form a continuous cavity.*

Figure 7.2.3 shows how the introduction of a 90 degree bend in a groove to form an 'L' shape can be used to increase the groove length, *l* without increasing the thickness, *t*. Introducing a second 90 degree bend to form an inverted 'T' gives a symmetric structure with identical boundary conditions at each end. Since the electric field is zero at the ends of the grooves they can be joined together to form a periodic structure with the grooves united forming a cavity common to all unit cells of the structure. This structure design allows easier fabrication as a double sided printed circuit board (PCB) can be etched in a single process. This idea was utilised and its absorbing properties experimentally investigated by Hibbins et al.[18]

The standing waves supported on resonance are now in the plane of the structure with the fundamental having half a wavelength fitted across one period (*Figure 7.2.4*).

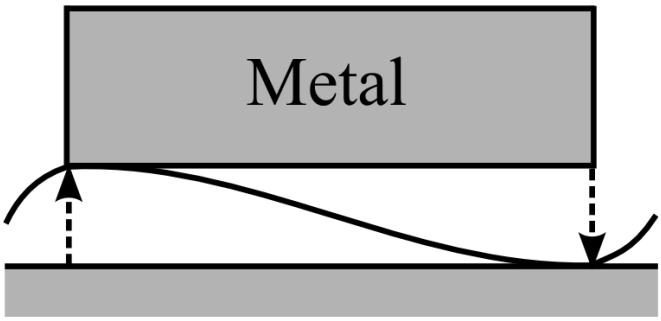

***Figure 7.2.4**. Schematic illustration of the electric field solutions on resonance for the fundamental mode supported within the thin connected groove structure.*

The electric fields are reversed across the small slit width, this phase compression phenomenon leading to the title of the paper by Hibbins et al. 'Squeezing millimetre waves into microns'[18]. There will be an infinite series of these modes approximately equally spaced in frequency; however the even harmonics require the phase of the electric field at neighbouring slits to be reversed (*Figure 7.2.5*). These modes therefore cannot be excited with radiation incident normal to the array ($\theta = 0°$) or with s-polarised radiation as a phase delay is required in the incident wave front.

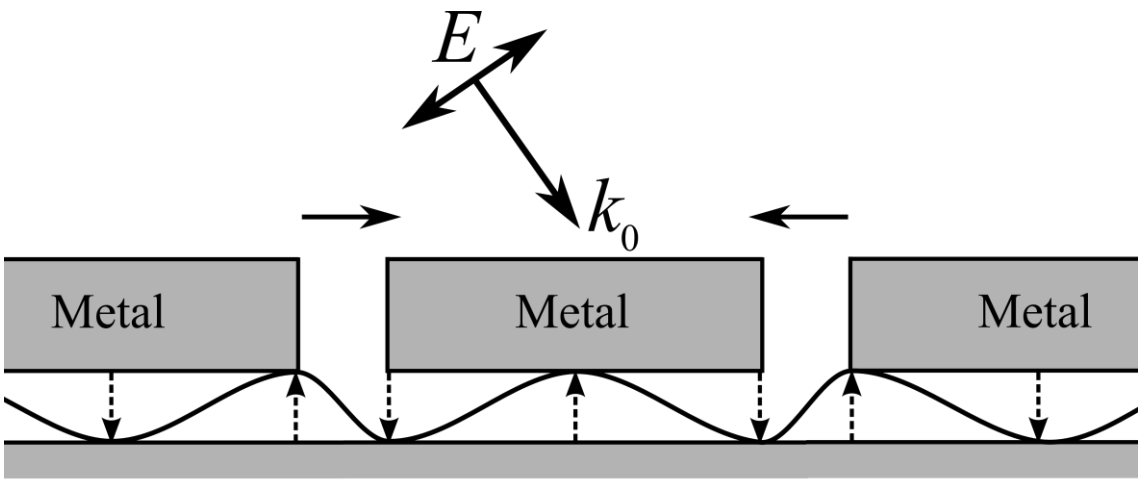

***Figure 7.2.5**. Schematic illustration of the electric field solutions on resonance for the second order mode supported within the thin connected groove structure.*

7.2.3 Transmission Structure

The structure of connected grooves discussed in the previous section was also studied as a transmission structure by Hibbins et al. This structure supports similar modes but this

time allowing selective transmission at the resonant frequencies. *Figure 7.2.6* shows the fields for the fundamental mode.

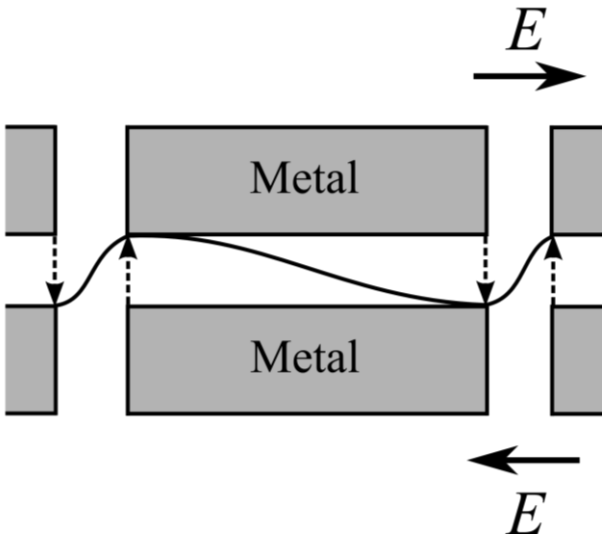

***Figure 7.2.6**. Schematic illustration of the electric field solutions on resonance for the fundamental mode supported within the connected groove transmission structure.*

The modes supported within the transmission structure are similar in character to those supported within the absorption structure in that half a wavelength is supported across the pitch of the structure with a π - radian phase change across the slit width.

7.2.4 Impedance Matching Model of the Resonant Cavity

Impedance matching (or tuning) is an important concept in microwave engineering and is commonly discussed in textbooks[125]. Consider the system in *Figure 7.2.7*.

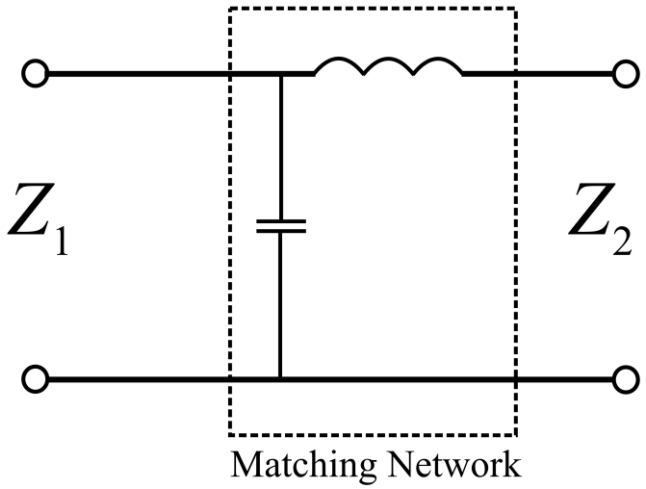

Figure 7.2.7*. Schematic illustration of a transmission line with source impedance* Z_1*, load impedance* Z_2 *and a matching network.*

A matching network is placed between a load impedance and a transmission line and is designed such that the impedance seen from the transmission line is Z_1, therefore eliminating any reflections. These matching networks are important in microwave engineering since they allow maximum power transfer to the load providing an improved signal to noise ratio for applications such as amplifiers and antennas.

In optical systems impedance mismatches are often discussed in terms of refractive index matching and reflection losses can be calculated using the Fresnel equation, (*Equation 7.2.3*)

$$r = \frac{Z_2 - Z_1}{Z_1 + Z_2} = \frac{n_1 - n_2}{n_2 + n_1}, \qquad \textit{Equation 7.2.3}$$

here Z_i and n_i are the impedance and refractive index of medium *i.*

One practical implementation of impedance matching in optical systems is the use of anti-reflection coatings[164,165]. A thin layer of dielectric with refractive index between that of the surface being coated and the incident medium is applied, thus reducing the impedance mismatch and therefore the reflection coefficient. Interference is also used in these systems, with the anti-reflection coating typically being λ/4 thick so that destructive interference occurs between reflections from the back and front face, further reducing the reflection coefficient.

In the resonant cavity studied, the matching network is the resonant cavity as this provides the means to match the impedance of free space to that of the metal film, therefore reducing the reflection coefficient and enabling power to be transferred into the film.

7.2.5 Tunnelling

Waves and particles are known to be able to penetrate classically impenetrable potential barriers through the process of quantum tunnelling[166]. This process is also commonly utilised in optics through the method of frustrated total internal reflection (F-TIR)[167,168]. If two prisms are placed within a few wavelengths of one another transmission is possible even beyond the critical angle due to evanescent wave tunnelling. The experimental study in this chapter investigates the effect of introducing a tunnel barrier in the form of a metallic film into a resonant transmitting structure. Since metals have a large complex refractive index at microwave frequencies only evanescent waves will be supported in the metal film. Metal films however are not ideal tunnel barriers since the finite real part of their refractive index makes them absorbing. Transmission through classically opaque metallic films has been experimentally demonstrated previously at optical frequencies through the excitation of coupled surface modes on each side of the film[169]. This has been further extended to metal-dielectric metamaterial stacks by Tomita et al[170]. Tunnelling of microwave radiation through an effective negative permittivity (sub-wavelength metal mesh) slab clad with two high refractive index slabs has also been experimentally demonstrated by Zhou et al.[171] The observed transmission in this case was determined to be mediated by high magnetic fields at the interfaces. The experiment in this thesis chapter differs from previous studies as the transmission through a negative permittivity slab in the form of a continuous metal film is measured.

7.2.6 Power Absorbed by a Good Conductor

When considering the transmission through a good conductor it is useful to know how much power is absorbed. This can be calculated from the fields at the surface. Consider the system in *Figure 7.2.8*, an interface between a lossless medium and a good conductor.

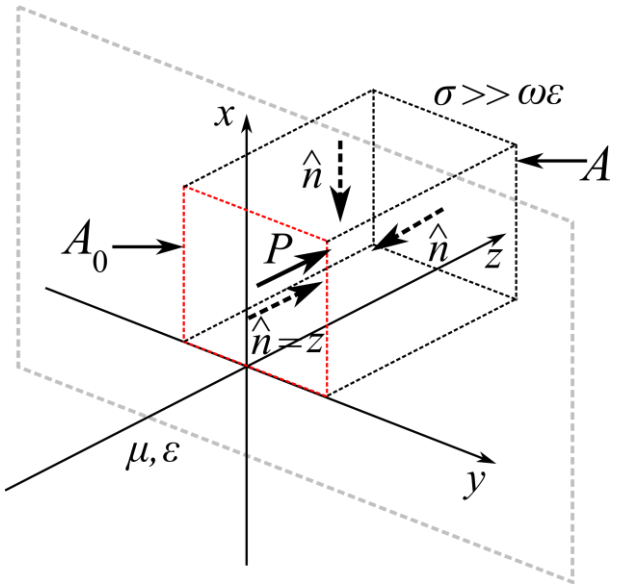

***Figure 7.2.8**. Interface between a lossless medium and a good conductor represented by grey rectangle on the $z = 0$ plane. Red and black dashed lines represent the closed surface used for calculation of power dissipated into the conductor.*

The fields are incident from $z < 0$, with the interface between the incident medium and the conductor lying on the $z = 0$ plane. The average power transferred across the interface, P_{av} into the region defined by the cross-sectional surface A_0 at the interface and A is given by *Equation 7.2.4*,

$$P_{av} = \frac{1}{2}\mathrm{Re}\int_{A_0+A} \overline{E} \times \overline{H}^{*} \cdot \hat{n} dA, \qquad \textit{Equation 7.2.4}$$

here $\hat{n}$ is the unit vector normal to the surface $A_0 + A$ and $\overline{E}$ and $\overline{H}$ are the fields at this surface. By careful selection of the surface A, its contribution to the average power transfer can be made to be negligible. If the incident wave is normal to the surface the Poynting vector will be parallel to the z axis leaving the contributions from the surface parallel to the z axis to be zero. If the right hand side of A is defined such that it is far from the interface A_0 and the decay of the fields is fast then this contribution will also be negligible, therefore simplifying *Equation 7.2.4* to *Equation 7.2.5* one has,

$$P_{av} = \frac{1}{2}\mathrm{Re}\int_{A_0} \overline{E} \times \overline{H}^{*} \cdot \hat{z} dA. \qquad \textit{Equation 7.2.5}$$

Using the following vector identity:

$$\hat{z}\cdot\left(\overline{E}\times\overline{H}^{*}\right)=\left(\hat{z}\times\overline{E}\right)\cdot\overline{H}^{*}=\eta\overline{H}\cdot\overline{H}^{*}, \qquad \textit{Equation 7.2.6}$$

since $\overline{H}=\overline{E}/\eta$, where η is the impedance of the conductor, this simplifies the average power transfer to *Equation 7.2.7*.

$$P_{av}=\frac{R_s}{2}\int_{A_0}\left|\overline{H}\right|^2 dA, \qquad \textit{Equation 7.2.7}$$

here R_s is the surface resistivity of the conductor.

$$R_s=\mathrm{Re}(\eta)=\mathrm{Re}\left[(1+i)\sqrt{\frac{\omega\mu}{2\sigma}}\right]=\sqrt{\frac{\omega\mu}{2\sigma}}=\frac{1}{\sigma\delta_s} \qquad \textit{Equation 7.2.8}$$

The average power transferred into the conductor is therefore directly related to the magnitude of the *H* fields. Transmission will be enhanced through a metal film therefore if large *H* fields are present, this can be achieved through the use of a resonant system.

7.3 Experimental

The sample under study consists of two gratings comprised of strips of copper 3.68 mm wide with a pitch, λ_g = 3.8 mm and 17.5 μm thickness. Between the gratings is a 75 μm Mylar® layer with a 60 nm aluminium film coated on one side. On the other side of the aluminium film is another 75 μm dielectric layer forming a symmetrical cavity. *Figure 7.3.1* shows a schematic of a section of the resonant cavity.

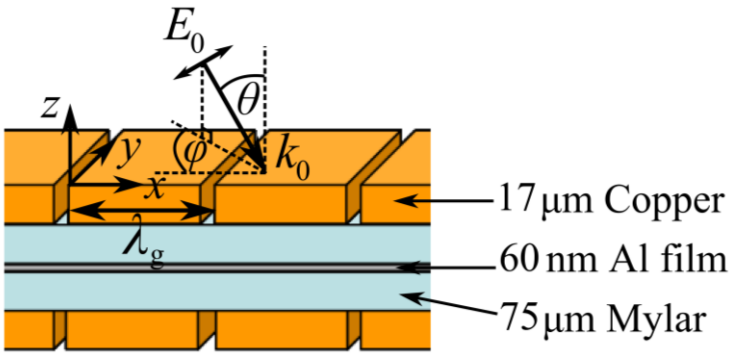

Figure 7.3.1. *Cross-section through the resonant cavity, illustrating the plane of incidence, coordinate system, polar angle, θ, azimuth angle, φ, pitch, λ_g and the thickness of the layers.*

In order to construct the sample for this experiment the gratings were fabricated by standard PCB etching techniques[172]. The boards used were 0.8 mm thickness FR4 with a 17.5 μm thickness coating of copper. The FR4 and copper gratings were arranged so that the FR4 was the outermost layer, this meant that there was only one dielectric layer between the grating and thin metal film, reducing the complexity of the analysis of the system. The whole sample was sandwiched together between two sheets of 7.44 mm thick Perspex and fastened with six nylon screws. This was required to ensure that the whole sample remains flat and reduces the chances of air gaps as the response is very sensitive to changes in thickness. The sample size was kept to 165 mm × 255 mm as keeping a consistent flat sample over a larger area was found to be very difficult.

Initially a large (~ 580 mm × 480 mm) sample mounted in a wooden frame without Perspex cladding was used to maximise the amount of measurable signal and minimise angle spread in the beam resulting from diffraction off the edges of the sample. This however proved to be infeasible as there was not enough tension from the frame to compress the layers in the central region of the sample resulting in air gaps and weak coupling to the modes. Another method was tried in which the sample area was reduced to a much smaller (~ 150 mm × 100 mm) area to improve the amount of tension in the central region, this improved the coupling to the modes however air gaps were still present and resulted in lowered transmission and a shift in the peak transmission to higher frequencies. Finally it was decided that the best way to reduce the air gaps was to clad the sample in Perspex to ensure that all unwanted air was evacuated, this was

still not perfect but was found to be the best solution without resorting to the use of a vacuum pump to evacuate the sample.

7.4 Results and Discussion

7.4.1 Transmission through a Continuous Metal Film

Since metals at microwave frequencies are nearly perfectly conducting and have a very large complex refractive index, transmission through the isolated thin metal film is expected to be near zero. *Figure 7.4.1* shows modelled normal incidence transmission through a 60 nm layer of aluminium described using the Drude model $\left(\varepsilon(\mathrm{Al}) = -10^4 + 10^7 i\right)$. The transmission was calculated using the Fourier Modal Method (chapter 3) and setting the layer to be continuous (no modulation of the surface profile). The transmission measured was < 0.05 % as expected and would be below the noise floor of the experimental apparatus.

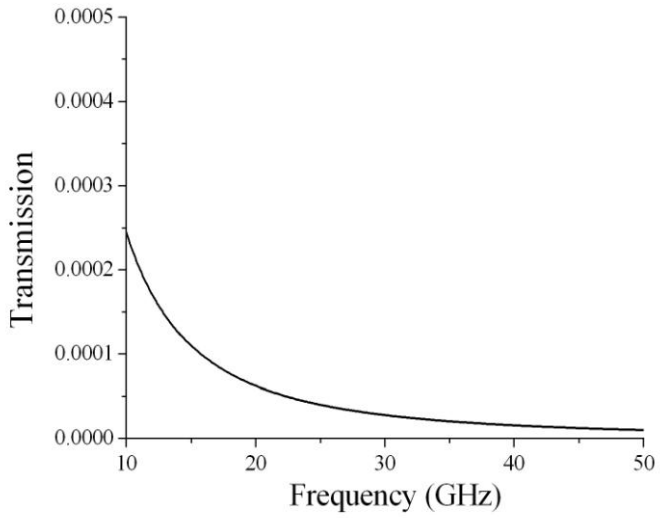

Figure 7.4.1. *Modelled normal incidence transmission for a 60 nm layer of aluminium.*

7.4.2 Transmission through a Continuous Metal Film in a Resonant Cavity

Normal incidence transmission measurements for the fundamental mode are shown in *Figure 7.4.2*. Modelled results with measured material and geometrical parameters are also shown for comparison.

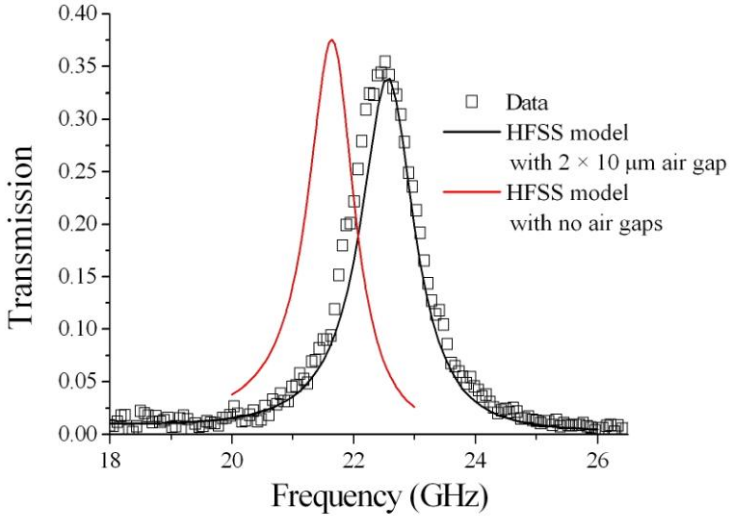

Figure 7.4.2. *Normal incidence transmission measurements and modelling for the fundamental mode,* $\varphi = 0°$.

Transmission of ~ 35 % is achieved through the resonant cavity; this is a significant enhancement over the transmission through the stand alone thin metal film (< 0.1%). The finite element modelled results in *Figure 7.4.2* uses geometrical values that have been checked with a travelling microscope or Vernier callipers. A Scanning Electron Microscope (SEM) with Focused Ion Beam (FIB) was used by a colleague to mill a trench into the metal film, allowing the thickness to be measured (*Figure 7.4.3*). This image also shows that the surface of the film is rough with pits and holes and is therefore not a perfect planar film but it does not however contain holes of any significant size.

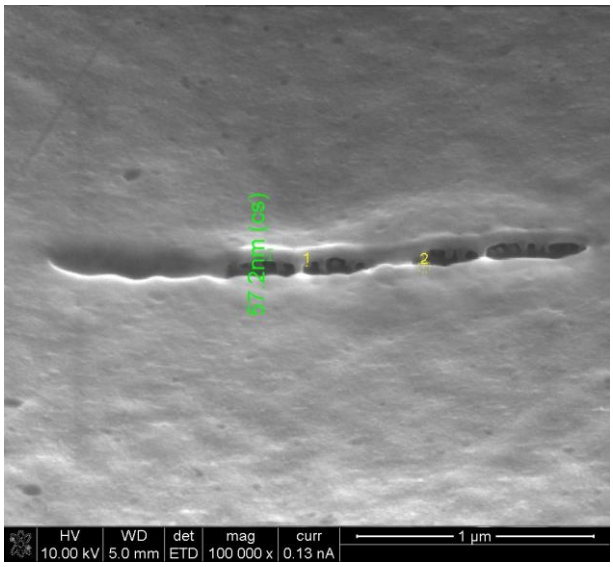

***Figure 7.4.3**. SEM image of the surface of a small section of aluminised Mylar. A trench has been milled allowing the cross-section to be visible showing the metal thickness to be ~ 60 nm.*

Material parameters for the various dielectrics in the system were determined by performing separate independent experiments, the results of which were fitted to finite element modelling. Transmission through one of the Perspex layers was measured on its own and the Fabry Perot modes recorded were fitted to modelling, this gave a value for the permittivity of $\varepsilon(\text{perspex}) = 2.6 + 0.015i$. The Mylar was cut into strips and placed between two metallic plates, creating a slit such as that shown in *Figure 7.2.1*. The resonant frequency of the Fabry Perot modes was then fit with FEM modelling to determine the real component of the permittivity, ε_r. The size of the incident beam and the boundaries of the finite-sized sample could not be replicated precisely in the modelling therefore normalisation was not identical and the imaginary component of the permittivity, ε_i had to be approximated. The value of ε_i used was the same as polyester due to the similar low-loss nature of the material. Therefore estimating the value of the permittivity of $\varepsilon(\text{Mylar}) = 2.6 + 0.003i$. A section of the FR4 PCB with copper grating patterning was sandwiched between an aluminium plate and a Perspex layer and reflectivity measurements performed. This formed the same type of structure fabricated by Hibbins et al. and discussed in *Section 7.2.2*. The modes were then fitted using FEM modelling to determine a value of $\varepsilon(\text{FR4}) = 4.1 + 0.082i$. The properties of the metal film used were, $\varepsilon(\text{Al film}) = -10^4 + 10^7 i$, i.e. assumed to be the same as a bulk metal at microwave frequencies using the Drude model. The transmission maximum is

slightly asymmetric with the high frequency side of the resonance transmitting less than the low frequency side; this is due to the resonance response being superimposed on the frequency selective behaviour of the gratings. The gratings act as capacitive low-pass filters as discussed in chapter 2. The resonant frequency appears to be higher in the data than in the model, requiring a 10 μm air gap between the interface of the copper grating and the Mylar in order to achieve a good fit. Any air layers in the cavity will reduce the effective refractive index of the cavity therefore making it appear shorter to the incident radiation and thus raising the resonant frequency. This was a particular issue when initially performing this experiment and many different configurations were tried to minimise air gaps.

FEM modelling was used to predict the response of this resonant cavity; however there were initial problems that needed to be overcome due to the large aspect ratio and small thickness of the thin metal film which caused problems with the meshing of the model. These problems are discussed further in chapter 3. Vector electric fields for the fundamental mode are shown in *Figure 7.4.4*.

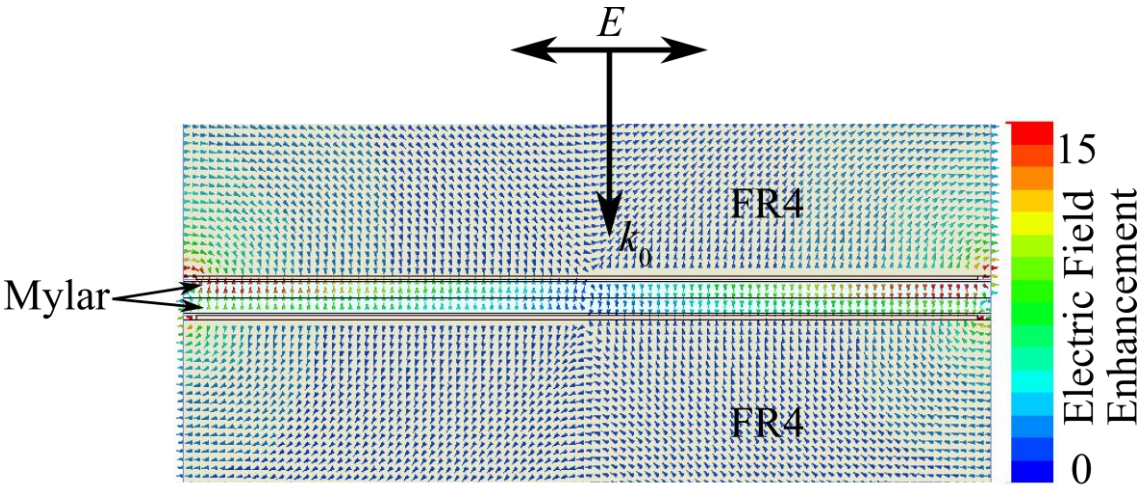

***Figure 7.4.4**. Instantaneous electric vector plotted on resonance of the fundamental mode through a plane running through the centre of a unit cell of the array. Electric fields are plotted at a phase corresponding to maximum field enhancement.*

The largest region of electric field enhancement lies at the slit openings and exits (far left and far right of *Figure 7.4.4*). The electric field is zero in the region under the centre of the metal strip. Since the mode is a standing wave the regions of zero electric

field are also regions of high magnetic, *H* field (*Figure 7.4.5*) since the energy density $\left(\frac{\varepsilon E^2}{2}+\frac{\mu H^2}{2}\right)$ has to remain constant for a standing wave.

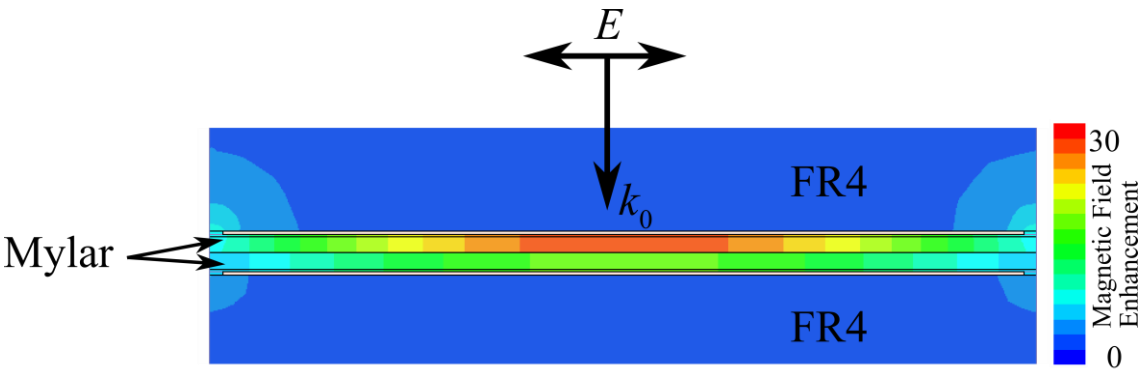

Figure 7.4.5*. Time-averaged magnetic (H) field on resonance of the fundamental mode.*

The *H* fields supported in the cavity on resonance provide the mechanism of power transfer across the metal layer for transmission of the incident fields

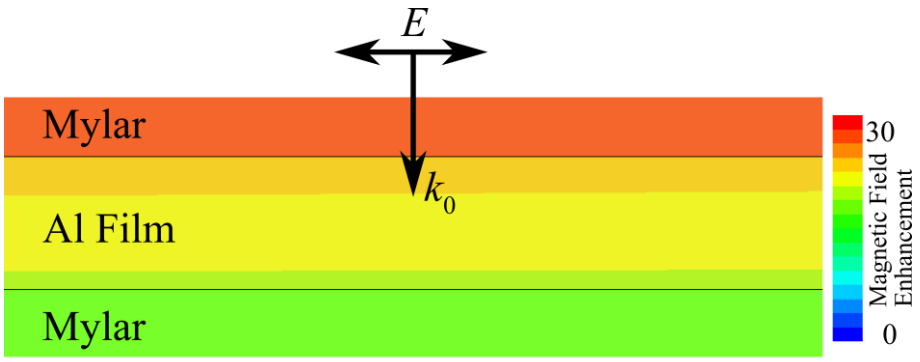

Figure 7.4.6*. Time-averaged H field plotted across a plane containing the incident electric vector and running through the centre of the unit cell. Image scale chosen to allow the metal film to be clearly seen.*

Figure 7.4.6 shows the time-averaged *H* fields on resonance of the fundamental mode of the cavity in the region of the metal film and surrounding dielectric. The magnetic fields decay across the metal film layer into the dielectric region the other side, allowing excitation of the cavity mode both sides of the metal film. These two resonators oscillate in phase coupled together by the evanescent fields in the film. Due to the symmetric nature of the system, radiation is able to couple out efficiently to free space resulting in measurable transmission.

Figure 7.4.7 shows the experimentally measured p-polarised (TM) transmission measurements for φ = 0°. The frequency position and width of the mode remains fairly

constant across the 30° angle that has been swept. This angle-invariant response occurs since the length of the slits in the array appears constant for this plane of incidence therefore not changing the resonant frequency of the system.

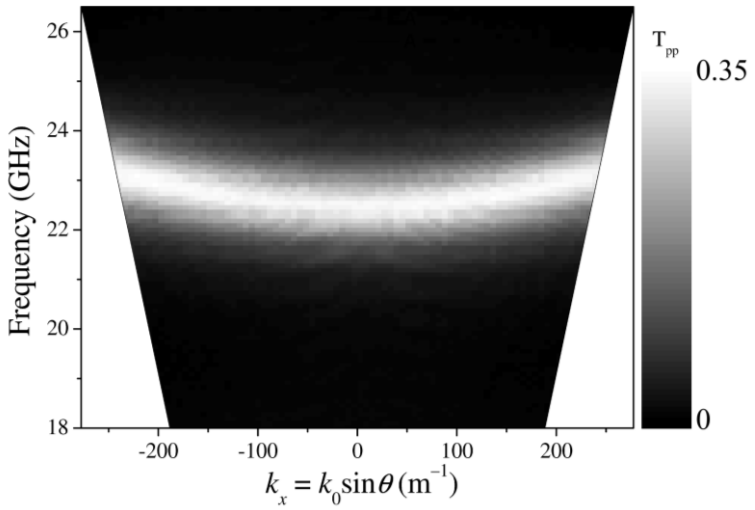

Figure 7.4.7*. Transmission measurements for p-polarised (TM) radiation of the fundamental mode of the resonant cavity, φ=0°.*

The mode rises in frequency slightly at larger angles mainly due to the small phase difference being imparted across the slit opening, affecting the field matching conditions between the fields in the cavity and free space. Also as large angles of incidence are approached the mode will be influenced by the zero order light line, typically resulting in an anti-crossing behaviour whereby the mode will rise in frequency to avoid intersection with the light line. This is illustrated schematically in *Figure 7.4.8*.

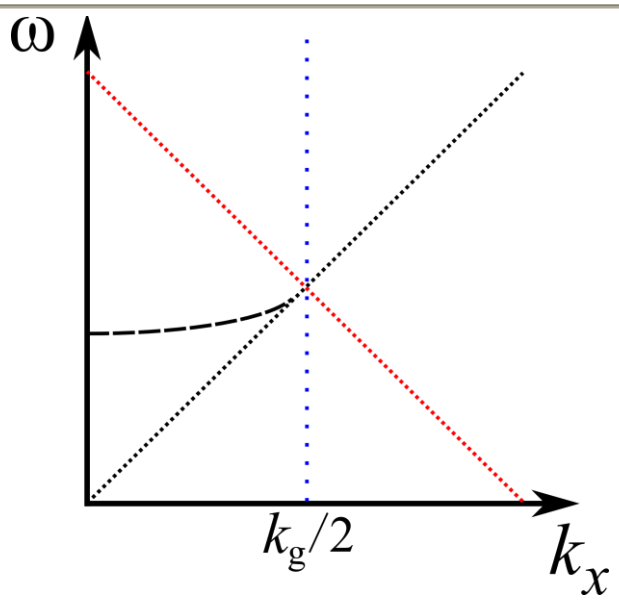

***Figure 7.4.8**. Schematic illustration of the interaction of the fundamental mode with the zero-order light line. Mode illustrated by the dashed black line, black dotted line is the zero order light line, red dotted line is the diffracted light line, blue dotted line is the Brillouin zone boundary.*

Figure 7.4.9 shows the dispersion of the fundamental mode for s-polarised (TE) radiation with the sample mounted such that φ = 90°, i.e. there is always a component of the electric field in the direction of the grating vector.

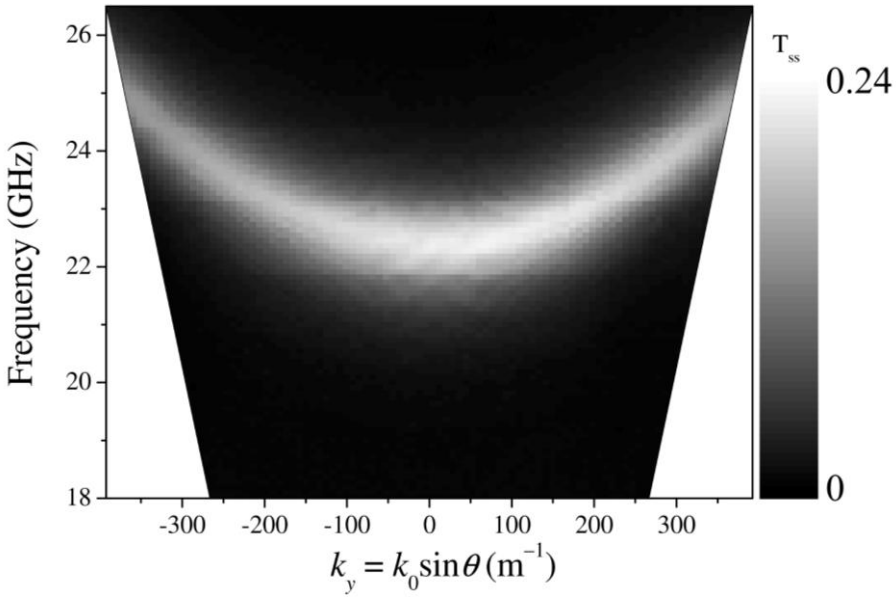

***Figure 7.4.9**. Transmission measurements for s-polarised (TE) radiation of the fundamental mode of the resonant cavity, φ=90°.*

There is a discrepancy between the transmission levels observed at normal incidence ($k_x = k_y = 0$) in *Figure 7.4.7* and *Figure 7.4.9* due to the small size of the sample. At normal incidence the response should be identical however since the sample is small and rectangular in shape there is an error associated with the normalisation that is not consistent between the measurements for $\varphi = 0°$ and $\varphi = 90°$. The edges of the sample scatter signal, this effect cannot be normalised out correctly and is a result of having a finite size sample. The frequency of the mode follows an inverse relationship with the cosine of the incident angle θ. Since $k_0{}^2 = k_x{}^2 + k_y{}^2 + k_z{}^2$, $k_x = 0$ and $k_z = 2\pi/\lambda_z = 2\pi(N/2L)$. Therefore, $f \approx \dfrac{Nc}{2l\cos\theta}$.

The modes which have even harmonic field solutions cannot be coupled to at normal incidence due to the field symmetry. The electric field of the even modes is reversed in phase from one slit to the next therefore requiring a phase variation in the incident wavefront for coupling to occur (*Figure 7.4.10*).

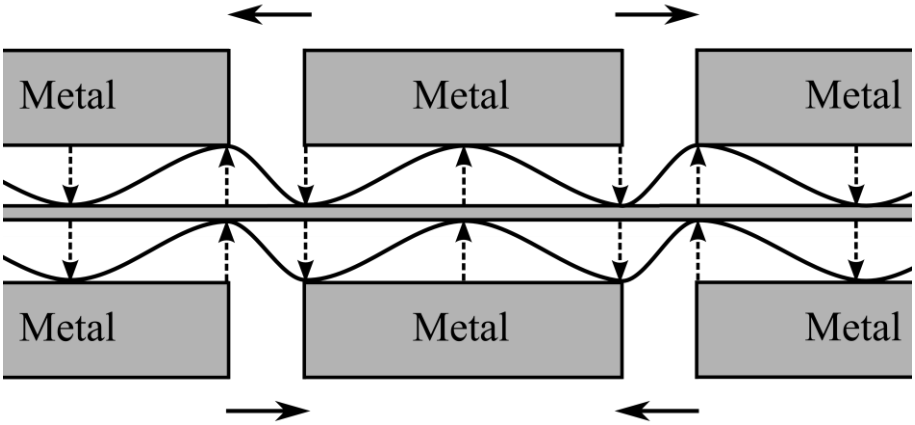

Figure 7.4.10*. Schematic field solution for the 2nd order mode of the resonant cavity.*

Experimental transmission measurements for the $N = 2$ mode at $\theta = 20°, \varphi = 0°$ are shown in *Figure 7.4.11*.

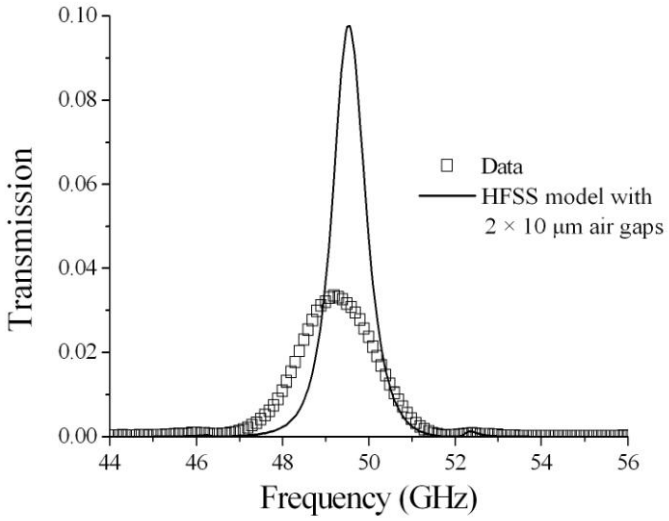

Figure 7.4.11*. Transmission measurements and finite element model for the second order mode for p-polarised (TM) radiation, $\theta = 20°$, $\varphi = 0°$.*

Since the second order mode is reliant on a phase variation in the incident electric field across the slit opening, the mode is very sensitive to the incident angle. This results in a discrepancy between the model and data due to the incident beam in the experiment being not a perfect plane wave. The beam will have some curvature due to scattering from the apertures in the system and from the edges of the sample. This leads to the broadening, reduced intensity and slight frequency shift of the mode observed in *Figure 7.4.11*.

The electric fields from FEM modelling for the $N = 2$ mode are shown in *Figure 7.4.12*.

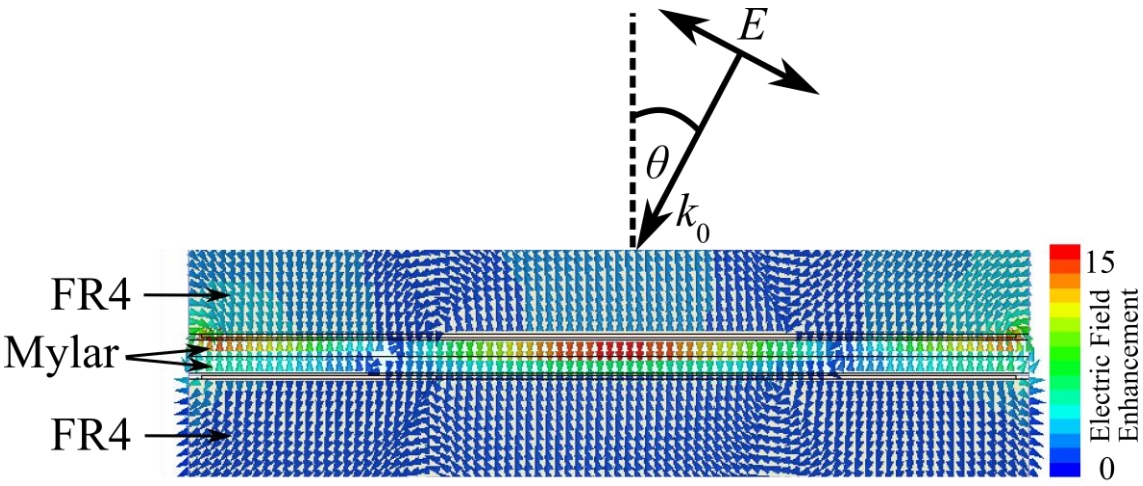

***Figure 7.4.12**. Instantaneous electric field direction and magnitude plotted through the centre of the unit cell. Fields plotted at a phase corresponding to maximum field enhancement on resonance of the second order mode. $\theta = 20°$, $\varphi = 0°$.*

There are two nodes in the electric field under the metal strip indicating that the mode is the second order mode of the cavity. Due to the symmetry of the electric field coupling to this mode is not possible at normal incidence. There are features in the model in *Figure 7.4.11* other than the main peak at 49.5 GHz, such as the small peak at 52.35 GHz, this feature can be seen in the experiment but is weakly coupled to and is a result of having extra layers of dielectric above and below the resonant cavity. These extra features are as a result of the method of fabricating the sample. Due to the thickness of the Perspex and the periodicity of the grating, diffraction inside the dielectric region results in a series of waveguide modes being excited that have their electric field quantised in the direction of the grating vector and orthogonal to the plane of the sample.

Figure 7.4.13 shows transmission measurements as a function of in-plane momentum and frequency for the second and third order modes. Coupling to the second order mode is non – existent at normal incidence ($k_x = 0$) and strengthens as the in-plane momentum and therefore phase shift is increased.

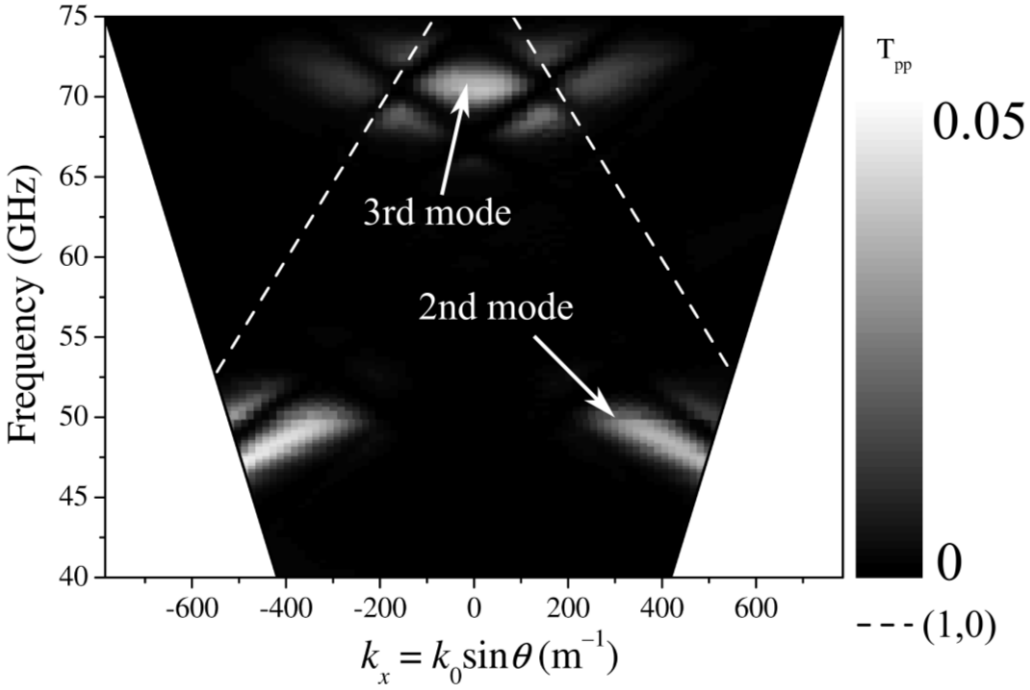

***Figure 7.4.13**. Transmission measurements for p-polarised (TM) radiation showing the second order and third mode of the resonant cavity, $\varphi = 0°$. Diffracted light lines for air are also illustrated.*

Since the structure is only transmitting on resonance of the cavity modes the extra features that are a result of the dielectric layers only appear to be present close to the resonant frequency. If *Figure 7.4.13* however is plotted on a logarithmic scale the extent of these modes is clearer (*Figure 7.4.14*) although the transmission level is very small.

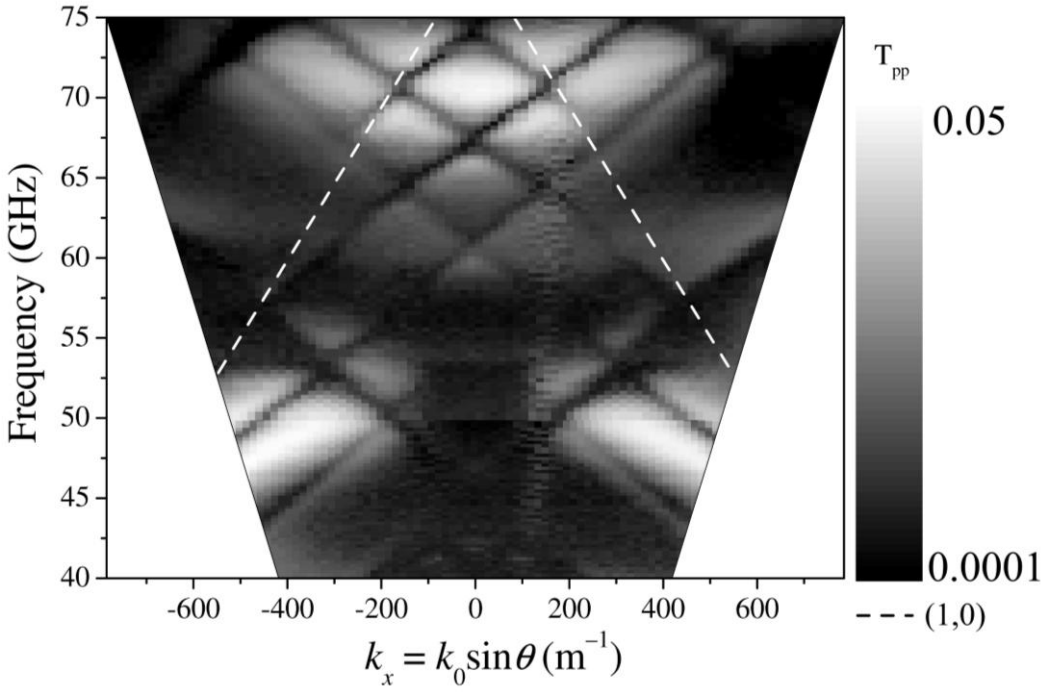

Figure 7.4.14*. Log scale plot of transmission measurements for p-polarised (TM) radiation showing the second and third order mode of the resonant cavity,* $\varphi = 0°$*. Diffracted light lines for air are also illustrated.*

Figure 7.4.15 shows the normal incidence transmission response of the third order (N = 3) mode.

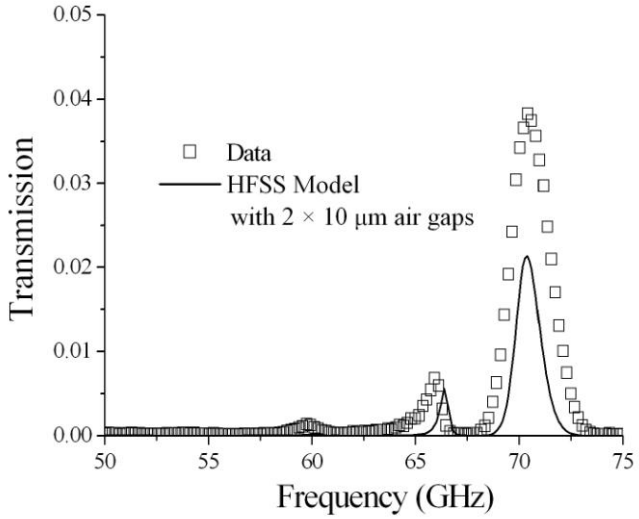

Figure 7.4.15*. Normal incidence transmission measurements and modelling for the third order mode,* $\varphi = 0°$*.*

The third order mode can be seen at 70.5 GHz along with waveguide modes of the Perspex layer at 59.8 GHz and 65.9 GHz. Electric fields on resonance of the third order mode are shown in *Figure 7.4.16*.

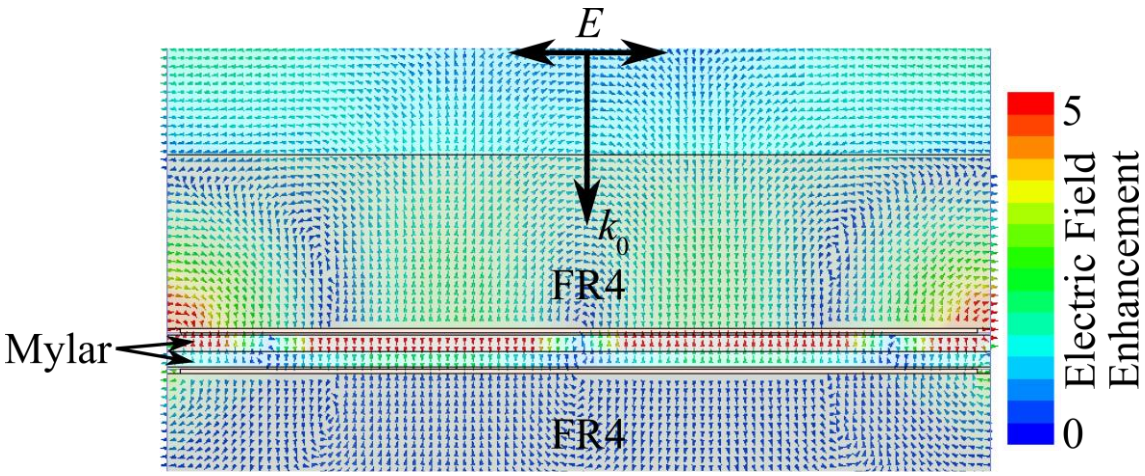

***Figure 7.4.16**. Instantaneous electric field direction and magnitude plotted at a phase corresponding to maximum field enhancement on resonance of the third order mode. $\theta = 0°$, $\varphi = 0°$.*

The third order mode has three nodes in the electric field underneath the metal strips. Since the electric fields reverse across the slit opening the mode does not require a phase variation in the incident electric field and can be coupled to at normal incidence.

The dispersion of the third order ($N = 3$) mode for p-polarised (TM) incident radiation is shown in *Figure 7.4.13*. The third order mode follows a similar dispersion to the 1st order mode, rising in frequency as the in-plane momentum is increased. The first and third modes have a similar electric field distribution, having the same symmetry and coupling conditions which possibly explain this behaviour.

Similarly the third order ($N = 3$) mode can be seen in *Figure 7.4.17* for s-polarised (TE) radiation and has a similar dispersion to that of the 1st order mode excited by the same incident polarisation.

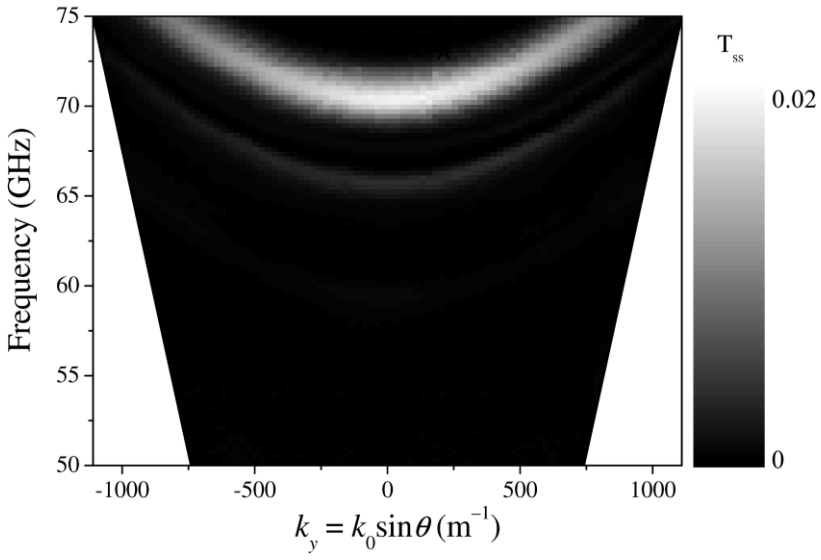

Figure 7.4.17*. Transmission measurements for s-polarised (TE) radiation showing the third order (N=3) mode of the resonant cavity, φ=0°.*

7.4.2.1 Transmission Dependence on Metal Film Thickness

Due to the very large aspect ratio of the metal film in the unit cell of this structure (60 nm × 3.8 mm) and large complex refractive index, accurate modelling using the finite-element method is very computationally intensive. A very high density mesh of tetrahedral elements is required in the region of the metal film; this mesh then has to be graded in density to provide a smooth transition across to the regions of larger volume and lower refractive index where a less dense mesh is required. The aspect ratio of the thin film component of the sample is at the upper limit of the capabilities of the finite-element method due to the difficulty of accurate representation by a mesh, the finite amount of computer memory and available computation time therefore another modelling method has been used to study the effect of changing film thickness. A Fourier Modal Method[93] (FMM) code has been used to model the structure in this chapter when FEM modelling was not capable of producing an accurate result, such as for very small (< 60 nm) film thicknesses. This method is discussed further in chapter 3. This method was unable to produce electric field plots however and so was only used when necessary. The dependence of the thickness of the thin metal film on the level of resonant transmission is shown in *Figure 7.4.18*. The level of transmission falls rapidly as the film thickness is increased, being close to zero for films of 1000 nm or greater. The thickness of the metal film is the most significant parameter in controlling the level

of microwave transmission through this system as it is equivalent to changing the height of the tunnel barrier if the quantum tunnelling analogy is considered.

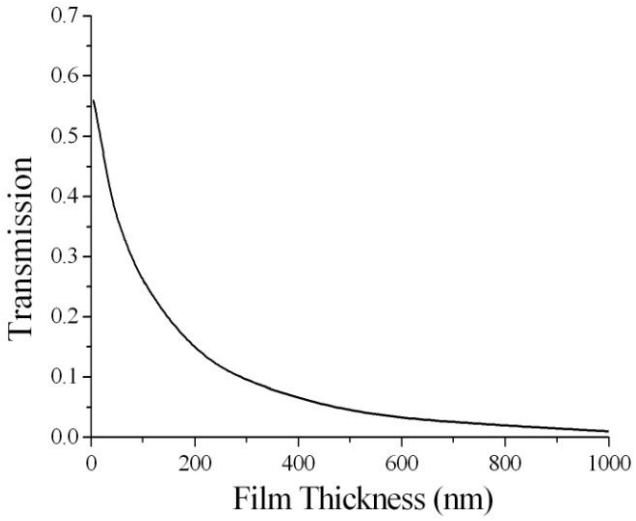

***Figure 7.4.18**. Theoretical dependence of the peak transmission of the first order mode of the resonant cavity on the metal film thickness.*

The approximate Drude parameters for a metal at microwave frequencies ($\varepsilon = -10^4 + 10^7 i$) were used to describe the thin aluminium film. Since the film is thin, these parameters may not necessarily be applicable as the conductivity of thin (< skin depth) films is commonly lower than the bulk metal[119-121]. These Drude parameters give a reasonable agreement with experiment but may not be applicable for films of a much smaller thickness. For very thin films the classical resistivity size effect will become significant, the thickness of the metal can become comparable to the mean free path of the electrons thus increasing the surface scattering and therefore increasing the resistivity. Grain boundary scattering will also make a significant contribution to the resistivity[122] if the size of the grains composing the film are comparable to the electron mean free path. It is a common consensus that it is not known what relative contribution each of these scattering mechanisms has on the conductivity. Grain boundary scattering and surface scattering have a similar geometrical dependence; they are both inversely proportional to the film thickness and grain size. Also for very small film thicknesses (~ < 10 nm), one would expect the metal film to be discontinuous leading to a further increase in the resistivity compared to the bulk properties. (Smaller thicknesses could well be below the percolation threshold leading to the film having properties closer to that of a dielectric insulator than a bulk metal). The effect of an

increased resistivity would greatly increase the transmission as the impedance mismatch across the dielectric/metal interface would be greatly reduced.

7.5 Summary

In this chapter the experimental study of a novel resonant cavity containing a thin continuous metal film has been performed and results found to be in good agreement with modelling. Remarkable resonant transmission of ~ 30 % through the structure has been recorded; this is a significant enhancement over the < 0.1 % expected through the stand-alone thin film. Transmission through the stand-alone film is very small due to the large impedance mismatch at the air/metal interface due to the large complex refractive index of metals at microwave frequencies. When placed inside the resonant cavity, the large enhanced electric and magnetic fields present at the film surface on resonance of the cavity enable power to be transferred across the metal/dielectric interface thus exciting an equivalent resonance on the other side of the film. These cavity resonances oscillate together in phase, coupled by evanescent fields within the metal film. Symmetry of the structure aids efficient coupling to free space on the exit side, producing measurable transmission. This system can be considered as behaving as the photonic analogue of a quantum tunnel barrier, where the tunnel barrier is the metal film. Experimental measurements and modelling have been presented for the first three modes of the system and the coupling conditions discussed. Excellent model fits to the first and third order modes – coupled to at normal incidence have been found. Additional modes due to waveguide resonances within the dielectric cladding of the sample have also been observed. Angle of incidence studies were performed to further characterise the first three modes and the difference in the coupling strength between the odd and even modes has been discussed.

8 Microwave Transmission through arrays of Metallic Crosses

8.1 Introduction

In this chapter, study of the microwave transmissive properties of metallic structures is continued through the investigation of another interesting geometry, arrays of metallic crosses. Arrays of metallic crosses and their complement, arrays of cross-apertures have been used for many years as band-stop/band-pass filters[19,173-175]. As discussed briefly in chapter 2 these arrays exhibit a resonance which is dipolar in character. The resonant wavelength is approximately twice the length of the cross bar that lies parallel to the incident electric field. An array of crosses is similar to an array of rods but with the added benefit of an azimuth-angle-independent response due to their 90° rotational symmetry.

A Fabry-Perot cavity[161] is typically composed of a slab of material with reflecting surfaces or two reflecting mirrors. On resonance, the reflected waves interfere constructively to produce a series of transmission maxima. These types of structure are well understood[176] as the reflections from the surfaces experience either a 0° or 180° phase change in the electric field, depending on the refractive index mismatch at the interface (see *Section 8.2.2*). This leads to a resonant fundamental standing wave having a wavelength of twice the optical pathlength of the cavity.

In this chapter, an array of metallic crosses is experimentally investigated and two of these arrays are then used as reflecting surfaces to compose a Fabry-Perot cavity. Use of structured resonant mirrors to form the cavity produces remarkably different behaviour from a traditional Fabry-Perot etalon due to the frequency dependent reflectivity and frequency dependent phase response of the mirrors.

8.2 Background

8.2.1 Cross Arrays

Cross arrays, like the square meshes briefly introduced in chapter 2 are structures that can be utilised as a filter to produce a frequency selective response.

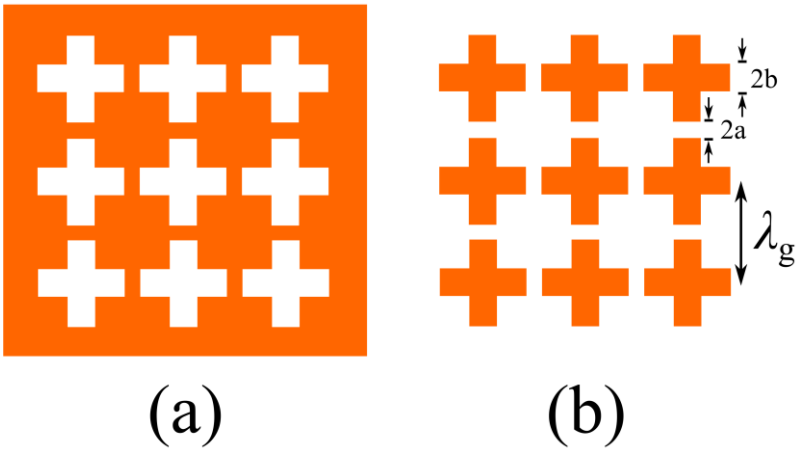

***Figure 8.2.1**. Schematic diagram illustrating the **(a)** Inductive cross array **(b)** Capacitive cross array. Shaded area represents metallic regions.*

These types of structures along with regular square metal meshes have been the subject of a number of studies performed in the 1960s in the infrared region of the electromagnetic spectrum. Many of these studies were performed by Ulrich[19,21,177], who developed transmission line theory (TLT) for calculating the response of single and multiple mesh filters. His theory was later extended by Whitbourn and Compton[75] and Timusk and Richards[178] to allow the inclusion of dielectric layers. Cross arrays differ from regular square meshes since they exhibit a narrow passband/stopband at frequencies well below the onset of diffraction. This makes them very useful for filtering since diffraction effects can be avoided and they are thus a popular choice as filters particularly in the astrophysical community[179,180]. Many studies on arrays of crosses have focused on inductive cross arrays[181-183] (cross-shaped slots in continuous metal) as they can be studied without the need for a supporting dielectric substrate. The findings from studies of inductive crosses can of course be applied to the complementary structure through the use of Babinet's principle. Cross shaped structures can be thought of geometrically as the superposition of an inductive square mesh and a capacitive square mesh. The resultant array can therefore be described as having both inductive and capacitive electrical characteristics. An inductive cross array

can be considered to be the limit of a square inductive mesh with its opposite corners brought inwards to form cross-shaped apertures. This increases the capacitance since the opposite corners of the holes are now much closer together. This increased capacitance leads to a reduction of the resonant frequency since the array can be described as an LC circuit model where, $\omega_{res} = 1/\sqrt{LC}$. As the width of the crosses is reduced to zero, the limit of crossed dipoles is approached and the resonant frequency will decrease[184]. In the other limit where the width of the cross bars approaches their length to become a square mesh the resonant frequency will increase, moving closer to the diffraction edge[21]. An attempt to formulate an equation to predict the position of the general resonance of an array of such crosses was made by Chase and Joseph[173] (*Equation 8.2.1*).

$$\lambda_r = 2.1\lambda_g - 4.2a + 2.1b = 2.1(l + b) \qquad \textit{Equation 8.2.1}$$

Where λ_r is the resonant wavelength, λ_g is the pitch, *l* is the length of the cross bars, *2a* is the gap between the crosses and 2*b* is the width of the cross bars, as illustrated on *Figure 8.2.1*. This equation was found by producing a least squares fit to experimental data measured from six samples of differing dimensions. This behaviour is also expected from antenna theory which predicts that a dipole antenna will resonate at $\lambda_r \sim 2l$ with an increase in the resonant wavelength observed as the width of the antenna is increased. The correction to the resonant frequency for the finite width is due to the end-effect. An increase in the width increases the capacitance and lowers the inductance of the characteristic impedance of the cross, leading to an apparent lengthening of the cross-bar and therefore an increase in the resonant wavelength[185]. They also observed an increase in the bandwidth of the response as the width of the cross bars is increased which is a common technique for increasing operational bandwidth for an antenna. An antenna which occupies more space within a spherical volume typically has a larger bandwidth[186] and therefore lower Q factor. The radiated fields from the antenna can be written in terms of spherical modes within a virtual sphere which surrounds the antenna. If the sphere is too small to support a propagating mode, the modes are then cut-off and the Q is high as the evanescent modes contribute very little real power in the far-field.

8.2.2 Fabry-Perot Cavity

As already mentioned above, two partially reflecting planes separated by a distance, *d*, form a Fabry-Perot cavity[187] which can support a series of standing wave resonances. The frequencies of these resonances are equally spaced and can be determined by *Equation 8.2.2*.

$$f_N = \frac{Nc}{2nd}, \qquad \textit{Equation 8.2.2}$$

where *N* is the mode number, *c* is the speed of light and *n* is the refractive index of the material in the cavity.

For a cavity bounded by high index non-magnetic ($\mu = \mu_0$) media which may be metallic or dielectric (*Figure 8.2.2a*), the boundary conditions on the surface impose a 180° phase change on the electric field on reflection. This leads to a maximum in the electric field at the centre of the cavity. Since the energy has to be equally distributed between the electric and magnetic fields the magnetic field is a maximum at the interface and zero at the centre of the cavity.

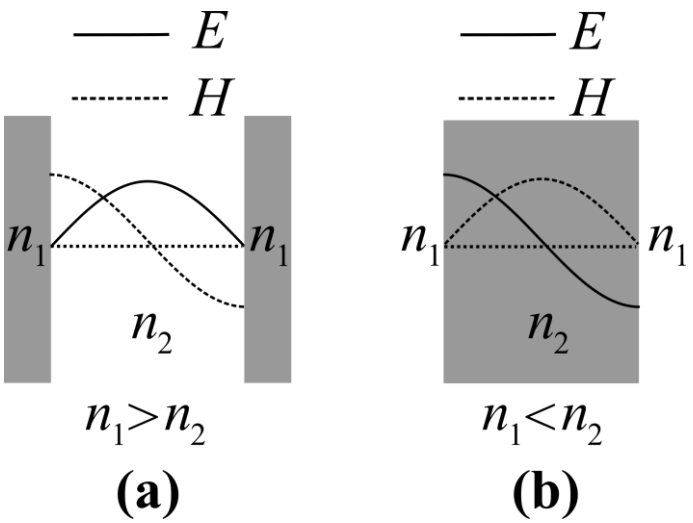

***Figure 8.2.2**. Tangential electric and magnetic field solutions for a Fabry-Perot resonant cavity composed of **(a)** reflecting interfaces with $n_1 > n_2$ **(b)** high index dielectric slab with $n_1 < n_2$.*

If the refractive index of the regions in *Figure 8.2.2a* are switched such that reflections are occurring at a high/low index interface (*Figure 8.2.2b*) the electric field will be

reflected in phase and the position of the peak electric and magnetic fields will be reversed. This results in maximum electric field at the walls and for the odd modes a zero at the centre of the cavity[176].

Metallic square meshes have been used as partially reflecting surfaces in Fabry-Perot cavities in previous studies[177,188-190]. Using meshes to construct a Fabry-Perot cavity allows the reflectivity coefficient of the reflecting surfaces to be tuned by adjusting the geometrical properties of the mesh. This gives a larger freedom to the designer of the structure to produce a tailor-made response than is possible with planar metallic mirrors.

In this work the transmission response of a Fabry-Perot cavity formed from resonant cross-arrays, a 'resonant mirror' Fabry-Perot is further explored. Multilayer systems comprised of inductive cross-shaped meshes have been modelled in the infrared regime by Möller et al., with[191] and without[175] dielectric cladding. These systems were also found to support Fabry-Perot modes between the filter layers for large ($> \lambda/2$) separations. For small separations the cross-meshes interact through near-fields allowing two coupled modes to be excited[175]. However in this study, two capacitive cross arrays are used instead of the inductive arrays that have been explored by previous authors[173-175,181,191,192]. Due to the three dimensional nature of the structure, Babinet's principle cannot be applied to predict the response of this previously unexplored structure from the known behaviour of multi-layer inductive arrays. The resonant behaviour of the crosses was found to shift the frequency of the Fabry-Perot modes from that predicted by the classical analytical prediction (*Equation 8.2.2*). This is due to the frequency dependent phase shift experienced at the walls of the cavity allowing the cavity to appear longer or shorter depending on the position in frequency of the modes relative to the resonant frequency of the crosses. This behaviour is illustrated through the use of phase measurements and field plots generated by finite-element method modelling.

8.3 Experimental

A regular square array of crosses was fabricated using a standard 'print and etch' technique[172]. A copper-coated printed circuit board (PCB) with a dielectric core of thickness 0.762 mm and a copper cladding of thickness 35 μm was used. The dimensions of the structure and orientation of the sample are illustrated in *Figure 8.3.1*.

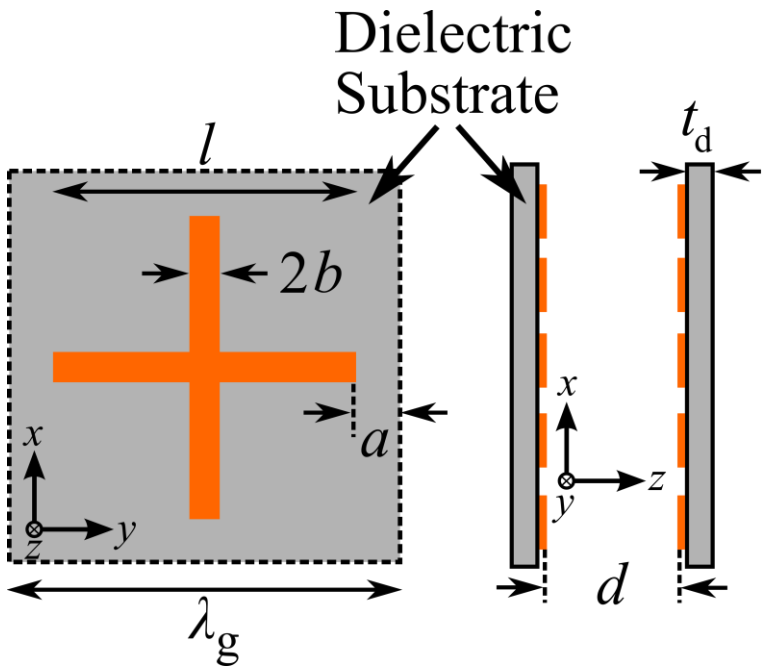

Figure 8.3.1. *(a) A unit cell of the periodic array illustrating its dimensions. (b) Sample orientation when used to create a resonant cavity.* $l = 3.45\ mm,\ 2a = 0.75\ mm,$ $2b = 0.2\ mm, \lambda_g = 4.2\ mm,\ t_d = 0.762\ mm.$

The sample size was reduced to ~ 30 cm × 30 cm, in order to minimise any bowing in the PCBs as maintaining a constant separation, *d* between the surfaces of the crosses was important when they formed a resonant cavity. The boards were taped with masking tape to wooden frames and spaced around the edges with Mylar (500 μm and 250 μm thickness) and Perspex (6 mm thickness) spacers. Initial experiments found that the boards were bowing outwards making the separation non-uniform and greater than expected. In order to minimise this bowing the boards were attached taut to the frames with 'gaffer' tape which was able to provide a greater amount of tension.

The coordinate system and the plane of incidence referred to the unit cell of the array of crosses are shown in *Figure 8.3.2*.

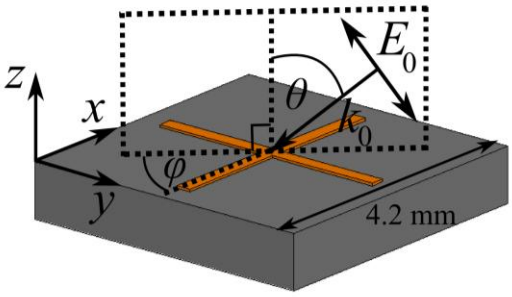

***Figure 8.3.2**. Unit cell of cross array illustrating coordinate system, incident polar angle, θ, azimuth angle, φ, and plane of incidence.*

8.4 Results and Discussion

8.4.1 Normal incidence Transmission Response of a Single Layer of Crosses

Transmission measurements were performed on a single layer of crosses for the frequency range 18-75 GHz; these are shown along with the modelled response generated by the finite-element package, HFSS in *Figure 8.4.1*. Measurements were taken with a series of microwave horn antennas that cover a range of frequency bands, this results in a small change in the noise level at the end of the frequency band (26.5 GHz and 40 GHz) as each set of horns has a different specification.

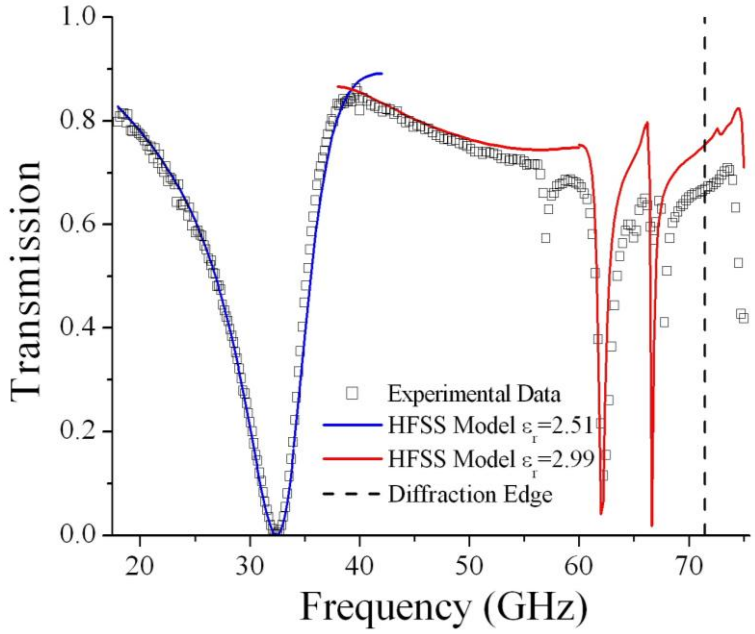

Figure 8.4.1. *Transmission measurements for a single layer of* $l = 3.45\ mm$, $2a = 0.75\ mm$, $2b = 0.2\ mm$, $\lambda_g = 4.2\ mm$, $t_d = 0.762\ mm$ *35 μm thick copper crosses. Modelling uses two values of substrate permittivity,* $\varepsilon = 2.51$ *for* $18 < f < 40\ GHz$ *and* $\varepsilon = 2.99$ *for* $40 < f < 75\ GHz$.

The dipolar resonance of the crosses occurs at ~ 32.5 GHz which does not agree with the prediction of 40.2 GHz calculated from Chase and Joseph's equation (*Equation 8.2.1*); this is due to the dielectric substrate reducing the resonant frequency as the effective length of the dipoles is increased in the dielectric region[76,192]. Beyond 50 GHz a series of high Q-factor modes are excited, some of which are a result of the array being on a substrate. There are more modes seen in the experimental data than in the modelling, this is due to the incident beam being not perfectly planar allowing coupling to modes that at normal incidence would otherwise not be possible. A fit to the experimental data could not be achieved using a single value of permittivity for the substrate. The low frequency data were fit using a value of $\varepsilon_r = 2.51$, $\varepsilon_i/\varepsilon_r = 0.0018$ this is within the error of the quoted value from the manufacturer ($\varepsilon_r = 2.55 \pm 0.04$ at 10 GHz). At higher frequencies this value however does not produce a good fit as the dielectric properties appear to be dispersive. A value of $\varepsilon_r = 2.99$ was found to give a good fit to the background level and the observed modes. The exact form of the frequency dependent permittivity is not known. However it is the lower frequency regime (< 40 GHz) that will be focused on for much of this study.

The transmission response of a single layer of crosses was also measured with a Vector Network Analyser (VNA), allowing the phase response to also be determined (*Figure 8.4.2a*).

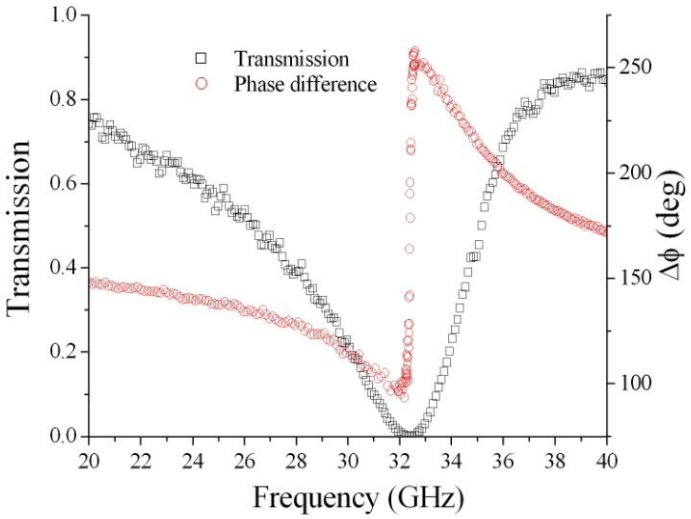

(a)

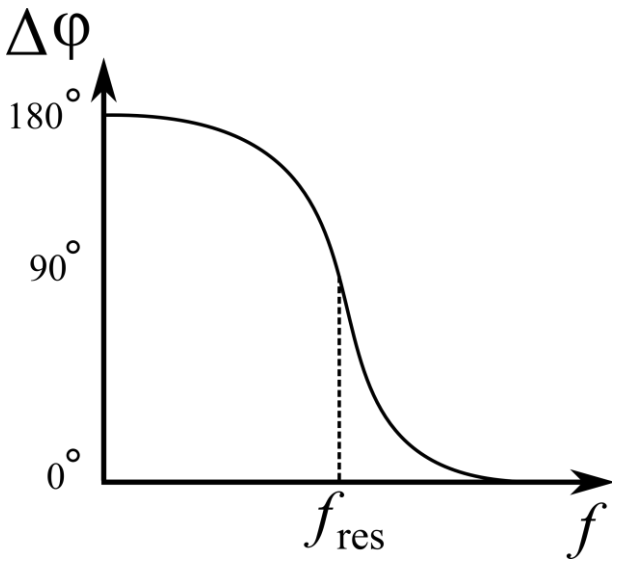

(b)

Figure 8.4.2.(a) *Transmission intensity and phase measured through a single layer of crosses with a Vector Network Analyser (VNA).* ***(b)*** *Phase response of a classical resonator*

The signal has been normalised to a measurement without the sample, thereby removing the phase shift associated with propagation over the distance between the source and

detector horns. The data shows that the phase of the electric field changes as the frequency is swept through the resonance. The measured phase shift is the combination of the phase of reradiated radiation from the resonators and the radiation which is transmitted straight through the sample. This combination of two sources of phase change results in the differing response from that exhibited by a classical resonator (*Figure 8.4.2b*). On resonance where the transmission is a minimum and the gradient of the phase ($d\varphi/df$) is a maximum the measured phase is 180° since the reradiated electric field destructively interferes with the straight through transmission. The power on resonance will either be reradiated in the backward direction as the reflected signal or absorbed into the metal/dielectric substrate. The fast reversal of the gradient of the phase across the resonant frequency can be understood by considering *Figure 8.4.3*.

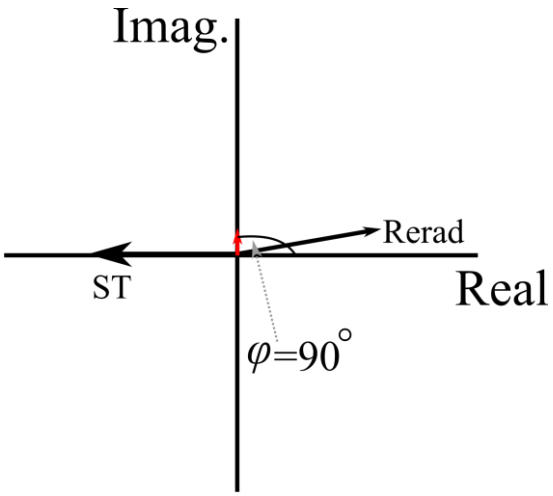

(a)

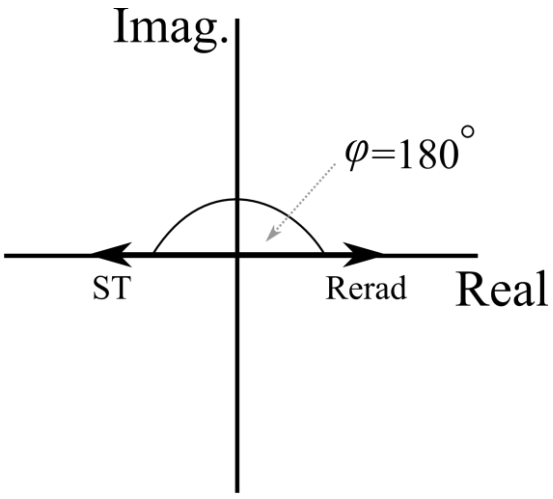

(b)

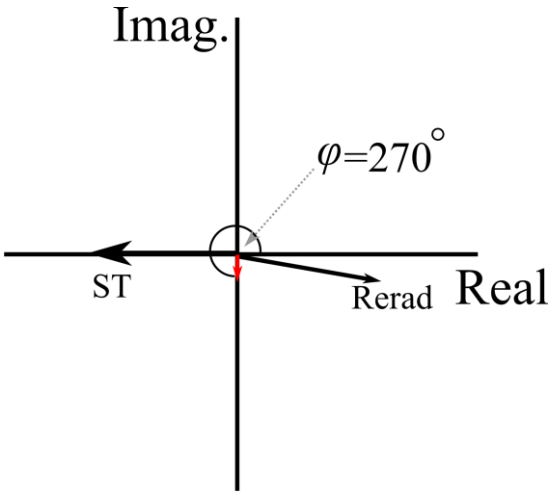

(c)

Figure 8.4.3*. Argand diagrams illustrating the phase of the measured transmission and its constituent components.* ***(a)*** *A frequency just below resonance* ***(b)*** *On resonance* ***(c)*** *A frequency just above resonance. Black arrows represent straight through (ST) and re-radiated (Rerad) transmission components. Red arrow illustrates the resultant transmission from the vector sum of ST and Rerad.*

Figure 8.4.3a shows the relative phases of the straight through and reradiated transmission components just below the resonant frequency. The reradiated component is close to being equal in magnitude and opposite in phase (180°). If the vector sum of these two components is considered the resultant measured transmission will have a small magnitude and be ~ 90° out of phase with the straight through transmission as seen in *Figure 8.4.2a*. On resonance (*Figure 8.4.3b*) the reradiated component will be equal in magnitude and 180° out of phase with the straight through component thereby perfectly cancelling out all transmission. Above the resonant frequency (*Figure 8.4.3c*) the reradiated component is now a little more than 180° out of phase with the straight through transmission resulting in the measured transmission being out of phase by 270°. The transition from 90° to 270° will be instantaneous for a perfect non-damped system, producing a discontinuity in the phase response. However experimental imperfections and losses result in the phase response having a finite width. The sample also has a dielectric substrate which induces a linear phase shift onto the background of the phase response since for higher frequencies/shorter wavelengths the 'optical pathlength' will be greater thereby imparting a greater phase shift.

Fields for the dipolar resonance generated from the finite element model are shown in *Figure 8.4.4*; the dipolar character of the fields can be seen with high electric fields excited in the region around the bar of the cross parallel to the incident electric field vector. There is also some interaction between neighbouring crosses in the array as the electric fields extend beyond the edges of the unit cell.

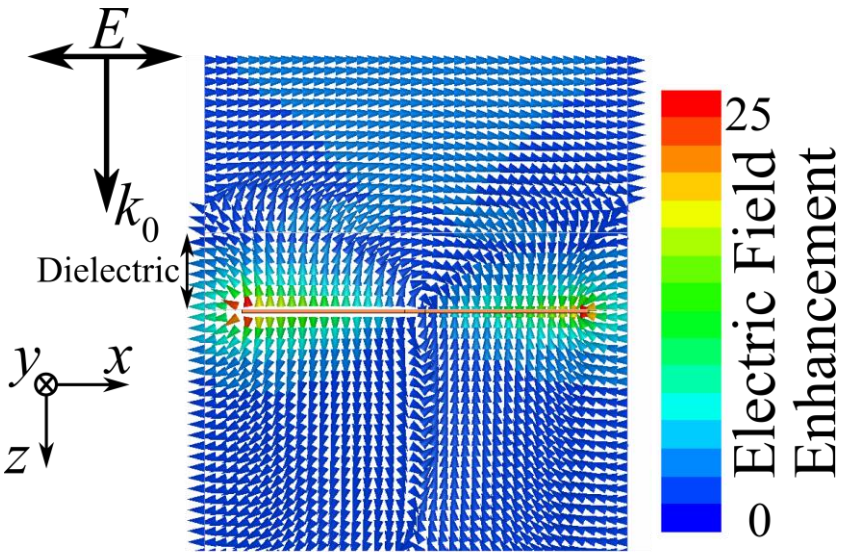

(a)

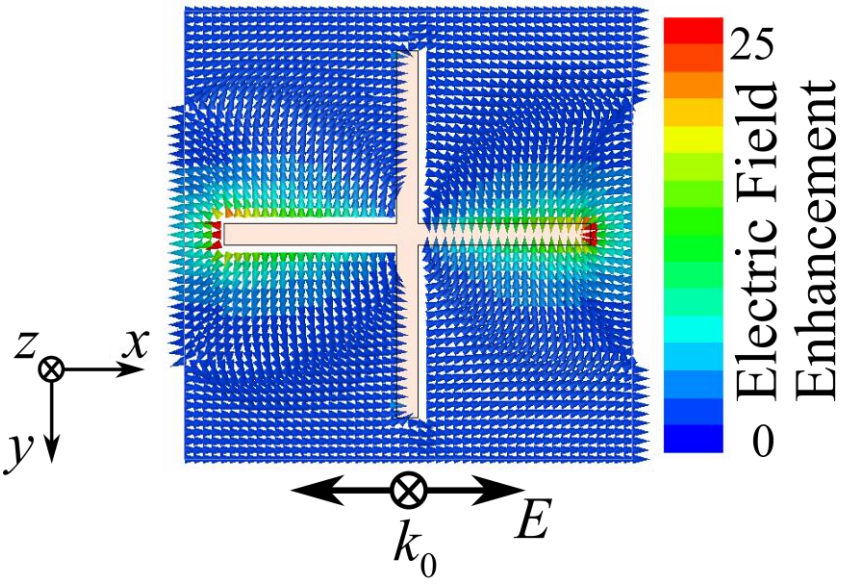

(b)

Figure 8.4.4*. Electric field magnitude and direction for the dipolar mode (32.5 GHz), plotted at a phase corresponding to maximum field enhancement. Fields plotted through* ***(a)*** *plane of incidence* ***(b)*** *plane of sample.*

Electric fields for the higher frequency modes are shown in *Figure 8.4.5*. The first mode at 62 GHz (*Figure 8.4.5a*) appears to be a higher order mode with a $(-+-+)$ charge configuration accounting for the mode appearing at approximately twice the frequency of the first mode. This mode also appears to have a large portion of the field enhancement in the dielectric region. The mode at 66.5 GHz (*Figure 8.4.5b*) has a similar charge configuration to the mode at 62 GHz however there is some asymmetry near the centre of the crosses, the charges on the dielectric/cross interface are opposite to that of the air/cross interface $(-\pm\mp+)$ resulting in a very different field distribution. The regions of large field enhancement are outside of the dielectric, this leads to a higher resonant frequency as the effective resonant wavelength will be shorter.

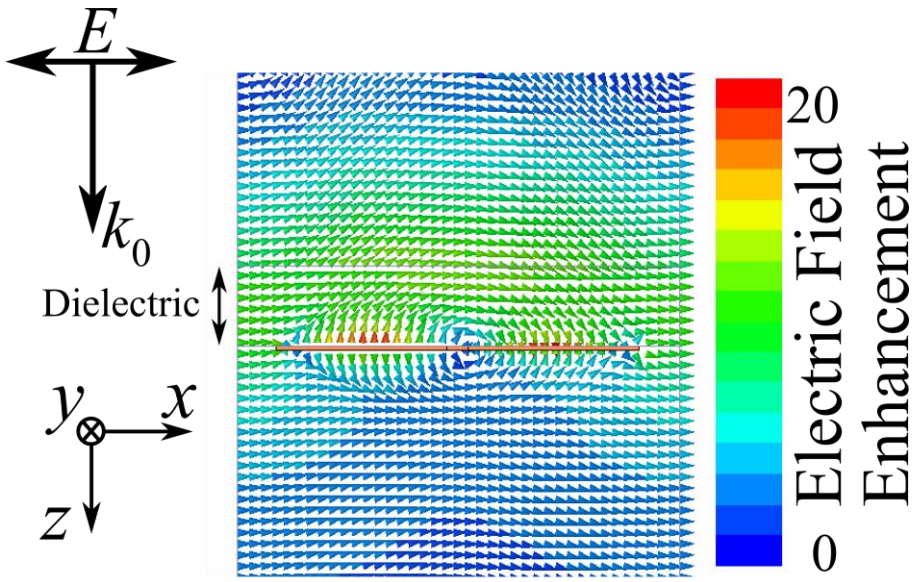

(a)

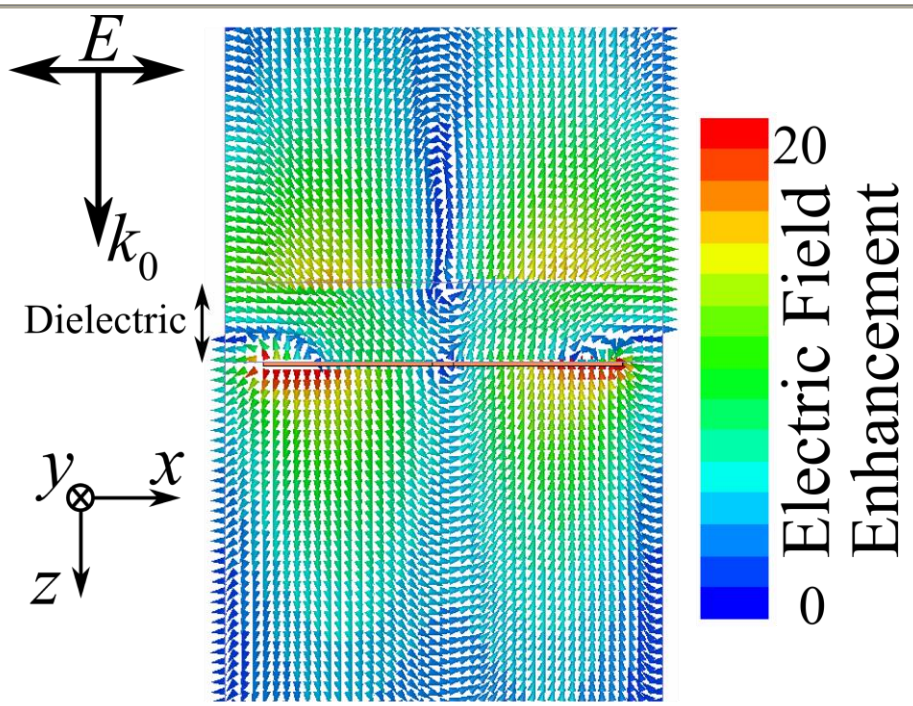

(b)

Figure 8.4.5*. Electric field magnitude and direction for the high frequency modes, plotted at a phase corresponding to maximum field enhancement. Fields plotted through the plane of incidence through the centre of the crosses at* ***(a)*** *62 GHz and* ***(b)*** *66.5 GHz.*

8.4.2 Angle dependent transmission response, $\varphi = 0$

Figure 8.4.6 shows the experimental transmission response for p and s-polarised radiation for a single layer of crosses on a dielectric substrate.

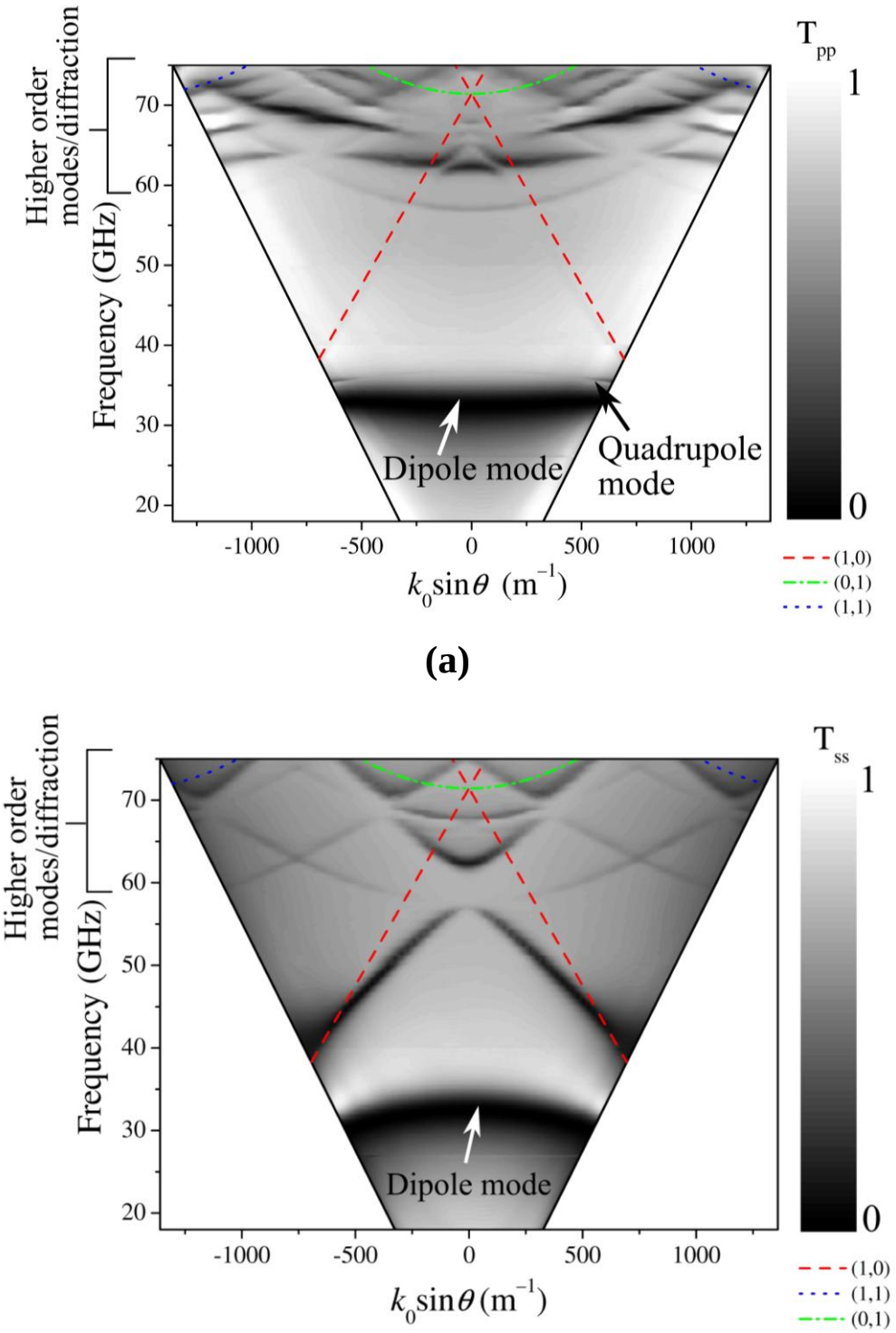

Figure 8.4.6*. Transmission measurements as a function of angle and frequency for a single layer of metallic crosses on a dielectric substrate.* ***(a)*** *p-polarised incident radiation* ***(b)*** *s-polarised incident radiation. Diffracted light lines are also illustrated.*

The wide stop-band at ~ 32.5 GHz is the mode that has dipolar character and can be coupled to at normal incidence $k_x = 0$ for both s and p-polarised radiation since the

crosses have square rotational symmetry. The modes however clearly exhibit very different angle dependences. When excited by p-polarised incident radiation the mode shows a flat response for small angles and rises in frequency at larger angles following a slow parabolic behaviour. Conversely when the mode is coupled to with s-polarised radiation its frequency falls with increasing angle. The dispersive character of these modes is similar to that discussed in chapter 5 where the metallic connectivity of the structure influences which grating vector produces the most dominant scattering and therefore dispersion of the modes. The crosses are disconnected so no real currents are allowed to flow across the system. In chapter 5 the arrays that were disconnected experienced dominant scattering out of the plane of incidence for p-polarised incident radiation and dominant scattering in the plane of incidence for s-polarised incident radiation. The mode excited with p-polarised radiation is following a similar dispersion to that of the (0,1) diffracted light line however due to the different geometry of the elements in this array compared to those in chapter 5 the frequency of the modes is much lower relative to the diffraction edge and therefore the influence of the out of plane diffraction is significantly reduced. The diffracted light lines plotted on *Figure 8.4.6* show the onset of diffraction in air. These lines don't follow clear features in the experimental data as was previously observed in the experimental study included in chapter 5. This could possibly be due to the thicker dielectric substrate (~ × 10) and the onset of diffraction occurring within the dielectric at a lower frequency. The mode excited with s-polarised radiation is following the (1,0) set of in-plane diffracted light lines and since the onset of in-plane diffraction falls in frequency with increasing angle the mode is perturbed greater than for the s-polarised case.

In *Figure 8.4.6a* (p-polarised data) a higher Q mode is excited at a frequency above that of the dipolar resonance. This mode can be seen more clearly in *Figure 8.4.7* which is plotting the same data on a smaller frequency and $k_0 \sin\theta$ scale for clarity.

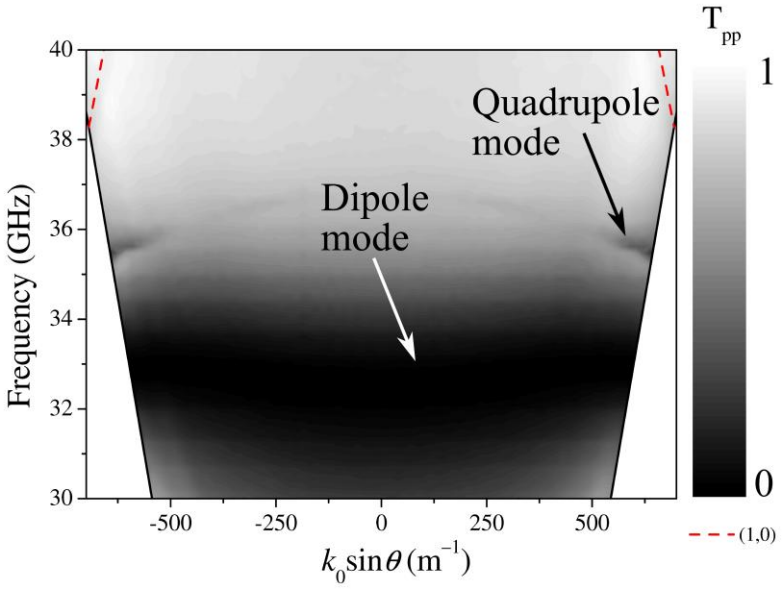

Figure 8.4.7*. Transmission measurements for p-polarised incident radiation as a function of angle and frequency for a single layer of metallic crosses on a dielectric substrate. Data reduced to frequency region containing dipole and quadrupole modes. Diffracted light lines also illustrated.*

This mode is only coupled to at non-zero angles of incidence $(k_x \neq 0)$. This mode is quadrupolar in character as seen in the finite element modelling in *Figure 8.4.8*.

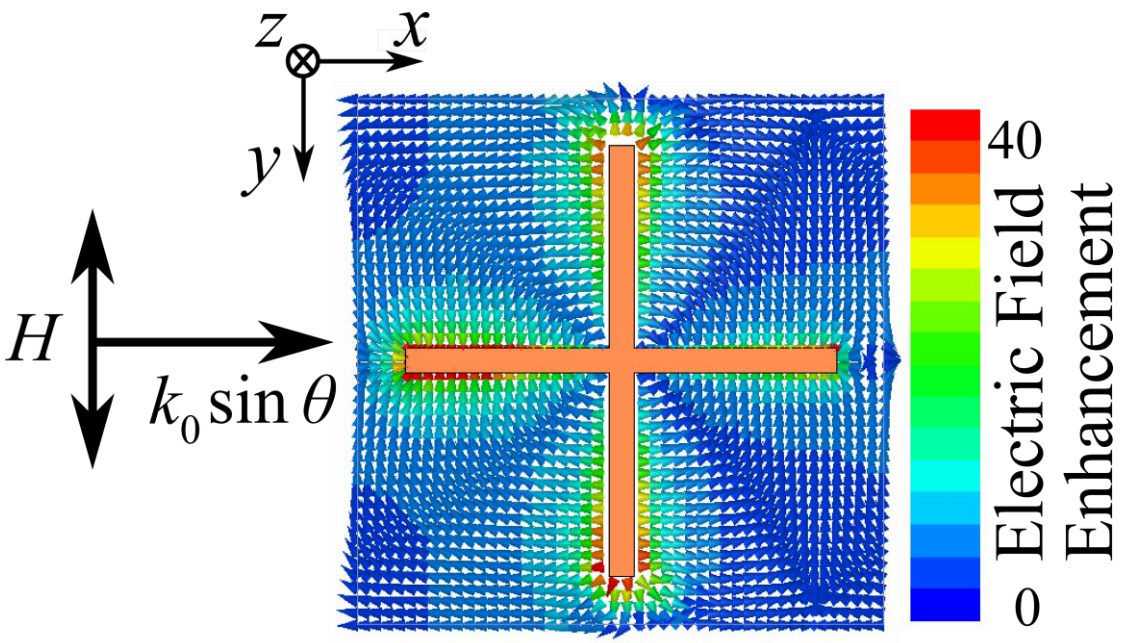

Figure 8.4.8*. Electric vector fields plotted on resonance at a phase corresponding to maximum field enhancement. θ=10°, φ=0°, 36.6 GHz.*

Due to the symmetry of the charge distribution in *Figure 8.4.8* this mode cannot be coupled to at normal incidence as a phase variation in the incident field is required across the unit cell.

8.4.3 Angle dependent transmission response, φ = 45°

Transmission measurements for p and s-polarised radiation incident at $\varphi = 45°$ are shown in *Figure 8.4.9*.

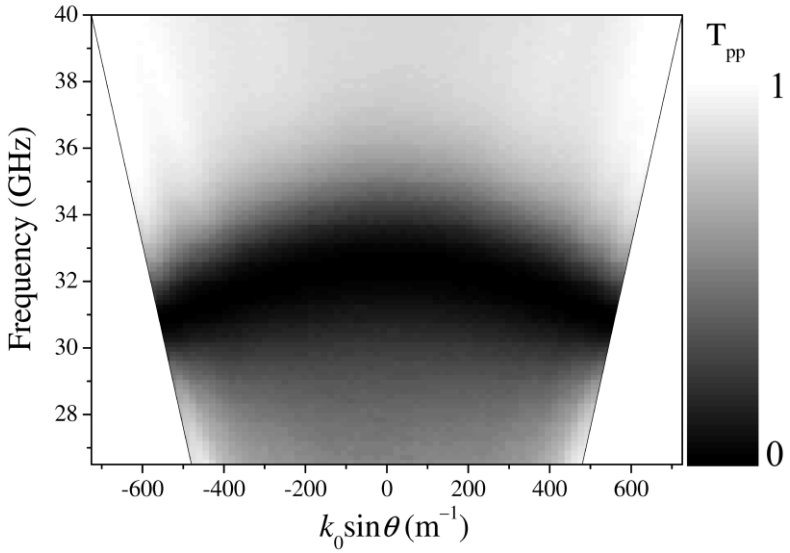

(a)

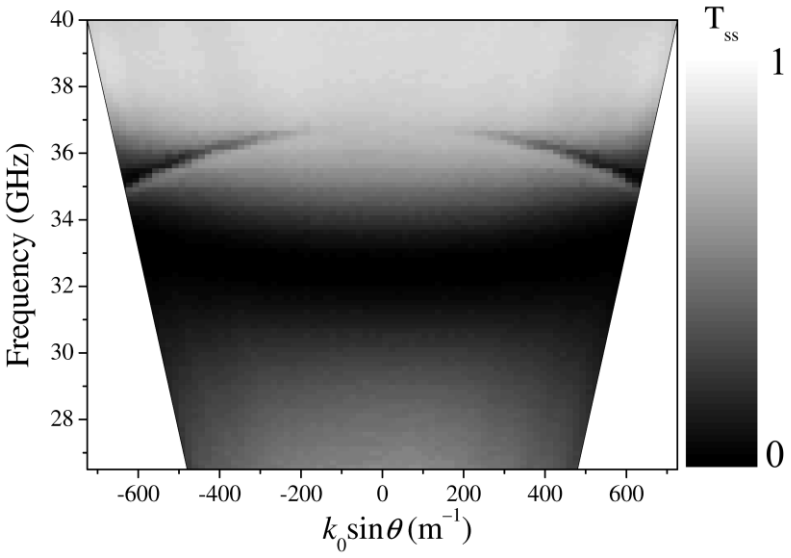

(b)

Figure 8.4.9*. Transmission measurements as a function of angle and frequency for a single layer of metallic crosses on a dielectric substrate, φ=45°,* ***(a)*** *p-polarised incident radiation,* ***(b)*** *s-polarised incident radiation.*

When the array of crosses is illuminated with radiation incident at an azimuth angle of 45° the coupling to the quadrupolar mode is now very different. The mode cannot be coupled to at any polar angle of incidence (θ) for p-polarised incident radiation however s-polarised radiation can now couple to the mode for non-zero polar angles of incidence. This can be understood by considering the direction across the unit cell where a phase difference in the electric field is present (*Figure 8.4.10*).

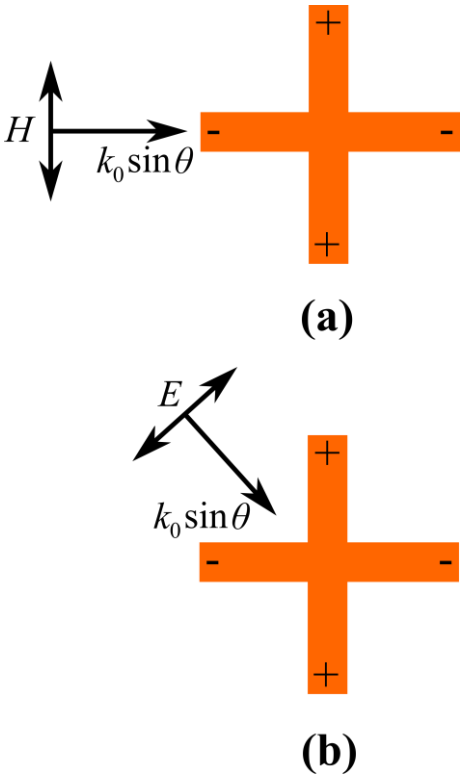

Figure 8.4.10**. Illustration of the charge distribution on resonance of the quadrupolar mode at an instant in the phase cycle,* ***(a) *p-polarised,* $\varphi = 0°$ ***(b)*** *s-polarised,* $\varphi = 45°$.

At $\varphi = 0°$ (*Figure 8.4.10a*) a phase difference in the electric field across the length of the cross bars is only achieved if p-polarised radiation is incident for $\theta > 0$. At $\varphi = 45°$, $k_0 \sin\theta$ is not co-linear with the bars of the cross and the electric field when p-polarised no longer provides the required conditions for coupling to the mode. The quadrupolar mode can however be coupled to with s-polarised radiation as the non-zero azimuth angle introduces the necessary phase difference across the length of the cross bars.

8.4.4 Fabry-Perot Cavity Composed of Resonant Crosses

Two arrays of crosses were spaced a separation, *d* apart to form a cavity similar to a Fabry-Perot etalon. Transmission was measured through the cavity and it was found that a series of additional modes were observed. Measurements of the transmission through a cavity with a separation of 11.9 mm are shown in *Figure 8.4.11* alongside measurements for a single layer of crosses.

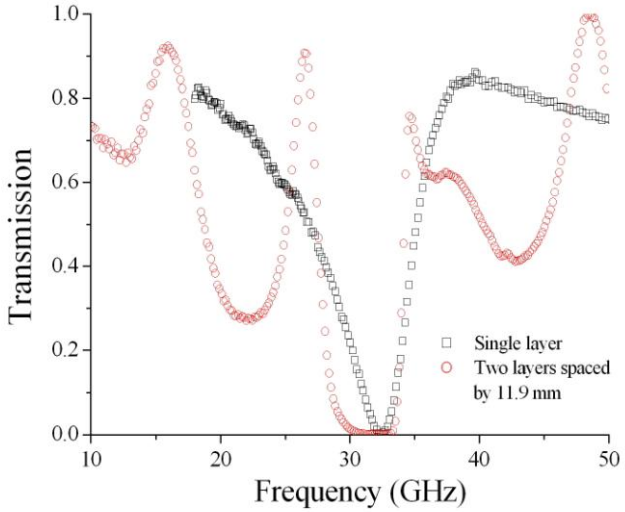

Figure 8.4.11. *Experimentally measured transmission through a cavity composed of two arrays of crosses separated by 11.9 mm and a single layer of crosses.*

The phase response of the cavity was also measured; this is shown in *Figure 8.4.12*.

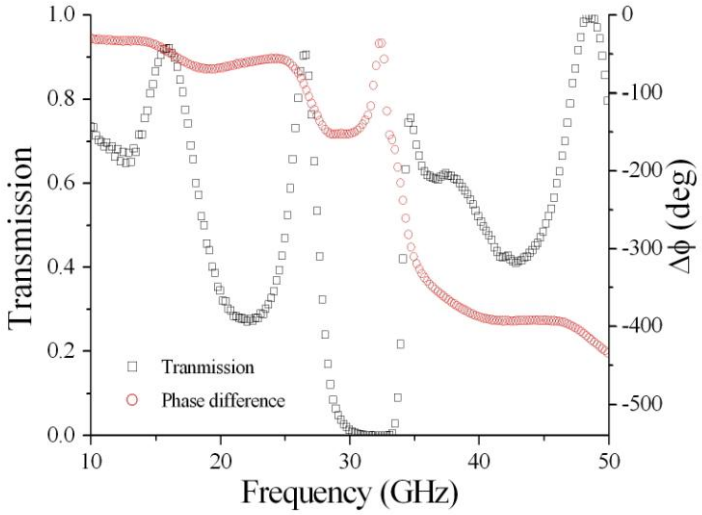

Figure 8.4.12. *Experimentally measured transmission intensity and phase through a cavity composed of two arrays of crosses separated by 11.9 mm.*

These measurements were performed with a Vector Network Analyser (VNA) using the free space measurement setup previously discussed in chapter 3. The dipolar mode is still present at ~ 32 GHz but the transmission response is now much broader with the transmission being zero over a larger range of frequencies. This effect is due to the presence of the second array acting as a second filter with its own transmission response

which produces a multiplying filtering effect. Outside of this stop-band region the response has also changed significantly as there are now a series of peaks in the transmission. These peaks can be attributed to Fabry-Perot resonances between the two arrays of crosses. Each array is acting as a partial mirror, with the pair making a sophisticated Fabry-Perot etalon with mirrors that have a frequency dependent reflection and phase response due to their resonant properties. The effect of having resonant mirrors can be seen by examining the width and frequency of the modes in *Figure 8.4.12*. The effect of the frequency dependent reflectivity can be seen in the finesse of the modes. The coefficient of finesse is typically defined as $4R/(1-R)^2$, where R is the reflection coefficient of the mirrors forming the Fabry- Perot cavity. If the reflectivity of the mirrors is high, the coefficient of finesse will be high and the Fabry-Perot modes will be well defined with sharp peaks and deep minima. If the mirrors have low reflectivity and therefore the cavity has a low coefficient of finesse, the Fabry-Perot modes will have shallower minima and broad peaks. The mode at ~ 15 GHz has a lower finesse than the one at ~ 26 GHz seen by its broader transmission peak and higher transmission minimum. This is because the reflectivity of the individual layers is increasing as their resonant frequency (32.5 GHz) is approached. The frequency of the modes is also not equally spaced as they would be for a typical Fabry-Perot etalon. This is due to the frequency dependent phase response of the mirrors. The phase between the incident electric field and the electric field re-emitted from the resonator goes through a 180° shift on resonance. This phase shift changes the boundary conditions that the electric field experiences therefore altering the resonant frequency of the Fabry-Perot mode. The measured phase response of the system is shown in *Figure 8.4.12*, this has been normalised to the phase measured without the sample in the same way that the transmission intensity is normalised. One can see that a step in the phase is seen for each resonant feature in the transmission response with the resonance being located at the frequency at which the phase has a maximum gradient. The phase steps that are measured are not all the same size; this is due to the measurement of the phase being determined from the entire transmitted signal which is composed of a background contribution and a resonant contribution. Since the phase steps are only due to the resonant contribution, when the background transmission is high the relative contribution by the resonant component is smaller and the phase steps appear smaller. If the background transmission were near zero, as is the case in the region near the stop band the phase jumps would be close to 180°.

An FEM modelling comparison is shown in *Figure 8.4.13* for the cavity with 11.9 mm separation.

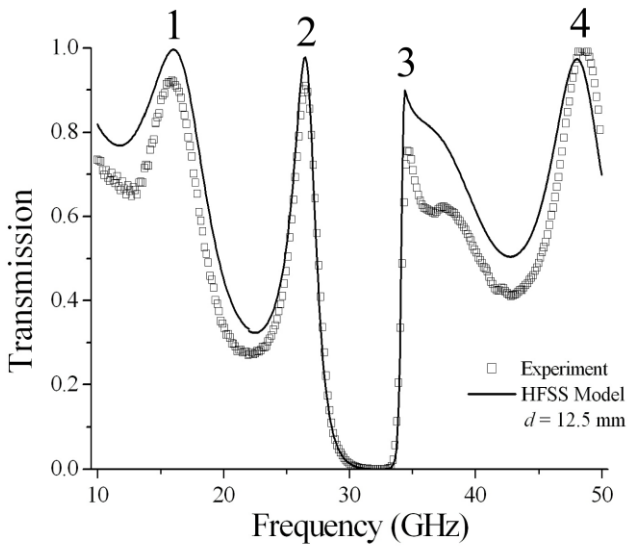

***Figure 8.4.13**. Measured and modelled transmission intensity through two layers of crosses separated by 11.9 mm. Mode numbers illustrated.*

To achieve a fit of the peak frequencies to the experimental data the separation between the two layers used in the model had to be set to 12.5 mm. This is greater than the 11.9 mm measured at the edges of the sample but confirms the observation that the PCBs were bowing outwards making the cavity longer in the centre part of the sample. This bowing increases the average separation between the two arrays and also reduces the quality of the data as the cavity length will be non-uniform introducing inhomogeneous mode broadening and a loss of intensity.

Electric fields for the mode at 16 GHz are plotted in *Figure 8.4.14*.

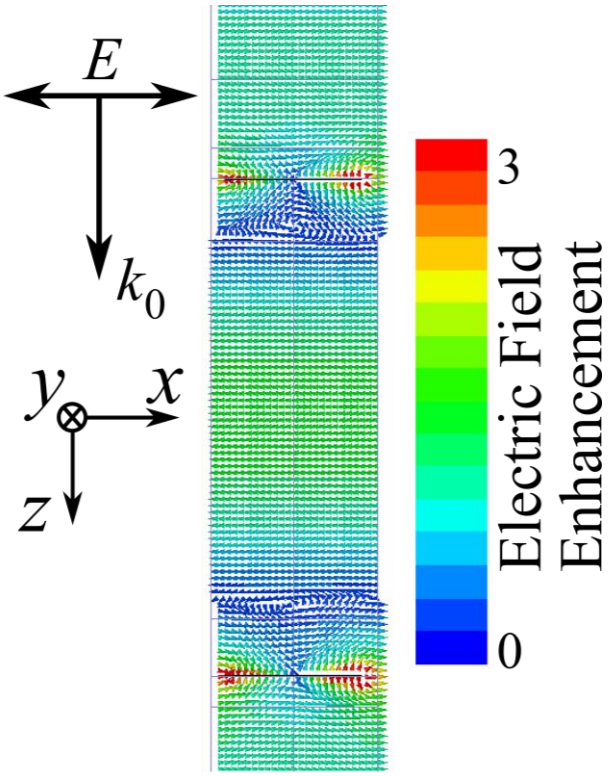

Figure 8.4.14. *Electric field magnitude and direction plotted at a phase corresponding to a maximum field enhancement for the mode at 16GHz.*

The field plot shows that there is electric field enhancement in the region between the two layers of crosses as expected for a Fabry-Perot cavity. There is only one large region of electric field enhancement inside the cavity which is similar to the fundamental resonance of a Fabry-Perot etalon. There are however also two nodes in the electric field inside the cavity in the region near the crosses and also large near- field enhancement close to the surfaces of the crosses. The fundamental mode for an unfilled Fabry-Perot cavity with a length of 12.5 mm would typically occur at $f = c/2d$, i.e. 12 GHz. The mode observed however occurs at 16 GHz, this is due to the presence of the nodes in the electric field inside the cavity which would otherwise occur at the mirrors. The resonant wavelength has effectively become shorter due to the phase conditions imposed by the resonant crosses.

The electric fields for the second Fabry-Perot mode are plotted in *Figure 8.4.15*.

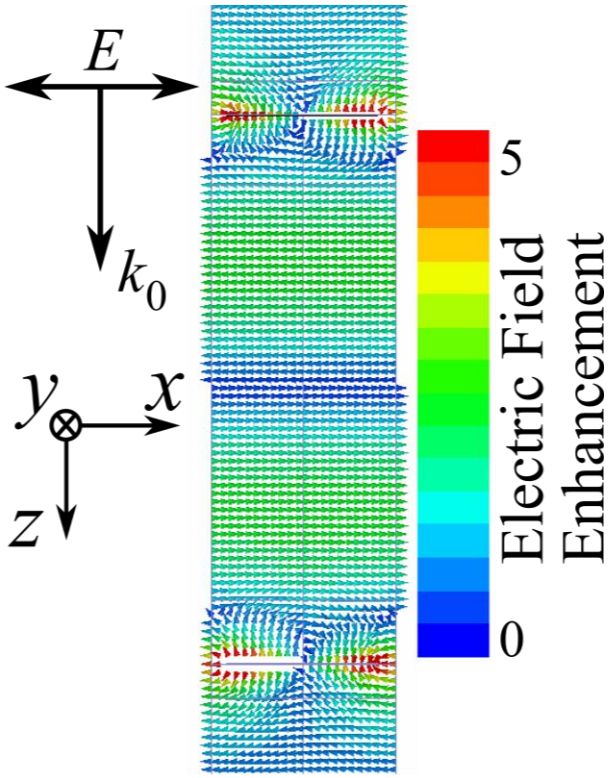

Figure 8.4.15. *Electric field magnitude and direction plotted at a phase corresponding to a maximum field enhancement for the mode at 26.4 GHz.*

This mode also experiences the same effect observed with the first mode in that the resonant frequency is higher than predicted by the simple analytical expression. The mode is expected to occur at 24 GHz ($f = 2c/2d$) yet is measured at 26.4 GHz. This shift from the simple prediction is smaller than for the first mode and this is also reflected in the electric field distribution. The electric field falls to zero much closer to the crosses, thereby giving a resonant condition and wavelength much closer to the typical $\lambda = 2d/N$ analytical prediction.

Electric fields for the third order mode are shown in *Figure 8.4.16*.

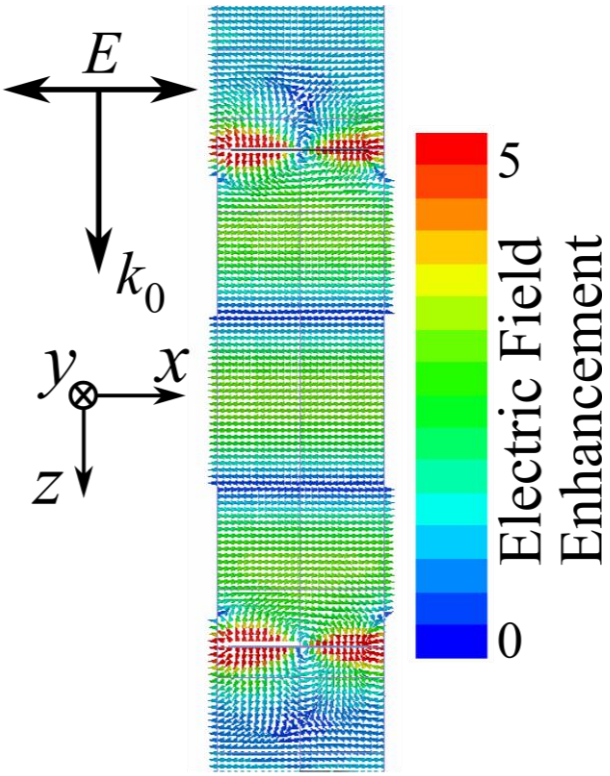

***Figure 8.4.16**. Electric field magnitude and direction plotted at a phase corresponding to a maximum field enhancement for the mode at 34.3 GHz.*

This mode has three regions of large electric field enhancement inside the cavity as expected for the third order Fabry-Perot mode. The expected resonant frequency for this mode would be 36 GHz however the mode is observed at 34.3 GHz, lower than expected. The electric fields near the crosses for this mode appear very different to the previous modes. Field enhancement does not fall to zero close to the crosses, indicating that the boundary conditions for this mode have changed. The difference between this mode and the first two is that this mode lies above the resonant frequency of the individual cross layers. As shown in *Figure 8.4.2a* the phase response of the cross layers varies with frequency, this changes the boundary conditions as the Fabry-Perot modes sweep through the resonance thus changing the effective length of the cavity.

8.4.4.1 Mapping out of modes

Section 8.4.4 showed the results for a cavity with a single separation, however further understanding can be gained by studying how the frequency of the modes moves with variation of the cavity separation.

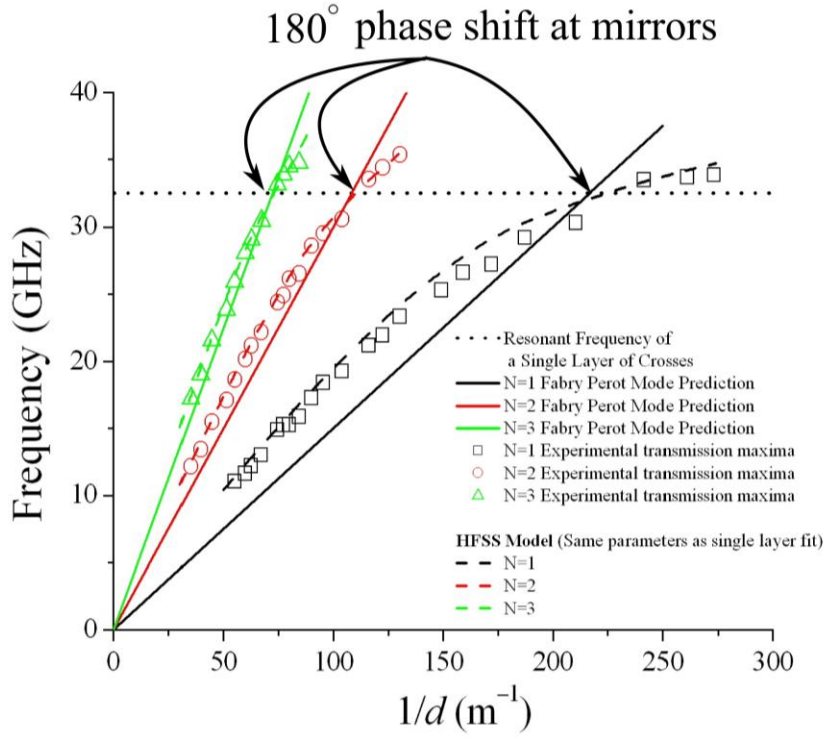

***Figure 8.4.17**. Experimentally measured transmission maxima for two arrays of crosses separated by a distance, d. Only the first three modes are shown.*

Figure 8.4.17 shows the measured transmission maxima for two arrays of crosses at various separations. The dotted line indicates the position of the resonance for a single layer of crosses. The solid lines indicate the position of the first three Fabry-Perot modes for an ideal Fabry-Perot resonator, i.e. one that is composed of mirrors that impose a 0° or 180° phase change on the electric field on reflection and thereby support a mode that has the electric field quantised in integer numbers of half the wavelength $(N\lambda/2)$. The frequency of the modes is plotted against the inverse separation between the arrays, since a linear dependence is expected for an ideal cavity. There would of course be an infinite number of Fabry-Perot modes to plot on *Figure 8.4.17* , all starting from the origin (infinite separation → infinite wavelength (zero frequency)), having an increasing gradient and a decreasing separation from the lower order modes as the quantisation number, *N* is increased. The experimental data shows that there is a consistency in the behaviour of the modes. The low frequency modes (< resonant frequency of a single layer) appear at frequencies higher than that predicted by the Fabry-Perot equation. Below the resonant frequency of the crosses the arrays can be considered to have a surface impedance that is capacitive leading to the cavity appearing shorter than its physical length. This effect is due to the phase shift on reflection not being 180° and therefore shifting the frequency of the Fabry-Perot modes.

As the separation between the two layers is reduced the frequency of these modes increases as one would expect however the dependence is non-linear with the modes approaching the frequency predicted by the Fabry-Perot equations as the resonant frequency of the crosses is approached. The modes intersect the Fabry-Perot equation at the resonant frequency and then appear lower in frequency than the Fabry-Perot equation above the resonant frequency of the crosses. At the resonant frequency the arrays are acting as a PEC, exhibiting minimal transmission, high reflection and a 180° phase change in the electric field on resonance. In this region the modes supported between the arrays are similar to those supported between two metal mirrors. Due to the reflectivity of the layers approaching 100% on resonance the modes will tend towards a delta function in the region of the resonant frequency, this makes coupling to them difficult in the experiment due to sample imperfections and angle spread in the incident beam resulting in a reduced number of data points in this region. Above the resonant frequency the array's surface impedance is inductive leading to the cavity appearing longer than its physical length as the phase shift on reflection is not exactly 180°.

8.4.5 Cross Aperture Arrays

The complementary structure to an array of crosses, an array of cross-shaped apertures in a metal, will exhibit a transmission maximum on resonance and low transmission off resonance. This can be easily predicted through the use of Babinet's principle as discussed in chapter 2. The modelled response for an array of cross-shaped apertures, the complement to that shown in *Figure 8.4.1* is presented in *Figure 8.4.18*.

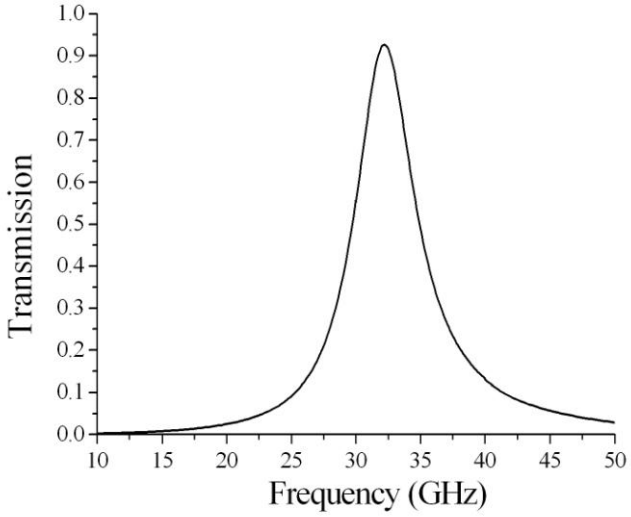

Figure 8.4.18*. Normal incidence modelled transmission for an array of cross-shaped apertures in 35 μm thickness copper,* $l = 3.45\ mm,\ 2a = 0.75\ mm,$ $2b = 0.2\ mm, \lambda_g = 4.2\ mm,\ t_d = 0.762\ mm..$

The permittivity of the dielectric layer in this modelling has been kept constant at $\varepsilon = 2.51 + 4.5\times10^{-3}i$ across the frequency range modelled, the same value used for the cross arrays. Arrays of cross apertures can also be used to form a resonant cavity however these results cannot be expected to be complementary to those from the cavity of crosses. Babinet's principle only applies to a two dimensional PEC screen and so cannot be used to predict the response of structures which exhibit structure in the third dimension. *Figure 8.4.19* shows the transmission response for two cross-aperture arrays separated by 12.5 mm.

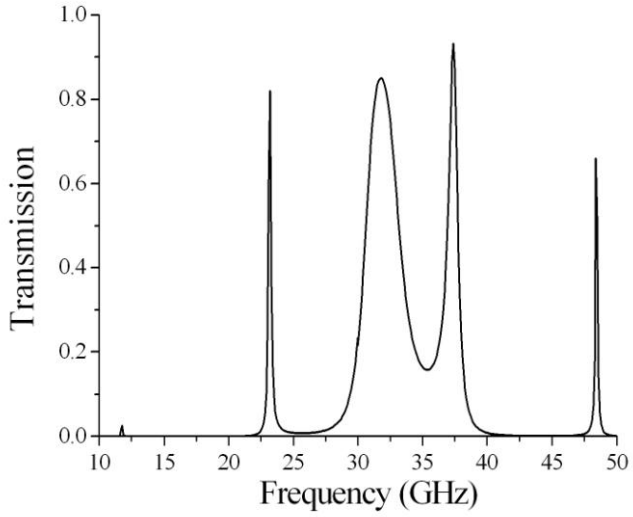

***Figure 8.4.19**. Modelled transmission intensity through two layers of cross-aperture arrays separated by 12.5 mm.*

A series of additional transmission peaks are observed, similar to that seen for the cross arrays. These transmission peaks are Fabry-Perot modes supported between the two arrays; it is clear that Babinet's principle does not hold for this system as the modes are observed as transmission peaks for both the original cross arrays and their complement, the cross-aperture arrays. The Fabry-Perot modes do have a different shape than those measured from the cross arrays, due to the reflection coefficient of the individual arrays being complementary. The modes that are far in frequency from the 'single layer' resonance have a high finesse due to the arrays being highly reflective off resonance. Closer to the resonant frequency the arrays are transmitting and therefore have a lower reflection coefficient resulting in Fabry-Perot modes with a lower finesse. This behaviour is the opposite to that observed with the cavity formed from arrays of crosses. Since all of the modes in this system are observed as transmission maxima on a low transmission background it is easier to distinguish and track their behaviour as the separation between the two arrays, *d* is varied.

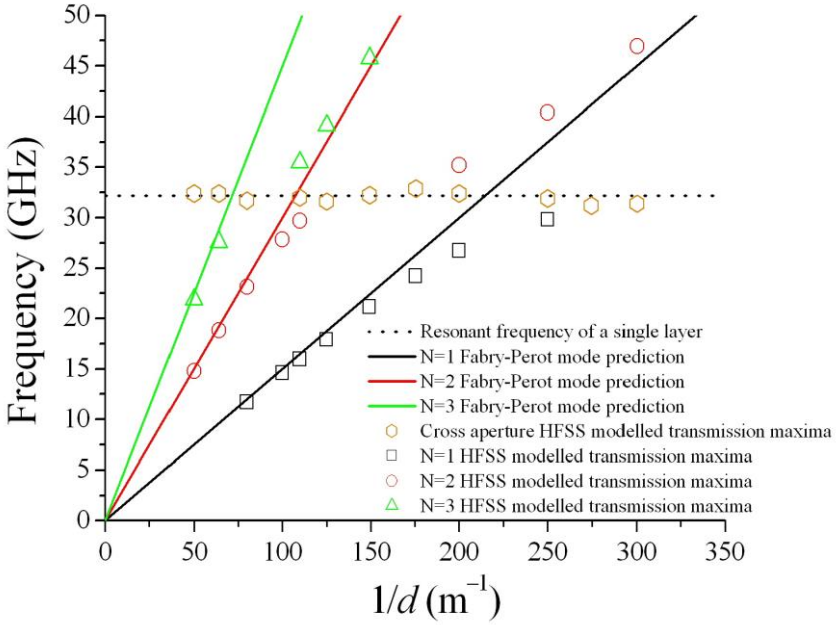

Figure 8.4.20*. Modelled transmission maxima for two arrays of cross apertures separated by a distance, d.*

The frequency of the modelled transmission maxima observed for two arrays of cross-apertures separated by a distance *d* is shown in *Figure 8.4.20*. For all the values of *d* the resonance observed for a single layer is also present and does not move significantly in frequency. The Fabry-Perot modes however do move in frequency as the separation is varied but like the previous structure the modes do not follow the typical Fabry-Perot analytical prediction which predicts that their frequency would be inversely proportional to the separation. At low frequencies, well below the resonance of the individual layers, the Fabry-Perot modes appear at frequencies that one may anticipate by the analytical prediction ($f = Nc/2l$) represented by the coloured solid lines on *Figure 8.4.20*. In this region the array can be described as having a surface impedance that is inductive, this is similar to the description of the corrugated metallic surfaces in chapter 2 and the reverse of the cross arrays described in *8.4.4*. The electric fields for the mode at 23.2 GHz for a separation of 12.5 mm, i.e. $(1/d) = 80$ are shown in *Figure 8.4.21*.

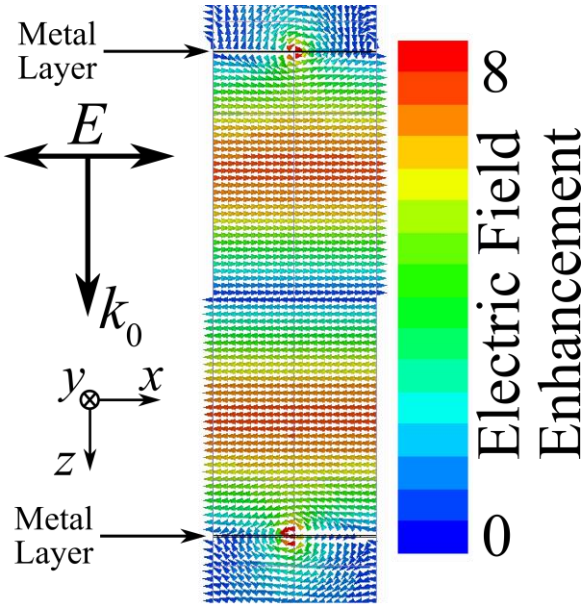

Figure 8.4.21. *Electric fields plotted at 23.2 GHz through the centre of the unit cell of two arrays of cross-apertures separated by 12.5 mm.*

The fields for this mode are very similar to a 2nd order Fabry-Perot mode of an etalon with two regions of high electric field and a node in the centre of the cavity. As the separation between the two arrays is reduced the mode diverges from the solid red Fabry-Perot line and converges with the resonance of the individual layers. The mode reappears on the high frequency side of the individual layer resonance and then converges towards the Fabry-Perot line associated with a quantisation of one less. In this region the surface impedance of the crosses can be described as being capacitive. The electric fields for this second order mode on the high frequency side of the cross resonance is shown in *Figure 8.4.22*.

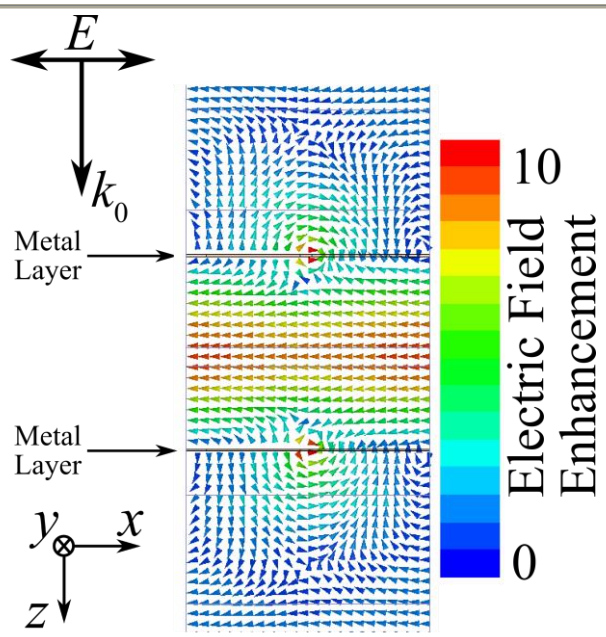

***Figure 8.4.22**. Electric fields plotted at 47 GHz through the centre of the unit cell of two arrays of cross-apertures separated by 3.33 mm.*

The fields of the mode are now very different to how they appeared at lower frequencies and resemble a first order Fabry-Perot mode with large electric field enhancement in the centre of the cavity. There has been a switch in the character of the fields of the Fabry-Perot modes as they have been swept through the resonant frequency. This is similar to the behaviour of the cross arrays and is due to the changing phase response of the crosses with frequency. At low frequencies the phase of the reflection/transmission from the cross-arrays is 180° as it is acting as a continuous metal layer inhibiting any transmission. This allows the cavity to support etalon-like Fabry-Perot modes. On resonance the phase change will be 0° as the structure is now transmitting, the change in phase causes the divergence from the Fabry-Perot prediction until the mode is no longer distinguishable from the single layer resonance. At high frequencies the phase of the reflection/transmission returns to a multiple of 180° and the Fabry-Perot modes return to the frequencies expected by a typical etalon. The modes supported between the cross-shaped apertures make a full transition from an *N* th order Fabry-Perot mode to an $(N-1)$ order Fabry-Perot mode (*Figure 8.4.20*) across the resonant frequency whereas the modes supported by the cavity formed from the cross arrays (*Figure 8.4.17*) appear to transition from and to a midpoint between the Fabry-Perot analytical predictions. At the present time it is not clear why there is a difference between the two scenarios.

8.5 Summary

In summary the transmission response of single and dual layer arrays of metallic crosses has been measured in the microwave regime. An array of crosses was found to support a dipole-like resonance with large electric fields along the length of the cross bars. At oblique angles of incidence and p-polarised incident radiation (or s-polarised at $\varphi = 45°$) it is possible to couple radiation to a high Q-factor quadrupole mode. The dispersive character of these modes has been experimentally measured and their field character investigated through the use of finite-element method modelling. Higher order modes have also been observed and discussed. Two arrays of crosses were used to form a Fabry-Perot cavity which can support modes which have electric field solutions that are quantised along the length of the cavity. The resonant frequency of these Fabry-Perot modes was found to be shifted from the typical etalon condition of $\lambda = Nc/2l$, with the shift dependent on the position of the Fabry-Perot modes relative to the resonant frequency of the crosses. This shift is due to the frequency dependent phase response of the arrays resulting in a change of the boundary conditions at the walls of the cavity thus making the cavity appear longer or shorter depending on the frequency.

The complementary structure to cross arrays, cross-aperture arrays have been modelled and it has been found that as predicted by Babinet's principle the transmission response of a single layer is complementary to that of the cross arrays. The response of a Fabry-Perot cavity composed of cross-apertures is however very different due to Babinet's principle now being not valid because of structure in the third dimension. The Fabry-Perot modes supported still shift with frequency but due to the phase response being such that the phase is zero on resonance of the crosses the Fabry-Perot modes are shifted greatest from the analytical prediction at the resonant frequency of the crosses.

The use of resonant mirrors to form Fabry-Perot cavities and multilayer frequency selective filters gives another freedom to designers to create tailor made transmission and reflection responses. The geometry of the resonant layers can be tuned to produce the desired frequency dependent reflection/transmission and phase responses. When combined to form a resonant cavity the separation between filters provides another dimension which can be used to customise the response.

9 Conclusions

9.1 Summary of Thesis

The studies within this thesis have shown that with appropriate structuring of metallic surfaces, the tailored control of the transmission of microwave radiation is possible. Through the excitation of coupled surface waves on regular hole arrays it is possible to observe transmission well below the waveguide cut-off of the holes. Likewise resonant phenomena can be observed on the complementary structure, an array of patches, whereby enhanced reflection is observed. The first three experimental chapters of this thesis focused on original studies of metallic arrays of patches and holes, the resonant enhanced transmission/reflection phenomena that they possess and the importance of metallic connectivity of the arrays on their electromagnetic response.

In chapter 4 the transmission of microwaves through regular square metallic patch and hole arrays is reported. The patches are oriented at 45° with respect to the square lattice; this unique geometry enables the size of them to be increased until they connect at the corners at a 50% metallic occupancy. This allows a study of the influence of the metallic connectivity of the arrays on the transmission properties. The results obtained from these studies were remarkably different to what one may expect when compared to a D.C. percolation study. One may have anticipated the transmission to fall suddenly across the connectivity threshold as the D.C. conductivity rises rapidly however this is not always the case. Since these arrays have a regular periodicity they can support surface waves which dominate their transmission response resulting in a remarkably counter-intuitive metallic filling fraction dependence at some frequencies where the transmission increased as the metallic content was increased. This is due to the transition across the connectivity threshold from a disconnected patch array which exhibits enhanced reflection on resonance to a connected hole array which exhibits enhanced transmission. These results are compared with results from a percolation study that was performed with arrays of overlapping metallic discs with random position and size. The random arrays however have no defined periodicity and therefore do not support strongly coupled surface modes. The lack of surface modes results in a much smoother metallic-filling-fraction-dependent transmission response. The complementary structure, a random array of holes, was also studied which

exhibited no fast transition behaviour although the response was different to the random disc structures indicating that the choice of structure is important as well as the amount of metallic content in the system.

In chapter 5 the regular patch and hole arrays studied in chapter 4 are further explored through measurements of their incident-angle-dependent transmission response. Through these measurements the dispersion of the surface modes supported are mapped out. It is found, that as predicted by Babinet's principle, the response of a complementary pair of patch and hole arrays only produces a complementary response if the polarisation of the incident radiation is rotated by 90°. The dispersion of the modes is found to either follow the linear in-plane or parabolic out-of-plane diffracted light lines depending on the incident polarisation and connectivity of the structure. It is found through examination of electric and magnetic field plots obtained through finite-element method modelling that the dominant scattering mechanism (in-plane or out-of-plane) is related to periodicity present within these fields. The connected structure showed periodicity in the magnetic fields as a result of being able to support currents across the surface of the structure, whereas the complementary patch structure exhibited periodicity in the electric fields.

In chapter 6 the transmission response of hole arrays was further studied however this time focused on the situations where multiple modes can be supported. Two regimes were studied, large holes where the waveguide cut-off frequency of the holes lies below the diffraction edge and small holes where the cut-off lies above the diffraction edge. Modal matching modelling predicted that a series of coupled surface modes are supported on hole arrays with the electric field quantised along the length of the hole. The periodicity and size of the holes in the array determines the band structure and which modes can be coupled to at normal incidence with a plane wave. It was found that if the cut-off lies above the onset of diffraction only two modes were present, a symmetric and an anti-symmetric mode, these modes have an evanescent field character in the holes since propagating fields cannot be supported below the cut-off frequency. If the cut-off frequency lies above the onset of diffraction a series of symmetric and anti-symmetric propagating modes can be supported between the cut-off frequency and the diffraction edge. The number of modes supported is dependent on the thickness of the array due to the electric field being quantised along the length of the hole.

In chapter 7 remarkable transmission enhancement through a thin continuous metal film is achieved through the use of resonant cavities either side of the film. Each resonant cavity consists of arrays of metallic strips separated from the metal film by a dielectric layer. On resonance a standing wave is supported within the dielectric layer, the structure is symmetric allowing efficient coupling on the transmitted side to free space. Transmission on resonance of the fundamental mode of the system is recorded at ~ 35 %, a significant enhancement on the < 0.1 % transmission achievable through the standalone film. The first three modes of the system are recorded and explained with the use of electric fields produced from finite-element method modelling. Due to the symmetry of the fields only the odd order modes can be coupled to at normal incidence, this is highlighted through incident angle dependent measurements.

In chapter 8 the transmission of another novel resonant cavity was experimentally investigated; a Fabry-Perot cavity formed from an array of resonant crosses, a 'resonant mirror' Fabry Perot. Measurements were performed for a single layer of crosses and its resonant dipolar stop-band behaviour observed. Incident-angle-dependent studies were performed and the dispersion of supported modes mapped out. Two arrays were then spaced apart to form a cavity which supports a series of Fabry-Perot modes. These modes manifest themselves as a series of transmission maxima whose frequency and finesse depends on the spacing of the arrays and the modes' relative position to the resonant frequency of the crosses. The relative frequency of the cross mode is important due to the frequency dependent phase and transmission/reflection response of the crosses. On resonance the reflection coefficient is high leading to modes with a high finesse; in the wings of the resonance the modes have a lower finesse as the reflectivity coefficient of the arrays is lower. The frequency dependent phase response shifts the frequency of the Fabry-Perot modes due to the change in boundary conditions at the walls of the cavity and hence the wavelength that is fit inside on resonance. Since the geometry of the arrays can be tuned to produce the desired frequency dependent reflection/transmission and phase response this structure could provide a versatile frequency selective screen solution.

Overall, the experimental studies within this thesis have shown that there are numerous ways in which one can manipulate the transmission of microwave radiation with metallic structure. Experimental results give good agreement with modelling techniques and phenomena explained through the use of modelled field plots. Through

careful consideration of structures' geometries, responses can potentially be tailor-made to suit the purpose. Further potential ideas for controlling and manipulating microwaves are discussed in *Section 9.2*.

9.2 Future Work

In this section some ideas for possible future study are considered and discussed. Since a number of different areas of microwave photonics have been discussed in this thesis there are many ways in which some of the work can be expanded.

The work in chapter 4 explored the response of regular and random metallic arrays and showed that the response they exhibited were both very different. One of the interesting areas that could be investigated further is the regime between regular arrays and highly random arrays, i.e. the effect of gradually introducing randomness to a regular structure to observe how much disorder is needed to have a significant effect. This could mean taking a regular array of patches and adding small levels of disorder by introducing rotation, translation or size and pitch variation across the array (*Figure 9.2.1*).

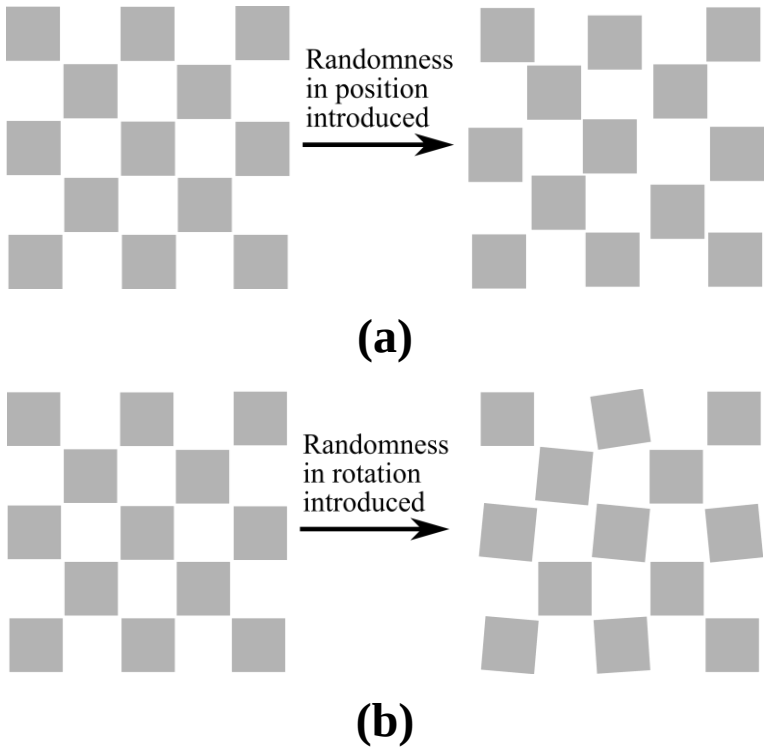

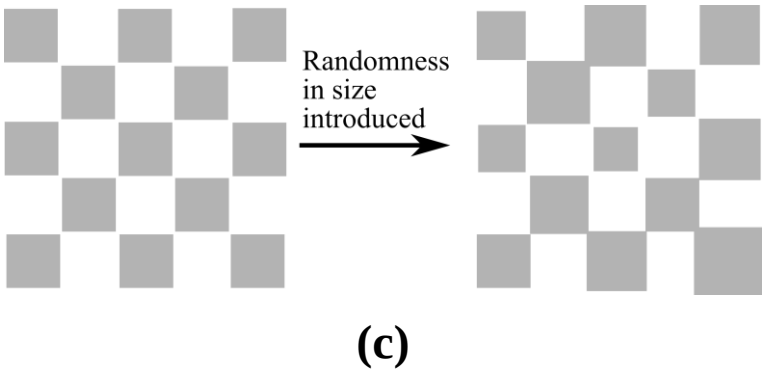

Figure 9.2.1. *Schematic illustration of introduction of randomness into a periodic array.* ***(a)*** *Random position,* ***(b)*** *Random rotation,* ***(c)*** *Random size*

Reducing the order of the arrays will weaken coupling to surface modes as the reduction in perfect periodicity weakens diffraction. This is likely to reduce the presence of sudden transitions in the metallic filling fraction response as deep strongly coupled modes will not be present in the transmission spectra. Near the transition threshold introducing disorder will also introduce some localised connectivity which occurs in the formation of random arrays. The major challenge with a study of this type is the modelling of such systems because, as previously mentioned, the system cannot be reduced to a unit cell thus requiring the whole array to be modelled.

An interesting geometry that is not periodic is deterministic aperiodic tiling[193]. This type of tiling uses a set of rules to define the structure however it is non-periodic and so lies between the regular and random regimes discussed in this thesis. Since it is non-periodic it exhibits no translational symmetry however it may have short range order (e.g. Penrose tiling[194]) and may produce a diffraction pattern.

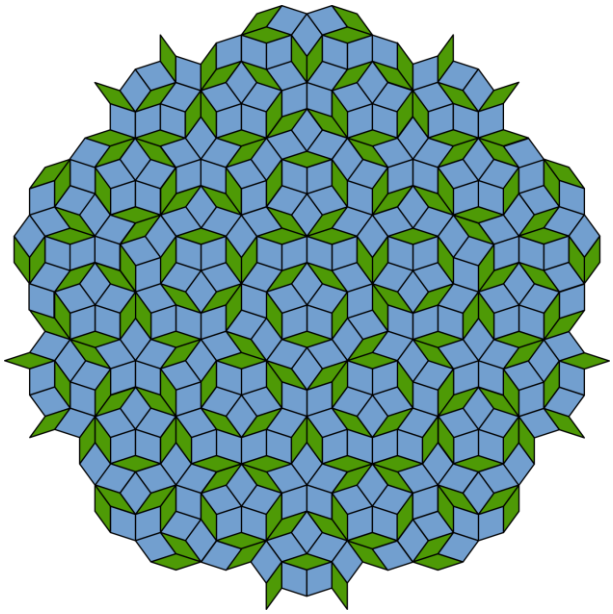

***Figure 9.2.2**. A schematic illustration of Penrose tiling[195] formed from 2 different sub-units.*

This type of geometry has been studied in the visible regime[196-198] but does not appear to have been studied extensively at microwave frequencies[199-201] and may provide a useful and interesting response that cannot be achieved with traditional regular or random arrays.

The regular arrays investigated in chapter 4 exhibited a sudden change in transmission behaviour across the connectivity threshold. This response could be manipulated so that a switching is obtained by turning connectivity on or off as desired. An array of patches which are close to 50 % occupancy could be joined together at the corners with a photo-reactive element whose conductivity can be altered by adjusting the amount of light incident upon it (*Figure 9.2.3*).

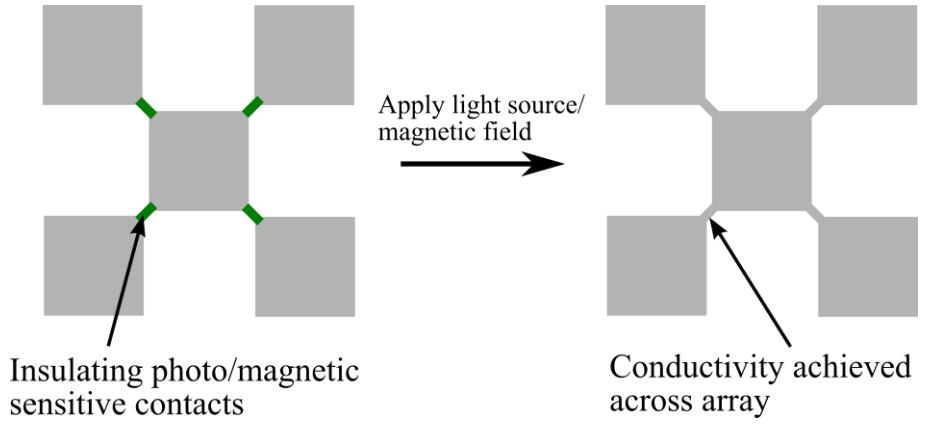

Figure 9.2.3*. Schematic illustration of an array of patches connected by photo/magnetic sensitive contacts which form a conducting array on application of a light source/magnetic field*

This type of contact would allow the array to be switched from being disconnected to connected very quickly resulting in a switching from a transmitting screen to a reflecting screen. Switching of this type could also possibly be implemented with the use of a magnetic material that would perform switching on application of an external magnetic field.

9.3 List of Publications, Presentations and Awards

J. D. Edmunds, E. Hendry, A. P. Hibbins, J. R. Sambles and I. J. Youngs
Multi-modal transmission of microwaves through hole arrays
Optics Express, **19**, 13793, 2011

M. C. Taylor, **J. D. Edmunds**, E. Hendry, A. P. Hibbins, J. R. Sambles
Microwave response of hole and patch arrays
Physical Review B **82**, 155105, 2010

J. D. Edmunds, M. C. Taylor, A. P. Hibbins, J. R. Sambles and I. J. Youngs
Babinet's Principle and the band structure of surface waves on patterned metal arrays
Journal of Applied Physics **107**, 103108, 2010

J. D. Edmunds, A. P. Hibbins, J. R. Sambles and I. J. Youngs
Resonantly inverted microwave transmissivity threshold of metal grids
New Journal of Physics **12**, 063007, 2010

J. D. Edmunds, M. C. Taylor, A. P. Hibbins, J. R. Sambles and I. J. Youngs
Babinet's Principle and the dispersion of surface waves on complementary patterned metal arrays
Meta'10, Cairo, Egypt (Oral presentation)

M. C. Taylor, **J. D. Edmunds**, E. Hendry, A. P. Hibbins and J. R. Sambles
Enhanced reflection from arrays of metal patches
Metamorphose 2009, London, U. K. (Poster)

J. D. Edmunds, A. P. Hibbins, J. R. Sambles and I. J. Youngs
Microwave studies of thin structured metal-dielectric films
Dielectrics 2009, Reading, U. K. (Oral presentation)

J. D. Edmunds
Mansel Davies Award (best presentation by an early career researcher)
Dielectrics 2009, Reading, U. K.

J. D. Edmunds, A. P. Hibbins, J. R. Sambles and I. J. Youngs
Microwave transmission of thin composite metal-dielectric films
Nanometa 2009, Seefeld, Austria (Poster)

10 References

[1] B. A. Munk, *Frequency Selectve Surfaces:Theory and Design* (Wiley-Interscience, New York, 2000).

[2] J. B. Pendry, L. Martin-Moreno, and F. J. Garcia-Vidal, Science **305,** 847 (2004).

[3] A. P. Hibbins, B. R. Evans, and J. R. Sambles, Science **308,** 670 (2005).

[4] D. R. Smith and N. Kroll, Physical Review Letters **85,** 2933 (2000).

[5] K. Uller, Thesis, University Rostock, 1903.

[6] J. Zenneck, Annalen Der Physik **28** (1909).

[7] A. Sommerfeld, Ann. Phys. Chem. **67** (1899).

[8] R. W. Wood, Philos. Mag. **4** (1902).

[9] H. M. Barlow, A. L. Cullen, G. G. Macfarlane, B. I. Stuart, J. G. Linhart, R. B. Dyott, and A. E. Karbowiak, Proceedings of the Institution of Electrical Engineers-London **100,** 329 (1953).

[10] A. L. Cullen, Proceedings of the IEE - Part IV: Institution Monographs **101,** 225 (1954).

[11] D. Sievenpiper, Z. Lijun, R. F. J. Broas, N. G. Alexopolous, and E. Yablonovitch, Microwave Theory and Techniques, IEEE Transactions on **47,** 2059 (1999).

[12] T. W. Ebbesen, H. J. Lezec, H. F. Ghaemi, T. Thio, and P. A. Wolff, Nature **391,** 667 (1998).

[13] H. A. Bethe, Physical Review **66,** 163 (1944).

[14] H. F. Ghaemi, T. Thio, D. E. Grupp, T. W. Ebbesen, and H. J. Lezec, Physical Review B **58,** 6779 (1998).

[15] M. Babinet, C. R. Acad. Sci. **4,** 638 (1837).

[16] H. G. Booker, Electrical Engineers - Part IIIA: Radiolocation, Journal of the Institution of **93,** 620 (1946).

[17] HFSS, (Ansoft Corporation, Pittsburgh).

[18] A. P. Hibbins, J. R. Sambles, C. R. Lawrence, and J. R. Brown, Physical Review Letters **92,** 4 (2004).

[19] R. Ulrich, Applied Optics **7,** 1987 (1968).

[20] R. Levy and S. B. Cohn, Microwave Theory and Techniques, IEEE Transactions on **32,** 1055 (1984).

[21] R. Ulrich, Infrared Physics **7,** 37 (1967).

[22] F. J. G. de Abajo, Reviews of Modern Physics **79,** 1267 (2007).

[23] F. J. Garcia-Vidal, L. Martin-Moreno, T. W. Ebbesen, and L. Kuipers, Reviews of Modern Physics **82,** 729 (2010).

[24] M. J. Lockyear, A. P. Hibbins, J. R. Sambles, and C. R. Lawrence, Applied Physics Letters **84,** 2040 (2004).

[25] M. J. Lockyear, A. P. Hibbins, J. R. Sambles, and C. R. Lawrence, Applied Physics Letters **83,** 806 (2003).

[26] M. J. Lockyear, A. P. Hibbins, and J. R. Sambles, Physical Review Letters **102,** 073901 (2009).

[27] N. Engheta and R. W. Ziolkowski, *Metamaterials: Physics and Engineering Explorartions* (John Wiley and Sons Inc., Danvers, 2006).

[28] J. B. Pendry, A. J. Holden, W. J. Stewart, and I. Youngs, Physical Review Letters **76,** 4773 (1996).

[29] J. B. Pendry, A. J. Holden, D. J. Robbins, and W. J. Stewart, Microwave Theory and Techniques, IEEE Transactions on **47,** 2075 (1999).

[30] V. G. Veselago, Sov. Phys. Usp. **10** (1968).

[31] R. Liu, C. Ji, J. J. Mock, J. Y. Chin, T. J. Cui, and D. R. Smith, Science **323,** 366 (2009).

[32] B. J. Justice, J. J. Mock, L. Guo, A. Degiron, D. Schurig, and D. R. Smith, Opt. Express **14,** 8694 (2006).

[33] D. Schurig, J. B. Pendry, and D. R. Smith, Opt. Express **14,** 9794 (2006).

[34] D. Schurig, J. J. Mock, B. J. Justice, S. A. Cummer, J. B. Pendry, A. F. Starr, and D. R. Smith, Science **314,** 977 (2006).

[35] J. B. Pendry, Physical Review Letters **85,** 3966 (2000).

[36] R. W. Ziolkowski and E. Heyman, Physical Review E **64,** 056625 (2001).

[37] J. Valentine, S. Zhang, T. Zentgraf, E. Ulin-Avila, D. A. Genov, G. Bartal, and X. Zhang, Nature **455,** 376 (2008).

[38] B. Wang and et al., Journal of Optics A: Pure and Applied Optics **11,** 114003 (2009).

[39] S. Tretyakov, A. Sihvola, and L. Jylhä, Photonics and Nanostructures - Fundamentals and Applications **3,** 107 (2005).

[40] E. Hecht, *Optics* (Addison-Wesley Publishing Company, London, 1974).

[41] E. A. Parker, in *17th QMW Antenna Symposium* (London, 1991).

[42] M. Born and E. Wolf, *Principles of Optics* (Cambridge University Press, Cambridge, 1997).

[43] R. W. Wood, Philosophical Magazine **4,** 396 (1902).

[44] L. Rayleigh, Philos. Mag. **14** (1907).

[45] R. W. Wood, Philosophical Magazine **23,** 310 (1912).

[46] R. W. Wood, Physical Review **48,** 928 (1935).

[47] L. R. Ingersoll, Astrophysical Journal **51,** 129 (1920).

[48] J. Strong, Phys. Rev. **48** (1935).

[49] U. Fano, Journal of the Optical Society of America **31,** 213 (1941).

[50] D. Pines and D. Bohm, Physical Review **85,** 338 (1952).

[51] R. A. Ferrell, Physical Review **111,** 1214 (1958).

[52] W. Steinmann, Physical Review Letters **5,** 470 (1960).

[53] W. Rotman, Proceedings of the IRE **39,** 952 (1951).

[54] G. Goubau, Journal of Applied Physics **21,** 1119 (1950).

[55] G. Goubau, Proceedings of the IRE **40,** 865 (1952).

[56] C. H. Palmer, Journal of the Optical Society of America **42,** 269 (1952).

[57] Y. Y. Teng and E. A. Stern, Physical Review Letters **19,** 511 (1967).

[58] R. H. Ritchie, E. T. Arakawa, J. J. Cowan, and R. N. Hamm, Physical Review Letters **21,** 1530 (1968).

[59] D. Beaglehole, Physical Review Letters **22,** 708 (1969).

[60] R. E. Collin, *Field Theory of Guided Waves* (John Wiley & Sons, New York, 1991).

[61] P. Drude, Annalen Der Physik **1,** 566 (1900).

[62] C. F. Bohren and D. R. Huffman, *Absorption and Scattering of Light by Small Particles* (Wiley-VCH, New York, 1998).

[63] C. C. Cutler and Ieee, in *Ieee Antennas and Propagation Society International Symposium 1994, Vols I-Iii* (I E E E, New York, 1994), p. 1456.

[64] A. Otto, Zeitschrift Fur Physik **216,** 398 (1968).

[65] E. Kretchmann and H. Raether, Z. Naturf. A **23** (1968).

[66] E. Yablonovitch, Journal of the Optical Society of America B-Optical Physics **10,** 283 (1993).

[67] Y. J. Chen, E. S. Koteles, R. J. Seymour, G. J. Sonek, and J. M. Ballantyne, Solid State Communications **46,** 95 (1983).

[68] W. L. Barnes, T. W. Preist, S. C. Kitson, and J. R. Sambles, Physical Review B **54,** 6227 (1996).

[69] R. A. Watts, A. P. Hibbins, and J. R. Sambles, Journal of Modern Optics **46,** 2157 (1999).

[70] E. N. Economou, Physical Review **182,** 539 (1969).

[71] L. Martin-Moreno, F. J. Garcia-Vidal, H. J. Lezec, K. M. Pellerin, T. Thio, J. B. Pendry, and T. W. Ebbesen, Physical Review Letters **86,** 1114 (2001).

[72] S. A. Darmanyan and A. V. Zayats, Physical Review B **67,** 035424 (2003).

[73] W. L. Barnes, W. A. Murray, J. Dintinger, E. Devaux, and T. W. Ebbesen, Physical Review Letters **92,** 4 (2004).

[74] S. T. Shanahan and N. R. Heckenberg, Applied Optics **20,** 4019 (1981).

[75] L. B. Whitbourn and R. C. Compton, Applied Optics **24,** 217 (1985).

[76] D. H. Dawes, R. C. Mcphedran, and L. B. Whitbourn, Applied Optics **28,** 3498 (1989).

[77] F. J. G. de Abajo, R. Gomez-Medina, and J. J. Saenz, Physical Review E **72** (2005).

[78] B. Hou, Z. H. Hang, W. J. Wen, C. T. Chan, and P. Sheng, Applied Physics Letters **89,** 3 (2006).

[79] M. Beruete, M. Sorolla, I. Campillo, J. S. Dolado, L. Martin-Moreno, J. Bravo-Abad, and F. J. Garcia-Vidal, Optics Letters **29,** 2500 (2004).

[80] M. Beruete, M. Sorolla, I. Campillo, and J. S. Dolado, Ieee Microwave and Wireless Components Letters **15,** 116 (2005).

[81] F. J. Garcia-Vidal, L. Martin-Moreno, and J. B. Pendry, Journal of Optics a-Pure and Applied Optics **7,** S97 (2005).

[82] L. F. Shen, X. D. Chen, and T. J. Yang, Optics Express **16,** 3326 (2008).

[83] J. Bravo-Abad, L. Martin-Moreno, F. J. Garcia-Vidal, E. Hendry, and J. G. Rivas, Physical Review B **76,** 4 (2007).

[84] E. Hendry, A. P. Hibbins, and J. R. Sambles, Physical Review B **78,** 10 (2008).

[85] J. Bravo-Abad, Garc, iacute, F. J. a-Vidal, Mart, and L. n-Moreno, Physical Review Letters **93,** 227401 (2004).

[86] K. Yee, Antennas and Propagation, IEEE Transactions on **14,** 302 (1966).

[87] A. Taflove, Electromagnetic Compatibility, IEEE Transactions on **EMC-22,** 191 (1980).

[88] T. Weiland, Aeu-International Journal of Electronics and Communications **31,** 116 (1977).

[89] P. B. Johns and R. L. Beurle, Electrical Engineers, Proceedings of the Institution of **118,** 1203 (1971).

[90] W. C. Gibson, *The Method of Moments in Electromagnetics* (Taylor and Francis, Boca Raton, 2008).

[91] J. R. Bell, Commun. ACM **11,** 498 (1968).

[92] R. Knop, Commun. ACM **12,** 281 (1969).

[93] M. R. Gadsdon, Thesis, University of Exeter, 2009.

[94] M. G. Moharam and T. K. Gaylord, Journal of the Optical Society of America **71,** 811 (1981).

[95] L. C. Botten, M. S. Craig, and R. C. McPhedran, Optica Acta **28,** 1103 (1981).

[96] L. C. Botten, M. S. Craig, R. C. McPhedran, J. L. Adams, and J. R. Andrewartha, Optica Acta **28,** 1087 (1981).

[97] J. Chandezon, D. Maystre, and G. Raoult, Journal of Optics-Nouvelle Revue D Optique **11,** 235 (1980).

[98] C. Genet and T. W. Ebbesen, Nature **445,** 39 (2007).

[99] I. V. Antonets, L. N. Kotov, S. V. Nekipelov, and E. N. Karpushov, Technical Physics **49,** 1496 (2004).

[100] R. J. Kelly, M. J. Lockyear, J. R. Suckling, J. R. Sambles, and C. R. Lawrence, Applied Physics Letters **90** (2007).

[101] R. C. Hansen and W. T. Pawlewicz, Ieee Transactions on Microwave Theory and Techniques **30,** 2064 (1982).

[102] A. N. Lagarkov, K. N. Rozanov, A. K. Sarychev, and N. A. Simonov, Physica A **241,** 199 (1997).

[103] Kirkpatr.S, Reviews of Modern Physics **45,** 574 (1973).

[104] I. J. Youngs, Iee Proceedings-Science Measurement and Technology **147,** 202 (2000).

[105] I. J. Youngs, Journal of Physics D-Applied Physics **35,** 3127 (2002).

[106] B. J. Last and D. J. Thouless, Physical Review Letters **27,** 1719 (1971).

[107] R. C. Compton, Ieee Transactions on Microwave Theory and Techniques **33,** 1083 (1985).

[108] R. C. Compton, J. C. Macfarlane, L. B. Whitbourn, M. M. Blanco, and R. C. Mcphedran, Optica Acta **31,** 515 (1984).

[109] P. J. Flory, Journal of the American Chemical Society **63,** 3083 (1941).

[110] W. H. Stockmayer, Journal of Chemical Physics **11,** 45 (1943).

[111] S. R. Broadbent and J. M. Hammersley, Proceedings of the Cambridge Philosophical Society **53,** 629 (1957).

[112] J. M. Hammersley, Proceedings of the Cambridge Philosophical Society **53,** 642 (1957).

[113] D. Stauffer, *Introduction to Percolation Theory* (Taylor and Francis, London and Philadelphia, 1985).

[114] S. Galam and A. Mauger, Physical Review E **56,** 322 (1997).

[115] J. Gurland, Transactions of the Metallurgical Society of Aime **236,** 642 (1966).

[116] A. Malliaris and D. T. Turner, Journal of Applied Physics **42,** 614 (1971).

[117] D. S. McLachlan, Journal of Physics C-Solid State Physics **20,** 865 (1987).

[118] I. V. Antonets, L. I. Kotov, S. V. Nekipelov, V. G. Shavrov, and V. I. Shcheglov, Journal of Communications Technology and Electronics **49,** 1164 (2004).

[119] J. J. Thomson, Proceedings of the Cambridge Philosophical Society **11,** 120 (1901).

[120] E. H. Sondheimer, Advances in Physics **1,** 1 (1952).

[121] K. Fuchs, Proceedings of the Cambridge Philosophical Society **34,** 100 (1938).

[122] A. F. Mayadas and M. Shatzkes, Physical Review B **1,** 1382 (1970).

[123] Inkscape, (The Inkscape Team, 2008).

[124] F. J. G. de Abajo and J. J. Saenz, Physical Review Letters **95** (2005).

[125] D. M. Pozar, *Microwave Engineering* (John Wiley and Sons Inc, 2005).

[126] U. Fano, Physical Review **1,** 1866 (1961).

[127] S. Tretyakov and S. Constantin, in *Electromagnetic response of thin metamaterial layers*, 2008 (SPIE Newsroom).

[128] P. Ikonen, E. Saenz, R. Gonzalo, C. Simovski, and S. Tretyakov, Metamaterials **1,** 89 (2007).

[129] E. Saenz, P. M. T. Ikonen, R. Gonzalo, and S. A. Tretyakov, Journal of Applied Physics **101,** 114910 (2007).

[130] C. R. Simovski and S. A. Tretyakov, Physical Review B **75,** 195111 (2007).

[131] H. Raether, *Surface Plasmons on Smooth and Rough Surfaces and on Gratings* (Springer-Verlag, Berlin, 1988).

[132] U. Schroter and D. Heitmann, Physical Review B **58,** 15419 (1998).

[133] J. A. Porto, F. J. Garcia-Vidal, and J. B. Pendry, Physical Review Letters **83,** 2845 (1999).

[134] H. E. Went, A. P. Hibbins, J. R. Sambles, C. R. Lawrence, and A. P. Crick, Applied Physics Letters **77,** 2789 (2000).

[135] S. Astilean, P. Lalanne, and M. Palamaru, Optics Communications **175,** 265 (2000).

[136] S. Collin, G. Vincent, R. Haidar, N. Bardou, S. Rommeluere, and J. L. Pelouard, Physical Review Letters **104,** 4 (2010).

[137] C. C. Chen, Ieee Transactions on Microwave Theory and Techniques **MT19,** 475 (1971).

[138] R. Ulrich and M. Tacke, Applied Physics Letters **22,** 251 (1973).

[139] T. Thio, H. F. Ghaemi, H. J. Lezec, P. A. Wolff, and T. W. Ebbesen, Journal of the Optical Society of America B-Optical Physics **16,** 1743 (1999).

[140] E. Popov, M. Neviere, S. Enoch, and R. Reinisch, Physical Review B **62,** 16100 (2000).

[141] A. Krishnan, T. Thio, T. J. Kima, H. J. Lezec, T. W. Ebbesen, P. A. Wolff, J. Pendry, L. Martin-Moreno, and F. J. Garcia-Vidal, Optics Communications **200,** 1 (2001).

[142] J. Braun, B. Gompf, G. Kobiela, and M. Dressel, Physical Review Letters **103** (2009).

[143] S. Collin, C. Sauvan, C. Billaudeau, F. Pardo, J. C. Rodier, J. L. Pelouard, and P. Lalanne, Physical Review B **79,** 7 (2009).

[144] B. K. Minhas, W. Fan, K. Agi, S. R. J. Brueck, and K. J. Malloy, Journal of the Optical Society of America a-Optics Image Science and Vision **19,** 1352 (2002).

[145] A. A. Kirilenko and A. O. Perov, Ieee Transactions on Antennas and Propagation **56,** 3210 (2008).

[146] V. Lomakin and E. Michielssen, Physical Review B **71** (2005).

[147] J. R. Suckling, J. R. Sambles, and C. R. Lawrence, New Journal of Physics **9** (2007).

[148] O. Heaviside, *Electromagnetic Theory*, Vol. 1 (1893).

[149] L. Rayleigh, Philos. Mag. **43,** 125 (1897).

[150] G. C. Southworth, Bell System Technical Journal **15,** 284 (1936).

[151] G. C. Southworth, Proceedings of the Institute of Radio Engineers **25,** 807 (1937).

[152] K. S. Packard, Trans. Micro. Theory and Tech. **32,** 961 (1984).

[153] R. C. Mcphedran, G. H. Derrick, and L. C. Botten, *Electromagnetic Theory of Gratings* (Springer-Verlag, Berlin, 1980).

[154] J. W. Gadzuk, Physical Review B **1,** 1267 (1970).

[155] D. Sarid, Physical Review Letters **47,** 1927 (1981).

156 J. J. Burke, G. I. Stegeman, and T. Tamir, Physical Review B **33,** 5186 (1986).

157 F. Yang, J. R. Sambles, and G. W. Bradberry, Physical Review B **44,** 5855 (1991).

158 J. D. Edmunds, M. C. Taylor, A. P. Hibbins, J. R. Sambles, and I. J. Youngs, Journal of Applied Physics **107** (2010).

159 I. R. Hooper and J. R. Sambles, Optics Express **16,** 17249 (2008).

160 I. R. Hooper, T. W. Preist, and J. R. Sambles, Physical Review Letters **97,** 4 (2006).

161 C. Fabry and A. Perot, Annales de Chimie et de Physique **115** (1899).

162 Y. Takakura, Physical Review Letters **86,** 5601 (2001).

163 J. R. Suckling, A. P. Hibbins, M. J. Lockyear, T. W. Preist, J. R. Sambles, and C. R. Lawrence, Physical Review Letters **92,** 4 (2004).

164 L. Rayleigh, Proceedings of the Royal Society of London **41,** 275 (1886).

165 I. Moreno, J. J. Araiza, and M. Avendano-Alejo, Opt. Lett. **30,** 914 (2005).

166 M. Razavy, *Quantum Theory of Tunneling* (World Scientific Publishing Co., Singapore, 2003).

167 E. E. Hall, Physical Review **15,** 73 (1902).

168 S. Zhu, A. W. Yu, D. Hawley, and R. Roy, American Journal of Physics **54,** 601 (1986).

169 R. Dragila, B. Lutherdavies, and S. Vukovic, Physical Review Letters **55,** 1117 (1985).

170 S. Tomita, T. Yokoyama, H. Yanagi, B. Wood, J. B. Pendry, M. Fujii, and S. Hayashi, Optics Express **16,** 9942 (2008).

171 L. Zhou, W. J. Wen, C. T. Chan, and P. Sheng, Physical Review Letters **94,** 4 (2005).

172 Eurotech(PLC), (Exmouth, U.K.).

173 S. T. Chase and R. D. Joseph, Applied Optics **22,** 1775 (1983).

174 K. D. Möller, J. B. Warren, J. B. Heaney, and C. Kotecki, Appl. Opt. **35,** 6210 (1996).

175 K. D. Moller, O. Sternberg, H. Grebel, and K. P. Stewart, Applied Optics **41,** 1942 (2002).

176 A. P. Hibbins, M. J. Lockyear, and J. R. Sambles, Journal of Applied Physics **99,** 5 (2006).

177 R. Ulrich, K. F. Renk, and L. Genzel, Microwave Theory and Techniques, IEEE Transactions on **11,** 363 (1963).

[178] T. Timusk and P. L. Richards, Appl. Opt. **20,** 1355 (1981).

[179] V. P. Tomaselli, D. C. Edewaard, P. Gillan, and K. D. Möller, Appl. Opt. **20,** 1361 (1981).

[180] L. A. Page, E. S. Cheng, B. Golubovic, J. Gundersen, and S. S. Meyer, Appl. Opt. **33,** 11 (1994).

[181] O. Sternberg, K. D. Moller, H. Grebel, K. P. Stewart, and R. M. Henry, Infrared Physics & Technology **44,** 17 (2003).

[182] H. A. Smith, M. Rebbert, and O. Sternberg, Applied Physics Letters **82,** 3605 (2003).

[183] D. W. Porterfield, J. L. Hesler, R. Densing, E. R. Mueller, T. W. Crowe, and R. M. Weikle, Applied Optics **33,** 6046 (1994).

[184] A. F. Wickersham, Journal of Applied Physics **29,** 1537 (1958).

[185] E. C. Jordan and K. G. Balmain, *Electromagnetic Waves and Radiating Systems* (Prentice-Hall, New Jersey, 1950).

[186] R. C. Hansen, Proceedings of the Ieee **69,** 170 (1981).

[187] R. N. Clarke and C. B. Rosenberg, Journal of Physics E-Scientific Instruments **15,** 9 (1982).

[188] R. Sauleau, P. Coquet, J. P. Daniel, T. Matsui, and N. Hirose, International Journal of Infrared and Millimeter Waves **19,** 1693 (1998).

[189] R. Sauleau, P. Coquet, J. P. Daniel, T. Matsui, and N. Hirose, Ieee Microwave and Guided Wave Letters **9,** 189 (1999).

[190] C. A. M. Butler, J. Parsons, J. R. Sambles, A. P. Hibbins, and P. A. Hobson, Applied Physics Letters **95,** 3 (2009).

[191] K. D. Moller, O. Sternberg, H. Grebel, and K. P. Stewart, Applied Optics **41,** 3919 (2002).

[192] K. D. Möller, K. R. Farmer, D. V. P. Ivanov, O. Sternberg, K. P. Stewart, and P. Lalanne, Infrared Physics & Technology **40,** 475 (1999).

[193] B. Grunbaum and G. C. Shephard, *Tilings and Patterns* (W. H. Freeman and Company, 1986).

[194] M. Gardner, *Penrose tiles to trapdoor ciphers* (W. H. Freeman and Company, 1988).

[195] http://en.wikipedia.org/wiki/Penrose_tiling, *Penrose Tiling* (2009).

[196] F. Przybilla, C. Genet, and T. W. Ebbesen, Applied Physics Letters **89,** 121115 (2006).

[197] R. Shugayev, Optics Express **18,** 24946 (2010).

[198] A. Gopinath, S. V. Boriskina, N. N. Feng, B. M. Reinhard, and L. Dal Negro, Nano Letters **8,** 2423 (2008).

[199] I. Gallina, A. Della Villa, V. Galdi, V. Pierro, F. Capolino, S. Enoch, G. Tayeb, and G. Gerini, Ieee Antennas and Wireless Propagation Letters **7,** 54 (2008).

[200] H. Q. Li, Z. H. Hang, Y. Q. Qin, Z. Y. Wei, L. Zhou, Y. W. Zhang, H. Chen, and C. T. Chan, Applied Physics Letters **86,** 3 (2005).

[201] X. Gong, W. H. She, and W. J. Chappell, Iet Microwaves Antennas & Propagation **1,** 240 (2007).